

AN ABSTRACT OF THE DISSERTATION OF

Joshua Flynn for the degree of Doctor of Philosophy in Chemistry presented on March 7, 2017.

Title: Substitution Effects on the Structure and Electronic Behavior of Ternary Precious Metal Oxides.

Abstract approved: _____
Munirpallam A. Subramanian

Due to the high cost of precursor materials, complex oxides of *4d* and *5d* transition metals are under-studied compared to their *3d* counterparts. Recent studies have shown that oxides containing heavier transition metals can exhibit exotic electronic states due to presence of strong spin-orbit coupling. The goal of this dissertation is to investigate and to learn more about the chemical and electronic behavior of Ir and Rh. Four oxide systems were prepared and studied: $\text{Ba}_2\text{In}_{2-x}\text{Ir}_x\text{O}_{5+\delta}$, $\text{Ba}_{2-x}\text{La}_x\text{InIrO}_6$, $\text{BaLaIn}_{1-y}\text{Ca}_y\text{IrO}_6$, and $\text{A}_{1+x}\text{Rh}_{2-x}\text{O}_4$ ($\text{A}^{2+} = \text{Co}, \text{Ni}, \text{Cu}$).

The solid solution series $\text{Ba}_2\text{In}_{2-x}\text{Ir}_x\text{O}_{5+\delta}$ ($x = 0-1.4, 2$) was synthesized and its structural, magnetic, and charge transport properties were measured. With increasing Ir content, three transitions in the room temperature structure were observed: orthorhombic to tetragonal, tetragonal to cubic, and cubic to a monoclinic distortion of a hexagonal BaTiO_3 structure. Neutron diffraction refinements showed $\text{Ba}_2\text{In}_{1.6}\text{Ir}_{0.4}\text{O}_{5.4}$ was cubic and $\text{Ba}_2\text{InIrO}_6$ was monoclinic. The latter result contradicts previously published XRD refinements. Magnetization measurements show Curie-Weiss behavior for $x = 0.2-0.6$, which arises from near 50:50 ratio

of Ir(V) and Ir(VI). To our knowledge, this is the first time Ir(VI) has been stabilized with standard solid state methods under ambient conditions. Electrical resistivity measurements show all the compounds studied were semiconducting, and that resistivity decreases with increasing Ir content which suggests proximity to a metal-insulator transition. A sign reversal in the high-temperature Seebeck coefficient is observed indicating both electron and hole charge transport.

Two novel solid solution series, $\text{Ba}_{2-x}\text{La}_x\text{InIrO}_6$ ($x = 0-1.0$) and $\text{BaLaIn}_{1-y}\text{Ca}_y\text{IrO}_6$ ($y = 0-1.0$), were prepared and several changes in structure, magnetic moment, and charge transport were observed. The $\text{Ba}_{2-x}\text{La}_x\text{InIrO}_6$ series exhibits a transition from a 6M polytype to an orthorhombic perovskite structure with increased La content whereas the $\text{BaLaIn}_{1-y}\text{Ca}_y\text{IrO}_6$ series transitioned from a disordered orthorhombic perovskite to an ordered cubic perovskite with increased Ca content. Seebeck measurements for both systems showed that Ir(IV)-rich compounds tended to have a n-type conduction mechanism while Ir(V)-rich compounds appeared to be p-type. Both systems were found to be semiconducting and the magnitude of the resistivity is dependent on the crystal structure and Ir environment. Magnetic measurements show that the μ_{eff} values for both systems are significantly less than predicted for Ir(IV) ($1.73 \mu_B$) and greater than predicted for Ir(V) ($0 \mu_B$). These results are compared to other iridate compound families.

The spinels $A_{1+x}\text{Rh}_{2-x}\text{O}_4$ ($A^{2+} = \text{Co}, \text{Ni}, \text{Cu}$) were previously reported but information on their structures and magnetic behavior was lacking. CoRh_2O_4 , CuRh_2O_4 , and the novel composition $\text{Ni}_{1.25}\text{Rh}_{1.75}\text{O}_4$ were prepared using standard solid state methods and characterized using diffraction and magnetic susceptibility techniques. CoRh_2O_4 was found to have the cubic

spinel structure ($Fd\bar{3}m$) whereas CuRh_2O_4 and $\text{Ni}_{1.25}\text{Rh}_{1.75}\text{O}_4$ crystallized in tetragonally distorted spinel structures ($I4_1/amd$) due to Jahn-Teller effects. Antiferromagnetic behavior was observed in $\chi(T)$ data for CoRh_2O_4 ($T_N = 24.9(1)$ K, $\mu_{\text{eff}} = 4.42(1)$ μ_B) and CuRh_2O_4 ($T_N = 24(1)$ K, $\mu_{\text{eff}} = 1.97(1)$ μ_B) and their magnetic structures were determined to be an antiferromagnetic A-type and an *ab*-plane helical structure, respectively. An upward deviation from Curie-Weiss behavior in the $\chi(T)$ data and a positive θ value for $\text{Ni}_{1.25}\text{Rh}_{1.75}\text{O}_4$ suggests the presence of competing ferromagnetic and antiferromagnetic correlations. A divergence in ZFC and FC $\chi(T)$ data was observed for $\text{Ni}_{1.25}\text{Rh}_{1.75}\text{O}_4$ as well as a lack of long-range ordering in low temperature neutron data both of which suggest spin-glass behavior.

©Copyright by Joshua Flynn

March 7, 2017

All Rights Reserved

Substitution Effects on the Structure and Electronic Behavior of Ternary Precious Metal
Oxides

by
Joshua Flynn

A DISSERTATION

submitted to

Oregon State University

in partial fulfillment of
the requirements for the
degree of
Doctor of Philosophy

Presented March 7, 2017
Commencement June 2017

Doctor of Philosophy dissertation of Joshua Flynn presented on March 7, 2017

APPROVED:

Major Professor, representing Chemistry

Chair of the Department of Chemistry

Dean of the Graduate School

I understand that my dissertation will become part of the permanent collection of Oregon State University libraries. My signature below authorizes release of my dissertation to any reader upon request.

Joshua Flynn, Author

ACKNOWLEDGEMENTS

First, I would like to thank my PhD advisor Dr. Mas Subramanian for the patience, guidance and support that he has shown me over the course of my graduate career. He has stood behind me since I joined his group and brought many development opportunities to my attention including summer workshops and presenting my work multiple prestigious solid state conferences. The knowledge and skills I learned during my time in Dr. Subramanian's lab have helped me become a better researcher and solid state chemist and I will continue to utilize them in the future.

I am grateful to all the past and present members of Dr. Subramanian's group I've had the pleasure of working with. Dr. Jun Li, Dr. Alvin Gatimu, Dr. Peng Jiang, Dr. Geneva Laurita, Dr. Whitney Schmidt, and Dr. Rosa Grajczyk, thank you for sharing your knowledge, expertise, and patience when answering my "stupid" questions. My research would have been much more difficult without your help. I would also like to thank Joseph Tang, Sarah Synnestvedt, Bella Giampaoli, Elena Medina, Maxwell Wallace for creating a fun work environment and helping me hone my understanding of chemistry through numerous research discussions.

I would also like to thank Dr. Michael Lerner, Dr. Janet Tate, Dr. Brady Gibbons, and Dr. David McIntyre for taking the time to sit on my graduate committee and for reviewing this work. Dr. Lerner, Dr. Tate, and Dr. Gibbons have also been excellent teachers and their courses gave me different perspectives on the science of solid state materials and helped me become a more rounded scientist.

My time in graduate school would have been a lot less enjoyable if not for both old friends and new ones I've made throughout the department and community. Thank you to Wes Surta, Joseph Tang, and Dr. Ashley Mason for reviewing and helping me improve this dissertation. Additionally, I'd like to thank Ryan McQuade, Dr. Lauren McQuade, Dr. Geneva Laurita, Michelle Jenyns, Jonathan King, Victor Mendiola, Nick Genovia, and Ryan Flynn for helping keep me grounded and sane through the rite of passage that is graduate school.

I would also like to acknowledge the collaborators I've had the privilege of working with: Dr. Arthur Ramirez, Dr. Jennifer Trinh, Dr. Martin Mourigal, Luwei Ge, and Dr. Joe Paddison. Your discussions have taught so much more about solid state materials than I would have discovered on my own and this dissertation would certainly be lacking without your efforts.

Last but certainly not least, I thank my parents, David and Debbie Flynn. Without your guidance and insistence that I better myself, I would not where I am today. Thank you for your unwavering support and love.

CONTRIBUTION OF AUTHORS

Chapter 2: Dr. Mas Subramanian, Dr. Jun Li, Dr. Art Sleight, Dr. Arthur Ramirez contributed in the preparation and review of the manuscript on which this chapter is primarily based; J. Flynn, J. Li, A.W. Sleight, A.P. Ramirez, M.A. Subramanian, Structure and Properties of Ir-Containing Oxides with Large Spin–Orbit Coupling: $\text{Ba}_2\text{In}_{2-x}\text{Ir}_x\text{O}_{5+\delta}$, *Inorg. Chem.* **55** (2016) 2748–2754. Dr. Jun Li also contributed to discussions of structure refinements and performed Rietveld refinements for $\text{Ba}_2\text{In}_{1.6}\text{Ir}_{0.4}\text{O}_{5.4}$. Dr. Ramirez also performed magnetic experiments at UC Santa Cruz using a Magnetism Property Measurement System (MPMS) and contributed to the analysis and discussion of the provided data.

Chapter 3: Dr. Mas Subramanian, Dr. Jun Li, Dr. Arthur Ramirez contributed in the preparation and review of the manuscript on which this chapter is primarily based; J. Flynn, J. Li, A.P. Ramirez, M.A. Subramanian, The effect of iridium oxidation state on the electronic properties of perovskite-type solid solutions: $\text{Ba}_{2-x}\text{La}_x\text{InIrO}_6$ and $\text{BaLaIn}_{1-y}\text{Ca}_y\text{IrO}_6$, *J. Solid State Chem.* **247** (2017) 53–59. Dr. Jun Li also contributed to discussions of structure refinements. Dr. Ramirez also performed magnetic experiments at UC Santa Cruz using a MPMS and contributed to the analysis and discussion of the provided data.

Chapter 4: Dr. Mas Subramanian, Dr. Arthur Ramirez, Dr. Martin Mourigal, Dr. Joseph Paddison, and Luwei Ge contributed to in the preparation of the manuscripts on which this

chapter is primarily based; L. Ge, J. Flynn, J.A.M. Paddison, M.B. Stone, S. Cadler, A.P. Ramirez, M.A. Subramanian, M. Mourigal, Spin order and dynamics in the perfect and distorted diamond-lattice Heisenberg antiferromagnets CoRh_2O_4 and CuRh_2O_4 and J. Flynn, J. Li, M.A. Subramanian, The true composition of NiRh_2O_4 . Dr. Jun Li contributed to discussions of room-temperature structure refinements. Dr. Ramirez also performed magnetic experiments at UC Santa Cruz using a MPMS and contributed to the analysis and discussion of the provided data. Dr. Mourigal, Dr. Paddison, and Luwei collected and performed refinements of low-temperature neutron diffraction data and contributed to discussions of magnetic structures.

Appendix A: Dr. Ramirez and Dr. Jennifer Trinh of UC Santa Cruz collected and analyzed magnetotransport data for the BaIrO_3 single crystals. The data is published in Dr. Trinh's PhD thesis, "Low temperature properties of strong spin-orbit systems".

TABLE OF CONTENTS

	<u>Page</u>
1 Introduction to Structure-Property Relationships in a Material	1
1.1 Transition Metal Oxides	1
1.2 Preparation of Solid State Oxides.....	2
1.2.1 Ceramic Method.....	2
1.2.2 Crystal Growth via Flux Method	3
1.3 Structures of Crystalline Materials	4
1.3.1 Symmetry operations	4
1.3.2 Close packing of atoms and ions.....	6
1.4 Crystal Structures in this Dissertation	8
1.4.1 The Perovskite Structure	8
1.4.1.1 Non-stoichiometry in Perovskites	13
1.4.1.2 Hexagonal Polytypes.....	15
1.4.1 The Spinel Structure.....	17
1.5 Structural Analysis	19
1.5.1 Scattering of Light by Crystalline Materials	19
1.5.2 Powder Diffraction.....	21
1.5.2.1 X-ray Diffraction.....	21
1.5.2.2 Time-of-Flight Neutron Diffraction	23
1.5.2.3 Structure Modeling	24
1.5.3 Diffraction Instrumentation.....	26
1.6 Magnetism	27

TABLE OF CONTENTS (Continued)

	<u>Page</u>
1.6.1 Fundamentals	27
1.6.2 Magnetic Ordering	30
1.6.3 Spin Glasses	33
1.6.4 Spin-Orbit Coupling.....	34
1.6.5 Magnetism Instrumentation	34
1.7 Electrical Properties.....	39
1.7.1 Electrical Conduction.....	39
1.7.2 Seebeck Effect.....	43
1.7.3 Electronic Transport Instrumentation	44
1.7.3.1 High-Temperature Measurements.....	44
1.7.3.2 Low-Temperature Measurements	45
1.8 References	47
2 Solid Solution Between $\text{Ba}_2\text{In}_2\text{O}_5$ and BaIrO_3	52
2.1 Introduction to $\text{Ba}_2\text{In}_2\text{O}_5$ and BaIrO_3	54
2.2 Investigation of $\text{Ba}_2\text{In}_{2-x}\text{Ir}_x\text{O}_{5+\delta}$	55
2.2.1 Motivation for Solid Solution	55
2.2.2 Structural Characterization.....	56
2.2.3 Magnetism.....	65
2.2.4 Electronic Transport Properties.....	69
2.3 Conclusions	70
2.4 Methods and Materials	71

TABLE OF CONTENTS (Continued)

	<u>Page</u>
2.5 References	73
3 Tuning Ir Oxidation State in $\text{Ba}_2\text{InIrO}_6$ and BaLaInIrO_6 via <i>A</i> - and <i>B</i> -site Substitutions	77
3.1 Motivation for Solid Solutions	79
3.2 Substitutions and Structural Characterization	80
3.2.1 $\text{Ba}_{2-x}\text{La}_x\text{InIrO}_6$	80
3.2.2 $\text{BaLaIn}_{1-y}\text{Ca}_y\text{IrO}_6$	86
3.3 Electronic Properties.....	89
3.3.1 Transport Characterization.....	89
3.3.2 Magnetism.....	91
3.4 Conclusions	95
3.5 Materials and Methods	96
3.6 References	97
4 Structural Refinement and Magnetic Characterization of $A_{1+x}\text{Rh}_{2-x}\text{O}_4$ ($A^{2+} = \text{Co}, \text{Ni}, \text{Cu}$) Spinel.....	103
4.1 Motivation for Study	105
4.2 Structural Characterization	106
4.3 Magnetic Characterization.....	116
4.3.1 CoRh_2O_4	116
4.3.2 $\text{Ni}_{1.25}\text{Rh}_{1.75}\text{O}_4$	119
4.3.3 CuRh_2O_4	123

TABLE OF CONTENTS (Continued)

	<u>Page</u>
4.4 Conclusions	126
4.5 Methods and Materials	127
4.6 References	129
General Conclusions and Future work.....	133
Bibliography.....	136
Appendix A: Linear Magnetoresistance in BaIrO ₃	148
A.1 Introduction.....	148
A.1.1 BaIrO ₃	148
A.1.2 Magnetoresistance	150
A.3 Characterization of BaIrO ₃	151
A.3.1 Single Crystals	151
A.3.1 Electronic Properties	152
A.4 Conclusions.....	155
A.5 Materials and Methods	156
A.6 References	157

LIST OF FIGURES

<u>Figure</u>	<u>Page</u>
1.1 Simple diagram illustrating the formation of a new material (purple) at the interface of two larger particles.....	2
1.2 The 14 Bravais lattices.....	5
1.3 Schematics illustrating AB and ABC stacking types.....	6
1.4 Illustration of the octahedral and tetrahedral holes between stacked layers.....	7
1.5 Crystal structures of NaCl and Na ₂ O illustrating octahedral (O _h) and tetrahedral (T _d) hole filling.....	8
1.6 Periodic table colored to indicate the elements that have been to crystallize in the perovskite structure (ABX ₃).....	9
1.7 Unit cell of the ideal perovskite structure with space group Pm $\bar{3}$ m.....	10
1.8 Projections of NaTaO ₃ (<i>a</i> ⁰ <i>b</i> ⁺ <i>c</i> ⁺) demonstrating the different tilting patterns observed in distorted perovskites.....	13
1.9 Comparison of the perovskite and brownmillerite structures. The brownmillerite structure can be created by removing O ions from the perovskite in alternating layers along the [110].....	15
1.10 Comparison of the perovskite polytype structures created by all ccp (3C) and all hcp (2H) stacking of AX ₃ layers.....	16
1.11 Crystal structures of commonly observed perovskite polytypes created by varying the ratio of ccp and hcp stacking of the AX ₃ layers.....	17
1.12 Unit cell of the cubic (<i>Fd</i> $\bar{3}$ <i>m</i>) spinel crystal structure.....	18
1.13 Projections showing the diamond and pyrochlore sublattices formed respectively by the A and B sites of the spinel structure.....	18
1.14 Plot displaying the Z dependence of X-ray scattering factors and neutron scattering cross sections. Note the highly linear trend for X-rays compared to the much more irregular trend for the neutron cross sections.....	20
1.15 Schematic representation of conditions leading to Bragg diffraction.....	22

LIST OF FIGURES (Continued)

<u>Figure</u>	<u>Page</u>
1.16 Photos of the exterior of the Rigaku Miniflex II diffractometer and sample chamber illustrating the geometry of the X-ray tube, sample, and detector	26
1.17 Schematic showing the electron spin ordering and temperature dependence of the magnetization for ferromagnetic behavior. The Curie temperature (T_C) indicates the beginning of magnetic ordering while M_{sat} is the saturation magnetization	31
1.18 Schematic showing the electron spin ordering and temperature dependence of the magnetization for antiferromagnetic behavior. The Néel temperature (T_N) indicates the beginning of magnetic ordering.....	32
1.19 Commonly observed antiferromagnetic structures	33
1.20 Diagrams illustrating the geometric frustration of magnetic moment moments (arrows) in triangular and tetrahedral atomic arrangements.....	34
1.21 Schematic illustration of the magnetic field (\mathbf{B}_0) for the angular momentum of an electron. The generation of \mathbf{B}_0 can be rationalized by considering the motion of a nucleus with charge $+Ze$ around an electron with charge $-e$	35
1.22 Splittings of the Ir(IV) and Ir(V) t_{2g} orbitals caused by SOC. Note that electron filling for Ir(V) leads to a non-magnetic state	36
1.23 Quantum Design PPMS with the ACMS equipment installed	37
1.24 Representation of the ACMS coilset and tube assemblage, expanded view with labels of the ACMS coilset detection unit, and mounted ‘as prepared’ sample. ACMS coilset illustrations taken and modified from Quantum Design application notes.....	38
1.25 Schematic demonstrating the formation of energy bands from molecular orbitals via the addition of an increasing number of atomic orbitals	40
1.26 Simple two-band diagrams for: (a) metal, (b) extrinsic semiconductor, and (c) insulator. The conduction and valence bands are labeled by CB and VB, respectively. The point at which the electron filling stops is denoted by the Fermi level (E_F) while E_g is the energy gap between bands.....	41
1.27 Temperature-dependent plots of (a) $\rho(T)$ for a metal and semiconductor and (b) $\ln \rho$ vs. T for a semiconductor. Note that in (b) $E_g = \text{Slope} \times 2k$	42

LIST OF FIGURES (Continued)

<u>Figure</u>	<u>Page</u>
1.28 Diagrams demonstrating the (a) Seebeck and (b) Peltier effects	44
1.29 ZEM-3 Thermoanalyzer and mounted sample in the thermal chamber.....	45
1.30 PPMS resistivity puck with a bar sample connected to position 1 using the four probe contact technique. Contacts are made using conductive silver paint and copper wires that are soldered to the puck	46
2.1 Crystal structures of (a) brownmillerite $\text{Ba}_2\text{In}_2\text{O}_5$, (b) 6H polytype $\text{Ba}_2\text{InIrO}_6$ and (c) monoclinic 9R polytype BaIrO_3 (Ba = green, In = purple, Ir = brown, O = red)	56
2.2 Powder X-ray diffraction patterns and lattice parameters for $x = 0-0.5$. The c parameter of the tetragonal phase ($x = 0.1$) was divided by 2 to allow for direct comparison to the cubic phases.....	57
2.3 Structures of (a) tetragonal defect perovskite $\text{Ba}_2\text{In}_{1.9}\text{Ir}_{0.1}\text{O}_{5.1}$, (b) cubic defect perovskite $\text{Ba}_2\text{In}_{1.6}\text{Ir}_{0.4}\text{O}_{5.4}$ (Ba = green, In/Ir = purple, O = red)	58
2.4 Time-of-flight neutron diffraction pattern for $\text{Ba}_2\text{In}_{1.6}\text{Ir}_{0.4}\text{O}_{5.4}$ with calculated intensities (red), difference (blue) and background (green) curves. The allowed reflections for $Pm\bar{3}m$ are indicated by the magenta tick marks	59
2.5 Powder X-ray diffraction patterns for $x = 0.6-1.4$	60
2.6 Refined cell edges, β angles and cell volumes for $x = 0.6-1.4$	61
2.7 Time-of-flight neutron diffraction pattern of $\text{Ba}_2\text{InIrO}_6$ with calculated intensities (red) and difference curve (blue). Inset shows example of peak splitting not explained by hexagonal model (hkl : 1 – 224, 2 – $22\bar{4}$, 3 – 223, 4 – $22\bar{3}$)	62
2.8 Comparison of time-of-flight neutron diffraction patterns for $\text{Ba}_2\text{InIrO}_6$: experimental (blue), calculated $P\bar{3}m1$ (black) and $C2/c$ (red). Note that the 003 peak ($\sim 4.9 \text{ \AA}$) in the $P\bar{3}m1$ pattern is absent in the experimental pattern while a small 020,110 peak ($\sim 5.1 \text{ \AA}$) from $C2/c$ is present.....	63
2.9 Projections of the reported hexagonal and this work's monoclinic structure models illustrating the differences in the Ir/In ordering and canting of the octahedra.....	63
2.10 Comparison of bond distances within the face-sharing clusters and M-O-M' bond angles between the face-sharing cluster and the corner sharing octahedra in $\text{Ba}_2\text{InIrO}_6$ from the two models (In = purple, Ir = brown, O = red)	64

LIST OF FIGURES (Continued)

<u>Figure</u>	<u>Page</u>
2.11 Inverse magnetic susceptibility plot for $\text{Ba}_2\text{In}_{2-x}\text{Ir}_x\text{O}_{5+\delta}$. All data has been corrected for the contribution from the atomic cores of the constituent ions.....	66
2.12 Curie-Weiss fits and ratios of the possible Ir oxidations states for $\text{Ba}_2\text{In}_{2-x}\text{Ir}_x\text{O}_{5+\delta}$ ($x = 0.2-0.6$).....	67
2.13 Temperature-dependent, high temperature resistivity and Seebeck coefficient plots for $\text{Ba}_2\text{In}_{2-x}\text{Ir}_x\text{O}_{5+\delta}$. Note the sign change in the Seebeck coefficient for $x = 1.0$ and 1.2 at ~ 550 K	69
3.1 Powder X-ray diffraction patterns for $\text{Ba}_{2-x}\text{La}_x\text{InIrO}_6$ ($x = 0-1$).....	81
3.2 Crystal structures of (a) monoclinic 6H polytype $\text{Ba}_2\text{InIrO}_6$ (Ba = green, In = purple, Ir = light brown, O = red) and (b) orthorhombic perovskite BaLaInIrO_6 (Ba/La = green, In/Ir = purple, O = red).....	82
3.3 Lattice parameters for $\text{Ba}_{2-x}\text{La}_x\text{InIrO}_6$ ($x = 0-1$). The a and c parameters of the monoclinic phase (filled points) were divided by $\sqrt{3}$ for a more direct comparison to the orthorhombic parameters (open points)	82
3.4 Time-of-flight neutron diffraction pattern for BaLaInIrO_6 with calculated intensities (red) and difference curve (blue). The magenta tick marks are the allowed reflections for $Pbnm$	83
3.5 Comparison of experimental (black) and calculated $Pbnm$ (red) and $Imma$ (blue) XRD patterns for BaLaInIrO_6 . Note that the (111) peak ($\sim 24^\circ$) is the present in both the experimental and $Pbnm$ patterns but is absent in the $Imma$ pattern	85
3.6 Projections of BaLaInIrO_6 ($a^*a^*c^+$) showing the anti-phase tilting ($8.15(1)^\circ$) respect to the acubic axis and in-phase tilting ($5.21(1)^\circ$) along the c axis	85
3.7 Powder X-ray diffraction patterns and lattice parameters for $\text{BaLaIn}_{1-y}\text{Ca}_y\text{IrO}_6$ ($y = 0-1.0$). Successful substitution of In for Ca is indicated by the increase in the lattice parameters with increasing y . The orthorhombic b and c parameters were multiplied by $\sqrt{2}$ for a more direct comparison to the cubic phase	87
3.8 Crystal structure for ordered cubic perovskite BaLaCaIrO_6 . (Ba/La = green, Ca = blue, Ir = light brown, O = red).....	88
3.9 High temperature resistivity (ρ) and Seebeck coefficient plots for (a,b) $\text{Ba}_{2-x}\text{La}_x\text{InIrO}_6$ ($x = 0-1.0$) and (c,d) $\text{BaLaIn}_{1-y}\text{Ca}_y\text{IrO}_6$ ($y = 0-0.75$)	90

LIST OF FIGURES (Continued)

<u>Figure</u>	<u>Page</u>
3.10 $\mu(T)_{\text{eff}}$ plots for (a) $\text{Ba}_{2-x}\text{La}_x\text{InIrO}_6$ and (b) $\text{BaLaIn}_{1-y}\text{Ca}_y\text{IrO}_6$. The temperature independence of the data above 100 K suggests Curie-Weiss behavior	92
3.11 A plot of μ_{eff} as a function of Ir valence for $\text{Ba}_{2-x}\text{La}_x\text{InIrO}_6$ (triangles) and $\text{BaLaIn}_{1-y}\text{Ca}_y\text{IrO}_6$ (squares). The dashed line is the trend the expected μ_{eff} values should follow when considering spin-orbit coupling effects	94
4.1 Time-of-flight neutron diffraction pattern for $\text{Co}(\text{Rh}_{1.90(1)}\text{Co}_{0.10(1)})\text{O}_4$ with calculated intensities (red) and difference (blue) and background (green) curves. The magenta tick marks indicate the allowed reflections for $Fd\bar{3}m$ and the teal tick marks indicate the “strain phase” use to model the asymmetric broadening	106
4.2 Time-of-flight neutron diffraction pattern for $\text{NiRh}_{1.86(1)}\text{Ni}_{0.14(1)}\text{O}_4$ with calculated intensities (red) and difference (blue) and background (green) curves. The magenta tick marks indicate the allowed reflections for $I\bar{4}_1/amd$ and the teal tick marks indicate the “strain phase” used to model the asymmetric broadening.....	108
4.3 Temperature dependent plots of (top) the lattice parameters a and c and (bottom) the c/a_{cub} ratio and volume for $\text{Ni}_{1.25}\text{Rh}_{1.75}\text{O}_4$	111
4.4 Time-of-flight neutron diffraction pattern for CuRh_2O_4 with calculated intensities (red) and difference (blue) and background (green) curves. The magenta tick marks indicate the allowed reflections for $I\bar{4}_1/amd$ and the teal tick marks indicate the “strain phase” use to model the asymmetric broadening	112
4.5 Orbital diagrams illustrating of the splitting of the t_2 and e orbitals caused by Jahn-Teller elongation and compression	114
4.6 Schematic showing the different stabilization energies (SE) for Ni^{2+} and Cu^{2+} produced by Jahn-Teller compression and elongation. The values m and n are the number of electrons in the lower and upper orbitals, respectively. The grey dotted line represents the relative position of the unsplit t_2 orbitals	115
4.7 $1/\chi(T)$ plot for CoRh_2O_4 shows antiferromagnetic (AFM) behavior ($T_N = 25$ K) with the red line showing the fit to the Curie-Weiss Law. Inset shows close-up view of the AFM transition	117

LIST OF FIGURES (Continued)

<u>Figure</u>	<u>Page</u>
4.8 Rietveld refinement on CoRh_2O_4 powder neutron diffraction data collected at $T = 4$ K. Contribution from nuclear peaks (blue ticks), magnetic peaks (red ticks) and Al can (gray ticks) are considered. The inset shows the temperature dependence of the second magnetic peak intensity (highlighted with asterisk)	117
4.9 Unit cells displaying (a) the nearest neighbor interactions (J) and (b) the A -type antiferromagnetic magnetic structure (red and yellow arrows) of CoRh_2O_4	118
4.10 Schematics showing the relative position of one Co-O-Rh-O-Co superexchange pathways (green lines) within CoRh_2O_4 and illustrating how the superexchange results in AFM ordering.....	119
4.11 $1/(\chi(T) - \chi_0)$ plot for $\text{Ni}_{1.25}\text{Rh}_{1.75}\text{O}_4$ with the fit to Curie-Weiss behavior (red line) above 90 K. Upward deviation from CW below suggests AFM correlations. Inset shows close-up view reveals of large divergence between field-cooled (FC) and zero field-cooled (ZFC) data typical of spin-glass behavior. T_g is the spin-glass transition temperature	120
4.12 Superexchange mechanisms in $\text{Ni}_{1.25}\text{Rh}_{1.75}\text{O}_4$. Rh on the B -site allows for an antiferromagnetic A - A interaction between the. Substituting Ni for Rh interrupts the exchange and results in ferromagnetic A - A and antiferromagnetic A - B interactions	121
4.13 Variable temperature neutron diffraction data (4–200 K) for $\text{Ni}_{1.25}\text{Rh}_{1.75}\text{O}_4$. The lack of new peaks or intensity changes indicates there is no long-range magnetic ordering	122
4.14 $1/(\chi(T) - \chi_0)$ plot for CuRh_2O_4 shows AFM behavior ($T_N = 24.5$ K) with the red line showing the fit to the Curie-Weiss Law. Inset shows close-up view of the AFM transition with an upward trend beginning at ~ 11 K	123
4.15 Rietveld refinement on CuRh_2O_4 powder neutron diffraction data at $T = 4$ K. Contribution from nuclear peaks (blue ticks) and magnetic peaks (red ticks) are considered. The inset shows the temperature dependence of the second magnetic peak intensity (highlighted with asterisk).....	124
4.16 Unit cells displaying (a) the nearest neighbor interactions (J_n) with different colors to distinguish the different orders of neighbors and (b) the incommensurate helical magnetic structure (red arrows) of CuRh_2O_4 . The gray rings serve as a guide to the eye for the propagation and orientation of the magnetic moments	125

LIST OF FIGURES (Continued)

<u>Figure</u>	<u>Page</u>
A.1 Crystal structures of the (a) 9M, (b) 5M, and (c) 6M polymorphs of BaIrO ₃ (Ba = green, Ir = brown, O = red)	149
A.2 Photos of example BaIrO ₃ single crystals showing (a) relative size and (b) close-up view of crystal shapes	152
A.3 $\rho(T)$ plot for BaIrO ₃ exhibiting an anomaly at $T_C \approx 160$ K. Inset is an overlay plot of $-d \log \rho / d(T^{-1})$ and $\Delta\rho/\rho_0(T)$	152
A.4 Plots of $\Delta\rho/\rho_0(H)$ BaIrO ₃ (a) near $T_C \approx 160$ K and (b) well below T_C	153
A.5 $\rho_{xy}(T)$ plot for BaIrO ₃ for $T = 40$ – 160 K. The black arrow is a guide for the trend for decreasing T . The inset is a plot of $R_H(T)$ exhibiting a positive-negative-positive sign change near T_C	154

LIST OF TABLES

<u>Table</u>	<u>Page</u>
1.1 Perovskite Tilt Systems and Their Assigned Space Groups	12
2.1 Refined atomic parameters for $\text{Ba}_2\text{In}_{1.62(1)}\text{Ir}_{0.38(1)}\text{O}_{5.49(1)}$	59
2.2 Lattice parameter comparison of structure models for $\text{Ba}_2\text{InIrO}_6$	65
2.3 Refined atomic coordinates and occupancies for $\text{Ba}_2\text{InIrO}_6$	65
2.4 Estimated band gaps for $\text{Ba}_2\text{In}_{2-x}\text{Ir}_x\text{O}_{5+\delta}$	70
3.1 Refined unit-cell, coordinate and displacement parameters for BaLaInIrO_6 (<i>Pbnm</i>)	84
3.2 Estimated band gaps for $\text{Ba}_{2-x}\text{La}_x\text{InIrO}_6$ and $\text{BaLaIn}_{1-y}\text{Ca}_y\text{IrO}_6$	90
4.1 Summarized crystallographic information for $\text{CoRh}_{1.90(1)}\text{Co}_{0.10(1)}\text{O}_4$	107
4.2 Summarized crystallographic information for $\text{NiRh}_{1.86(1)}\text{Ni}_{0.14(1)}\text{O}_4$	109
4.3 Summarized crystallographic information for CuRh_2O_4	113

Chapter 1: Introduction to Transition Metal Oxides and Physical Properties

1.1 Transition Metal Oxides

Transition metal oxides (TMOs) have long been of interest for applications in consumer electronic devices. Their popularity is due to both their high degree of stability as well as being able to host a wide variety of magnetic and electrical properties. Due to the close relationship between a TMO's properties and crystal structure, the magnetic or electrical behavior can be enhanced or changed completely by manipulating metal oxidation states, distorting the crystal structure, or causing a transition to a new structure simply via elemental substitution. This is especially true of the perovskite and spinel structures.

The *4d* and *5d* transition metals, especially precious metals such as Ir, Rh, Pd, and Pt, have been less studied in oxides than their *3d* counterparts largely due to the high cost of precursor materials. Since the orbital interactions and spin-orbit coupling of heavier transition metals have comparable energy scales, they have been of recent interest, as many have been shown to exhibit exotic states such as spin-orbit Mott insulators [1,2], quantum spin liquids [3], Weyl semimetals [4,5] and, potentially, topological insulators [6,7]. The goal of research activities discussed in this dissertation is to fill in knowledge gaps in the chemical and electronic behavior of Ir and Rh by preparing and characterizing the perovskite and spinel oxide systems: $\text{Ba}_2\text{In}_{2-x}\text{Ir}_x\text{O}_{5+\delta}$, $\text{Ba}_{2-x}\text{La}_x\text{InIrO}_6$, $\text{BaLaIn}_{1-x}\text{Ca}_x\text{IrO}_6$, and $A_x\text{Rh}_{2-x}\text{O}_4$ ($A^{2+} = \text{Co}, \text{Ni}, \text{Cu}$). The next sections will cover fundamentals of the characterization methods and properties that will be discussed later.

1.2 Preparation of Solid State Oxides

1.2.1 Ceramic Method

There are several approaches a solid state chemist can take when preparing complex oxides. The most common methodology is the “ceramic method” which relies on the use of thermal energy to facilitate the diffusion of atoms or ions across the interface of particles in a mixture of two or more materials (Figure 1.1). Most of the compounds characterized in this dissertation were prepared using this method.

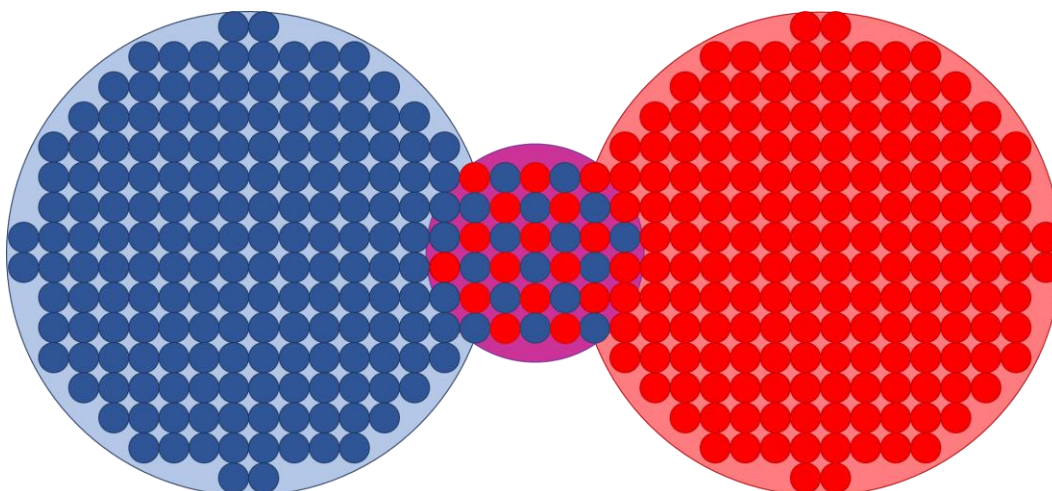


Figure 1.1. Simple diagram illustrating the formation of a new material (purple) at the interface of two larger particles (adapted from [8]).

To begin, stoichiometric amounts of metal precursors are mechanically ground and mixed together using a mortar and pestle or a ball mill. Metal oxides or carbonates are typically used as precursors though occasionally halide or elemental forms are employed. Once the precursors are mixed, the mixture is pressed into a pellet to reduce the distance between particles and make diffusion easier. The pellet is then heat treated, or “fired”, for several hours at temperatures typically ranging from 400 °C to 1700 °C. The optimal temperature to prepare

a compound can vary depending on the precursors or target structure involved and can be determined by searching literature for similar procedures or by trial and error. The longer the sample is held at the firing temperature, the lower the diffusion rate of the ions becomes due to the growth of the new phase along the particle interfaces. To combat this, the heat treatment is stopped and the sample is re-ground to both break up the old interfaces and create fresh ones. From here mixture is again pressed into a pellet and the heat treatment is resumed. This process of grinding, pelletizing, and heating is continued until a pure phase is obtained or the reaction ceases to progress.

The ceramic method is preferably performed under ambient pressure and atmosphere for reasons of simplicity though occasionally, it is desirable to stabilize crystal structures or unusual metal oxidation states that are difficult or impossible to form under ambient conditions. These compounds can often be realized by applying pressure or by changing the heating environment via the flow of an oxidative or reductive gas over the sample or heating the sample in an vacuum evacuated tube.

1.2.2 Crystal Growth via Flux Method

Compounds prepared using ceramic methods are polycrystalline meaning they are made up of multiple randomly oriented crystallites joined by grain boundaries. A single crystal, on the other hand, is a material where the crystal lattice of the entire sample is continuous and unbroken to the edges of the sample. The electronic properties and behavior of single crystals are often different from their polycrystalline analogs and can even be anisotropic. Additionally,

the absence of grain boundaries in single crystals makes them desirable for applications such as lasers, microprocessors, and gemstones.

There are several techniques that can be used to grow single crystals such as hydrothermal synthesis, sublimation, or the use of a molten flux. All single crystal samples discussed in this dissertation were grown using the flux method which involves dissolving metal precursors in a low-melting point solid solvent, typically an alkali or alkali earth metal halide or hydroxide [9]. A prototypical flux preparation begins by mixing the precursors together with the flux solvent and heating the mixture to just beyond the melting point of the solvent. After being held at this temperature for several hours, the solution is then typically cooled very slowly to give the crystals time to nucleate and grow. Once the flux has cooled, the single crystals can be extracted from the flux matrix and characterized.

1.3 Structures of Crystalline Materials

1.3.1 Symmetry operations

Crystalline solids can be thought of as atoms periodically arranged in a 3D lattice. The structure of these materials is often represented by a unit cell which is defined as the smallest unit that retains the symmetry of the structure as a whole. The crystal structure can then be “created” by translating the unit cell across three-dimensional space. The symmetry of a crystal structure can be described by one of 230 space groups that are subdivided into seven crystal systems: cubic, hexagonal, rhombohedral/trigonal, tetragonal, orthorhombic, monoclinic, and triclinic [10]. Using Hermann-Mauguin notation, space groups are expressed by combining an

uppercase letter that represents the Bravais lattice with additional symbols for representing symmetry elements. The 14 Bravais lattice symbols are P for primitive, I for body-centered, F for face-centered, A , B or C for base-centered, and R for rhombohedral (Figure 1.2). The remaining symbols specify the highest symmetry elements with respect to the crystallographic axes a , b , c . For example, the space group $Fd\bar{3}m$ represents a cubic crystal structure with a face-centered unit cell (F) that contains a diamond glide plane (d) along the a , b , c axes, a three-fold rotation axis with a center of inversion ($\bar{3}$) along each of the body diagonals, and mirror planes (m) that are perpendicular to the face diagonals.

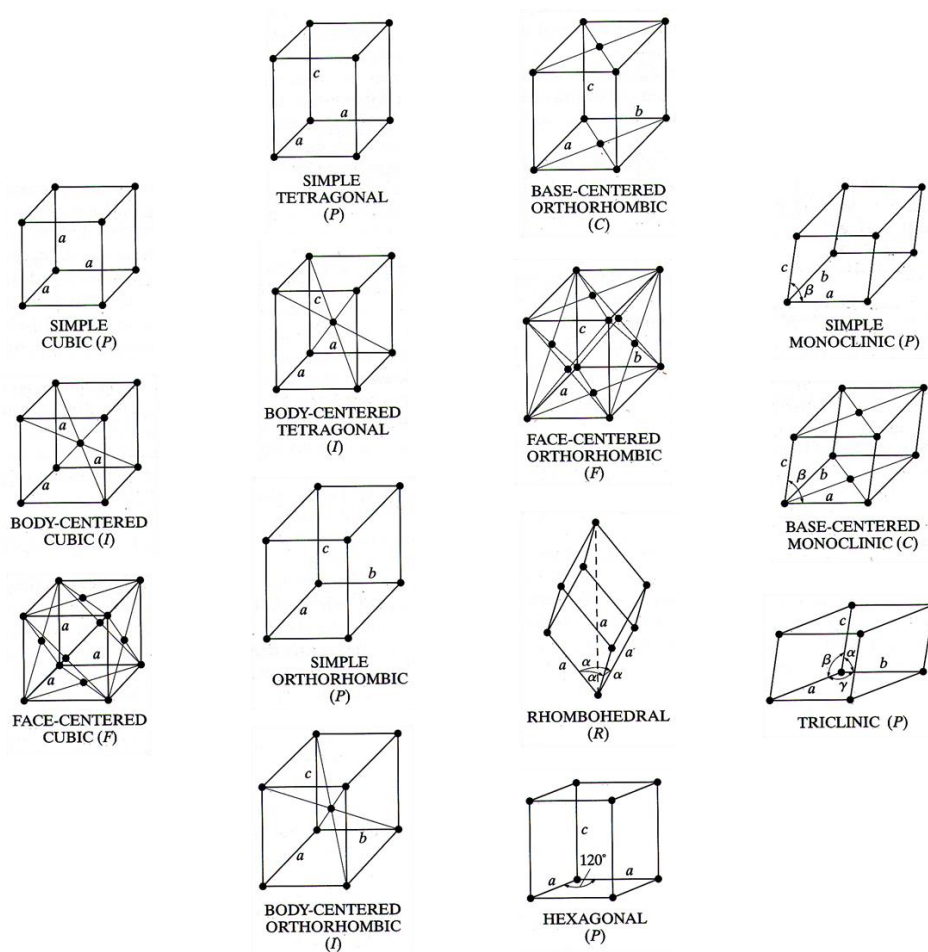


Figure 1.2. The 14 Bravais lattices (from [11]).

1.3.2 Close packing of atoms and ions

Another common way to describe crystal structures is through close packing of spheres. Close packing is the concept that spheres will tend to pack in a way that minimizes the void space between them. In 2D, this is accomplished by packing in a hexagonal manner as illustrated by the green spheres in Figure 1.3. In 3D, there are two positions for a 2nd layer to stack on to the first: a “B” position, indicated by the blue dots, and a “C” position, indicated by orange dots. If the 2nd layer stacks on the B sites, a 3rd layer can stack over either the original “A” layer or the “C” positions. The former is AB stacking and the latter is ABC stacking, illustrated in Figure 1.3; repeating these stacking motifs leads to hexagonal close packing (hcp) and cubic close packing (ccp), respectively.

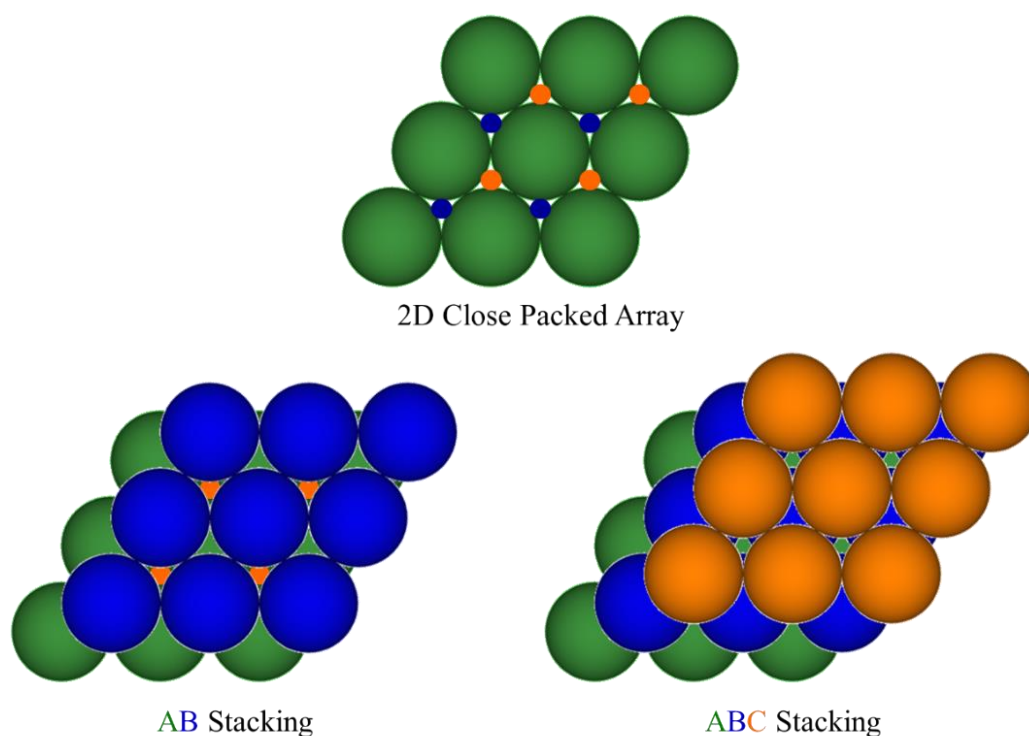


Figure 1.3. Schematics illustrating AB and ABC stacking types.

When considering ionic solids, the close packing is usually completed by anions rather than cations (due to their larger relative size), which then fill the interlayer voids. It should be noted that this is not always the case, as there are a few examples of “anti” structures in which the cations form the layers and the anions fill the voids. However, for simplicity, this discussion will not refer to these cases. There are two potential sites for the cations to occupy, a tetrahedral (T_d) site and an octahedral (O_h) site, as illustrated in Figure 1.4.

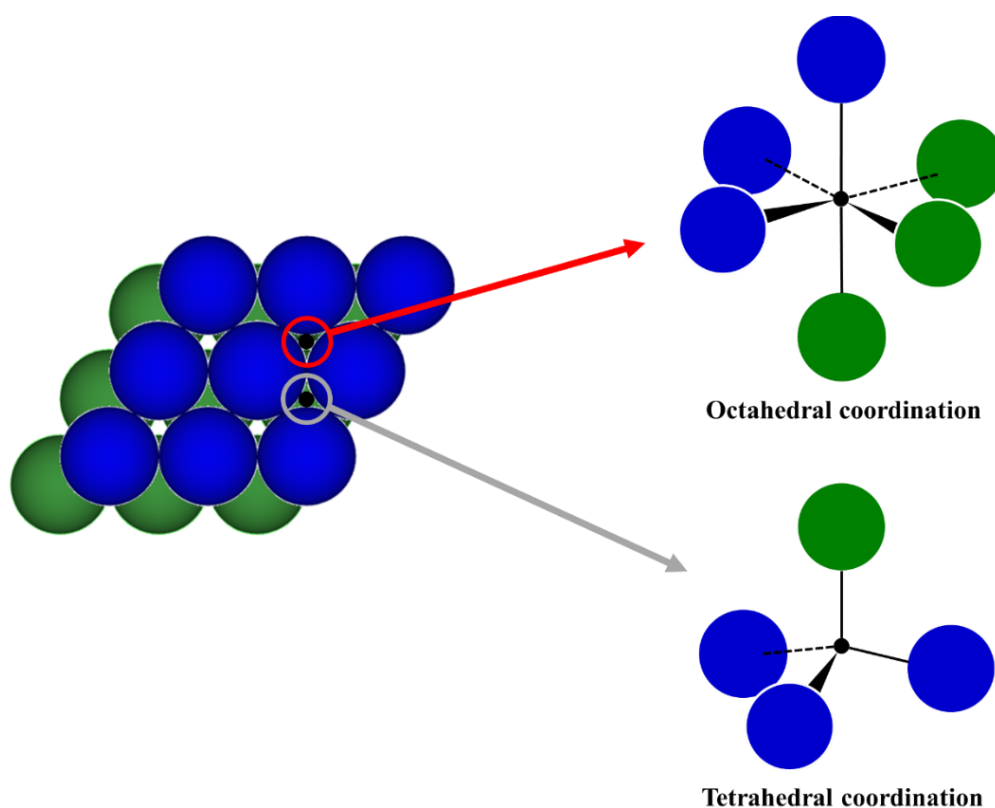


Figure 1.4. Illustration of the octahedral and tetrahedral holes between stacked layers.

For both hexagonal- and cubic-close packing patterns, there are two T_d sites for each O_h site and structures can often be described by the stacking and degree of occupation in the sites. For example, both the NaCl rocksalt structure and the anti-fluorite Na_2O structure (Figure 1.5)

are cubic-close packed, but NaCl has 100% of the octahedral sites filled while 100% of the tetrahedral sites are filled in Na₂O.

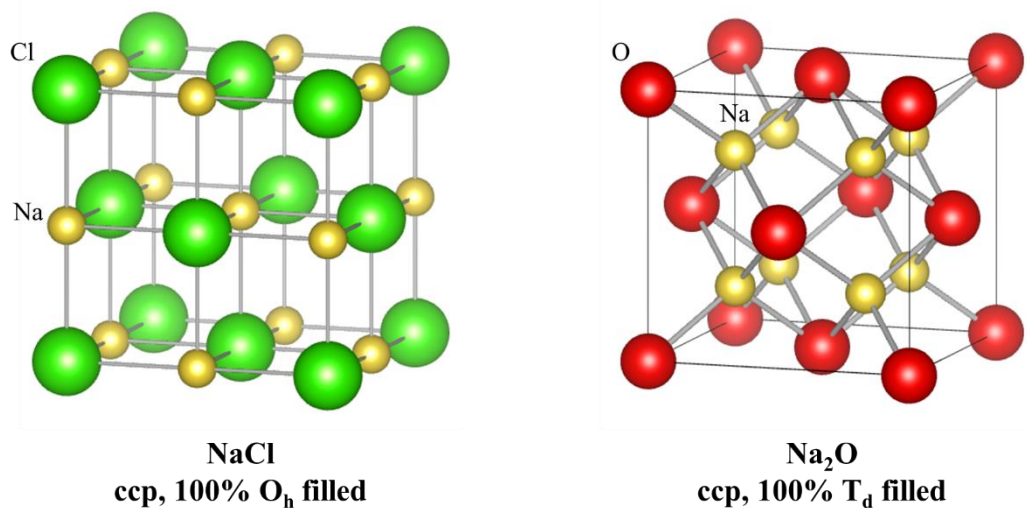


Figure 1.5. Crystal structures of NaCl and Na₂O illustrating octahedral (O_h) and tetrahedral (T_d) hole filling.

1.4 Crystal Structures in this Dissertation

1.4.1 Perovskite Structure

The mineral perovskite was first discovered by the mineralogist Gustav Rose in 1839 who named it after fellow mineralogist Lev Perovski [12]. The perovskite structure has a general formula of ABX_3 and is one of, if not the, most commonly adopted crystal structures for solid state ceramic materials. It can accommodate almost any element on the periodic table (Figure 1.6) largely due to the structure's ability to distort and accept vacancies. This flexibility has led to perovskites and their derivative structures hosting a number of properties, such as superconductivity, ferromagnetism, and high κ dielectric constants [13].

hydrogen 1 H 1.0079																	helium 2 He 4.0026						
lithium 3 Li 6.941	beryllium 4 Be 9.0122																	boron 5 B 10.811	carbon 6 C 12.011	nitrogen 7 N 14.007	oxygen 8 O 15.999	fluorine 9 F 18.998	neon 10 Ne 20.180
sodium 11 Na 22.990	magnesium 12 Mg 24.305																	aluminum 13 Al 26.982	silicon 14 Si 28.086	phosphorus 15 P 30.974	sulfur 16 S 32.065	chlorine 17 Cl 35.453	argon 18 Ar 39.948
potassium 19 K 39.098	calcium 20 Ca 40.078	scandium 21 Sc 44.956	titanium 22 Ti 47.867	vanadium 23 V 50.942	chromium 24 Cr 51.996	manganese 25 Mn 54.938	iron 26 Fe 55.845	cobalt 27 Co 58.933	nickel 28 Ni 58.693	copper 29 Cu 63.546	zinc 30 Zn 65.39	gallium 31 Ga 69.723	germanium 32 Ge 72.61	arsenic 33 As 74.922	selenium 34 Se 78.96	bromine 35 Br 79.904	krypton 36 Kr 83.80						
rubidium 37 Rb 85.468	strontium 38 Sr 87.62	yttrium 39 Y 88.906	zirconium 40 Zr 91.224	niobium 41 Nb 92.906	molybdenum 42 Mo 95.94	technetium 43 Tc [98]	ruthenium 44 Ru 101.07	rhodium 45 Rh 102.91	palladium 46 Pd 106.42	silver 47 Ag 107.87	cadmium 48 Cd 112.41	indium 49 In 114.82	tin 50 Sn 118.71	antimony 51 Sb 121.76	tellurium 52 Te 127.60	iodine 53 I 126.90	xenon 54 Xe 131.29						
caesium 55 Cs 132.91	barium 56 Ba 137.33	* 57-70 lanthanum 57 La 138.91	hafnium 72 Hf 178.49	tantalum 73 Ta 180.95	tungsten 74 W 183.84	rhenium 75 Re 186.21	osmium 76 Os 190.23	iridium 77 Ir 192.22	platinum 78 Pt 195.08	gold 79 Au 196.97	mercury 80 Hg 200.59	thallium 81 Tl 204.38	lead 82 Pb 207.2	bismuth 83 Bi 208.98	polonium 84 Po [209]	astatine 85 At [210]	radon 86 Rn [222]						
francium 87 Fr [223]	radium 88 Ra [226]	* 89-102 actinium 89 Ac [227]	hafnium 104 Hf [261]	tantalum 105 Ta [262]	tungsten 106 W [263]	rhenium 107 Re [264]	osmium 108 Os [269]	iridium 109 Ir [271]	platinum 110 Pt [272]	gold 111 Au [277]	mercury 112 Hg [277]	thallium 113 Tl [283]	lead 114 Pb [289]	bismuth 115 Bi [289]	polonium 116 Po [289]	astatine 117 At [289]	radon 118 Rn [289]						

* Lanthanide series													
lanthanum 57 La 138.91	cerium 58 Ce 140.12	praseodymium 59 Pr 140.91	neodymium 60 Nd 144.24	promethium 61 Pm [145]	samarium 62 Sm 150.36	europium 63 Eu 151.96	gadolinium 64 Gd 157.25	terbium 65 Tb 158.93	dysprosium 66 Dy 162.50	holmium 67 Ho 164.93	erbium 68 Er 167.26	thulium 69 Tm 168.93	ytterbium 70 Yb 173.04
** Actinide series													
actinium 89 Ac [227]	thorium 90 Th 232.04	protactinium 91 Pa 231.04	uranium 92 U 238.03	neptunium 93 Np [237]	plutonium 94 Pu [244]	americium 95 Am [243]	curium 96 Cm [247]	berkelium 97 Bk [247]	californium 98 Cf [251]	einsteinium 99 Es [252]	fermium 100 Fm [257]	mendelevium 101 Md [258]	nobelium 102 No [259]

Figure 1.6. Periodic table colored to indicate the elements that have been put in the perovskite structure (ABX_3).

The perovskite structure can be described as cubic close packed anion layers with one quarter of the anions replaced with an A cation forming layers of AX_3 . The B cation then fills one quarter of the octahedral holes. This results in a pseudo-FCC unit cell in which the A cations reside on the corners and X anions on the faces, forming octahedral coordination around the B cation in the center (Figure 1.7). This is considered the ideal perovskite structure and has $Pm\bar{3}m$ symmetry with Wyckoff positions of $1a$ (0,0,0), $1b$ (1/2,1/2,1/2), and $3c$ [(0,1/2,1/2), (1/2,0,1/2), (1/2,1/2,0)] for the A , B , and X ions, respectively.

Victor Moritz Goldschmidt [14] observed that for an ideal perovskite, the A cation is similar in size to the X anion, and as such, the X - A - X distance would be $\sqrt{2}$ times greater than the X - B - X distance. The ratio of these two distances is called the tolerance factor (t):

$$t = \frac{(R_X + R_A)}{\sqrt{2}(R_X + R_B)} \quad (\text{E1.1})$$

where R is the radii for each of the ions. For ideal perovskites, t would be equal 1 and any deviation will tend to cause the structure to distort or even crystallize in a non-perovskite structure. A t value of < 1 indicates that the A cation is too small and as a result, the octahedra will tilt to compensate (i.e. GdFeO_3 , $t = 0.904$). When the A cation is too large ($t > 1$), the ions will displace to compensate (i.e. BaTiO_3 , $t = 1.063$).

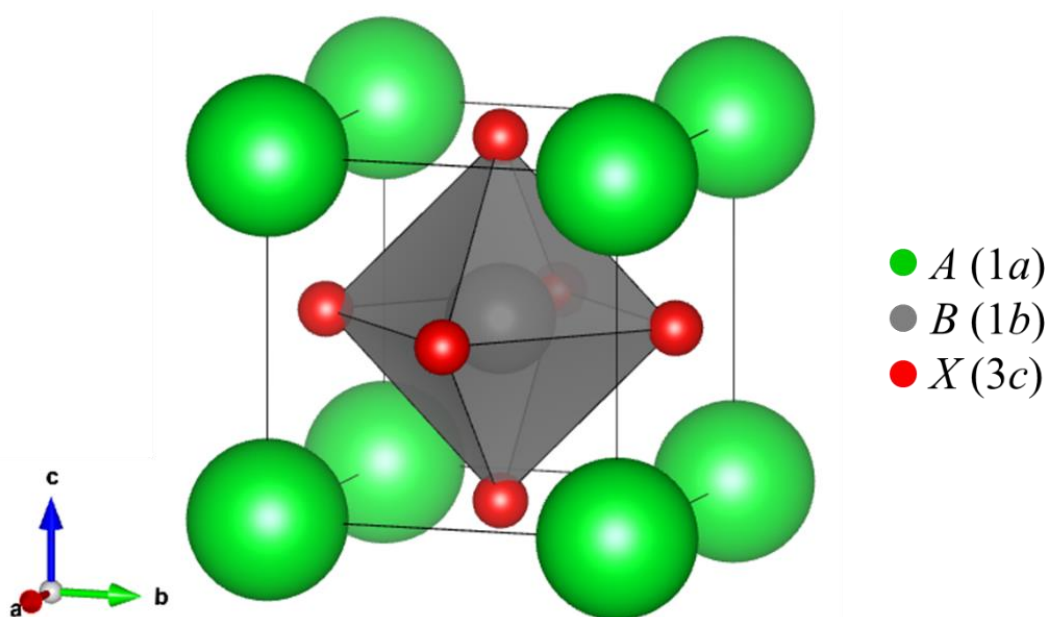


Figure 1.7. Unit cell of the ideal perovskite structure with space group $Pm\bar{3}m$.

If the deviation from 1 is large enough, the compound can crystallize in a completely different structure. For example, MgTiO_3 ($t = 0.747$) and RbNiF_3 ($t = 1.066$), crystallize in the ilmenite and 6H hexagonal polytype structures, respectively. It must be noted, however, that the tolerance factor is not an infallible predictor of structure type. There are many factors that influence the crystal structure other than ion size, including: degree of covalency, metal-metal

interactions, Jahn-Teller effects, and lone pair effects. Cubic perovskites tend to form when t falls within a range of 0.9–1.05. Examination of literature, however, shows that this range can be expanded to 0.81–1.11, which extends well into regions where one would expect non-cubic symmetry and/or non-perovskite structure types. The reverse is true as well. For example, PbTiO_3 has a t value of 0.999, suggesting it would crystallize with $Pm\bar{3}m$ symmetry; however, it is actually tetragonally distorted ($P4mm$) due to large ion displacement (facilitated by the presence of a lone pair on Pb^{2+}).

The most commonly observed distortion in perovskites is tilting of the BX_6 octahedra and occurs in order to achieve a lower energy mode when the A cation is too small (i.e. $t < 1$). This distortion also necessitates a lowering of symmetry from the ideal $Pm\bar{3}m$ symmetry. The tilting mechanisms have been heavily studied and classified by Glazer, Woodward and others [15–17]. Woodward and Glazer are credited for linking the possible tilting schemes to their respective space groups (Table 1.1). Glazer notation is used to classify the BX_6 tilting with respect to the Cartesian axes of the ideal cubic unit cell. Each unique tilting angle along the x , y , z axes is represented by the letters a , b , c . For example, an aab scheme indicates that the tilt angles along x and y are the same while the z angle is different. Superscripts are used to give an indication of the how the octahedra tilt with respect to their neighbors. Positive superscripts indicate an in-phase rotation of octahedra in successive layers in the same direction while an anti-phase tilt is represented by a negative superscript. If no rotation is present, a zero subscript is used.

Table 1.1. Perovskite Tilt Systems and Their Assigned Space Groups [15]

Number	Symbol	Space Group
<i>3-Tilt System</i>		
1	$a^+b^+c^+$	<i>Immm</i> (#71)
2	$a^+b^+b^+$	<i>Immm</i> (#71)
3	$a^+a^+a^+$	<i>Im$\bar{3}$</i> (#204)
4	$a^+b^+c^-$	<i>Pmmn</i> (#59)
5	$a^+a^+c^-$	<i>P4₂/nmc</i> (#137)
6	$a^+b^+b^-$	<i>Pmmn</i> (#59)
7	$a^+a^+a^-$	<i>P4₂/nmc</i> (#137)
8	$a^+b^-c^-$	<i>P2₁/m</i> (#11)
9	$a^+a^-c^-$	<i>P2₁/m</i> (#11)
10	$a^+b^-b^-$	<i>Pnma</i> (#62)
11	$a^+a^-a^-$	<i>Pnma</i> (#62)
12	$a^-b^-c^-$	<i>F-1</i> (#2)
13	$a^-b^-b^-$	<i>I2/a</i> (#15)
14	$a^-a^-a^-$	<i>R-3c</i> (#167)
<i>2-Tilt System</i>		
15	$a^0b^+c^+$	<i>Immm</i> (#71)
16	$a^0b^+b^+$	<i>I4/mmm</i> (#139)
17	$a^0b^+c^-$	<i>Cmcm</i> (#63)
18	$a^0b^+b^-$	<i>Cmcm</i> (#63)
19	$a^+b^-c^-$	<i>I2/m</i> (#12)
20	$a^+b^-b^-$	<i>Imma</i> (#74)
<i>1-Tilt System</i>		
21	$a^0a^0c^+$	<i>P4/mbm</i> (#127)
22	$a^0a^0c^-$	<i>I4/mcm</i> (#140)
<i>0-Tilt System</i>		
23	$a^0a^0a^0$	<i>Pm$\bar{3}m$</i> (#221)

To illustrate, NaTaO₃ crystallizes as an orthorhombic perovskite (*Cmcm*) at high temperature and has a Glazer tilting scheme of $a^0b^-c^+$. The different tilting patterns can be

easily observed upon the examination of projections of NaTaO_3 along the $[100]$, $[010]$, and $[001]$ directions (Figure 1.8). Tilting of octahedra can have a drastic effect on the properties of a material. For example, Subramanian et al. showed that substitution of Te for Se in ferromagnetic SeCuO_3 can induce a transition to an antiferromagnetic state by tuning the tilting angle of the CuO_6 octahedra [18].

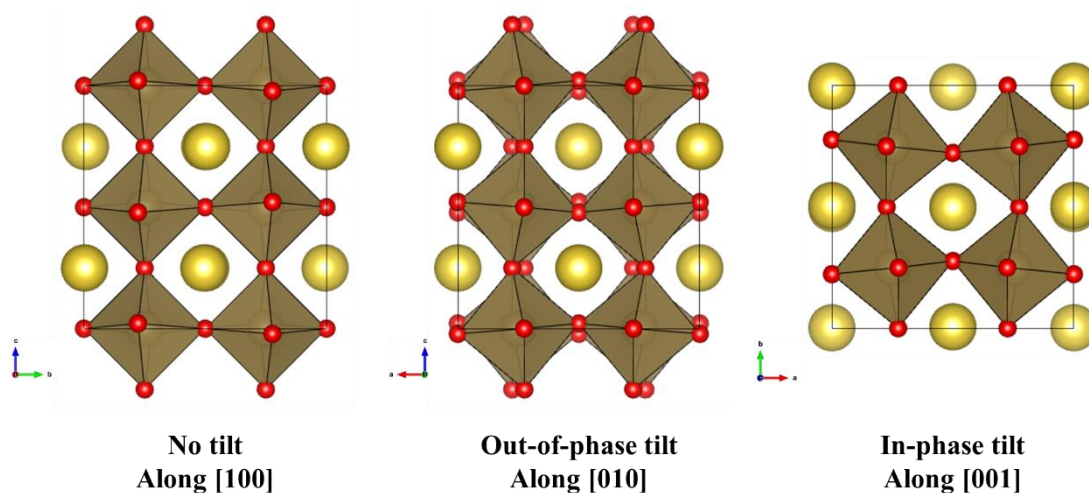
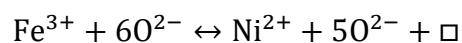


Figure 1.8. Projections of NaTaO_3 ($a^0b^-c^+$) demonstrating the different tilting patterns observed in distorted perovskites.

1.4.1.1 Non-stoichiometry in Perovskites

The two major ways non-stoichiometry is achieved in perovskites are either A-site or anion vacancies. B-site vacancies can occur in thin films [19] but have never been reported in bulk. A-site vacancies have a general formula of $A_{1-x}BX_3$ where $0 < x < 1$. Although there is no strict rule, compounds with $x < 0.75$ are generally classified as “bronzes” and those where $x > 0.75$ are simply called A-site deficient perovskites [20].

Anion-deficient or defect perovskites can be generalized with the formula $ABX_{3-\delta}$ where $0 \leq \delta \leq 0.5$. These vacancies typically occur in order to compensate for a charge imbalance when a cation in the structure is substituted for another of lower charge. This can be demonstrated by considering a solid solution between LaFeO_3 and $\text{La}_2\text{Ni}_2\text{O}_5$. When the Fe^{3+} is substituted for Ni^{2+} the positive charge on the B-site is lowered meaning the negative charge produced by the full oxygen content is too high and must be reduced by the production of a vacancy (\square):



Anion vacancies can be ordered or randomly oriented depending on the quantity and, in some cases, temperature. Generally, vacancy ordering occurs when one sixth of the anion positions are vacant giving a general formula of $A_2B_2O_5$ ($\delta = 0.5$). There are a few ways these compounds can order, but one of the most common orderings is along the [011], which forms the orthorhombic brownmillerite structure (Figure 1.9) named for Dr. Lorrin Thomas Brownmiller. This structure typically forms when A = late alkali earth and B^{3+} = Al, Sc, Fe, In, Cr, Ga. Examples of reported brownmillerites include $\text{Ca}_2\text{FeAlO}_5$, $\text{Ba}_2\text{In}_2\text{O}_5$, $\text{Ca}_2\text{FeCoO}_5$, and $\text{Sr}_2\text{MnGaO}_5$; they have been investigated for their magnetic and electronic transport behaviors, as well as their potential as pigments, oxide ion conductors, catalysts and thermoelectric materials [21–28].

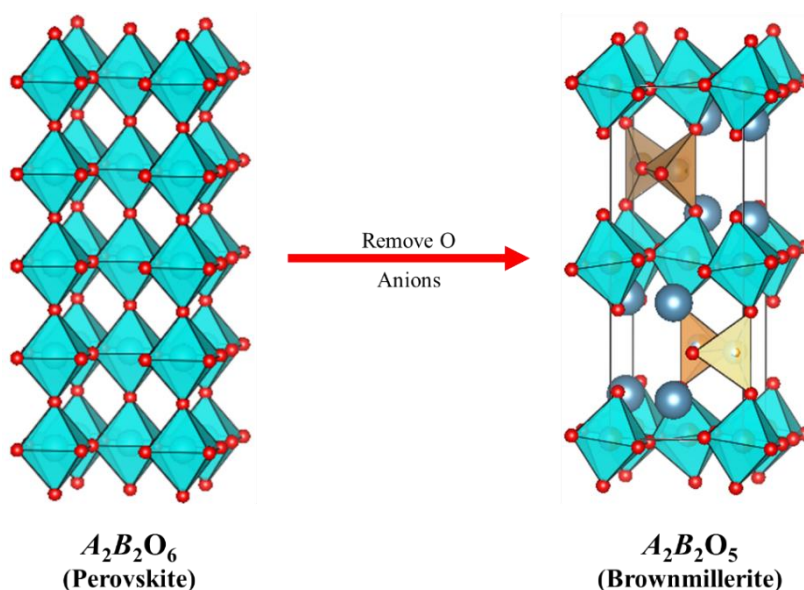


Figure 1.9. Comparison of the perovskite and brownmillerite structures. The brownmillerite structure can be created by removing O ions from the perovskite in alternating layers along the [110].

1.4.1.2 Hexagonal Polytypes

The ideal cubic perovskite can also be described in terms of a hexagonal unit cell where $a_{\text{hex}} = a_{\text{cub}}\sqrt{2}$ and $c_{\text{hex}} = a_{\text{cub}}\sqrt{3}$. Using this cell, the AX_3 layers stack perpendicular to [001] in a cubic-close packed manner. Because of this a cubic perovskite is often called a “3C” polytype due a *ccc* repeat sequence where *c* denotes corner sharing octahedra (Figure 1.10). There is also an ideal hexagonal perovskite structure where the AX_3 layers follow a hexagonal-close packing scheme. In this structure, the O_h sites are oriented to where they share faces. The ideal hexagonal perovskite is also called the 2H polytype as the repeat sequence is *hh* where *h* denotes face-sharing octahedra (Figure 1.10). 2H polytypes typically form when the *A* cation is too large (i.e. $t > 1$); therefore, a majority of 2H compounds are composed of an alkali or alkali earth *A* cation and a transition metal *B* cation (e.g. BaNiO_3).

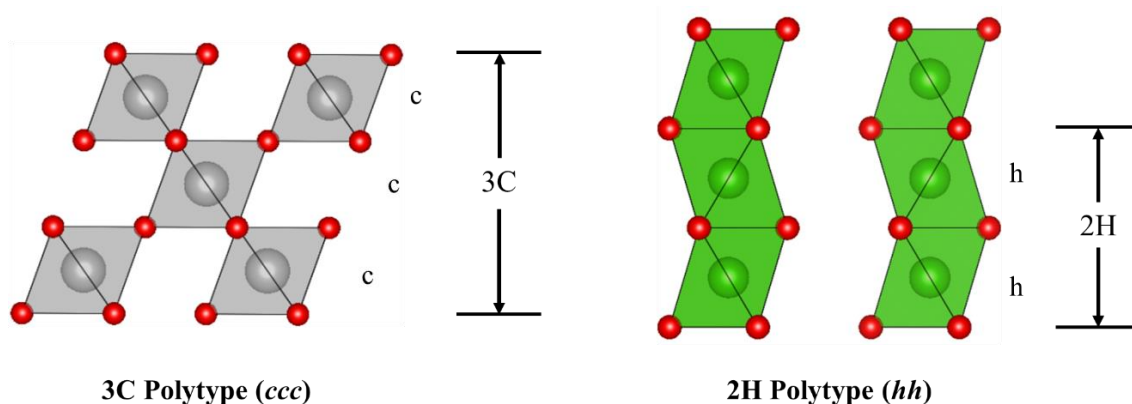


Figure 1.10. Comparison of the perovskite polytype structures created by all ccp (3C) and all hcp (2H) stacking of AX_3 layers.

Between the two ideal structures exists the possibility to create new structures by mixing cubic and hexagonal stacking motifs. In theory, there is a near-infinite number of possible structures. In practice, however, this number is limited to relatively few stacking sequences. Some of the more commonly occurring examples include the 6H, 4H, and 9R polytypes (Figure 1.11). The 6H and 4H polytypes both have hexagonal symmetry (hence the H) with the space group $P6_3/mmc$. The ratio of hexagonal to cubic stacking is 1:2 for 6H and 1:1 for 4H and therefore they have stacking sequences of $hcchcc$ and, $hchc$ respectively. The 9R polytype, on the other hand, has rhombohedral symmetry with the $R\bar{3}m$ space group. It has hexagonal-cubic ratio of 2:1 with the stacking sequence $hhchhchhc$ or $(hhc)_3$. While the 4H, 6H, and 9R polytypes are most common, more complex polytypes have been reported. Examples include: 8H, 10H, 14H, 12R, 15R, and 27R which have stacking sequences of $(cchc)_2$, $(cchcc)_2$, $(cchchch)_2$, $(cchh)_3$, $(cchc)_3$, and $(cchchchch)_3$, respectively. Examples of these structures include $Ba_4Ru_3NaO_{12}$, $Ba_6Nd_2Ti_4O_{17}$, and $SrMn_{1-x}Fe_xO_{3-\delta}$ [29–31].

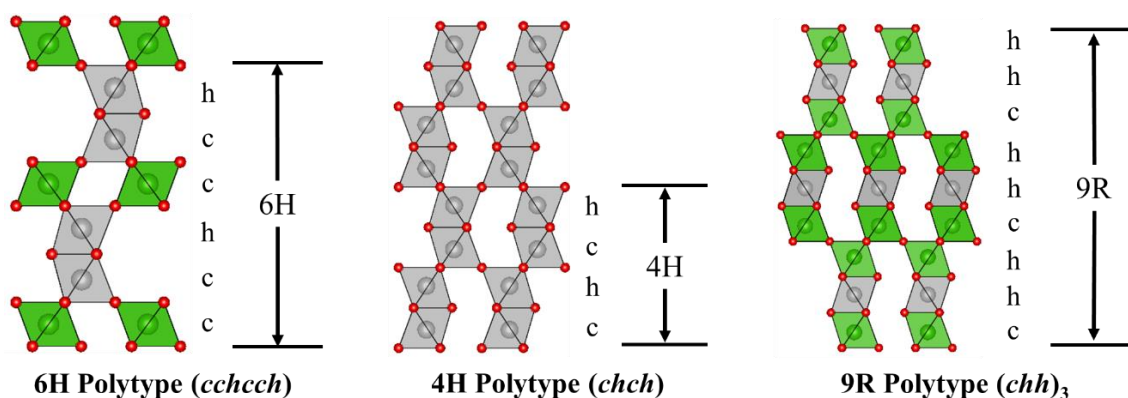


Figure 1.11. Crystal structures of commonly observed perovskite polytypes created by varying the ratio of ccp and hcp stacking of the AX_3 layers.

1.4.2 The Spinel Structure

Spinel has the general formula AB_2X_4 where A and B are metal cations and X is an anion, usually oxygen. Their well-studied structure (shown in Figure 1.12), from a close packing point-of-view, can be described as a cubic-close packed X anion lattice with $1/8$ of the tetrahedral sites filled by the A cations and $1/2$ of the octahedral sites filled by the B cations. The robust and rigid nature of the spinel structure leads most examples to crystallize with cubic symmetry and a space group of $Fd\bar{3}m$ with Wyckoff positions of $8a$ ($1/8, 1/8, 1/8$), $16d$ ($1/2, 1/2, 1/2$) and $32e$ (x, x, x) for the A , B , and X ions, respectively. The most common distortion in cubic is displacement of the X ion from its ideal position ($x = 1/4$) toward or away from the B -site. This results in distortion of octahedral bond angles away from 90° . The tetrahedral sites typically remain rigid with ideal 109.4° bond angles and the cubic symmetry always remains intact. There are, however, a few reported examples of spinels, such as $CuCr_2O_4$ and $NiCr_2O_4$, that are tetragonally distorted due to Jahn-Teller effects at the A -site [32–34].

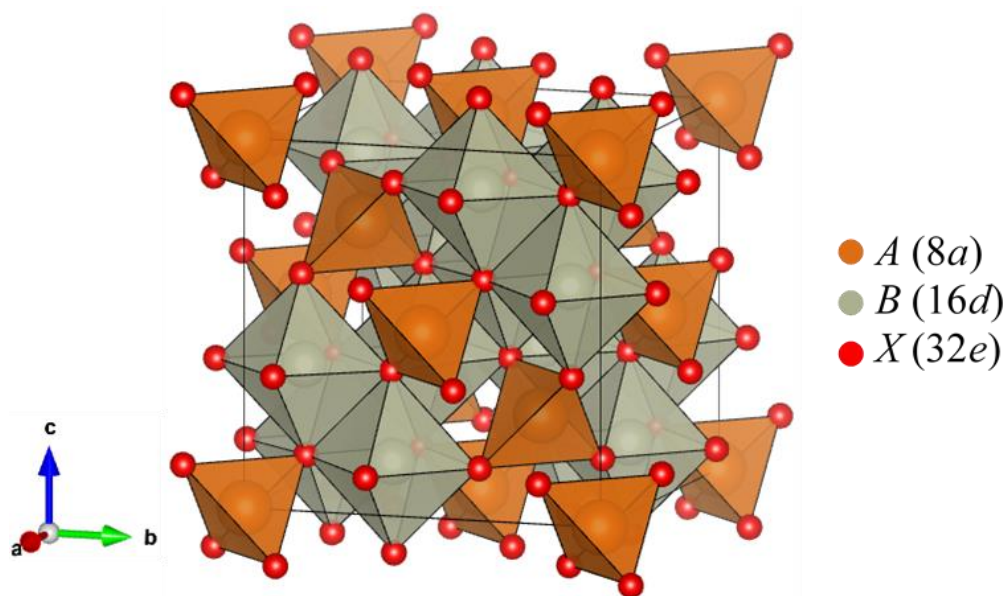


Figure 1.12. Unit cell of the cubic ($Fd\bar{3}m$) spinel crystal structure.

The spinel structure can be broken down into diamond and pyrochlore sublattices (Figure 1.13) created by the A and B sites, respectively. The atomic arrangement in these sublattices makes them useful systems for inducing and studying geometric frustration [35].

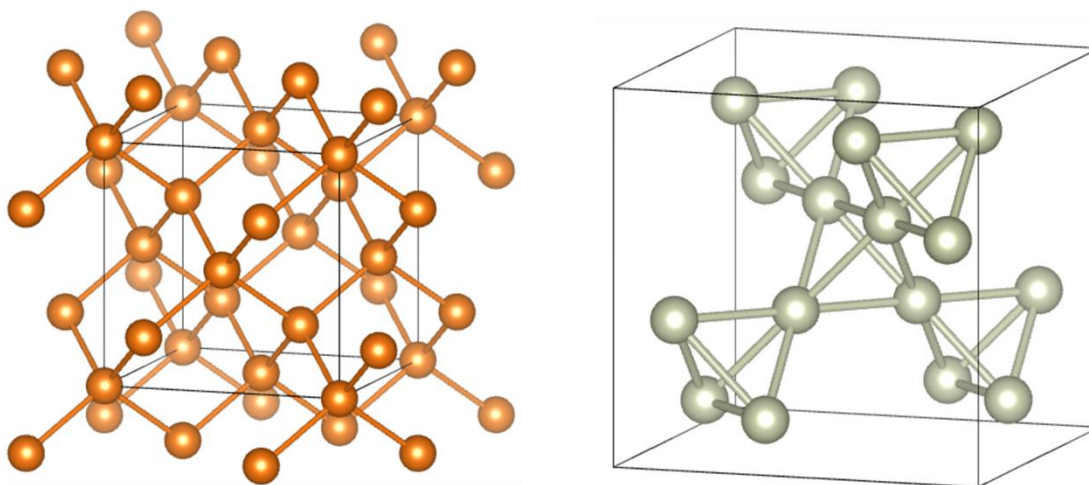


Figure 1.13. Schematics showing the (left) diamond and (right) pyrochlore sublattices formed respectively by the A and B sites of the spinel structure.

1.5 Structural Analysis

1.5.1 Scattering of Light by Crystalline Materials

When a material is irradiated with a beam of particles or light of an appropriate wavelength, the beam will be scattered. Depending on the type of beam, scattering, and interactions between the beam and the material, a variety of information about the material can be extracted. There are two main types of scattering: elastic and inelastic. In elastic scattering, there is a complete transfer of energy and momentum from the incident beam to the scattered beam. In inelastic scattering, the transfer is incomplete and some of the energy and momentum is transferred to the material.

For experiments on the atomic scale, the wavelength of the beam must be on the order of 0.01–100 Å, in which the best choices for crystal structure or chemical composition determination are electrons, neutrons and X-rays. While all three beams can yield crystallographic information, each type of beam has advantages or disadvantages depending on how it interacts with atoms. Electrons are scattered by repulsive forces from the electron cloud of the atom and due to the short wavelength (typically ~ 0.02 Å), the strong atomic scattering, and the ability to examine tiny sample sizes (~ 10 nm³), electron scattering is sensitive to small structural deviations caused by structural distortions, ordering, short-range ordering, or defects [36]. The biggest drawback of electron scattering is that the penetration depth of electrons in solid materials is relatively shallow. This means experiments must be performed using transmission electron microscopy (TEM), an expensive and time-consuming process. Scattering experiments using TEM also requires that samples be thin enough to allow for electron transmission (< 100 nm) which can be difficult to achieve for some samples.

X-rays also interact with the atomic electron cloud but have a deeper penetration depth than electrons because they lack charge. This allows for extraction of more detailed structural information such as lattice parameters and atomic positions to be obtained. One of the drawbacks for X-rays, however, is that their atomic scattering factors scale linearly (Figure 1.14) with atomic number, Z . Atomic scattering factors also vary as a function of $(\sin \theta)/\lambda$ meaning scattering gets weaker as the angle of the incident beam, θ , or the radiation wavelength, λ , increases.

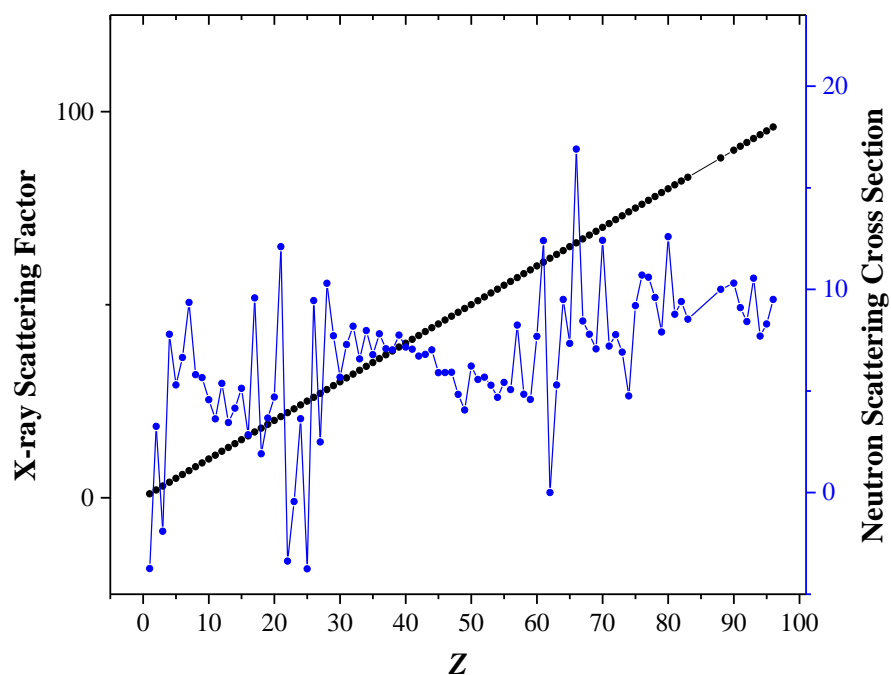


Figure 1.14. Plot illustrating the Z dependence of X-ray scattering factors and neutron scattering cross sections. Note the highly linear trend for X-rays compared to the much more irregular trend for the neutron cross sections.

A consequence of the linear relationship of scattering factors and Z is that X-rays are sufficient for determining position and occupancy of heavier elements, such as Pb or Ir, but poor for lighter elements, such as H or O; this can be problematic when dealing with oxides.

This also implies that elements that are close on the periodic table will have similar scattering factors and therefore be indistinguishable when they share a crystallographic site. Neutrons, on the other hand, interact directly with the atomic nucleus, and the atomic scattering cross sections are independent of Z . This effectively removes the limitations for lighter elements and those in close with similar values of Z . Neutrons, while lacking charge, have inherent spin, and are therefore subject to electron spin interactions throughout the crystal structure; this characteristic allows for refinement of the magnetic structure of a magnetically ordered material. Using neutrons, however, does introduce other challenges. Although they are more sensitive to certain elements, others, e.g. Cd and Gd, are very good neutron absorbers, and therefore any sample containing these would be very difficult to analyze. Additionally, the neutron sources used for structural analysis are expensive and large which limits viability of neutron diffraction experiments to national laboratories. X-rays, on the other hand, can be generated with small X-ray tubes which can be fitted in benchtop instruments making them more accessible to academic labs. Both X-rays and neutrons were employed in this dissertation and will be the focus of additional discussion.

1.5.2 Powder Diffraction

1.5.2.1 X-ray Diffraction

The most common method used for crystal structure elucidation is powder X-ray diffraction (PXRD). Diffraction is a special case of scattering in which, under the right conditions, scattered rays mutually reinforce each other resulting in a diffracted ray of greater intensity. The conditions for diffraction to occur can be illustrated using a simple diagram of a

crystal lattice with spacing d such as in Figure 1.15. The incident (1, 2) and diffracted (1', 2') beams will have the same wavelength, λ , and angle, θ , relative to the plane of atoms. Due to the interplanar spacing, beam 2 must travel further to reach atom C than beam 1 must to reach atom A . This can be stated for the diffracted beams as well. Geometrically, the total additional distance traveled by 2 and 2', shown in red, can be written in terms of d and θ :

$$BC + CD = d \sin \theta + d \sin \theta \quad (\text{E1.2})$$

When this sum is some integer multiple of λ , the diffracted beams will completely in phase and constructive interference occurs, or

$$n\lambda = 2d \sin \theta \quad (\text{E1.3})$$

This relationship was first developed by father and son William Henry Bragg and William Lawrence Bragg in 1913 [37] and is appropriately called Bragg's Law.

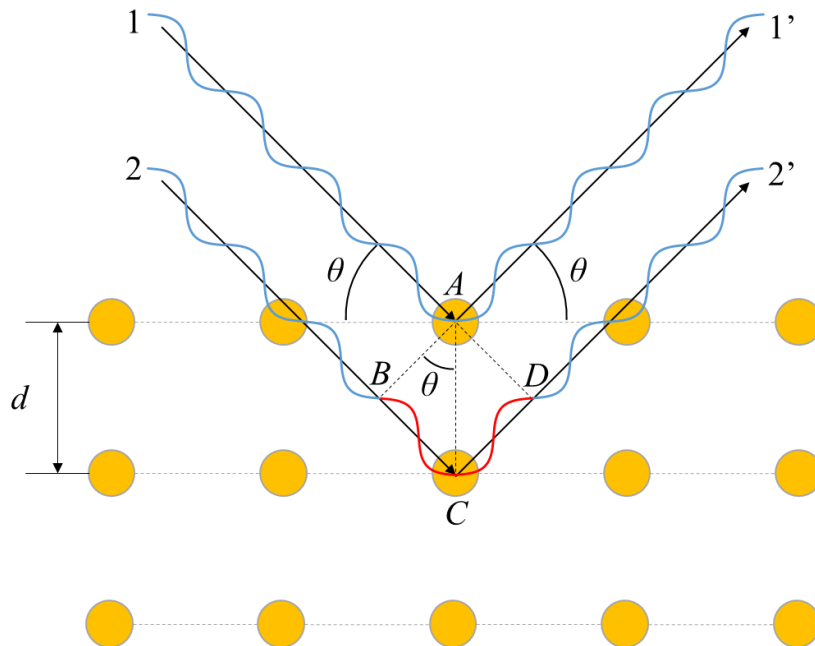


Figure 1.15. Schematic representation of conditions leading to Bragg diffraction.

According to Bragg's law, different d spacings will yield constructive interference at different angles. Therefore, by irradiating a material with a constant wavelength of X-rays from various angles and detecting the intensity of the diffracted beams, a PXRD pattern can be generated showing a series of peaks, typically as a function of scattering angle, 2θ . Based on the relative intensities and positions of these peaks, a large amount of information about the materials crystal structure can be extracted including atomic positions and thermal vibrations, site occupancies, and overall unit cell dimensions. Each peak is related to one or more crystallographic planes, labelled by Miller indices (hkl), formed by the atoms. The spacing of these planes is directly related to the dimensions of the unit cell based on the its symmetry [11]. For example, for an orthorhombic unit cell:

$$\frac{1}{d_{hkl}^2} = \frac{h^2}{a^2} + \frac{k^2}{b^2} + \frac{l^2}{c^2} \quad (\text{E1.4})$$

where a , b and c are the unit cell dimensions. For additional crystallographic information, modeling the entire pattern is required and will be discussed in §1.4.2.3.

1.5.2.2 Time-of-Flight Neutron Diffraction

Neutron powder diffraction (NPD), often done in conjunction with PXRD, is typically performed using one of two methods; this can be done using a beam of neutrons of a constant wavelength, similar to PXRD, or by using a pulsed beam containing a wide band of neutron wavelengths and therefore velocities. The latter of these is called time-of-flight (TOF) diffraction. In TOF diffraction, the neutron beam is directed down a long path, L , to the sample

and the time, t , it takes the neutrons to go from source to sample to detector, or time-of-flight, is recorded in addition to the scattering angle 2θ . Since the beam contains neutrons of different wavelengths and therefore different velocities, whether or not a neutron will be diffracted depends on the relationship between the neutron's wavelength, and therefore its time-of-flight, and the d spacing in the sample. This relationship can be obtained by combining the de Broglie equation with Bragg's law:

$$\lambda = \frac{ht}{m_n L} = 2d \sin \theta \quad (\text{E1.5})$$

where h is Planck's constant and m_n is the neutron mass. Patterns generated by NPD, generally expressed as a function of t , contain the same structural information as their PXRD counterparts.

1.5.2.3 Structure Modeling

The method most often used to obtain crystallographic information from a diffraction pattern is Rietveld method [38]. The basis of this method relies on accounting for fitting the peak shapes and intensities. The peak intensity, I , for a particular hkl value can be defined as:

$$I_{hkl} = F_{hkl}^2 \times M_{hkl} \times D \quad (\text{E1.6})$$

where F_{hkl} is the structure factor, M_{hkl} is the multiplicity of the hkl family and D is the displacement factor. For X-rays, the structure factor accounts for the contributions of the scattering factor, f , and location of atom j :

$$F_{hkl} = \sum_j f_j \exp(-2\pi i(hx_j + ky_j + lz_j)) \quad (\text{E1.7})$$

where x_j , y_j and z_j are the positional coordinates of j [11]. The displacement factor accounts for, as the name implies, any average displacement of the atom caused by structural distortion or thermal vibration. It is related to λ and θ through

$$D = \exp\left(\frac{U \sin \theta}{8\pi^2 \lambda}\right) \quad (\text{E1.8})$$

The value U is the atomic displacement parameter and is usually reported in scientific reports involving crystal structure refinements.

The Rietveld method involves using the above relationships to calculate intensities and fits them against the observed experimental data using least-squares analysis. The structure model and calculated intensities are tuned by methodically refining instrumental background, unit cell parameters, peak shape and broadening parameters, atomic positions, site occupancies, and atomic displacement parameters. Due to the sheer number of variables, however, it can be difficult to make progress if little is known about the structure. To facilitate this, refinements are usually begun with the LeBail method [39] which uses the same Rietveld algorithm but sets all F_{hkl} values to 1 thereby removing the dependency on the atomic identities and positions. This allows for space group determination, if needed, through peak indexing as well as refinement of the unit cell parameters and peak shapes. Once this information is extracted, it can be used directly to start a Rietveld refinement; the intensity determining parameters can then be refined, and the overall structure model can subsequently be fine-tuned and finalized.

1.5.3 Diffraction instrumentation

All XRD measurements discussed in this dissertation were performed using a Rigaku Miniflex II bench top diffractometer (Figure 1.16) over a range of 10–80° 2θ using Cu $K\alpha$ radiation ($\lambda = 1.54 \text{ \AA}$). The X-rays are generated by accelerating a beam of electrons from a heated tungsten filament toward an anode with a Cu metal target by applying a large voltage ($> 10 \text{ kV}$). The striking incident electrons ionize some of the Cu 1s electrons. Characteristic X-ray radiation is then given off when electrons from the outer orbitals relax to occupy the 1s vacancy [40]. These X-rays are directed out a Be window toward the sample to be measured. A graphite monochromator is often employed to absorb Cu $K\beta$ radiation which is undesirable. The Miniflex II operates at fixed tube voltage of 30 kV and a fixed tube output current of 15 mA [41].



Figure 1.16. Photos of (left) the exterior of the Rigaku Miniflex II diffractometer and (right) sample chamber illustrating the geometry of the X-ray tube, sample, and detector.

The Miniflex II utilizes either a 6-sample changer which rotates the sample during the measurement, or a single sample holder without rotation. Generally, the 6-sample changer is used for most fast scan measurements (scans where the 2θ variation is $> 2^\circ/\text{min}$) when phase

identification is the only objective. For analysis of unit cell parameters and structural refinements, high peak resolution and intensities are required which can be obtained by using a slower scan. This is done by decreasing the 2θ step increment and increasing the scan time at each step, allowing the intensity to reach its maximum.

Neutron diffraction data for the samples in this dissertation were collected at the Spallation Neutron Source (SNS) at Oak Ridge National Lab in Oak Ridge, Tennessee using the BL-11A (POWGEN) neutron powder diffractometer [42]. Sample masses were 1–2 g and samples were loaded into 6 mm vanadium sample cans and data was collected over approximately 2–4 h.

1.6 Magnetism

“Few subjects in science are more difficult to understand than magnetism.”

– Encyclopedia Britannica, 1989

1.6.1 Fundamentals

Everything, whether it be an oxide, polymer, wood, living, or dead, exhibits a response to a magnetic field. All substances are diamagnetic to an extent, meaning all electrons are paired and any external magnetic field would disturb the energy state. Consequently, a diamagnetic material repels an external magnetic field by generating its own field in the opposite direction resulting in a small negative magnetic moment that is temperature independent and on the order of 10^{-6} emu/mol. A paramagnetic material, on the other hand, has unpaired electrons whose spins are oriented randomly in the absence of a magnetic field. When a paramagnetic material is exposed to an external field, it responds by aligning some of its unpaired electron spins in the

same direction as the external field. This generates a positive magnetic moment that usually has a magnitude around 10^1 emu/mol. Thermal agitation (i.e. temperature) works against this alignment, with only a small portion of the unpaired spins aligning with the external field. This portion can, however, be increased by lowering the temperature of the material. Paramagnetic materials also have a diamagnetic electron core but since the diamagnetic moment is several orders of magnitude lower, it is often overshadowed and ignored.

When a material is put under the influence of a magnetic field, B , the response can be quantified by the magnetization, M . These two quantities are proportionally related by

$$M = \mu_0 \chi B \quad (\text{E1.6})$$

where μ_0 is the permeability of free space and χ is the magnetic susceptibility of the material.

The intensity of B , labeled as H , can be calculated via:

$$H = \mu_0 B \quad (\text{E1.7})$$

Solving E1.6 for χ and substituting for $\mu_0 B$ yields a definition of magnetic susceptibility in terms of magnetization and external field strength:

$$\chi = \frac{M}{H} \quad (\text{E1.8})$$

The observed magnetic susceptibility (χ_{obs}) of a material can be considered as the sum of several magnetic susceptibilities:

$$\chi_{\text{obs}} = \chi_{\text{para}} + \chi_{\text{dia}} + \chi_{\text{Vv}} + \chi_{\text{Pauli}} \quad (\text{E1.9})$$

where χ_{para} and χ_{dia} are the paramagnetic and diamagnetic susceptibilities. The Van Vleck term (χ_{Vv}) is a type of temperature independent paramagnetism that occurs when the electron

configuration of an atom or ion results in a state in which the total orbital momentum is equal to zero. χ_{Pauli} is the term for Pauli paramagnetism, which is a phenomenon only seen in materials that conduct electrons metallically; as none of the compounds described in this dissertation are metallic, it will not be discussed further. Most often with transition metal oxides, the most interesting term out of these four is χ_{para} , as a great deal of information can be extracted from it. χ_{para} can be isolated from χ_{obs} by subtracting out the other χ terms (or ignoring them if they are negligible) and it is defined by the Curie Law to be inversely proportional with temperature:

$$\chi_{\text{para}} = \frac{C}{T} \quad (\text{E1.10})$$

The Curie constant, C , is defined as

$$C = \frac{\mu_0 N_A}{3k_B} \mu_{\text{eff}}^2 \mu_B^2 \quad (\text{E1.11})$$

where N_A is Avogadro's number, k_B is Boltzmann's constant, μ_B is the Bohr magneton, and μ_{eff} is the effective magnetic moment of the material. Often the orbital contribution is small enough to be ignored, especially in $3d$ TMs, and the moment is considered "spin-only". The spin-only moment, μ_S , can be estimated by:

$$\mu_S^2 = g_S^2 S(S + 1) \quad (\text{E1.12})$$

where g_S is the electronic spin g-factor (usually estimated as 2) and S is the spin quantum number for the magnetic ion in the material.

Although there are some examples (e.g. Gd_2O_3 , gaseous O_2), very few materials are "pure" paramagnets due to electron-electron interactions. Consequently, a "corrected" variation

of E1.10, called the Curie-Weiss Law, is more often used when characterizing magnetic materials:

$$\chi_{\text{para}} = \frac{C}{(T-\theta)} \quad (\text{E1.13})$$

where θ is the Weiss constant which can give an indication of any magnetic ordering that may be present. When analyzing χ data, the Curie-Weiss law is often used in its linear form:

$$\frac{1}{\chi} = \frac{1}{C}(T) + \frac{\theta}{C} \quad (\text{E1.14})$$

Using this form, the values for C and θ can be extracted by fitting the linear paramagnetic region in a plot of χ^{-1} vs. T . This process is commonly done to infer or confirm oxidation states by comparing the μ_{eff} and μ_{S} values calculated using E1.12 and E1.13.

1.6.2 Magnetic Ordering

Some materials, while paramagnetic at high temperatures, are known to undergo spontaneous long-range ordering of their electron spins at sufficiently low temperatures. The two simplest types of magnetic ordering are ferromagnetism and antiferromagnetism. In ferromagnetism, the electron spins spontaneously coalign resulting in a large, sudden increase in the magnetization (Figure 1.17).

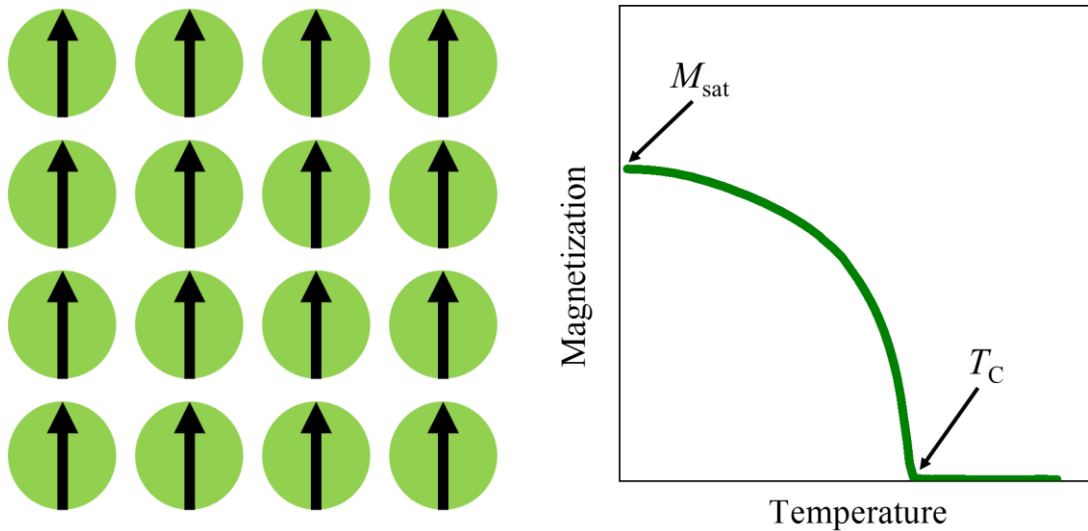


Figure 1.17. Schematic showing the (left) electron spin ordering and (right) temperature dependence of the magnetization for ferromagnetic behavior. The Curie temperature (T_C) indicates the beginning of magnetic ordering while M_{sat} is the saturation magnetization.

Similar to paramagnetism, the alignment is resisted by thermal agitation but as $T \rightarrow 0$, the magnetization approaches a saturation magnetization, M_{sat} . The temperature below which the ordering occurs is called the Curie temperature, T_C . Above this temperature, paramagnetic behavior is observed according to the Curie-Weiss law (E1.10) and for ferromagnetic materials, $\theta > 0$. Ferromagnetic materials tend to be metallic conductors, examples of which include metallic iron, Fe_2O_3 , and CrO_2 .

Antiferromagnetism is much more commonly observed in oxides than ferromagnetism and in contrast, results from spontaneous anti-alignment of electron spins (Figure 1.18). This causes, as one might suspect, a sudden decrease in the magnetization. This alignment and corresponding decrease in magnetization increases as $T \rightarrow 0$ due to the effects of thermal agitation.

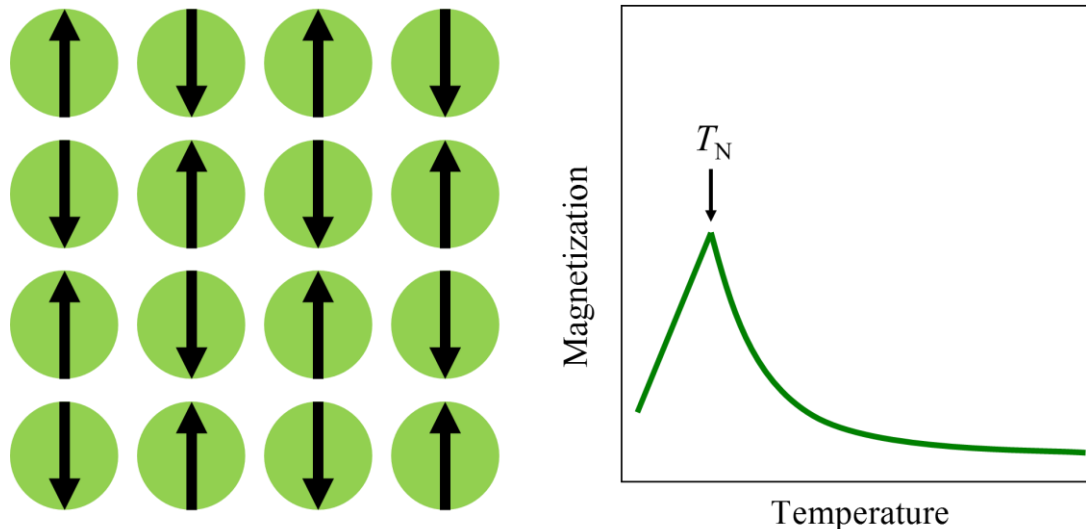


Figure 1.18. Schematic showing the (left) electron spin ordering and (right) temperature dependence of the magnetization for antiferromagnetic behavior. The Néel temperature (T_N) indicates the beginning of magnetic ordering.

This also means that, like its counterpart, antiferromagnetism only occurs below a certain threshold temperature called the Néel temperature, T_N , above which the material is paramagnetic and $\theta < 0$. For antiferromagnetic materials, there are several different ways the spins can order while still achieving long range antiferromagnetic order. Interestingly, many of these orderings are observed in the $\text{La}_{1-x}\text{Ca}_x\text{MnO}_3$ solid solution and were first labeled A through G by Wollan and Koehler [43]. A-, C- and G-types are illustrated in Figure 1.19 and the magnetic structures can be described in terms of the spin interactions within and between layers along the z axis. The G-type structure is the most commonly ordering seen outside $\text{La}_{1-x}\text{Ca}_x\text{MnO}_3$ and has antiferromagnetic ordering within the horizontal layers as well as between them. A- and C-type structures are a bit more complex. The A-type magnetic structure has intralayer ferromagnetic ordering while the interlayer interactions are antiferromagnetic. C-type

is the reverse with the intralayer ordering is antiferromagnetic with ferromagnetic interlayer ordering.

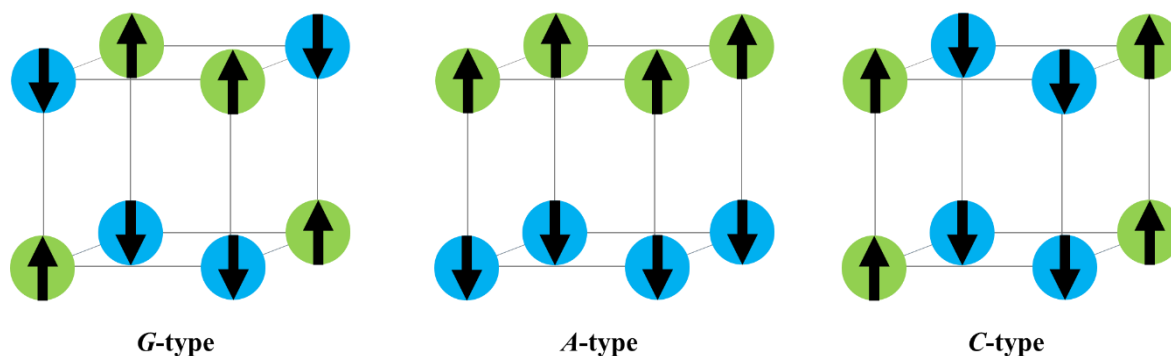


Figure 1.19. Commonly observed antiferromagnetic structures.

The remaining magnetic structure types labeled by Wollan and Koehler are more complex with the exception of *B*-type, which is actually the ferromagnetic structure. It should be noted that more exotic and complex antiferromagnetic structures exist that are not covered by these labels, such as those seen in La_2CuO_4 and La_2NiO_4 [44].

1.6.3 Spin Glasses

It is often observed that not all materials fit neatly into the types of magnetic behavior described above and many oxides exhibit unusual or exotic magnetic states. One of these states is called a spin glass. If the magnetic atoms in a material are arranged in a certain way, it's possible to create a situation where electron spins that want to order antiferromagnetically are not able to do so due to competing interactions. This is called geometrically frustrated magnetism [45] and, as illustrated in Figure 1.20, often occurs in triangular or tetrahedral arrangements of magnetic atoms or ions. These frustrated motifs occur in several lattices. Some

common ones include the FCC lattice, the Kagome lattice seen in layered honeycomb and magnetoplumbite structures [46,47], and the pyrochlore lattice seen in pyrochlores as well as spinels [48–50].

Magnetic frustration can cause a variety of unique and interesting magnetic states, many of which result in the absence of any long-range ordering. One of these states is called a spin glass. In this state, the electron spins are essentially frozen in a random pattern below a glass temperature, T_G . Spin glasses manifest themselves experimentally through many characteristics. The common ones include [45]: divergence between the field-cooled and zero field-cooled DC magnetic susceptibilities below T_G , a strong frequency dependence in the AC susceptibility, and the absence of long-range order in low temperature neutron diffraction data.

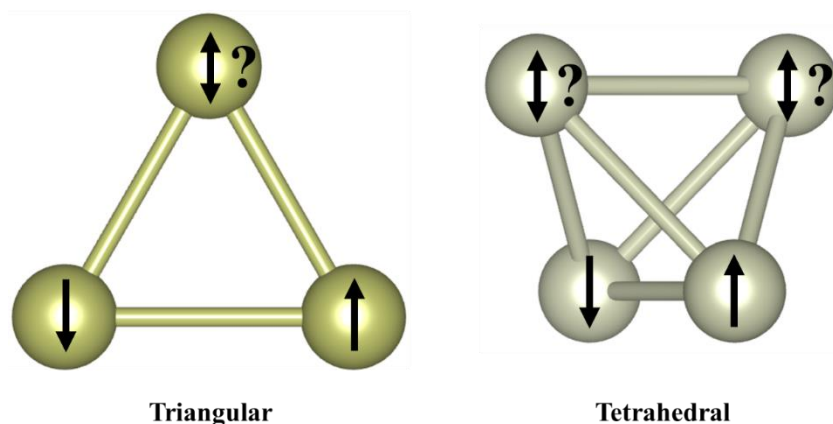


Figure 1.20. Diagrams illustrating the geometric frustration of magnetic moment moments (arrows) in triangular and tetrahedral atomic arrangements.

1.6.4 Spin-Orbit Coupling

Spin-orbit coupling (SOC) occurs when the spin of an electron magnetically interacts with its own orbital angular momentum. From the point of view of an observer at the electron,

the nucleus will appear to orbit the electron (Figure 1.21). This creates a magnetic field (\mathbf{B}_0) that interacts with the magnetic moment of the electron.

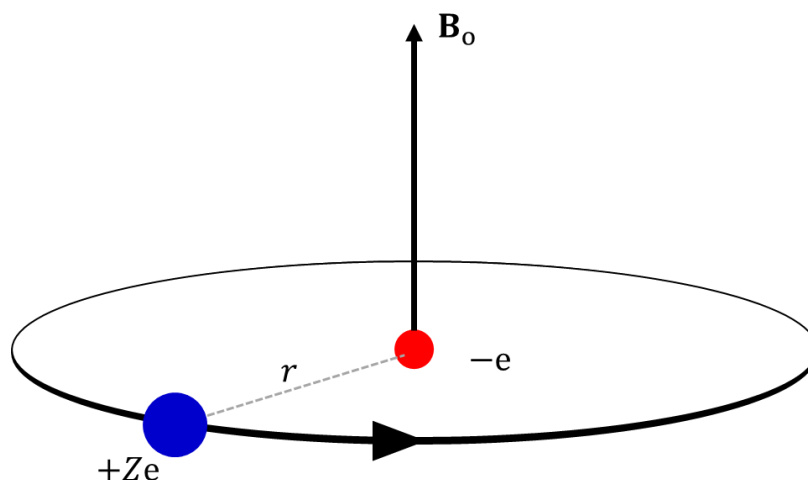


Figure 1.21. Schematic showing the magnetic field (\mathbf{B}_0) for the angular momentum of an electron. The generation of \mathbf{B}_0 can be rationalized by considering the motion of a nucleus with charge $+Ze$ around an electron with charge $-e$.

For a many-electron state, the energy of the spin-orbit interaction (E_{so}) scales with nuclear charge Z and be defined in terms of the spin and orbital angular momentum quantum numbers S and L :

$$E_{so} = \frac{\mu_0 Z e^2 g_s}{8\pi m_e^2 r^3} \mathbf{S} \cdot \mathbf{L} \quad (\text{E1.15})$$

where e is the charge of an electron, m_e is the electron mass, and r is the average radius of the electron cloud [51]. All elements have SOC to a degree but it much more prominent in heavier elements, such as the $5d$ TMs. E1.14 can be simplified to:

$$E_{so} = \lambda_{so} \frac{S \cdot L}{\hbar^2} \quad (\text{E1.16})$$

where λ_{so} is the SOC constant. It is useful at this point to define a total angular momentum quantum number $J = S + L$. The allowed values for J are $L + S, L + S - 1, \dots, |L - S|$ and each J state has a degeneracy of $2J + 1$. For example, an 3F state would be allowed $J = 4, 3,$ and 2 . Thus, SOC manifests itself by splitting the energy states which can have a direct effect on the electronic properties of a material. For instance, when SOC is applied to Ir(V) (d^4) and Ir(IV) (d^5) configurations in a strong octahedral field, the t_{2g} orbitals are split into new J states of $J = 2, 1, 0$ and $J = 3/2, 1/2$, respectively [52] (Figure 1.22).

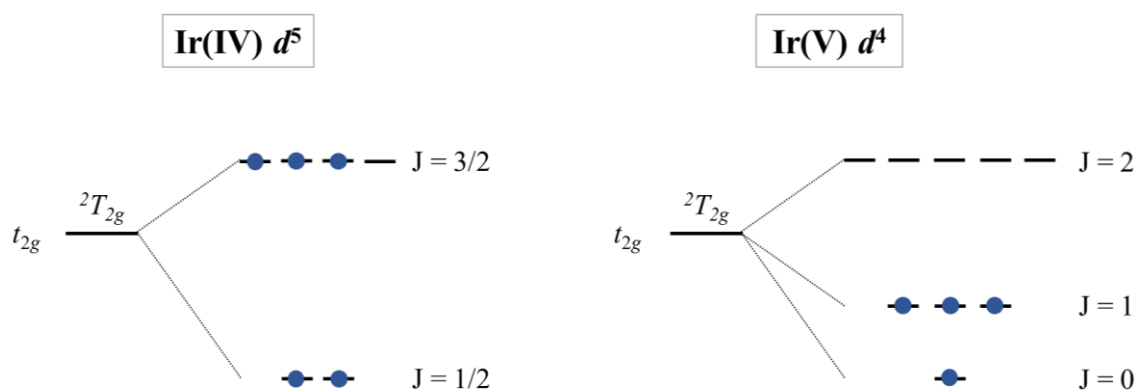


Figure 1.22. Splittings of the Ir(IV) and Ir(V) t_{2g} orbitals caused by SOC. Note that electron filling for Ir(V) leads to a non-magnetic state.

The J states can be thought of as “shells” and if a shell is partially filled, the state is magnetic. If the shells are filled, the state is non-magnetic. Thus, whether or not SOC is applied for Ir(IV), the result is effectively equivalent to $S = 1/2$ or one unpaired electron. For Ir(V), however, accounting for SOC is important. Without SOC, Ir(V) should have a magnetic ground state with two unpaired electrons while applying SOC results in the four d electrons completely filling the $J = 1$ and 0 states leading to a non-magnetic state. The role SOC plays in the electronic behavior of Ir oxides has been of much recent debate and discussion [53–56].

1.6.5 Magnetic Instrumentation

All of the magnetic susceptibility measurements discussed in this dissertation were done using either a Quantum Design Physical Property Measurement System (PPMS) at Oregon State University (Figure 1.23) or a Quantum Design Magnetic Property Measurement System (MPMS) at University of California Santa Cruz.

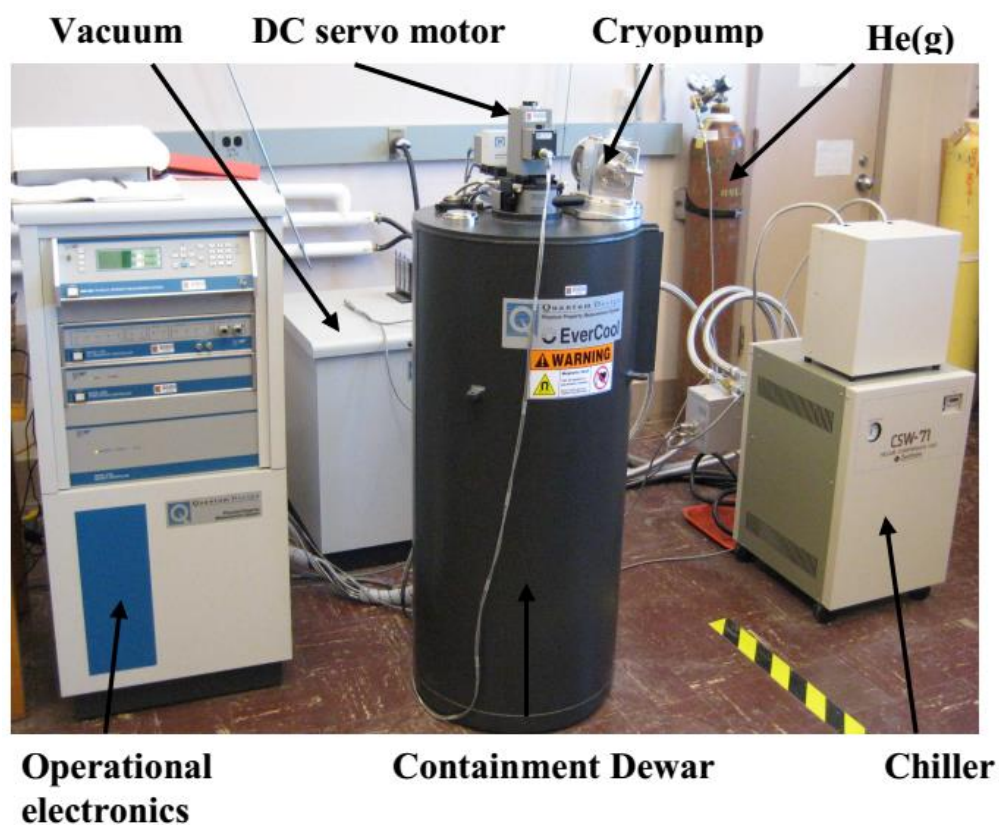


Figure 1.23. Quantum Design PPMS with the ACMS equipment installed.

The AC/DC Magnetometry System (ACMS) is an attachment of the PPMS which allows for AC susceptibility and DC magnetization. Most of the magnetic measurements performed in this dissertation utilize a technique for DC measurements known as extraction magnetometry. The ACMS coil set, Figure 1.24, is inserted into the main dewar chamber,

connected to the instrument via a 12-pin connector at the base of the sample chamber. The sample, loaded in a polycarbonate straw is vibrated vertically through the coil set by the DC servo motor. Sample preparation is an important aspect of the measurement process as the sample should not be allowed to move freely in the straw as it can affect the sample centering if the sample does not move according to the DC servo motor. Thus, the sample can be measured as a sintered mass or as a tightly packed powder.

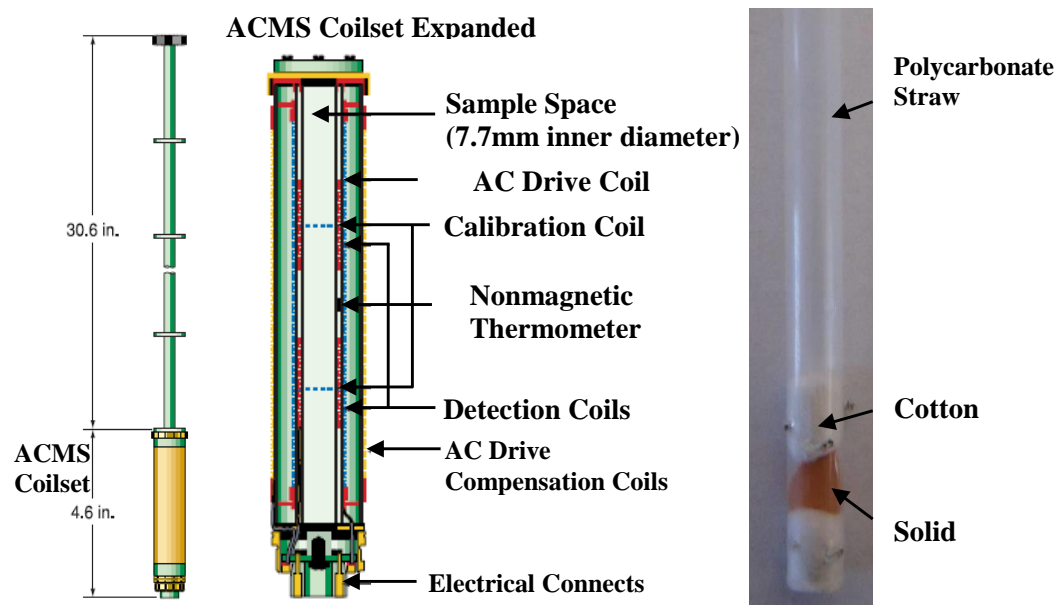


Figure 1.24. Representation of the ACMS coilset and tube assemblage (left), expanded view with labels of the ACMS coilset detection unit (center), and mounted ‘as prepared’ sample (right). ACMS coil set illustrations taken and modified from Quantum Design application notes [57].

An applied field induces a magnetization in the sample that is detected by the ACMS coil set as an induced voltage. The amplitude of the voltage signal is thus related to the magnetic moment and the speed of vertical movement for a given extraction. Although automated, an important aspect of the measurement is the speed in which an extraction is made. A faster speed for an extraction generally results in enhanced signal strength and thus directly relates to the

measurement accuracy. Equally important then is the samples location with respect to the detection coils. Thus, it is necessary to locate the sample using a single point DC extraction. This allows the instrument to correct for the sample displacement when the DC servo motor is engaged. If the sample has not been centered, the operator runs the risk of inaccurate magnetization measurements. Generally, locating with an AC excitation is more accurate as there is better resolution, but it is recommended to locate the sample using the method employed for actual measurements [57].

For DC magnetization measurements, an applied field is necessary. The PPMS at Oregon State University utilizes a superconducting magnet capable of magnetic fields as high as 7 T, however an applied field of 0.1–1 T is generally sufficient for temperature dependent measurements. It should be noted that if attempting to determine the effective moment, Curie constant and transition temperatures through the Curie-Weiss relationship, a sufficient temperature range above any transition temperature is required. This temperature range would be well into the paramagnetic region. Thus, it is necessary to have some insight into the potential magnetic interactions present for a sample, and may require several measurements to resolve temperature discrepancies.

1.7 Electronic Transport Properties

1.7.1 Electrical Conduction

A material's crystal structure, and therefore the arrangement of atoms, has a direct impact on the band structure of the material. In Molecular Orbital theory, molecular orbitals are

created from linear combinations of atomic orbitals. As more and more atomic orbitals are introduced, the molecular orbitals begin to cluster in high and low energy bands. When this concept is applied to an infinitely repeating lattice, the spacing between orbitals decreases to the point that they begin to mix and the bands become continuous (Figure 1.25). The relative position of these bands and the number of available electrons in a given material determines the nature of its electrical conductivity. This can be illustrated using a simple two-band diagram with a valence band and a conduction band [58].

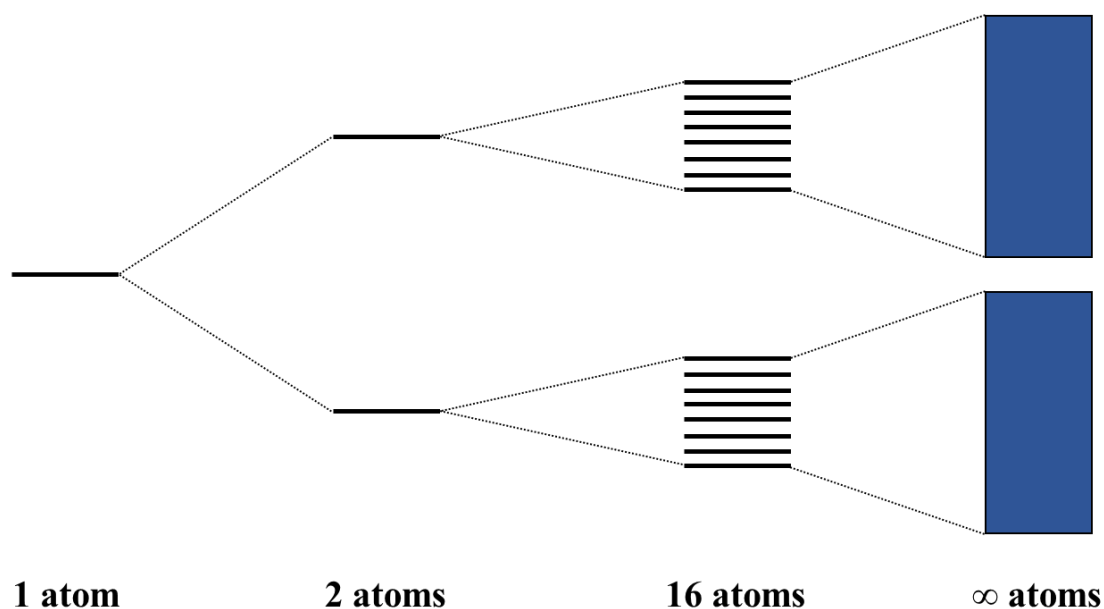


Figure 1.25. Schematic demonstrating the creation of energy bands from molecular orbitals via the addition of an increasing number of atomic orbitals.

The energy to which the available electrons fill is called the Fermi level (E_F). If the electrons partially fill one of the bands (i.e. E_F falls within a band) as in Figure 1.26a, they can freely flow to available energy levels and the material is said to be a metallic conductor. On the other hand, when E_F falls in a gap between bands (Figures 1.26b and c), the electrons must

jump from the valence band and across the band gap (E_g) to the conduction band in order for electronic conduction to occur.

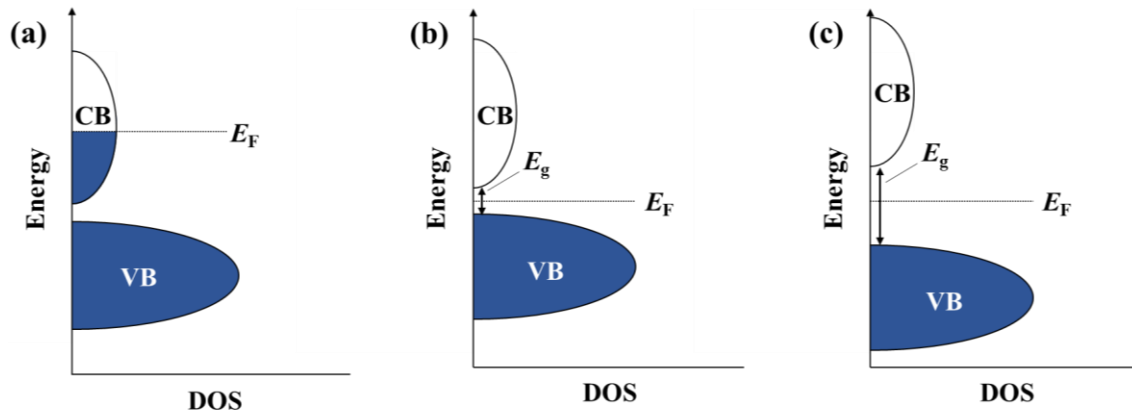


Figure 1.26. Simple two-band diagrams for: (a) metal, (b) extrinsic semiconductor, and (c) insulator. The conduction and valence bands are labeled by CB and VB, respectively. The point at which the electron filling stops is denoted by the Fermi level (E_F) while E_g is the energy gap between bands.

When E_g is large, the electrons need a sizable amount of energy to jump the gap, which leads to a low conduction band population and poor conduction, or insulator, behavior. Conversely, if E_g is small enough, the thermal energy of electrons is sufficient which allows more of them to populate the conduction band. The result is a material called a semiconductor that has decent conductivity. An insulator can be made more conductive through processes called n-type or p-type doping. This is accomplished by replacing, or “doping”, a small amount of the atoms for ones with more (n-type) or less (p-type) electrons which adds donor or acceptor levels to the band structure. These levels allow electrons to populate conduction bands more easily, thereby increasing conductivity. Doped conductors are labeled extrinsic semiconductors where as non-doped ones are intrinsic semiconductors.

The temperature dependence of conductivity (σ) and its reciprocal, resistivity (ρ), for each type of conductor is well known. For metals, resistivity is directly proportional with temperature (Figure 1.27a). In metals, the flow of electrons is interrupted only by scattering caused by collisions with atoms in the lattice. As temperature increases, thermal vibrations are intensified, causing more scattering events to occur, inhibiting conduction. In semiconductors, the proportionality of resistivity and temperature is an inverse trend. As temperature is increased, more electrons are able to jump across E_g into the conduction band, and resistivity decreases.

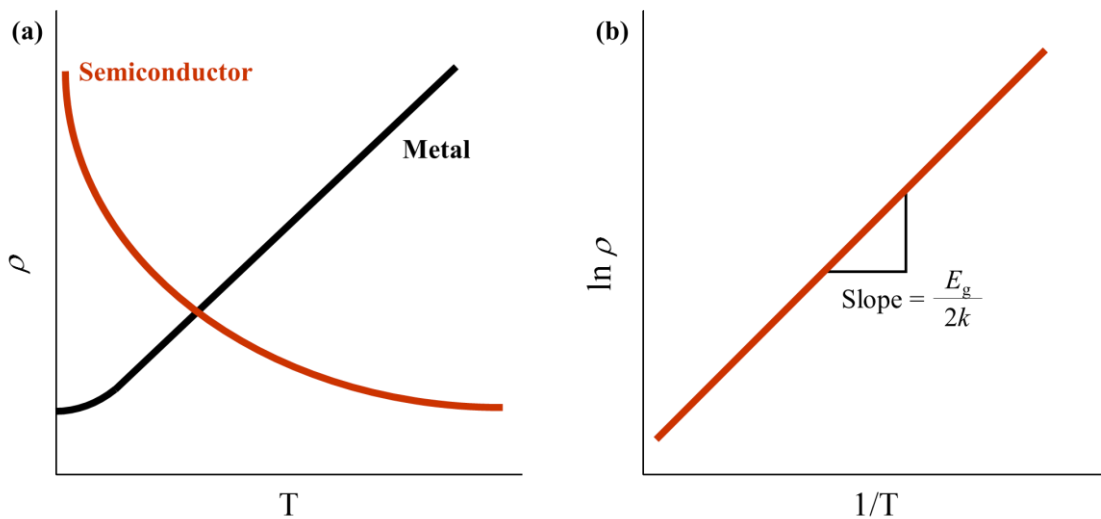


Figure 1.27. Temperature-dependent plots of (a) $\rho(T)$ for a metal and semiconductor and (b) $\ln \rho$ vs. $1/T$ for a semiconductor. Note that in (b) $E_g = \text{Slope} \times 2k$.

The temperature dependence of semiconductor resistivity can be expressed mathematically as an Arrhenius relationship:

$$\rho = \rho_0 \exp\left(\frac{E_g}{2kT}\right) \quad (\text{E1.17})$$

where ρ_0 is a preexponential constant and k is the Boltzmann constant. By taking the natural log of both sides, a linear relationship (Figure 1.27b) between $\ln \rho$ and T^{-1} can be established:

$$\ln \rho = \left(\frac{E_g}{2k}\right)\frac{1}{T} + \ln \rho_0 \quad (\text{E1.18})$$

E_g can then be estimated by multiplying the slope of the line by $2k$.

1.7.2 Seebeck Effect

Thermoelectric materials have the ability to produce electricity from thermal energy and vice versa. They can be utilized in devices for energy production and refrigeration, which rely on one of two thermoelectric effects: the Peltier effect or the Seebeck effect. Both effects involve the concept of heat conduction by the dominant charge carriers [59]. The first of these effects to be discovered was the Seebeck effect, in which a current is produced when a temperature gradient is applied to a material (Figure 1.28a). This effect is generally observed by measuring the voltage (ΔV) generated by the gradient ($\Delta T = T_H - T_C$), related through a proportionality constant, S , called the Seebeck coefficient:

$$\Delta V = S\Delta T \quad (\text{E1.19})$$

The magnitude and sign of S can give an impression of how well a material produces current under a thermal gradient and the type of dominant charge carrier.

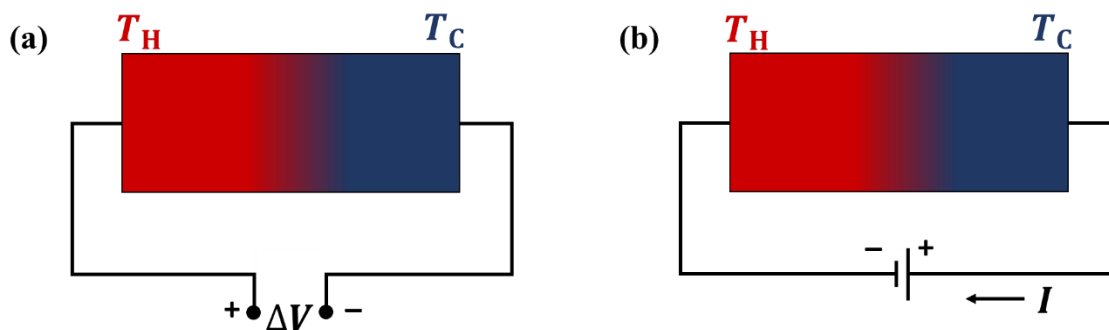


Figure 1.28. Diagrams demonstrating the (a) Seebeck and (b) Peltier effects.

If S is negative, it indicates the charge carriers are electrons while a positive value suggests hole carriers. Semiconductors tend to have higher S values than metals (e.g. 200 vs. $10 \mu\text{V}\cdot\text{K}^{-1}$). While this phenomenon seems counterintuitive (since metals are better electrical conductors relative to semiconductors), metallic materials tend to be very good thermal conductors, which increases the difficulty in establishing a large temperature gradient. The complement to the Seebeck effect is the Peltier effect, which describes the production of a temperature gradient by applying current through a material (Figure 1.28b).

1.7.3 Electronic Transport Instrumentation

1.7.3.1 High-Temperature Measurements

High-temperature (300–800 K) resistivity and Seebeck coefficients were measured using ULVAC-RIKO ZEM-3 Thermoanalyzer, Figure 1.29. The main components of the ZEM-3 consist of a heater and water cooling unit that encloses the sample chamber and probe contacts.



Figure 1.29. ZEM-3 Thermoanalyzer (left) and mounted sample in the thermal chamber (right).

The sample is placed on the spring-loaded electrode blocks (Ni contacts) which are then tightened against the sample. The Pt probes are then brought into contact with sample from the side. Once the sample is held firmly in place and electrical contact is confirmed, the chamber is sealed, evacuated, and filled with a low pressure static helium atmosphere. The voltage across the sample (ΔV) is measured using the Pt probes which are connected to a digital multi-meter. The current is flowed through the Ni side electrodes which are also used to generate and measure the thermal gradient (ΔT) across the sample. The sign of the Seebeck coefficient is determined by the charge flow for the thermal gradient. The cold end is then positive for holes and negative for electrons. An external thermocouple is used to measure the set furnace temperature of the thermal chamber [60].

1.7.3.2 Low-Temperature Measurements

In addition to magnetic susceptibility, the PPMS can be easily set up to perform low-temperature (5–300 K) DC resistivity measurements. The resistivity puck shown in Figure 1.30 uses the same 12-pin connector at the base of the sample chamber as that used for a connection

to the ACMS coil set mentioned previously. The PPMS resistivity puck is designed to measure four probe resistivity on 3 samples independently. Four probe resistivity is one of two general techniques used for measuring resistivity based on the resistivity of the sample. Normally the four-probe technique is employed when the sample resistivity is $\rho < 10 \text{ } \Omega\text{-cm}$. This is necessary as the voltage leads and current leads are separated thus removing the contribution of the lead wire and contact resistance.

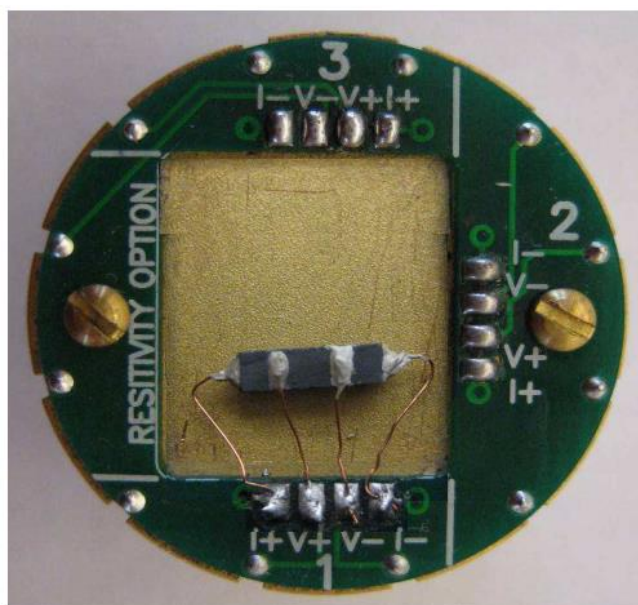


Figure 1.30. PPMS resistivity puck with a bar sample connected to position 1 using the four probe contact technique. Contacts are made using conductive silver paint and copper wires that are soldered to the puck.

Samples with resistivities above $\rho = 10 \text{ } \Omega\text{-cm}$ can be measured by the two-probe technique where the contact and lead wire resistance will not have much effect on the total resistivity. For samples measured in the PPMS, the four-probe technique is the only option. As shown in Figure 1.30, four contact wires are attached to the sample bar of known dimension by

means of silver paste or silver epoxy. Once the sample and contacts are in place, the puck is connected to the bottom of the PPMS sample chamber and the measurement can be started.

1.8 References

- [1] H. Okabe, M. Isobe, E. Takayama-Muromachi, A. Koda, S. Takeshita, M. Hiraishi, M. Miyazaki, R. Kadono, Y. Miyake, J. Akimitsu, Ba_2IrO_4 : A spin-orbit Mott insulating quasi-two-dimensional antiferromagnet, *Phys. Rev. B.* 83 (2011) 155118. doi:10.1103/PhysRevB.83.155118.
- [2] G. Cao, A. Subedi, S. Calder, J.-Q. Yan, J. Yi, Z. Gai, L. Poudel, D.J. Singh, M.D. Lumsden, A.D. Christianson, B.C. Sales, D. Mandrus, Magnetism and electronic structure of $\text{La}_2\text{ZnIrO}_6$ and $\text{La}_2\text{MgIrO}_6$: Candidate $J_{\text{eff}} = 1/2$ Mott insulators, *Phys. Rev. B.* 87 (2013) 155136. doi:10.1103/PhysRevB.87.155136.
- [3] Y. Okamoto, M. Nohara, H. Aruga-Katori, H. Takagi, Spin-liquid state in the $S=1/2$ hyperkagome antiferromagnet $\text{Na}_4\text{Ir}_3\text{O}_8$, *Phys. Rev. Lett.* 99 (2007) 4–7. doi:10.1103/PhysRevLett.99.137207.
- [4] W. Witczak-Krempa, G. Chen, Y.B. Kim, L. Balents, Correlated Quantum Phenomena in the Strong Spin-Orbit Regime, *Annu. Rev. Condens. Matter Phys.* 5 (2014) 57–82. doi:10.1146/annurev-conmatphys-020911-125138.
- [5] T. Bzdušek, A. Rüegg, M. Sigrist, Weyl semimetal from spontaneous inversion symmetry breaking in pyrochlore oxides, *Phys. Rev. B.* 91 (2015) 165105. doi:10.1103/PhysRevB.91.165105.
- [6] M.Z. Hasan, C.L. Kane, Colloquium: Topological insulators, *Rev. Mod. Phys.* 82 (2010) 3045–3067. doi:10.1103/RevModPhys.82.3045.
- [7] D. Hsieh, D. Qian, L. Wray, Y. Xia, Y.S. Hor, R.J. Cava, M.Z. Hasan, A topological Dirac insulator in a quantum spin Hall phase., *Nature.* 452 (2008) 970–974. doi:10.1038/nature06843.
- [8] S.A. Corr, R. Seshadri, Synthetic Methodologies, in: *Compr. Inorg. Chem. II From Elem. to Appl.*, 2nd ed., Elsevier Ltd., 2013: pp. 1–15. doi:10.1016/B978-0-08-097774-4.00401-0.
- [9] S.J. Mugavero, W.R. Gemmill, I.P. Roof, H.C. zur Loye, Materials discovery by crystal growth: Lanthanide metal containing oxides of the platinum group metals (Ru, Os, Ir, Rh, Pd, Pt) from molten alkali metal hydroxides, *J. Solid State Chem.* 182 (2009) 1950–1963. doi:10.1016/j.jssc.2009.05.006.
- [10] T. Hahn, ed., *International Tables for Crystallography Volume A: Space-group symmetry*, 5th ed., International Union of Crystallography, Chester, England, 2006. doi:10.1107/97809553602060000100.

- [11] B.D. Cullity, S.R. Stock, *Elements of X-Ray Diffraction*, 3rd ed., Prentice Hall, Upper Saddle River, 2001.
- [12] M. De Graef, M.E. McHenry, *Structure of materials: an introduction to crystallography, diffraction and symmetry*, Cambridge University Press, Cambridge, 2007.
- [13] F.S. Galasso, *Perovskites and High Tc Superconductors*, Routledge, London, 1990.
- [14] V.M. Goldschmidt, *Die Gesetze der Krystallochemie*, *Naturwissenschaften*. 14 (1926) 477–485. doi:10.1007/BF01507527.
- [15] P.M. Woodward, Octahedral Tilting in Perovskites. I. Geometrical Considerations, *Acta Crystallogr. Sect. B Struct. Sci.* 53 (1997) 32–43. doi:10.1107/S0108768196010713.
- [16] A.M. Glazer, The classification of tilted octahedra in perovskites, *Acta Crystallogr. Sect. B Struct. Crystallogr. Cryst. Chem.* 28 (1972) 3384–3392. doi:10.1107/S0567740872007976.
- [17] P.M. Woodward, Octahedral Tilting in Perovskites. II. Structure Stabilizing Forces, *Acta Crystallogr. Sect. B Struct. Sci.* 53 (1997) 44–66. doi:10.1107/S0108768196012050.
- [18] M.A. Subramanian, A.P. Ramirez, W.J. Marshall, Structural Tuning of Ferromagnetism in a 3D Cuprate Perovskite, *Phys. Rev. Lett.* 82 (1999) 1558–1561. doi:10.1103/PhysRevLett.82.1558.
- [19] D.J. Keeble, S. Wicklein, R. Dittmann, L. Ravelli, R.A. MacKie, W. Egger, Identification of *A*- and *B*-site cation vacancy defects in perovskite oxide thin films, *Phys. Rev. Lett.* 105 (2010) 3–6. doi:10.1103/PhysRevLett.105.226102.
- [20] R.H. Mitchell, *Perovskites: Modern and Ancient*, Almaz Press, Thunder Bay, 2002.
- [21] F. Ramezanipour, J.E. Greedan, A.P. Grosvenor, J.F. Britten, L.M.D. Cranswick, V.O. Garlea, Intralayer Cation Ordering in a Brownmillerite Superstructure: Synthesis, Crystal, and Magnetic Structures of $\text{Ca}_2\text{FeCoO}_5$, *Chem. Mater.* 22 (2010) 6008–6020. doi:10.1021/cm1023025.
- [22] A. Muñoz, C. de la Calle, J.A. Alonso, P. Botta, V. Pardo, D. Baldomir, J. Rivas, Crystallographic and magnetic structure of $\text{SrCoO}_{2.5}$ brownmillerite: Neutron study coupled with band-structure calculations, *Phys. Rev. B.* 78 (2008) 54404. doi:10.1103/PhysRevB.78.054404.
- [23] S. Shin, Y. Hatakeyama, K. Ogawa, K. Shimomura, Catalytic Decomposition of NO over brownmillerite-like compounds, $\text{Ca}_2\text{Fe}_2\text{O}_5$ and $\text{Sr}_2\text{Fe}_2\text{O}_5$, *Mater. Res. Bull.* 14 (1979) 133–136.
- [24] C.C. da Silva, A.S.B. Sombra, Temperature Dependence of the Magnetic and Electric Properties of $\text{Ca}_2\text{Fe}_2\text{O}_5$, *Mater. Sci. Appl.* 2 (2011) 1349–1353. doi:10.4236/msa.2011.29183.
- [25] E. Sullivan, C. Greaves, Fluorine insertion reactions of the brownmillerite materials

- $\text{Sr}_2\text{Fe}_2\text{O}_5$, $\text{Sr}_2\text{CoFeO}_5$, and $\text{Sr}_2\text{Co}_2\text{O}_5$, *Mater. Res. Bull.* 47 (2012) 2541–2546. doi:10.1016/j.materresbull.2012.05.002.
- [26] M.V. Patrakeev, V.V. Kharton, V.L. Kozhevnikov, Y.A. Bakhteeva, E.N. Naumovich, A.L. Shaula, A.A. Yaremchenko, I.A. Leonidov, F.M.B. Marques, Oxygen nonstoichiometry and mixed conductivity of $\text{SrFe}_{1-x}\text{M}_x\text{O}_{3-\delta}$ (M=Al, Ga): Effects of B-site doping, *Solid State Sci.* 8 (2006) 476–487.
- [27] P. Jiang, J. Li, A. Ozarowski, A.W. Sleight, M.A. Subramanian, Intense Turquoise and Green Colors in Brownmillerite-Type Oxides Based on Mn^{5+} in $\text{Ba}_2\text{In}_{2-x}\text{Mn}_x\text{O}_{5+x}$, *Inorg. Chem.* 52 (2013) 1349–57. doi:10.1021/ic3020332.
- [28] Q. Li, L. Sun, L. Huo, H. Zhao, J.-C. Grenier, Electrode properties of Co-doped $\text{Ca}_2\text{Fe}_2\text{O}_5$ as new cathode materials for intermediate-temperature SOFCs, *Int. J. Hydrogen Energy.* 35 (2010) 9151–9157. doi:10.1016/j.ijhydene.2010.06.048.
- [29] P.D. Battle, S.H. Kim, A.V. Powell, The crystal structure and electronic properties of $\text{Ba}_4\text{Ru}_3\text{MO}_{12}$ (M =Li, Na, Mg, Zn), *J. Solid State Chem.* 101 (1992) 161–172. doi:10.1016/0022-4596(92)90212-E.
- [30] X. Kuang, X. Jing, C.K. Loong, E.E. Lachowski, J.M.S. Skakle, A.R. West, A new hexagonal 12-layer perovskite-related structure: $\text{Ba}_6\text{R}_2\text{Ti}_4\text{O}_{17}$ (R = Nd and Y), *Chem. Mater.* 14 (2002) 4359–4363. doi:10.1021/cm020374m.
- [31] E.J. Cussen, J. Sloan, J.F. Vente, P.D. Battle, T.C. Gibb, 15R $\text{SrMn}_{1-x}\text{Fe}_x\text{O}_{3-\delta}$ ($x = 0.1$); A New Perovskite Stacking Sequence, *Inorg. Chem.* 37 (1998) 6071–6077.
- [32] W.A. Dollase, H.S.C. O'Neill, The Spinel CuCr_2O_4 and CuRh_2O_4 , *Acta Crystallogr. Sect. C Cryst. Struct. Commun.* 53 (1997) 657–659. doi:10.1107/S0108270197000486.
- [33] M. Tovar, R. Torabi, C. Welker, F. Fleischer, Structural and magnetic properties of Cu-Ni-Cr spinel oxides, *Phys. B Condens. Matter.* 385–386 I (2006) 196–198. doi:10.1016/j.physb.2006.05.181.
- [34] G. Ueno, S. Sato, Y. Kino, The low-temperature tetragonal phase of NiCr_2O_4 , *Acta Crystallogr. Sect. C Cryst. Struct. Commun.* 55 (1999) 1963–1966. doi:10.1107/S0108270199011713.
- [35] A.P. Ramirez, Strongly Geometrically Frustrated Magnets, *Annu. Rev. Mater. Sci.* 24 (1994) 453–480. doi:10.1146/annurev.ms.24.080194.002321.
- [36] L.A. Bendersky, F.W. Gayle, Electron diffraction using transmission electron microscopy, *J. Res. Natl. Inst. Stand. Technol.* 106 (2001) 997–1012. doi:10.6028/jres.106.051.
- [37] W.H. Bragg, W.L. Bragg, The Reflection of X-rays by Crystals, *Proc. R. Soc. A Math. Phys. Eng. Sci.* 88 (1913) 428–438. doi:10.1098/rspa.1913.0040.
- [38] H.M. Rietveld, A profile refinement method for nuclear and magnetic structures, *J. Appl. Crystallogr.* 2 (1969) 65–71. doi:10.1107/S0021889869006558.
- [39] A. Le Bail, Whole powder pattern decomposition methods and applications: A retrospection, *Powder Diffr.* 20 (2005) 316–326. doi:10.1154/1.2135315.

- [40] A.R. West, Basic Solid State Chemistry, 2nd ed., John Wiley & Sons, Ltd, New York, 1999.
- [41] Rigaku Corporation, X-Ray Diffractometer MiniFlex II Instruction Manual, 2nd ed., Rigaku Corporation, 2006.
- [42] A. Huq, J.P. Hodges, O. Gourdon, L. Heroux, Powgen: A third-generation high-resolution high-throughput powder diffraction instrument at the Spallation Neutron Source, *Zeitschrift Für Krist. Proc.* 1 (2011) 127–135. doi:10.1524/zkpr.2011.0019.
- [43] E.O. Wollan, W.C. Koehler, Neutron Diffraction Study of the Magnetic Properties of the Series of Perovskite-Type Compounds $[(1-x)\text{La}, x\text{Ca}]\text{MnO}_3$, *Phys. Rev.* 100 (1955) 545–563. doi:10.1103/PhysRev.100.545.
- [44] D. Petitgrand, S. V Maleyev, P. Bourges, A.S. Ivanov, Pseudodipolar interaction and antiferromagnetism in $R_2\text{CuO}_4$ compounds ($R = \text{Pr}, \text{Nd}, \text{Sm}, \text{and Eu}$), *Phys. Rev. B.* 59 (1999) 1079–1104. doi:10.1103/PhysRevB.59.1079.
- [45] J.E. Greedan, Geometrically frustrated magnetic materials, *J. Mater. Chem.* 11 (2001) 37–53. doi:10.1039/b003682j.
- [46] X. Obradors, A. Labarta, A. Isalgué, J. Tejada, J. Rodriguez, M. Pernet, Magnetic frustration and lattice dimensionality in $\text{SrCr}_8\text{Ga}_4\text{O}_{19}$, *Solid State Commun.* 65 (1988) 189–192. doi:10.1016/0038-1098(88)90885-X.
- [47] T. Takayama, A. Kato, R. Dinnebier, J. Nuss, H. Kono, L.S.I. Veiga, G. Fabbri, D. Haskell, H. Takagi, Hyperhoneycomb iridate $\beta\text{-Li}_2\text{IrO}_3$ as a platform for Kitaev Magnetism, *Phys. Rev. Lett.* 114 (2015) 2–6. doi:10.1103/PhysRevLett.114.077202.
- [48] J.E. Greedan, Frustrated rare earth magnetism: Spin glasses, spin liquids and spin ices in pyrochlore oxides, *J. Alloys Compd.* 408–412 (2006) 444–455. doi:10.1016/j.jallcom.2004.12.084.
- [49] J.E. Greedan, N.P. Raju, A. Maignan, C. Simon, J.S. Pedersen, A.M. Niraimathi, E. Gmelin, M.A. Subramanian, Frustrated pyrochlore oxides, $\text{Y}_2\text{Mn}_2\text{O}_7$, $\text{Ho}_2\text{Mn}_2\text{O}_7$, and $\text{Yb}_2\text{Mn}_2\text{O}_7$: Bulk magnetism and magnetic microstructure, *Phys. Rev. B.* 54 (1996) 7189–7200. doi:10.1103/PhysRevB.54.7189.
- [50] H. Takagi, S. Niitaka, Highly Frustrated Magnetism in Spinels, in: C. Lacroix, P. Mendels, F. Mila (Eds.), *Introd. to Frustrated Magn.*, Springer Berlin Heidelberg, Berlin, 2010: pp. 155–175. doi:10.1007/978-3-642-10589-0.
- [51] A.F. Orchard, *Magnetochemistry*, Oxford University Press, New York, 2003.
- [52] A. Abragam, B. Bleaney, *Electron Paramagnetic Resonance of Transition Ions*, Oxford University Press, London, 1970.
- [53] B.F. Phelan, J. Krizan, W. Xie, Q. Gibson, R.J. Cava, New material for probing spin-orbit coupling in iridates, *Phys. Rev. B - Condens. Matter Mater. Phys.* 91 (2015) 1–6. doi:10.1103/PhysRevB.91.155117.
- [54] H. Matsuura, K. Miyake, Effect of Spin–Orbit Interaction on $(4d)^3$ - and $(5d)^3$ -Based Transition-Metal Oxides, *J. Phys. Soc. Japan.* 82 (2013) 73703.

doi:10.7566/JPSJ.82.073703.

- [55] G. Cao, T.F. Qi, L. Li, J. Terzic, S.J. Yuan, L.E. DeLong, G. Murthy, R.K. Kaul, Novel Magnetism of Ir^{5+} ($5d^4$) Ions in the Double Perovskite Sr_2YIrO_6 , *Phys. Rev. Lett.* 112 (2014) 56402. doi:10.1103/PhysRevLett.112.056402.
- [56] X. Ou, H. Wu, Impact of spin-orbit coupling on the magnetism of Sr_3MIR_6 (M = Ni, Co), *Sci. Rep.* 4 (2014) 4609. doi:10.1038/srep04609.
- [57] Quantum Design, *Physical Property Measurement System Hardware and Operations Manual*, 2nd ed., Quantum Design, 1999.
- [58] R.J.D. Tilley, *Understand Solids: The Science of Materials*, 1st ed., John Wiley & Sons, Ltd, West Sussex, 2004.
- [59] P.M. Chaikin, A Introduction to Thermopower for Those Who Might Want to Use It to Study Organic Conductors and Superconductors, in: V.Z. Kresin, W.A. Little (Eds.), *Org. Supercond.*, Plenum Press, New York, 1990: pp. 101–115.
- [60] ULVAC-RIKO, Inc. Model ZEM-3 Thermoanalyzer: Power Conversion Efficiency Measuring Instrument Instruction Manual., n.d.

Chapter 2: Structural, Magnetic and Transport Characterization of the Solid Solution Between $\text{Ba}_2\text{In}_2\text{O}_5$ and BaIrO_3 : $\text{Ba}_2\text{In}_{2-x}\text{Ir}_x\text{O}_{5+\delta}$

Abstract

The solid solution series $\text{Ba}_2\text{In}_{2-x}\text{Ir}_x\text{O}_{5+\delta}$ ($x = 0-1.4, 2$) was prepared and its structural, magnetic, and charge transport properties were measured. With increasing Ir content, three transitions in the room temperature structure were observed: orthorhombic to tetragonal, tetragonal to cubic, and cubic to a monoclinic distortion of a hexagonal BaTiO_3 structure. Neutron diffraction refinements showed $\text{Ba}_2\text{In}_{1.6}\text{Ir}_{0.4}\text{O}_{5.4}$ was cubic and $\text{Ba}_2\text{InIrO}_6$ was monoclinic. The latter result contradicts previously published XRD refinements. Magnetization measurements show Curie-Weiss behavior for $x = 0.2-0.6$, which arises from near 50:50 ratio of Ir(V) and Ir(VI). To our knowledge, this is the first time Ir(VI) has been stabilized with standard solid state methods under ambient conditions. Electrical resistivity measurements show all the compounds studied were semiconducting, and that resistivity decreases with increasing Ir content which suggests proximity to a metal-insulator transition. A sign reversal in the high-temperature Seebeck coefficient is observed indicating both electron and hole charge transport.

Publications based on this chapter:

- [1] J. Flynn, J. Li, A.W. Sleight, A.P. Ramirez, M.A. Subramanian, Structure and Properties of Ir-Containing Oxides with Large Spin–Orbit Coupling: $\text{Ba}_2\text{In}_{2-x}\text{Ir}_x\text{O}_{5+\delta}$, *Inorg. Chem.* 55 (2016) 2748–2754. doi:10.1021/acs.inorgchem.5b02501.

2.1 Introduction to Ba₂In₂O₅ and BaIrO₃

The compounds Ba₂In₂O₅ and BaIrO₃ both crystallize in perovskite-related structures. Ba₂In₂O₅ is known to adopt the brownmillerite structure (Figure 2.1a) at room temperature. There has been some debate as to whether the correct space group is *Ibm2* or *Icmm* [1–5] which differ primarily in the periodicity of the orientation of tetrahedra. Ba₂In₂O₅ is often indexed as *Ibm2* but more recent spectroscopic and computational studies have suggested that the short-range structure contains *Icmm* symmetry [6]. The oxygen vacancies in Ba₂In₂O₅ at room temperature are ordered along the [001], but at higher temperatures, the oxygen vacancies begin to disorder. It transitions from the orthorhombic brownmillerite to a tetragonal perovskite phase at 925 °C and then to a cubic defect perovskite at 1116 °C [1]. The cubic phase has been found to have a relatively high oxide ion conductivity [7] and some substitutions for In have been reported in an effort to stabilize the cubic phase at room temperature [7–11]. Additionally, the solid solution Ba₂In_{2-x}Mn_xO_{5+x} yielded green and turquoise colors the cause of which was determined to be *d-d* transitions in tetrahedrally coordinated Mn⁵⁺ ions [12].

The crystal structure for BaIrO₃ at ambient pressure and temperature is a monoclinic distortion of the 9R BaRuO₃ structure with space group *C2/m*. The structure (Figure 2.1b) can be described as corner-sharing clusters made up of face-sharing IrO₆ octahedra. It displays unusual ferromagnetic charge ordering behavior [13–15].

2.2 Investigation of $\text{Ba}_2\text{In}_{2-x}\text{Ir}_x\text{O}_{5+\delta}$

2.2.1 Motivation for Study

Interest in topological insulators has sparked the search for materials with large spin orbit coupling, among which are oxides containing $5d$ transition metals, and iridium in particular [16–18]. The most common oxidation state of iridium in oxides is Ir(IV) although Ir(V) [19–23] and Ir(VI) [24–27] have been stabilized as well. These higher oxidation states have been observed in oxides of the types $\text{Ba}_2\text{M}\text{IrO}_6$ and $\text{Ba}_3\text{M}\text{Ir}_2\text{O}_9$, both of which crystallize in perovskite-related structures [28,29]. Limited work has been done on solid solutions of these families and the brownmillerite structure.

Two members of the related compound series $\text{Ba}_2\text{In}_{2-x}\text{Ir}_x\text{O}_{5+\delta}$ have been previously reported in the literature, $\text{Ba}_2\text{InIrO}_6$ ($x = 1$, $\delta = 1$) and $\text{Ba}_2\text{In}_{0.67}\text{Ir}_{1.33}\text{O}_6$ ($x = 1.33$, $\delta = 1$), with average Ir oxidation states of $5+$ and $4.5+$, respectively [28,30,31]. While the physical properties for $\text{Ba}_2\text{InIrO}_6$ have previously not been reported, $\text{Ba}_2\text{In}_{0.67}\text{Ir}_{1.33}\text{O}_6$ is known to be paramagnetic with short-range magnetic order which is supported by the susceptibility and specific heat data [28]. Both $\text{Ba}_2\text{InIrO}_6$ and $\text{Ba}_2\text{In}_{0.67}\text{Ir}_{1.33}\text{O}_6$ are reported to crystallize in the $6H$ hexagonal BaTiO_3 structure (Figure 2.1c) adopting different space groups of $P\bar{3}m1$ and $P6_3/mmc$, respectively. The differences in symmetry is presumably due to steric constraints on spatial ordering of In and Ir ions.

The difference in structure between known members of the $\text{Ba}_2\text{In}_{2-x}\text{Ir}_x\text{O}_{5+\delta}$ system motivates the present study to explore possible related physical states. In this work, we present the partial solid solution between $\text{Ba}_2\text{In}_2\text{O}_5$ and BaIrO_3 with a focus on the evolution of structural and physical behavior.

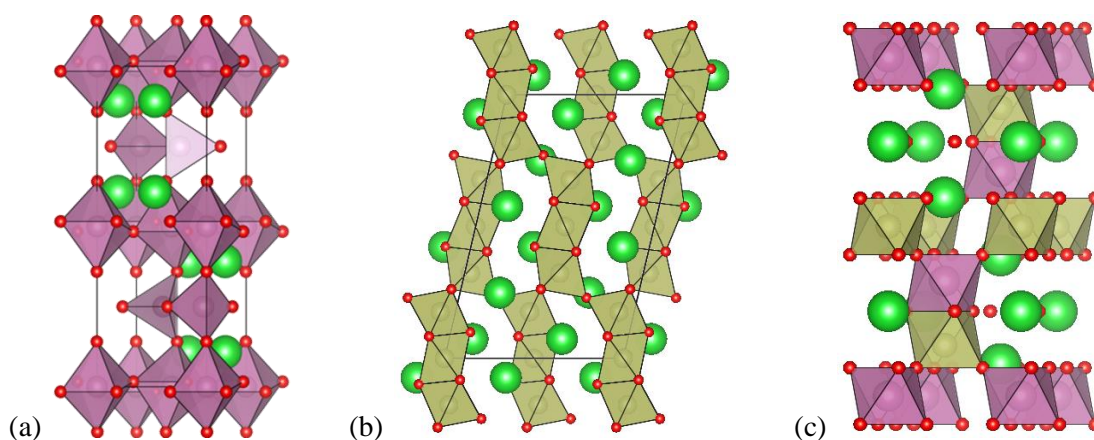


Figure 2.1. Crystal structures of (a) brownmillerite $\text{Ba}_2\text{In}_2\text{O}_5$, (b) monoclinic 9R polytype BaIrO_3 and (c) 6H polytype $\text{Ba}_2\text{InIrO}_6$ (Ba = green, In = purple, Ir = brown, O = red).

2.2.2 Structural Characterization

For $\text{Ba}_2\text{In}_{2-x}\text{Ir}_x\text{O}_{5+\delta}$, single phase samples were prepared for $x = 0-1.4, 2$. For $x = 1.5-1.9$, mixed phase samples were formed containing various barium indium oxides and barium iridium oxides. The XRD diffraction data shown in Figure 2.2 illustrates two structural transitions as Ir content is increased from $x = 0$ to 0.6.

When x is increased to 0.1, the structure transforms from the orthorhombic brownmillerite structure with space group $Icmm$ to a tetragonal defect perovskite structure with space group $P4/mmm$ (Figure 2.3a). In this structure, the oxygen vacancies become disordered within the ab plane but are confined to alternating layers along the c axis. Upon increasing x to 0.2, a cubic defect perovskite phase (Figure 2.3b) with space group $Pm\bar{3}m$ forms where the oxygen vacancies are now completely disordered throughout the entire lattice. This structure persists until x is increased beyond 0.5.

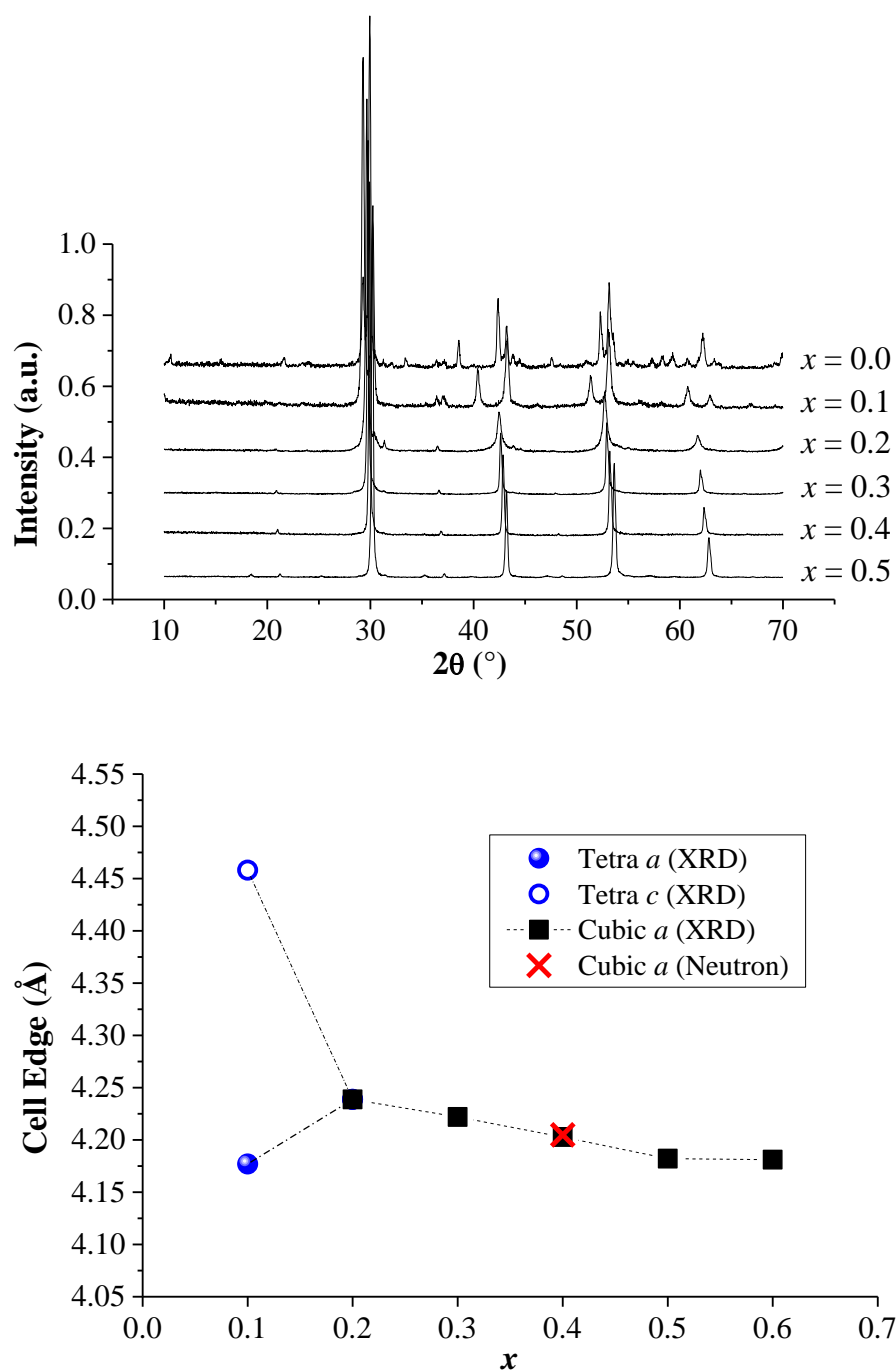


Figure 2.2. (Top) Powder X-ray diffraction patterns and (Bottom) lattice parameters for $x = 0$ – 0.5 . The c parameter of the tetragonal phase ($x = 0.1$) was divided by 2 to allow for direct comparison to the cubic phases.

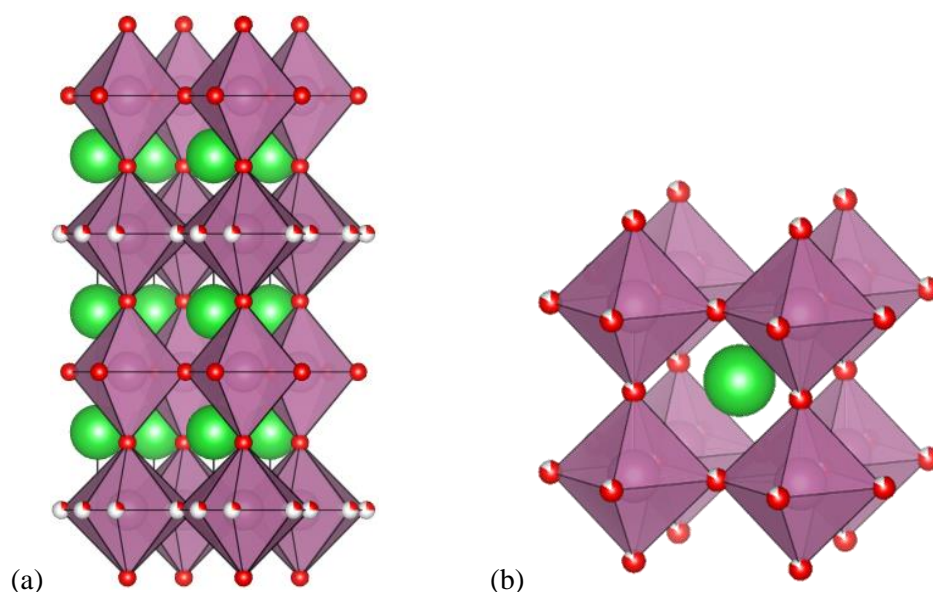


Figure 2.3. Structures of (a) tetragonal defect perovskite $\text{Ba}_2\text{In}_{1.9}\text{Ir}_{0.1}\text{O}_{5.1}$, (b) cubic defect perovskite $\text{Ba}_2\text{In}_{1.6}\text{Ir}_{0.4}\text{O}_{5.4}$ (Ba = green, In/Ir = purple, O = red).

A similar series of transitions is seen in pure $\text{Ba}_2\text{In}_2\text{O}_5$ at high temperatures [1]. A decrease in the unit cell parameters with increasing Ir content was observed as shown in Figure 2.2b. This trend is expected due to the large difference between the ionic radii of Ir^{5+} and In^{3+} (0.57 and 0.80 Å, respectively [32]). Refinement of neutron diffraction data for a sample with the nominal composition of $\text{Ba}_2\text{In}_{1.6}\text{Ir}_{0.4}\text{O}_{5.4}$ is depicted in Figure 2.4 and there is no evidence for ordering of the In and Ir ions; the refined formula was determined to be $\text{Ba}_2\text{In}_{1.62(2)}\text{Ir}_{0.38(2)}\text{O}_{5.49(6)}$. Table 2.1 contains a summary of the crystallographic data for $\text{Ba}_2\text{In}_{1.62(2)}\text{Ir}_{0.38(2)}\text{O}_{5.49(6)}$. The refined and nominal compositions correlate well and the additional oxygen content, represented by $\delta = 0.49(1)$, is slightly larger than the Ir content of $x = 0.38(2)$. This gives an average Ir oxidation state of 5.57(2) which indicates that a majority (~57%) of the Ir is in the 6+ state. This result is unexpected since stabilizing Ir(VI) typically requires the use of high oxygen pressures during heating [24,25,33,34] or the use of flux methods to grow single crystals [26,27,35].

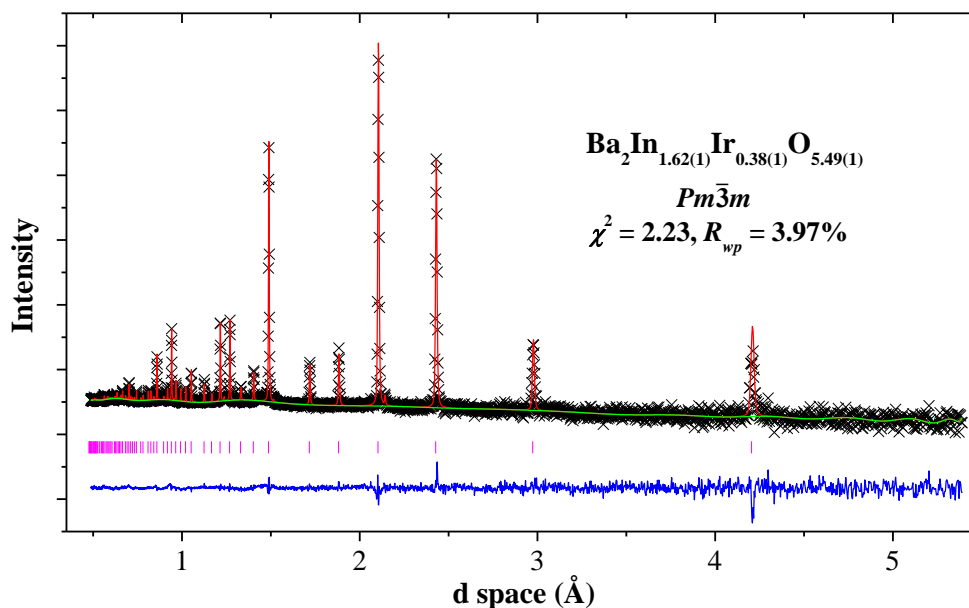


Figure 2.4. Time-of-flight neutron diffraction pattern for $\text{Ba}_2\text{In}_{1.6}\text{Ir}_{0.4}\text{O}_{5.4}$ with calculated intensities (red), difference (blue) and background (green) curves. The allowed reflections for $Pm\bar{3}m$ are indicated by the magenta tick marks.

Table 2.1. Refined atomic parameters for $\text{Ba}_2\text{In}_{1.62(2)}\text{Ir}_{0.38(2)}\text{O}_{5.49(6)}$.

	x	y	z	Occupancy	$U_{\text{iso}} (\text{\AA}^2)$	
Ba	1/2	1/2	1/2	1.0	0.0317(5)	
In	0	0	0	0.84(1)	0.0151(4)	
Ir	0	0	0	0.16(1)	0.0151(4)	
O	1/2	0	0	0.89(1)	0.0313	
Anisotropic atomic displacement parameters (\AA^2)						
	U_{11}	U_{22}	U_{33}	U_{12}	U_{13}	U_{23}
O	0.0223(6)	0.0374(4)	0.0374(4)	0.0	0.0	0.0

Iodometric titrations performed on the same sample used for neutron diffraction gave an average Ir oxidation state of 5.68(6) which compares well with the value obtained the

refinements and supports the presence of Ir(VI) in the samples with low Ir content. To our knowledge, this is the first time Ir(VI) has been stabilized using standard solid state methods with ambient pressure and atmosphere.

On increasing x beyond 0.6, a third structural transition is indicated by the emergence of several new diffraction peaks in the XRD data (Figure 2.5). These peaks increase further in intensity as Ir content approaches $x = 1.0$. Initial XRD refinements indexed the new peaks to a hexagonal 6H BaTiO₃-type phase which persists on increasing x to 1.4. Thus, in the region spanning $x = 1$, our XRD measurements are in agreement with the previously reported 6H polytype structure of Ba₂InIrO₆ [31].

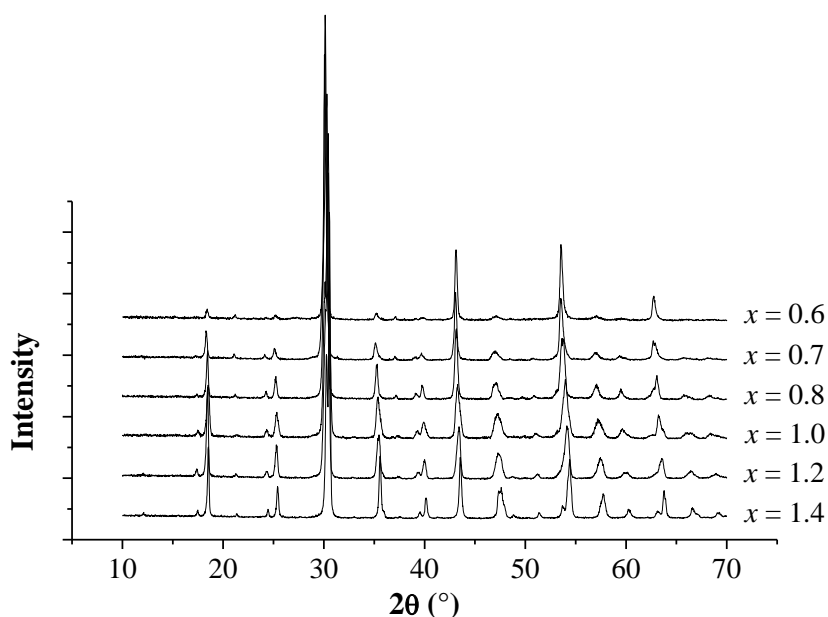


Figure 2.5. Powder X-ray diffraction patterns for $x = 0.6$ – 1.4 .

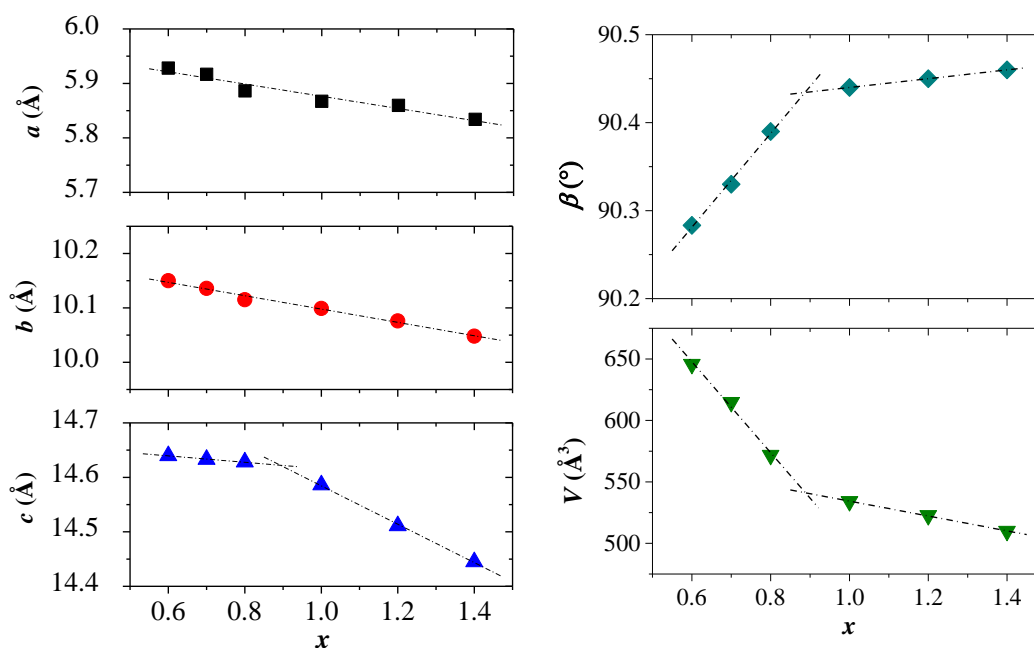


Figure 2.6. Refined (Left) cell edges and (Right) β angles and cell volumes for $x = 0.6$ – 1.4 .

Examination of the changes in the lattice parameters with increasing Ir content reveals a couple trends (Figure 2.6). The unit cell edges a and b decrease linearly whereas there are two linear trends in c , β , and V on either side of $x = 0.9$. This change in slope suggests that the cubic to hexagonal transition is completed after once the Ir content is increased beyond 0.8. Neutron diffraction refinements (Figure 2.7) for $\text{Ba}_2\text{InIrO}_6$ show a splitting in several of the peaks, in disagreement with the reported model (Figure 2.7 inset). These splittings, which were not observed in XRD data, can be indexed to a monoclinic distortion of 6H BaTiO_3 structure with a $C2/c$ space group. The absence of these splittings in the XRD patterns is likely due to lower resolution which causes the splittings to appear simply as peak broadening. Additionally, examination of the pattern at higher d -spacing reveals the presence of a peak at about 5.1 \AA that indexes to reflections for 020 and 110. This peak is absent in a calculated pattern of the structure proposed by Thumm, *et. al.* (Figure 2.8). After the monoclinic model was determined, all XRD

refinements for $0.6 \leq x \leq 1.4$ were revised using this model. As with the lower Ir content samples discussed previously, a decrease in all lattice parameters was observed with increasing Ir content due to the difference in ionic radii.

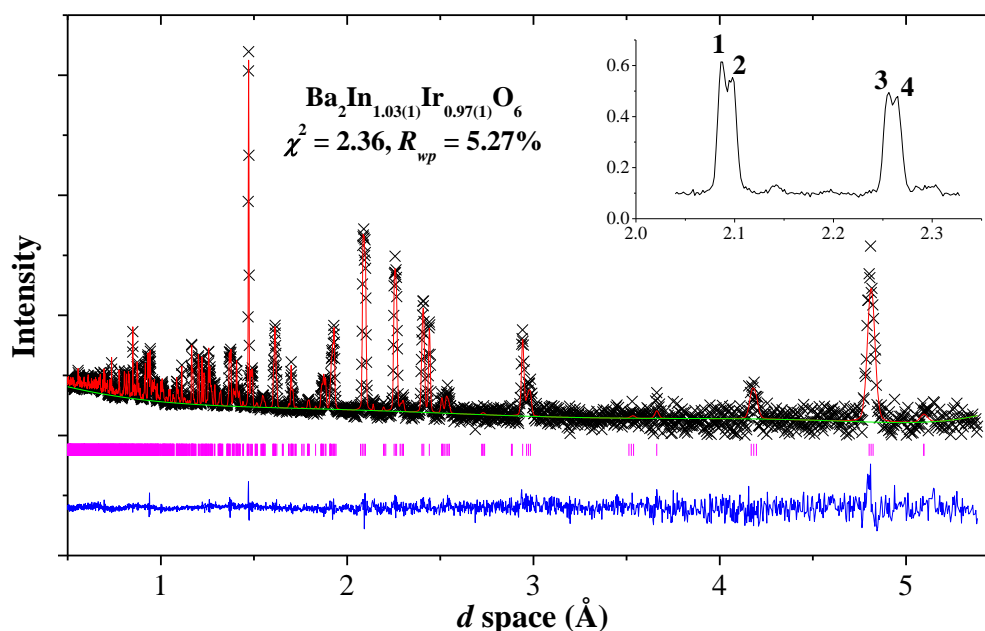


Figure 2.7. Time-of-flight neutron diffraction pattern of $\text{Ba}_2\text{InIrO}_6$ with calculated intensities (red) and difference curve (blue). Inset shows example of peak splitting not explained by hexagonal model (hkl : **1** – 224, **2** – $22\bar{4}$, **3** – 223, **4** – $22\bar{3}$).

The monoclinic model has important implications for the structure. First, in this model, the In and Ir are not ordered in alternating layers along the c axis. Instead, the corner-sharing sites are 100% In and the face-sharing site In:Ir ratio is 0.27:0.73. This gives a refined formula of $\text{Ba}_2\text{In}_{1.03(2)}\text{Ir}_{0.97(2)}\text{O}_6$ which correlates well to the nominal composition. In the previously published hexagonal model [31], all octahedra are oriented parallel to the c axis. The monoclinic model yields a slight canting with respect to the a axis in the corner-sharing octahedra and the

face-sharing clusters of 7.3° and -3.3° , respectively (Figure 2.9). Similar canting is seen in Ir-octahedra in $\text{Ba}_3\text{BiIr}_2\text{O}_9$ and $\text{Ba}_3\text{NdIr}_2\text{O}_9$ [36,37].

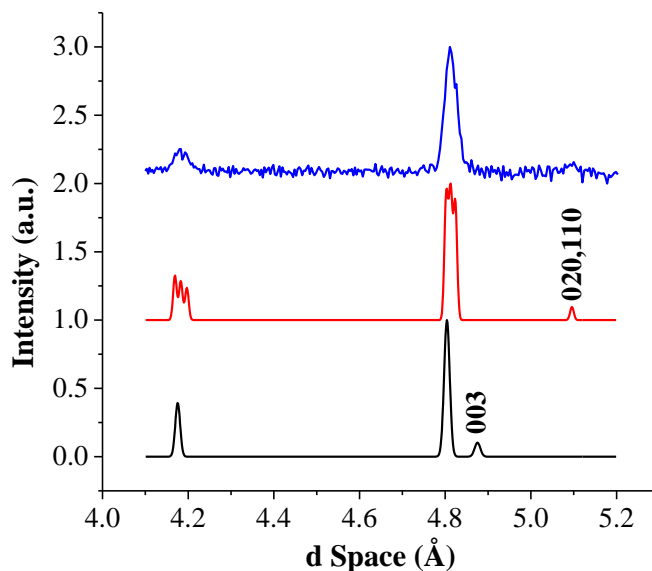


Figure 2.8. Comparison of time-of-flight neutron diffraction patterns for $\text{Ba}_2\text{InIrO}_6$: experimental (blue), calculated $P\bar{3}m1$ (black) and $C2/c$ (red). Note that the 003 peak ($\sim 4.9 \text{ \AA}$) in the $P\bar{3}m1$ pattern is absent in the experimental pattern where as a small 020,110 peak ($\sim 5.1 \text{ \AA}$) from $C2/c$ is present.

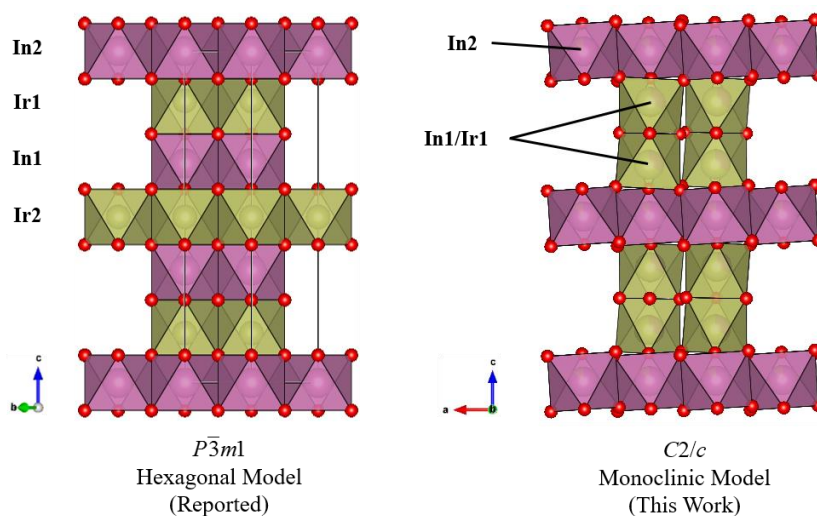


Figure 2.9. Projections of the hexagonal structure reported by Thumm *et al.* and this work's monoclinic structure models comparing the Ir/In ordering and the canting of the octahedra.

Figure 2.10 shows a comparison of bond angles and distances for the Thumm model and those from this work. When the Ir-O and In-O bond distances from the two models are compared with calculated lengths based on Shannon radii [32] (1.97 and 2.14 Å respectively), the bond lengths from our refinements are closer to theoretical values and thus more reasonable than those from the previously reported model. A comparison of the lattice parameters between this work's structure model for Ba₂InIrO₆ and that proposed by Thumm, *et al.* (Table 2.2) shows little difference in the size of the unit cell. Table 2.3 summarizes additional atomic parameters from our neutron refinements for Ba₂InIrO₆.

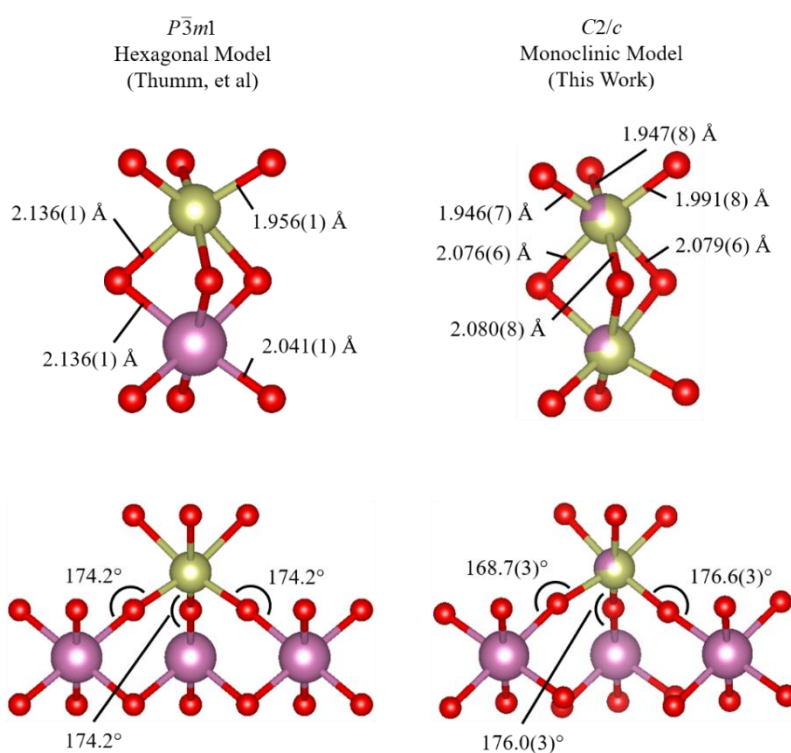


Figure 2.10. Comparison of bond distances within the face-sharing clusters (top) and M-O-M' bond angles between the face-sharing cluster and the corner sharing octahedra in Ba₂InIrO₆ (bottom) from the two models (In = purple, Ir = brown, O = red).

Table 2.2. Lattice parameter comparison of structure models for Ba₂InIrO₆.

	SG	<i>a</i> (Å)	<i>b</i> (Å)	<i>c</i> (Å)	β	<i>V</i> (Å ³)
This work	<i>C2/c</i>	5.885(1)	10.19(1)	14.65(1)	90.48(1)°	878.4(1)
Thumm et al. ^a	<i>P$\bar{3}$m1</i>	5.873	10.17	14.63	90°	873.8

^aLattice parameters transformed from reported hexagonal values [31] for comparison

Table 2.3. Refined atomic coordinates and occupancies for Ba₂InIrO₆.

	<i>x</i>	<i>y</i>	<i>z</i>	Occupancy	<i>U</i> _{iso} (Å ²)
Ba1	0	0.0012(1)	1/4	1.0	0.0061(7)
Ba2	0.5030(6)	0.8322(9)	0.0918(2)	1.0	0.0084(6)
In1	0.4945(3)	0.8330(4)	0.8453(1)	0.27(1)	0.0012(3)
Ir1	0.4945(3)	0.8330(4)	0.8453(1)	0.73(1)	0.0012(3)
In2	0	0	0	1.0	0.0027(8)
O1	0.7725(10)	0.7411(6)	0.2473(3)	1.0	0.0116(9)
O2	0.5	0.0158(9)	0.25	1.0	0.0188(21)
O3	0.2602(10)	0.5858(6)	0.0924(3)	1.0	0.0157(11)
O4	0.0108(14)	0.8287(7)	0.0840(4)	1.0	0.0194(13)
O5	0.7657(12)	0.5863(8)	0.0761(4)	1.0	0.0226(12)

2.2.3 Magnetism

The magnetization, M , was measured for $x = 0.2$ – 1.33 in a magnetic field, H , of 0.5 T, and converted to susceptibility (χ) via $\chi = M/H$. The susceptibility has been corrected for the contribution from the atomic cores of the constituent ions [38]. Field scans, $M(H)$, exhibit linear behavior over the range 0–4 T and $\chi(T)$ data had no anomalies from 2–300 K, consistent with

paramagnetism over the entire measurement range. When viewed as $1/\chi(T)$ (Figure 2.11), three distinct regimes of Ir concentration emerge. For low Ir content, $0.2 < x < 0.6$, $1/\chi(T)$ displays Curie-Weiss behavior. Fitting $1/\chi(T)$ between 200 and 300 K for these compounds yields μ_{eff} values in the range of $3.2\text{--}2.9 \mu_{\text{B}}$ per Ir ion. Since the average Ir oxidation state is greater than 5.5, we expect to have a mixture of different oxidation states among the ions. It is also expected that Ir(V) has a free spin of zero and thus does not contribute to the susceptibility, apart from a Van Vleck temperature independent moment [39]. Thus, since the expected spin-only μ_{eff} value for Ir(IV) in octahedral coordination is $1.73 \mu_{\text{B}}$, corresponding to $s = 1/2$, the measured moment must possess a contribution from Ir(VI), which has $s = 3/2$ by Hund's rule and no Van Vleck term.

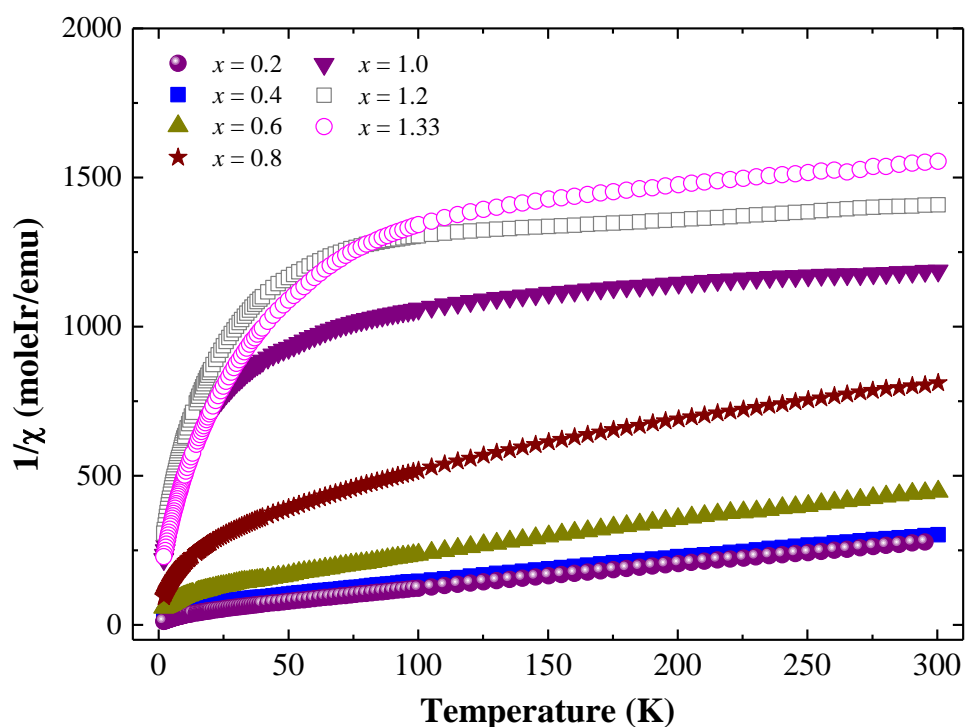


Figure 2.11. Inverse magnetic susceptibility plot for $\text{Ba}_2\text{In}_{2-x}\text{Ir}_x\text{O}_{5+\delta}$. All data has been corrected for the contribution from the atomic cores of the constituent ions.

Based on these concepts, we used the following procedure to fit the $\chi(T)$ data, letting the relative contributions of Ir(IV), Ir(V), and Ir(VI) be variable. The first step is to determine the fraction of Ir(V) by demanding that the resulting $\chi(T)$ be Curie-Weiss like (i.e. forms a straight line) in the temperature range 100-300 K after subtracting the Ir(V) Van Vleck contribution, χ_{VV} [39]. For $x = 0.2$ and 0.4, the resulting Ir(V) content was very close to 50% of the total Ir population, and the Weiss constant was extracted from the resulting $(\chi(T) - \chi_{VV})$. We found that, by assigning the remainder of the Ir ions to be Ir(VI), we obtained good fits to a Curie-Weiss form using the extracted Weiss constant.

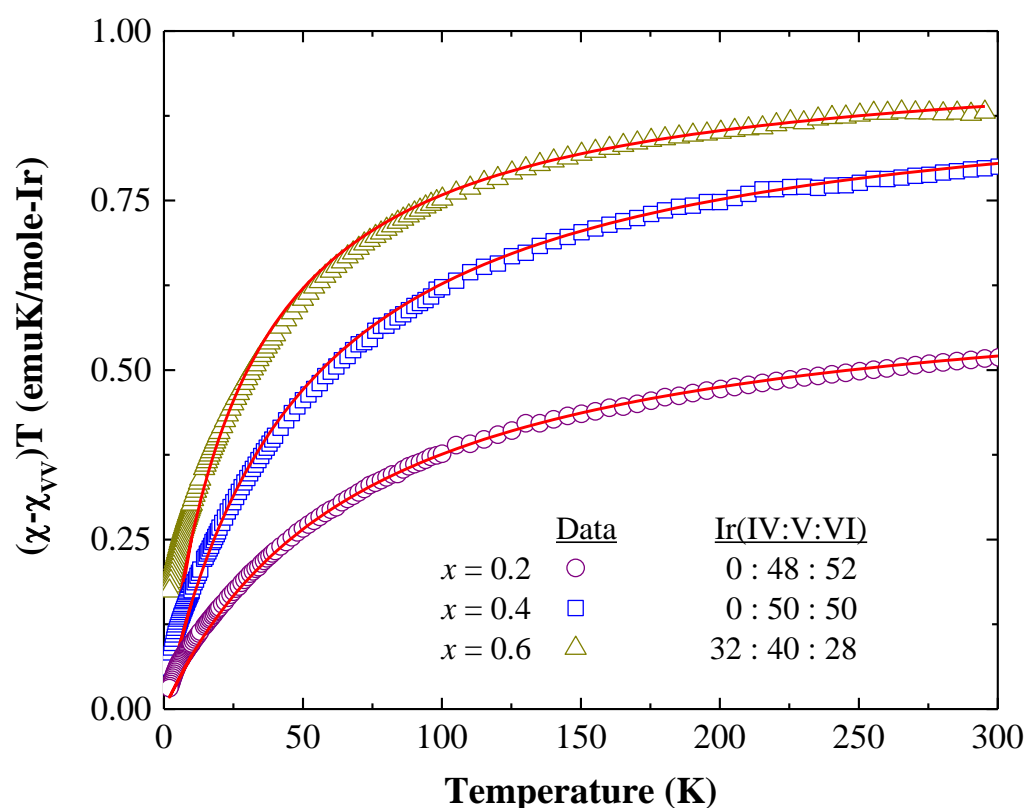


Figure 2.12. Curie-Weiss fits and ratios of the possible Ir oxidation states for $\text{Ba}_2\text{In}_{2-x}\text{Ir}_x\text{O}_{5+\delta}$ ($x = 0.2-0.6$).

The data, plotted as $\chi(T)$ multiplied by temperature (Figure 2.12), show a deviation from the Curie-Weiss fit at temperatures below 50 K, where super-paramagnetic effects due to spin clusters play a role. For $x = 0.6$, it was not possible to model the data with only Ir(V) and Ir(VI). Instead, we allowed the ratio of Ir(IV) to Ir(VI) to vary after determining the Ir(V) in the same manner as above until a reasonable fit was achieved. This ratio was found to be approximately 1:1 among the ~60% of non Ir(V) ions. Thus the $\chi(T)$ data suggest average Ir oxidation states of 5.5, 5.5, and 5.0 for $x = 0.2$, 0.4, and 0.6 respectively, consistent with the titration and neutron refinement values found for $x = 0.4$.

A second regime of magnetic behavior is seen for $x = 0.6$ –1.2 as cubic perovskite structure transitions to the 6H structure. In this x range, $\chi(T)$ decreases significantly, possibly indicating the compensation of moments through local spin cluster singlet formation. Given the large θ values observed for smaller x , long range order might be expected, but the two-dimensionality of the Ir site arrangement and quenched atomic disorder would suppress both its formation and detection via $\chi(T)$, similar to the behavior seen in Ba_2IrO_4 [40]. If an ordered moment exists in $x = 0.6$ –1.2, it might be detectable using μSR techniques as in the Ba_2IrO_4 study.

Finally, $1/\chi(T)$ for the $x = 1.33$ compound has a significantly larger slope than $x = 1.0$ and 1.2, which might reflect the development of magnetization in a state that has already developed long-range antiferromagnetic order. In this structure, the double-layer block has 100% Ir occupancy and the intermediate layers contain only In. Since the average oxidation state of Ir is 4.5+ for this compound, the double-layer most likely possesses a random 1:1 mixture of Ir(IV) and Ir(V). The average χ_{VV} for octahedral Ir(IV) and Ir(V) is 8×10^{-4}

emu/mole [39]. This value is larger than the room temperature $\chi(T)$ which is 7×10^{-4} emu/mole suggesting the Ir environment for $x = 1.33$ is distorted from that described by Hayashi, *et al.* [39].

2.2.4 Electronic Transport Properties

High-temperature Seebeck and resistivity data for $x = 0.8$ – 1.4 , 2 are displayed in Figure 2.13. Semiconductor behavior was observed for all samples and resistivity decreased with increasing Ir content. The band gaps (E_g) for each sample were extracted using $\sigma = \sigma_0 \exp(E_g/k_B T)$ and are listed in Table 2.4. The band gaps tend to decrease with increasing Ir content and decreasing Ir oxidation state.

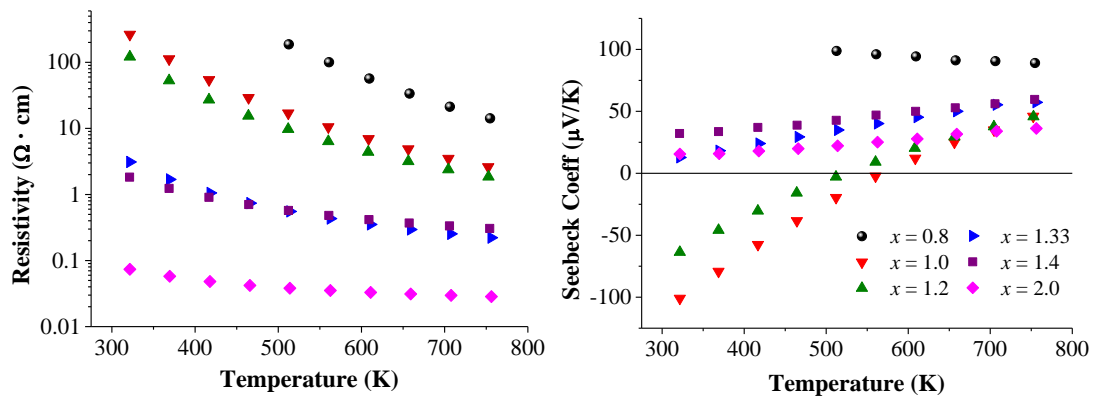


Figure 2.13. Temperature-dependent, high temperature resistivity (left) and Seebeck (right) coefficient plots for $\text{Ba}_2\text{In}_{2-x}\text{Ir}_x\text{O}_{5+\delta}$. Note the sign change in the Seebeck coefficient for $x = 1.0$ and 1.2 at ~ 550 K.

Below 600 K, the system changes from p-type to n-type as denoted by the sign change in the Seebeck coefficient when the Ir content is increased from $x = 0.8$ to $x = 1.0$ and then

changes back to p-type at $x = 1.33$. A transition from n-type to p-type is observed in Seebeck coefficient for $x = 1.0, 1.2$ which suggests the presence of carriers of both signs, but with different temperature dependencies.

Table 2.4. Estimated band gaps for $\text{Ba}_2\text{In}_{2-x}\text{Ir}_x\text{O}_{5+\delta}$.

x	E_g (eV)
0.8	0.713(13)
1.0	0.450(11)
1.2	0.406(8)
1.33	0.254(1)
1.4	0.174(1)
2.0	0.0907(19)

2.3 Conclusions

The solid solution $\text{Ba}_2\text{In}_{2-x}\text{Ir}_x\text{O}_{5+\delta}$ yielded three structural transitions with variation of the Ir content. A complete solid solution was not possible as samples for $x = 1.5-1.9$ resulted in a mixture of several phases. Neutron diffraction refinements showed that where $x \leq 1$, the increase in oxygen content is the greater than the Ir content which indicates that the Ir oxidation state is a mixture of Ir(IV), Ir(V), and Ir(VI) in these samples. While Ir(VI) has been previously reported in oxides, it was stabilized for the first time without the use of high oxygen pressures or molten flux techniques. The oxygen content in the Ir-poor phases is likely lower at our preparation temperature of 1200 °C than what we observe at room temperature. Thus, the Ir(VI) that we find in these samples may be due to the oxidation of Ir that occurred upon cooling our samples in air aided by the high electropositivity of Ba and the filling of oxygen vacancies. The monoclinic structure model for $\text{Ba}_2\text{InIrO}_6$ obtained from our neutron diffraction refinements

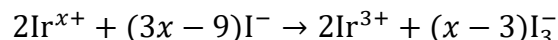
appears to be a better fit than the hexagonal model originally reported by Thumm, *et al.* This monoclinic structure is present through $x = 1.4$.

Our magnetic measurements suggest that the lower Ir content members ($x = 0.2$ – 0.6) display Curie-Weiss behavior due to the presence of Ir(VI). For $0.8 \leq x \leq 1.2$, the susceptibility rapidly decreases with the Ir concentration. The $x = 1.33$ exhibited no signs of magnetic ordering and its paramagnetic behavior did not obey the Curie-Weiss law. A modified Curie-Weiss fit yielded μ_{eff} values that were much lower than hypothetical spin-only values likely due to high degrees of spin-orbit coupling in the Ir. Electrical measurements showed semiconductor behavior for $x = 0.8$ – 1.4 , and increasing Ir content resulted in a decrease in resistivity. The resistivities for member with $x < 0.8$ were found to be above the upper limit for the instrument and were not measured. The Seebeck measurements revealed increased Ir content caused a p- to n-type transition. A very gradual n- to p-type transition was also observed in the $x = 1.0$ and 1.2 samples with increasing temperature.

2.4 Methods and Materials

Black, single-phase polycrystalline samples were prepared by intimately mixing and grinding stoichiometric amounts of BaCO₃ (Cerac, 99.9%), IrO₂, and In₂O₃ (Stanford Materials, 99.99%) using an agate mortar and pestle. The BaCO₃ was dried at 120 °C overnight, and the IrO₂ was obtained by decomposing IrCl₃ (Alfa Aesar, 99.9%) at 750 °C for 10 h under air flow. The samples were then pelletized and sintered at 1200 °C for 36 h with intermittent grinding.

Iodometric titrations were performed on $x = 0.2$ – 0.6 to confirm the Ir oxidation state by first dissolving ~ 25 mg of each sample in 5 mL of a 10% HCl solution then adding excess KI. The I^- in an acidic environment reduces the Ir ions from their original oxidation state to Ir^{3+} and produces I_3^- :



The resulting solutions were then titrated with $\text{Na}_2\text{S}_2\text{O}_3$ solution of a known concentration. The reaction of $\text{S}_2\text{O}_3^{2-}$ with the generated I_3^- can be monitored by using a starch solution as an end-point indicator. The Ir oxidation state can then be calculated from the volume of $\text{Na}_2\text{S}_2\text{O}_3$.

Initial X-ray diffraction (XRD) characterization of the samples was done on a Rigaku Miniflex II diffractometer using $\text{Cu K}\alpha$ radiation and a graphite monochromator. Single-crystal Si sample holders were used to maximize peak intensity and aid detection of minor impurities. A fixed-time scan was used with collection parameters of a 2θ range of 10 – 70° with a step size of 0.02° and a dwell time of 2.0 s. Lattice parameters for all samples were extracted using the Le Bail method [41] on the GSAS software with EXPGUI user interface [42,43]. Room-temperature (298 K) time-of-flight neutron diffraction data for $x = 0.4$ and 1.0 were collected at Oak Ridge National Laboratory on the POWGEN (BL-11A) beam line using center wavelengths of 1.33 and 2.66 Å. Approximately 2 g of each sample was loaded into 6 mm vanadium sample cans and data was collected over about 4 h. Structure refinement was performed using the Rietveld method [44] on the GSAS software with EXPGUI user interface [42,43]. Crystal structures were generated using the VESTA software [45]. Seebeck and resistivity measurements were performed at high temperatures (300–800 K) on an ULVAC-

RIKO ZEM 3 under a static helium atmosphere. Low-temperature (5–300 K) magnetization measurements were obtained using a Quantum Design MPMS.

2.5 References

- [1] S.A. Speakman, S.T. Mixture, In-Situ X-Ray and Neutron Diffraction Study of $\text{Ba}_2\text{In}_2\text{O}_5$, *Mater. Sci. Forum.* 378–381 (2001) 339–339.
- [2] D.H. Gregory, M.T. Weller, Phases in the System $\text{Ba}_2\text{M}_{2-x}\text{Cu}_x\text{O}_{4+\delta}$, $\text{M} = \text{In, Sc}$: Structure and Oxygen Stoichiometry, 1993. doi:10.1006/jssc.1993.1331.
- [3] M. Mitome, M. Okamoto, Y. Bando, H. Yamamura, Structure analysis of $\text{Ba}_2\text{In}_2\text{O}_5$ and related compounds by electron microscopy, *J. Vac. Sci. Technol. B Microelectron. Nanom. Struct.* 19 (2001) 2284. doi:10.1116/1.1421566.
- [4] A. Rolle, P. Roussel, N. Giridharan, E. Suard, R. Vannier, A neutron diffraction study of the oxygen diffusion in molybdenum doped $\text{Ba}_2\text{In}_2\text{O}_5$, *Solid State Ionics.* 179 (2008) 1986–1995. doi:10.1016/j.ssi.2008.06.021.
- [5] A. Rolle, S. Daviero-Minaud, P. Roussel, A. Rubbens, R.N. Vannier, Structure of $\text{Ba}_2\text{In}_{2-x}\text{V}_x\text{O}_{5+x}$ phases: Complementarity of diffraction, Raman and absorption techniques, *Solid State Ionics.* 179 (2008) 771–775. doi:10.1016/j.ssi.2008.01.068.
- [6] J. Bielecki, S.F. Parker, D. Ekanayake, S.M.H. Rahman, L. Börjesson, M. Karlsson, Short-range structure of the brownmillerite-type oxide $\text{Ba}_2\text{In}_2\text{O}_5$ and its hydrated proton-conducting form BaInO_3H , *J. Mater. Chem. A.* 2 (2014) 16915–16924. doi:10.1039/C4TA03213F.
- [7] J.B. Goodenough, Oxide-ion conduction in $\text{Ba}_2\text{In}_2\text{O}_5$ and $\text{Ba}_2\text{In}_2\text{MO}_8$ ($\text{M} = \text{Ce, Hf, or Zr}$), *Solid State Ionics.* 44 (1990) 21–31.
- [8] G.B.B. Zhang, D.M.M. Smyth, Defects and transport of the brownmillerite oxides with high oxygen ion conductivity - $\text{Ba}_2\text{In}_2\text{O}_5$, *Solid State Ionics.* 82 (1995) 161–172. doi:10.1016/0167-2738(95)00196-2.
- [9] T. Yao, Y. Uchimoto, M. Kinuhata, T. Inagaki, H. Yoshida, Crystal structure of Ga-doped $\text{Ba}_2\text{In}_2\text{O}_5$ and its oxide ion conductivity, *Solid State Ionics.* 132 (2000) 189–198. doi:10.1016/S0167-2738(00)00658-5.
- [10] K. Kakinuma, H. Yamamura, H. Haneda, T. Atake, Oxide-ion conductivity of $(\text{Ba}_{1-x}\text{La}_x)_2\text{In}_2\text{O}_{5+x}$ system based on brownmillerite structure, *Solid State Ionics.* 140 (2001) 301–306. doi:10.1016/S0167-2738(01)00853-0.
- [11] J.B. Goodenough, Ceramic solid electrolytes, *Solid State Ionics.* 94 (1997) 17–25. doi:10.1016/S0167-2738(96)00501-2.

- [12] P. Jiang, J. Li, A. Ozarowski, A.W. Sleight, M.A. Subramanian, Intense Turquoise and Green Colors in Brownmillerite-Type Oxides Based on Mn^{5+} in $Ba_2In_{2-x}Mn_xO_{5+x}$, *Inorg. Chem.* 52 (2013) 1349–57. doi:10.1021/ic3020332.
- [13] T. Siegrist, B.L. Chamberland, The crystal structure of $BaIrO_3$, *J. Less-Common Met.* 170 (1990) 93–99.
- [14] A.V. Powell, P.D. Battle, The electronic properties of non-stoichiometric barium iridate, $BaIrO_{3-\delta}$, *J. Alloys Compd.* 191 (1993) 313–318. doi:10.1016/0925-8388(93)90085-2.
- [15] G. Cao, J.E. Crow, R.P. Guertin, P.F. Henning, C.C. Homes, M. Strongin, D.N. Basov, E. Lochner, Charge density wave formation accompanying ferromagnetic ordering in quasi-one-dimensional $BaIrO_3$, *Solid State Commun.* 113 (2000) 657–662.
- [16] D. Pesin, L. Balents, Mott physics and band topology in materials with strong spin-orbit interaction, *Nat. Phys.* 6 (2010) 376–381. doi:10.1038/nphys1606.
- [17] H.-M. Guo, M. Franz, Three-Dimensional Topological Insulators on the Pyrochlore Lattice, *Phys. Rev. Lett.* 103 (2009) 206805. doi:10.1103/PhysRevLett.103.206805.
- [18] J.-M. Carter, V.V. Shankar, M.A. Zeb, H.-Y. Kee, Semimetal and Topological Insulator in Perovskite Iridates, *Phys. Rev. B.* 85 (2012) 115105. doi:10.1103/PhysRevB.85.115105.
- [19] A.W. Sleight, New ternary oxides of Re, Os, Ir and Pt with cubic crystal structures, *Mater. Res. Bull.* 9 (1974) 1177–1184. doi:10.1016/0025-5408(74)90035-X.
- [20] R. Hoppe, K. Claes, Über oxoiridate: zur kenntnis von $KIrO_3$, *J. Less Common Met.* 43 (1975) 129–142. doi:10.1016/0022-5088(75)90132-0.
- [21] S. Frenzen, H. Müller-Buschbaum, Zur Kristallchemie eines Natrium-Cadmium-Oxoiridats: $Na_3Cd_2IrO_6$, *Zeitschrift Für Naturforsch. B.* 51 (1996) 822–825. doi:10.1515/znb-1996-0611.
- [22] M.J. Davis, M.D. Smith, K.E. Stitzer, H.-C. zur Loye, High temperature flux growth, structural characterization, and magnetic properties of $Ca_{3.15}Li_{0.85}IrO_6$, Sr_3LiIrO_6 , Ca_3LiRuO_6 and Sr_3LiRuO_6 , *J. Alloys Compd.* 351 (2003) 95–100. doi:10.1016/S0925-8388(02)01082-4.
- [23] S.J. Mugavero, M.D. Smith, H.-C. zur Loye, $La_9RbIr_4O_{24}$: A Rubidium-Containing Oxide with a New Structure Type, *Inorg. Chem.* 45 (2006) 946–948. doi:10.1021/ic051890s.
- [24] G. Demazeau, D.-Y. Jung, J.-P. Sanchez, E. Colineau, A. Blaise, L. Fournes, Iridium(VI) stabilized in a perovskite-type lattice: Ba_2CaIrO_6 , *Solid State Commun.* 85 (1993) 479–484. doi:10.1016/0038-1098(93)90004-7.
- [25] D.-Y. Jung, P. Gravereau, G. Demazeau, Stabilization of six-coordinated iridium(VI) in a perovskite oxygen lattice $Ba_2M'IrO_6$ ($M' = Ca, Sr$), *Eur. J. Solid State Inorg. Chem.* 30 (1993) 1025–1037.

- [26] S.J. Mugavero, M.D. Smith, W.-S. Yoon, H.-C. zur Loye, $\text{Nd}_2\text{K}_2\text{IrO}_7$ and $\text{Sm}_2\text{K}_2\text{IrO}_7$: Iridium(VI) Oxides Prepared under Ambient Pressure, *Angew. Chemie Int. Ed.* 48 (2009) 215–218. doi:10.1002/anie.200804045.
- [27] L. Yang, A. Pisoni, A. Magrez, S. Katrych, A. Arakcheeva, B. Dalla Piazza, K. Prša, J. Jaćimović, A. Akrap, J. Teyssier, L. Forró, H.M. Rønnow, Crystal Structure, Transport, and Magnetic Properties of an Ir^{6+} Compound $\text{Ba}_8\text{Al}_2\text{IrO}_{14}$, *Inorg. Chem.* 54 (2015) 4371–4376. doi:10.1021/acs.inorgchem.5b00157.
- [28] T. Sakamoto, Y. Doi, Y. Hinatsu, Crystal structures and magnetic properties of 6H-perovskite-type oxides $\text{Ba}_3\text{M}\text{Ir}_2\text{O}_9$ (M=Mg, Ca, Sc, Ti, Zn, Sr, Zr, Cd and In), *J. Solid State Chem.* 179 (2006) 2595–2601. doi:10.1016/j.jssc.2006.04.055.
- [29] M. Wakeshima, D. Harada, Y. Hinatsu, Crystal structures and magnetic properties of ordered perovskites $\text{A}_2\text{R}^{3+}\text{Ir}^{5+}\text{O}_6$ (A=Sr, Ba; R=Sc, Y, La, Lu), *J. Alloys Compd.* 287 (1999) 130–136.
- [30] I. Thumm, U. Treiber, S. Kemmler-Sack, Über Sauerstoffperovskite mit fünf- und vierwertigem Iridium Verbindungen vom Typ $\text{Ba}_2\text{B}^{3+}\text{Ir}^{5+}\text{O}_6$ und $\text{Ba}_3\text{B}^{3+}\text{Ir}^{4,5+}_2\text{O}_9$, *J. Solid State Chem.* 35 (1980) 156–166. doi:10.1016/0022-4596(80)90488-0.
- [31] I. Thumm, U. Treiber, S. Kemmler-Sack, Zur Struktur von $\text{Ba}_3\text{SmRu}_2\text{O}_9$, $\text{Ba}_3\text{SmIrRuO}_9$ und $\text{Ba}_2\text{InIrO}_6$, *Zeitschrift Für Anorg. Und Allg. Chemie.* 477 (1981) 161–166. doi:10.1002/zaac.19814770622.
- [32] R.D. Shannon, Revised effective ionic radii and systematic studies of interatomic distances in halides and chalcogenides, *Acta Crystallogr. Sect. A.* 32 (1976) 751–767. doi:10.1107/S0567739476001551.
- [33] J.-H. Choy, D.-K. Kim, S.-H. Hwang, G. Demazeau, D.-Y. Jung, XANES and EXAFS Studies on the Ir-O Bond Covalency in Ionic Iridium Perovskites, *J. Am. Chem. Soc.* 117 (1995) 8557–8566. doi:10.1021/ja00138a010.
- [34] D.-Y. Jung, G. Demazeau, J. Etourneau, M.A. Subramanian, Preparation and characterization of new perovskites containing Ir(VI) and Ir(V) [$\text{BaM}_{0.50}\text{Ir}_{0.50}\text{O}_{2.75}$ and $\text{BaM}_{0.25}\text{Ir}_{0.75}\text{O}_3$ (M = Li or Na)], *Mater. Res. Bull.* 30 (1995) 113–123. doi:10.1016/0025-5408(94)00115-4.
- [35] S.-J. Kim, M.D. Smith, J. Darriet, H.-C. zur Loye, Crystal growth of new perovskite and perovskite related iridates: $\text{Ba}_3\text{LiIr}_2\text{O}_9$, $\text{Ba}_3\text{NaIr}_2\text{O}_9$, and $\text{Ba}_{3.44}\text{K}_{1.56}\text{Ir}_2\text{O}_{10}$, *J. Solid State Chem.* 177 (2004) 1493–1500. doi:10.1016/j.jssc.2003.11.037.
- [36] C.D. Ling, B.J. Kennedy, Q. Zhou, J.R. Spencer, M. Avdeev, Synthesis, structures, and phase transitions of barium bismuth iridium oxide perovskites $\text{Ba}_2\text{BiIrO}_6$ and $\text{Ba}_3\text{BiIr}_2\text{O}_9$, *J. Solid State Chem.* 183 (2010) 727–735. doi:10.1016/j.jssc.2010.01.017.
- [37] Y. Doi, Y. Hinatsu, Y. Shimojo, Y. Ishii, Crystal Structure and Magnetic Properties of 6H-Perovskite $\text{Ba}_3\text{NdRu}_2\text{O}_9$, *J. Solid State Chem.* 161 (2001) 113–120. doi:10.1006/jssc.2001.9296.

- [38] V.E. König, Landolt-Börnstein. Neue Serie. Vol II/2, Springer, Berlin, 1966.
- [39] K. Hayashi, G. Demazeau, M. Pouchard, P. Hagenmuller, Preparation and Magnetic Study of a New Iridium(V) Perovskite: $\text{LaLi}_{0.5}\text{Ir}_{0.5}\text{O}_3$, Mater. Res. Bull. 15 (1980) 461–467.
- [40] H. Okabe, M. Isobe, E. Takayama-Muromachi, A. Koda, S. Takeshita, M. Hiraishi, M. Miyazaki, R. Kadono, Y. Miyake, J. Akimitsu, Ba_2IrO_4 : A spin-orbit Mott insulating quasi-two-dimensional antiferromagnet, Phys. Rev. B. 83 (2011) 155118. doi:10.1103/PhysRevB.83.155118.
- [41] A. Le Bail, Whole powder pattern decomposition methods and applications: A retrospection, Powder Diffr. 20 (2005) 316–326. doi:10.1154/1.2135315.
- [42] A.C. Larson, R.B. Von Dreele, General Structure Analysis System (GSAS), Los Alamos Natl. Lab. Rep. LAUR 86-74 (1994).
- [43] B.H. Toby, EXPGUI, a graphical user interface for GSAS, J. Appl. Crystallogr. 34 (2001) 210–213. doi:10.1107/S0021889801002242.
- [44] H.M. Rietveld, A profile refinement method for nuclear and magnetic structures, J. Appl. Crystallogr. 2 (1969) 65–71. doi:10.1107/S0021889869006558.
- [45] K. Momma, F. Izumi, VESTA 3 for three-dimensional visualization of crystal, volumetric and morphology data, J. Appl. Crystallogr. 44 (2011) 1272–1276. doi:10.1107/S0021889811038970.

Chapter 3: Tuning the Ir Oxidation State in $\text{Ba}_2\text{InIrO}_6$ and BaLaInIrO_6 via *A*- and *B*-site Substitutions

Abstract

Two novel solid solution series, $\text{Ba}_{2-x}\text{La}_x\text{InIrO}_6$ ($x = 0-1.0$) and $\text{BaLaIn}_{1-y}\text{Ca}_y\text{IrO}_6$ ($y = 0-1.0$), were prepared and several changes in structure, magnetic moment, and charge transport were observed. The $\text{Ba}_{2-x}\text{La}_x\text{InIrO}_6$ series exhibits a transition from a 6M polytype to an orthorhombic perovskite structure with increased La content whereas the $\text{BaLaIn}_{1-y}\text{Ca}_y\text{IrO}_6$ series transitioned from a disordered orthorhombic perovskite to an ordered cubic perovskite with increased Ca content. Seebeck measurements for both systems showed that Ir(IV)-rich compounds tended to have a n-type conduction mechanism while Ir(V)-rich compounds appeared to be p-type. Both systems were found to be semiconducting and the magnitude of the resistivity is dependent on the crystal structure and Ir environment. Magnetic measurements show that the μ_{eff} values for both systems are significantly less than predicted for Ir(IV) ($1.73 \mu_B$) and greater than predicted for Ir(V) ($0 \mu_B$). These results are compared to other iridate compound families.

Publications based on this chapter:

- [1] J. Flynn, J. Li, A.P. Ramirez, M.A. Subramanian, The effect of iridium oxidation state on the electronic properties of perovskite-type solid solutions: $\text{Ba}_{2-x}\text{La}_x\text{InIrO}_6$ and $\text{BaLaIn}_{1-y}\text{Ca}_y\text{IrO}_6$, *J. Solid State Chem.* 247 (2017) 53–59.
doi:10.1016/j.jssc.2016.12.017.

3.1 Motivation for Study

Iridium oxides are of interest due to their novel magnetic properties [1–3] and potential as topological insulators [4–6]. A large amount of work has been done on iridate families with specific perovskite stoichiometries, such as $A_2B\text{IrO}_6$ [7–11] and $A_3B\text{Ir}_2\text{O}_9$ [12–14]), and numerous $A_2\text{Ir}_2\text{O}_7$ pyrochlores [15–18]. Fewer studies have focused on diluting the Ir content or tuning the Ir oxidation state. Since tuning the oxidation state and content of transition metals has long been known to bring about exotic and unexpected properties in oxides, such studies are important for determining the structure-property relationships of iridate systems.

The magnetism of iridates especially those containing Ir(IV) or Ir(V) has been the subject of recent debate and interest. One of the most informative physical properties is the value of the effective moment (μ_{eff}). Iridate compounds exhibit large variability in the reported moments. When including the splitting of the t_{2g} orbitals due to spin-orbit coupling (SOC), Ir(IV) should have an μ_{eff} value close to $1.73 \mu_B$ in an octahedral environment while Ir(V) should have no moment, but should instead exhibit Van Vleck temperature-independent paramagnetism [19]. However, this is not always the case. For example, compounds containing Ir(IV) as the only magnetic ion have reported μ_{eff} values ranging from close to the spin-only value for a low spin d^5 metal ($1.73 \mu_B$) [7,20–22] to much lower values ($0.1\text{--}0.5 \mu_B$) [13,23–27]. While SOC is an important factor to consider when defining magnetism in iridates, the on-site Coulombic interaction, U (not to be confused with U_{iso}), as well as the bandwidth, W , also play a role. The latter of these will affect the degree of localization for a particular system [28]. In particular, we note that when W , U , and SOC conspire to yield delocalized charges, the value of μ_{eff} will be less than the local moment value of $1.73 \mu_B$. Since W and U can depend on the

difference in orbital overlap (which is controlled by the spatial configuration of Ir ions in the lattice), one cannot assume that the local moment in one crystal structure can be compared with that in another. Therefore, the origin for variation of moment, and hence the degree of electron localization, needs to be examined for each structure type.

Iridium in oxides is somewhat flexible with respect to the oxidation state. The most common state is Ir(IV) though it is not difficult to stabilize Ir(V) and even Ir(VI) under the right conditions [29–33]. Ir(III) is most common in transition metal complexes but a few occurrences in extended oxide structures have been reported, including $\text{BaIrO}_{3-\delta}$, $\text{K}_{1-x}\text{Ir}_4\text{O}_8$ and $\text{Sr}_{2-x}\text{La}_x\text{IrO}_4$ [34–36]. To explore the influence of structure and Ir oxidation state on the magnetic and electrical properties, the other cations in the structure must have a closed shell configuration. In this work, the Ir oxidation state is systemically tuned between 4+ and 5+ in perovskite-related structures via *A*-site and *B*-site substitutions while monitoring the variation of structure, magnetic moment, and charge transport.

3.2 Substitutions and Structural Characterization

3.2.1 $\text{Ba}_{2-x}\text{La}_x\text{InIrO}_6$

$\text{Ba}_2\text{InIrO}_6$ crystallizes in a monoclinically distorted 6H polytype structure [29] similar to $\text{Ba}_3\text{BiIr}_2\text{O}_9$ and $\text{Ba}_3\text{NdIr}_2\text{O}_9$ [37,38] and was determined to be an ideal candidate for *A*-site substitution due to inflexibility of the Ba and In oxidation states. Despite its significantly smaller ionic radius, La(III) has been reported to substitute well for Ba(II) in a handful of BaLaMIrO_6 ($M = \text{Fe(III)}, \text{Co(II)}, \text{Mg(II)}, \text{Ni(II)}$) perovskites [7]. Thus, for the potential series

$\text{Ba}_{2-x}\text{La}_x\text{InIrO}_6$, substituting La for Ba in the A-site will force Ir to reduce from 5+ to 4+ to compensate for the charge difference. As demonstrated below, this substitution was successful and single phase samples were prepared for $x = 0-1$.

Powder XRD diffraction data (Figure 3.1) reveal a structural transition from the monoclinic $\text{Ba}_2\text{InIrO}_6$ $C2/c$ structure (Figure 3.2a) to a disordered orthorhombic $Pbnm$ perovskite structure (Figure 3.2b) with increasing La content. The transition starts gradually with the characteristic peaks of the 6H polytype slowly decreasing in intensity while a small peak corresponding to the 110 and 002 reflections of orthorhombic perovskite begins to appear at $\sim 21.5^\circ$.

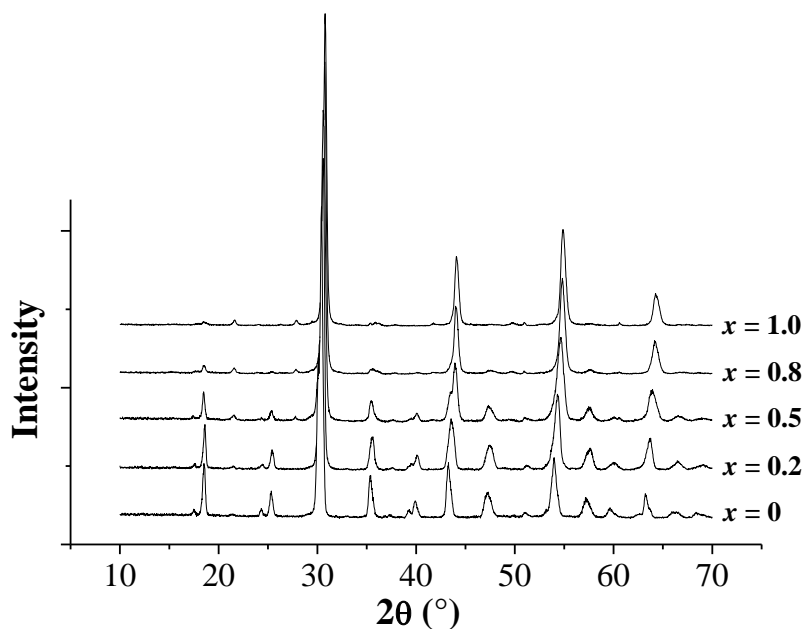


Figure 3.1. Powder X-ray diffraction patterns for $\text{Ba}_{2-x}\text{La}_x\text{InIrO}_6$ ($x = 0-1$).

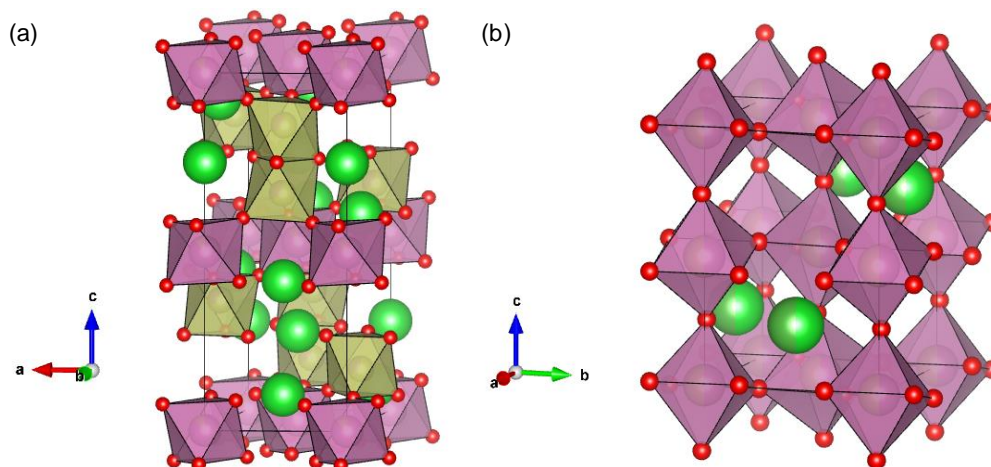


Figure 3.2. Crystal structures of (a) monoclinic 6H polytype $\text{Ba}_2\text{InIrO}_6$ (Ba = green, In = purple, Ir = light brown, O = red) and (b) orthorhombic perovskite BaLaInIrO_6 (Ba/La = green, In/Ir = purple, O = red).

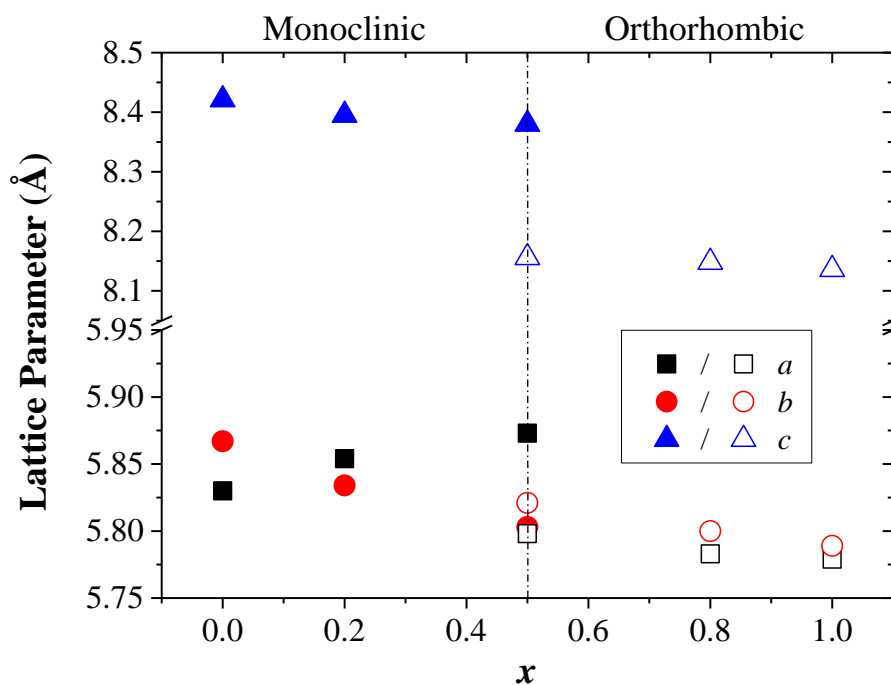


Figure 3.3. Lattice parameters for $\text{Ba}_{2-x}\text{La}_x\text{InIrO}_6$ ($x = 0-1$). The a and c parameters of the monoclinic phase (filled points) were divided by $\sqrt{3}$ for a more direct comparison to the orthorhombic parameters (open points).

Increasing x beyond 0.5 causes the monoclinic phase to disappear very quickly until only the orthorhombic perovskite phase is present at $x = 1$. Successful substitution of the La(III) for the Ba(II) is supported by the change in the lattice parameters (Figure 3.3) which show an overall decrease in the unit cell volume in both crystal structures despite the increase in the a parameter of the monoclinic phase.

Refinements of the TOF neutron diffraction data for BaLaInIrO_6 were performed for both $P2_1/n$ and $Pbnm$ to model order and disorder, respectively, on the B -site. The $P2_1/n$ model refined to show very little B -site ordering ($< 5\%$) and yielded a goodness-of-fit similar to that of the $Pbnm$ model so the latter was chosen due to its higher symmetry. Neither model showed ordering of the A -site.

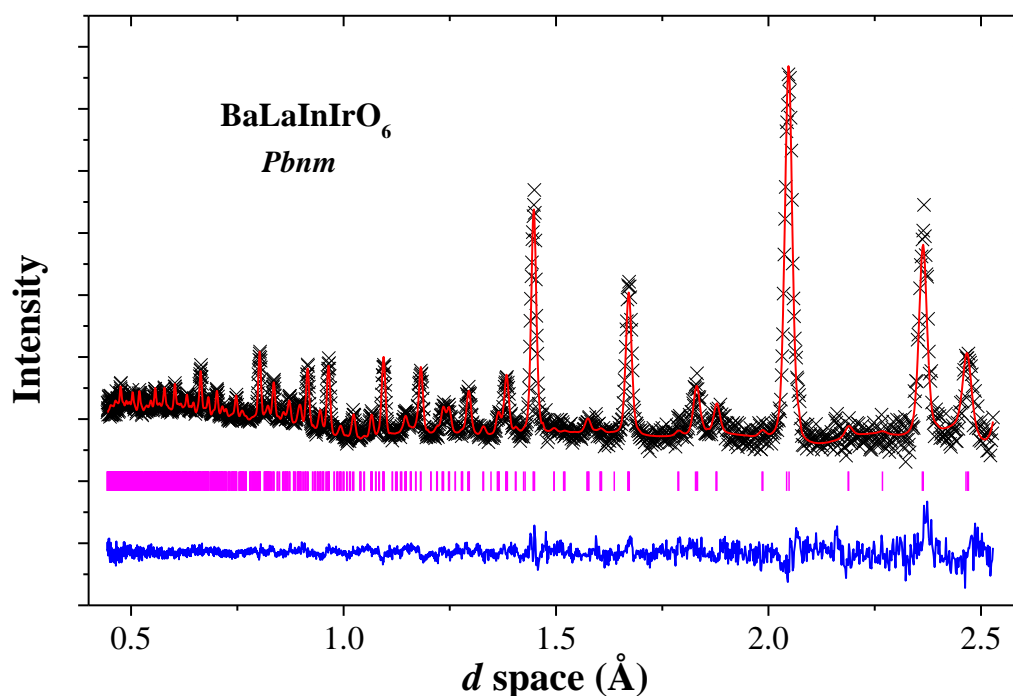


Figure 3.4. TOF diffraction pattern for BaLaInIrO_6 with calculated intensities (red) and difference curve (blue). The magenta tick marks are the allowed reflections for $Pbnm$.

Table 3.1. Refined unit-cell, coordinate and displacement parameters for BaLaInIrO₆ (*Pbnm*)^a

	<i>x</i>	<i>y</i>	<i>z</i>	Occupancy	<i>U</i> _{iso} (Å ²)
Ba/La	-0.0155(17)	0.5187(11)	0.25	0.5/0.5	0.0026(6)
In/Ir	0	0	0	0.5/0.5	0.0010(4)
O1	-0.0505(17)	-0.003(21)	0.25	1.0	0.0112(12)
O2	0.2321(17)	0.2768(14)	0.0358(8)	1.0	0.0210(11)

^aThe unit-cell parameters are $a = 5.789(1)$ Å, $b = 5.796(1)$ Å, $c = 8.174(1)$ Å, and $V = 274.28(2)$ Å³; the reliability parameters are $\chi^2 = 1.68$, $R_{wp} = 3.88\%$.

The Rietveld refinement for *Pbnm* is shown in Figure 3.4 and the extracted crystallographic data is summarized in Table 3.1. *Imma* was also considered as a possible space group and fit the neutron data as well as *Pbnm*; however, it was ruled out due to the presence of a peak in the XRD pattern at $\sim 24^\circ$ which indexes to the 111 reflection under *Pbnm* but is not allowed under *Imma* (Figure 3.5). The orthorhombic distortion from the ideal perovskite is two-fold: a slight displacement of the Ba/La site along the [110] direction as well as tilting of the octahedral sites. The *Pbnm* space group has a $a^-a^-c^+$ Glazer tilt scheme [39] (Figure 3.6). The tilting angles θ and φ were calculated using anion coordinates [40] and found to be 8.158° and 5.208° , respectively. These tilt angles are somewhat lower than expected when compared to values observed for other orthorhombic perovskites [41,42].

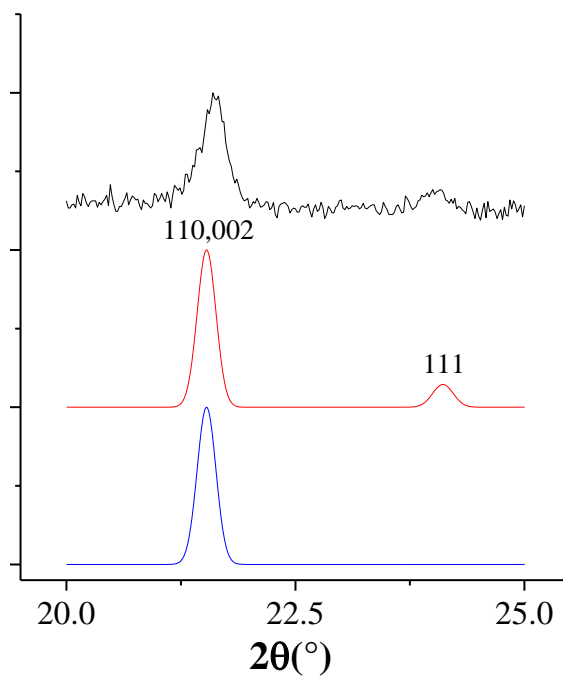


Figure 3.5. Comparison of experimental (black) and calculated *Pbnm* (red) and *Imma* (blue) XRD patterns for BaLaInIrO_6 . Note that the 111 peak ($\sim 24^\circ$) is present in both the experimental and *Pbnm* patterns but is absent in the *Imma* pattern.

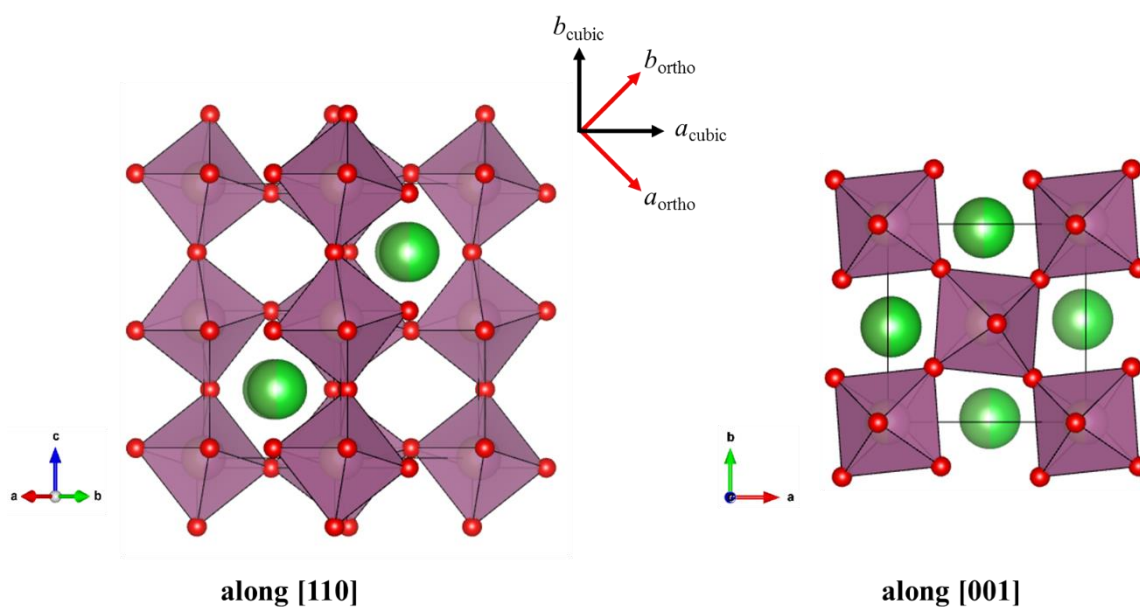


Figure 3.6. Projections of BaLaInIrO_6 showing the anti-phase tilting respect to the a_{cubic} axis and in-phase tilting along the c axis.

3.2.2 *BaLaIn_{1-y}Ca_yIrO₆*

Although BaLaInIrO₆ had not been previously reported in the literature, the double perovskite Ba₂CaIrO₆ had [31], suggesting BaLaCaIrO₆ would a viable target in a BaLaIn_{1-y}Ca_yIrO₆ series allowing for tuning of the Ir oxidation state from 4+ to 5+. Single phase samples were successfully prepared for $y = 0-1$. XRD diffraction data (Figure 3.7) shows that as Ca content is increased, the structure transitions from the disordered orthorhombic perovskite ($y = 0-0.75$) to an ordered cubic perovskite ($y = 1.0$) with the space group $Fm\bar{3}m$ (Figure 3.8). The orthorhombic lattice parameters (Figure 3.7) gradually come together with increasing Ca content. There is also an overall increase in the size of the unit cell, which is expected due to the larger ionic radius of Ca compared to In. The transition is gradual and although the intermediate members can be indexed to the $Pbnm$ space group, the degree of B -site ordering likely increases with Ca content suggesting these members would have a partially ordered, yet distorted, structure with a likely space group of $P2_1/n$. The ordering in BaLaCaIrO₆ is due to the large size and charge separation between Ca(II) and Ir(V). It is unexpected to see the transition to higher symmetry (orthorhombic to cubic) given that the tolerance factor decreases from 0.966 for BaLaInIrO₆ to 0.934 for BaLaCaIrO₆ though there is literature on cubic rhenium-based double perovskites with tolerance factors [43] similar to the value observed for BaLaCaIrO₆.

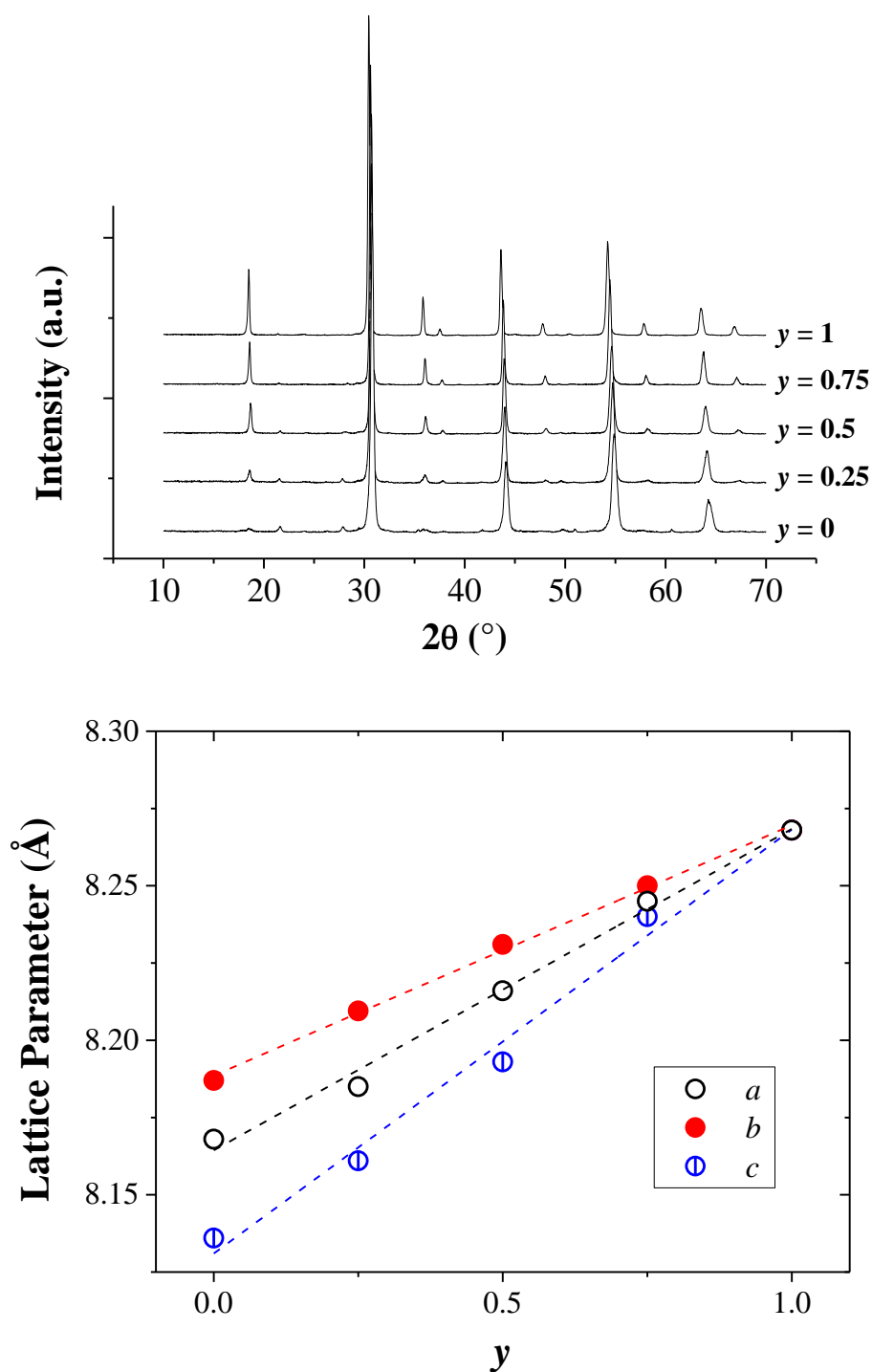


Figure 3.7. (Top) Powder X-ray diffraction patterns and (bottom) lattice parameters for $\text{BaLaIn}_{1-y}\text{Ca}_y\text{IrO}_6$ ($y = 0-1$). Successful substitution of In for Ca is indicated by the increase in the lattice parameters with increasing y . The orthorhombic b and c parameters were multiplied by $\sqrt{2}$ for a more direct comparison to the cubic phase.

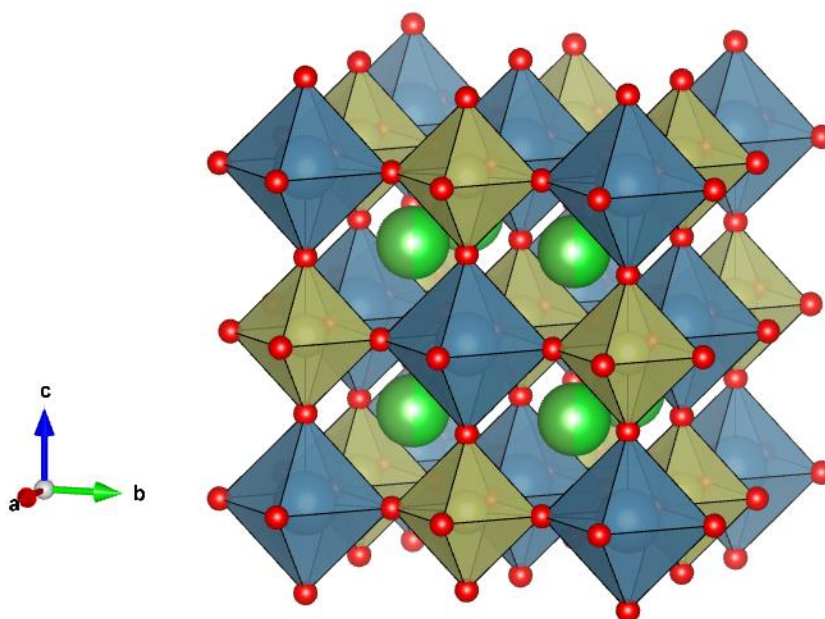


Figure 3.8. Crystal structure for ordered cubic perovskite BaLaCaIrO_6 . (Ba/La = green, Ca = blue, Ir = light brown, O = red).

The presence of In(III) in the B -site seems to induce disorder, which is unexpected considering the size difference between Ir(IV) and In(III). One might suggest that the charge separation is too small; however, no ordering is observed in the $\text{Ba}_2\text{In}_{2-x}\text{Ir}_x\text{O}_{5+\delta}$ family [29] where the charge difference is 2 or greater. Additionally, ordering is known to occur based solely on difference in ionic radii of the B cations in several $A_2B^{4+}B'^{4+}O_6$ ($A^{2+} = \text{Ba, Sr}$; $B^{4+} = \text{Ce, Tb, Pr}$; $B'^{4+} = \text{Ir, Pt}$) double perovskites [44,45,9]. The B -site ionic radii differences, based on Shannon radii [46], in these compounds range from 0.245 to 0.14 Å which encloses the value 0.175 Å for Ir(IV) and In(III) well. Both In and Ir are also known to order with other similarly sized ions as seen in $\text{Ba}_2\text{InOsO}_6$ and $\text{Ba}_2\text{ScIrO}_6$ [47,48]. Based on these examples, it is reasonable to expect In and Ir to order in a perovskite structure; the fact that they do not suggests there is a unique characteristic about the In/Ir pair.

3.3 Electronic Properties

3.3.1 Transport Characterization

High-temperature electrical resistivity and Seebeck data are shown in Figure 3.9 for $\text{Ba}_{2-x}\text{La}_x\text{InIrO}_6$ ($x = 0-1$) and $\text{BaLaIn}_{1-y}\text{Ca}_y\text{IrO}_6$ ($y = 0-0.75$) and estimated band gaps are listed in Table 3.2. Semiconductor behavior is observed for all compositions of both systems based on the trends seen in the $\rho(T)$ data. For $\text{Ba}_{2-x}\text{La}_x\text{InIrO}_6$, there seems to be no apparent trend or large changes in the resistivity behavior as the La content is changed. Analysis of the band gaps shows a slight increase in the values from $x = 0$ to 0.2, followed by a sudden drop at $x = 0.5$ and a subsequent increase as La content is increased beyond 0.5. The increasing trends in the band gaps for $x = 0-0.2$ and $x = 0.5-1$ can be attributed to the increase in orbital overlap as the crystal structure contracts. The sudden drop is likely due to the structure transition from the 6H structure, where the Ir environment is more localized, to the disordered perovskite structure where there is increased long-range connectivity between IrO_6 octahedra.

The data for $\text{BaLaIn}_{1-y}\text{Ca}_y\text{IrO}_6$, display a much clearer trend where the resistivity and band gaps increase with increasing Ca content. This increase is unexpected considering the expansion of the unit cell and the associated decrease in metal-oxygen orbital overlap as Ca is substituted into the structure. Since the *B*-site ordering increases with increasing y , the trend is likely due to the loss of connectivity between the IrO_6 octahedra caused by their growing isolation from one another.

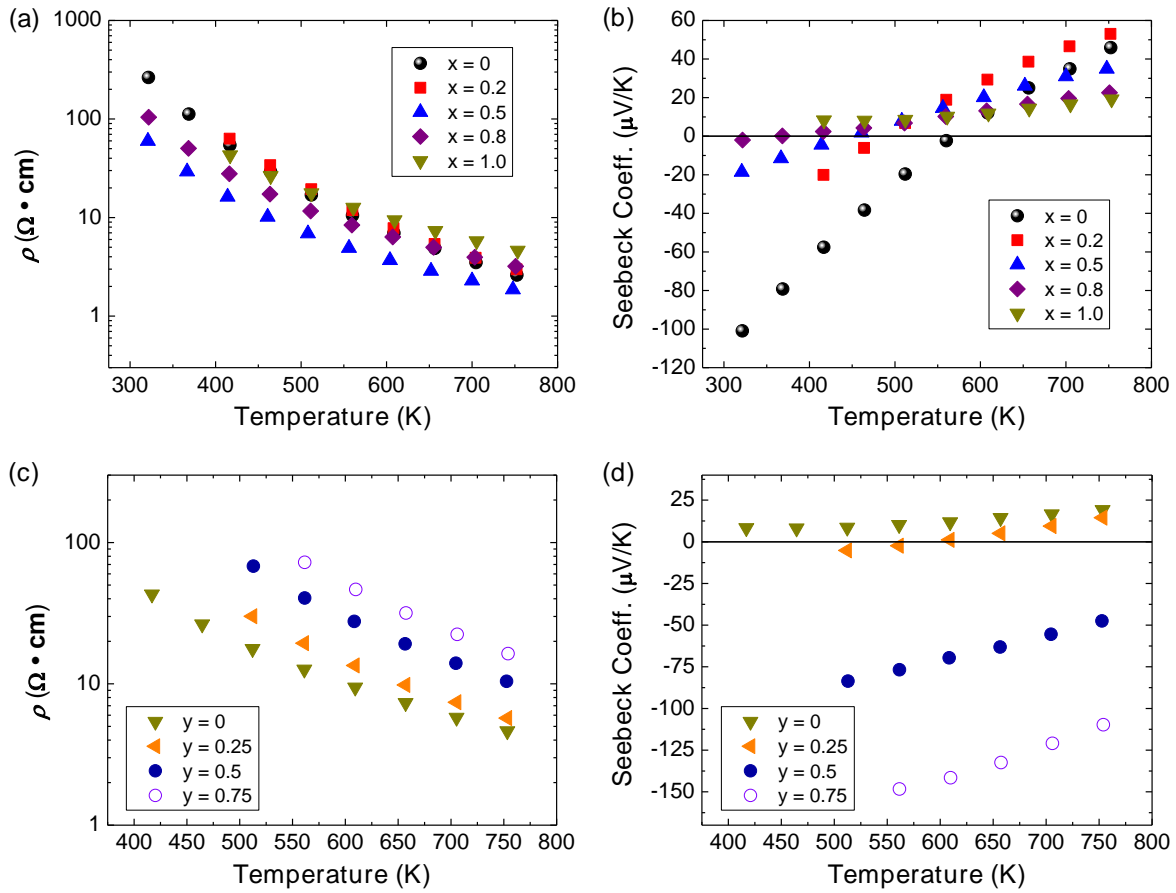


Figure 3.9. High temperature resistivity (ρ) and Seebeck coefficient plots for (a,b) $\text{Ba}_{2-x}\text{La}_x\text{InIrO}_6$ ($x = 0-1.0$) and (c,d) $\text{BaLaIn}_{1-y}\text{Ca}_y\text{IrO}_6$ ($y = 0-0.75$).

Table 3.2. Calculated band gaps for $\text{Ba}_{2-x}\text{La}_x\text{InIrO}_6$ and $\text{BaLaIn}_{1-y}\text{Ca}_y\text{IrO}_6$.

$\text{Ba}_{2-x}\text{La}_x\text{InIrO}_6$		$\text{BaLaIn}_{1-y}\text{Ca}_y\text{IrO}_6$	
x	E_g (eV)	y	E_g (eV)
0	0.450(11)	0	0.356(3)
0.2	0.496(7)	0.25	0.456(4)
0.5	0.335(3)	0.5	0.516(5)
0.8	0.336(3)	0.75	0.563(6)
1.0	0.356(3)		

The Seebeck behavior (Figure 3.9) for $\text{Ba}_{2-x}\text{La}_x\text{InIrO}_6$ is similar to that seen in the $\text{Ba}_2\text{In}_{2-x}\text{Ir}_x\text{O}_{5+\delta}$, in which a negative to positive sign change occurs, suggesting that both hole and electron charge carriers are present and their relative dominance is temperature dependent. As the La content increases and the Ir is reduced from 5+ to 4+, this transition is suppressed and the system eventually becomes p-type throughout the temperature range at $x = 1$. Unlike the resistivity data, there is no dramatic change around $x = 0.5$, suggesting the crystal structure has limited influence on the behavior. The data for $\text{BaLaIn}_{1-y}\text{Ca}_y\text{IrO}_6$ shows p-type character initially, but transitions to n-type when $y > 0.25$, indicating that the electrons take over as the dominant charge carrier. Increasing the Ca content further caused the Seebeck behavior to grow more negative and increasingly temperature dependent.

3.3.2 Magnetism

The magnetization as a function of temperature, $M(T)$, was measured for all samples of both systems in a field, H , of 0.1 T. No non-linearity in $M(H)$ was observed, meaning the susceptibility, $\chi(T)$, can be expressed as M/H . After subtraction of the core diamagnetic component, a positive constant representing the Van Vleck susceptibility was subtracted from $\chi(T)$ to obtain a linear $1/\chi(T)$, from which an effective moment, μ_{eff} , was obtained using a least-squares fit in the region 100–300 K. These data are plotted in Figure 3.10 as $\mu(T)_{\text{eff}} = \chi(T)T \cdot 3k_B/N_A\mu_B^2$, and the near constant values above 100 K demonstrate the validity of the effective moment approximation. The data below 60 K for $x = 0.8$ and 1.0 are consistent with the onset of ferromagnetic correlations, while below 20 K, antiferromagnetic correlations dominate.

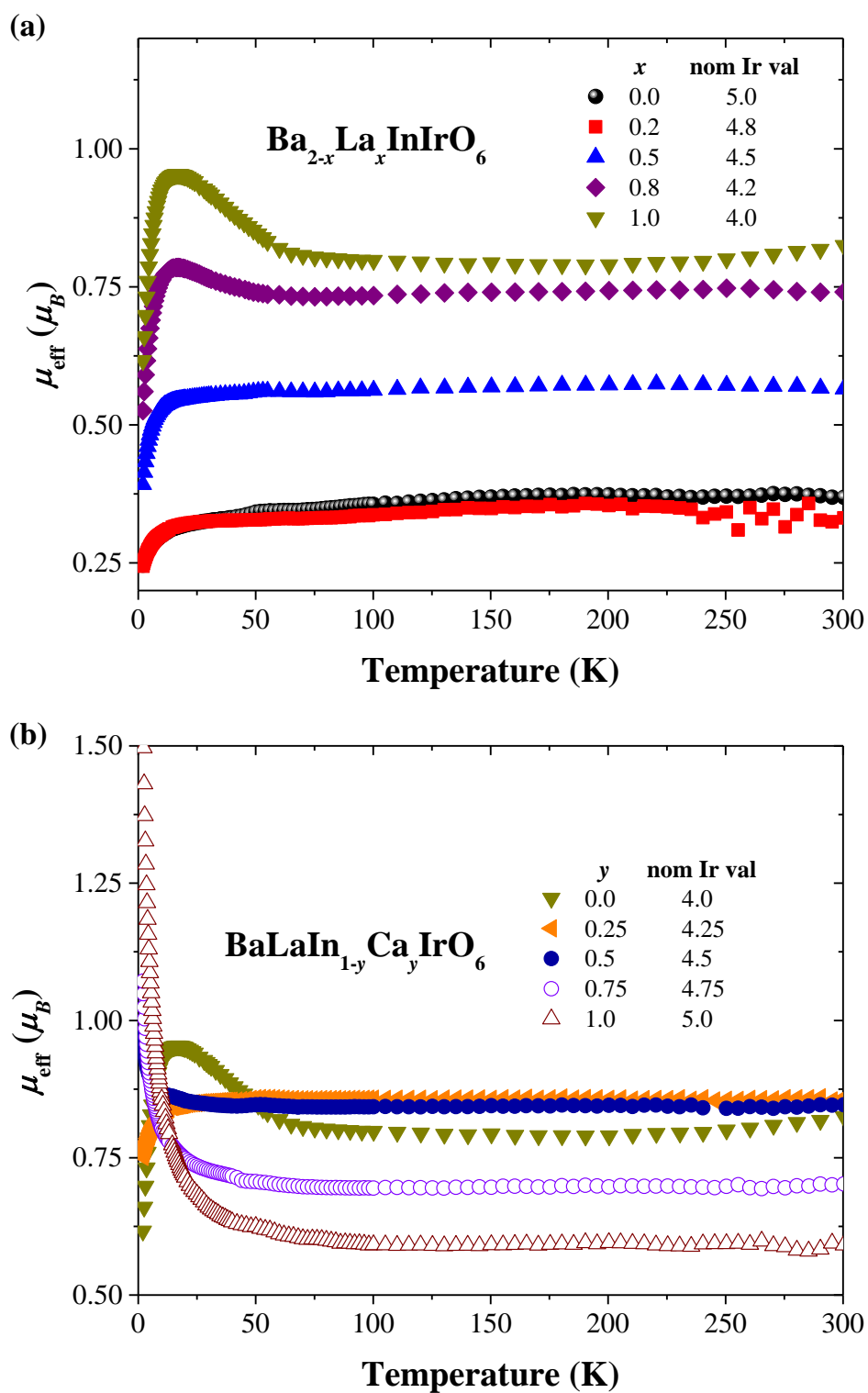


Figure 3.10. $\mu(T)_{\text{eff}}$ plots for (a) $\text{Ba}_{2-x}\text{La}_x\text{InIrO}_6$ and (b) $\text{BaLaIn}_{1-y}\text{Ca}_y\text{IrO}_6$. The temperature independence of the data above 100 K suggests Curie-Weiss behavior.

The ferromagnetic correlations in both systems are suppressed as Ir(IV) is oxidized to Ir(V) while the antiferromagnetic correlations in $\text{Ba}_{2-x}\text{La}_x\text{InIrO}_6$ are persistent even at the lowest La concentrations. Thus, the low temperature behavior is suggestive of antiferromagnetic nearest-neighbor interactions, and ferromagnetic next nearest-neighbor interactions, the latter of which only appear with high concentrations of Ir(IV). In $\text{BaLaIn}_{1-y}\text{Ca}_y\text{IrO}_6$, these cooperative correlations are suppressed much faster with Ir oxidation than in $\text{Ba}_{2-x}\text{La}_x\text{InIrO}_6$. This can be attributed to the increasing isolation of the IrO_6 octahedra leading to fewer Ir-O-Ir superexchanges. In Figure 3.10a are shown $\mu(T)_{\text{eff}}$ data for $\text{Ba}_{2-x}\text{La}_x\text{InIrO}_6$, with $0 \leq x \leq 1.0$ and we see that μ_{eff} ranges from $0.38 \mu_B$ for $x = 0$ (nominal Ir(V) ox. state) to $0.81 \mu_B$ for $x = 1.0$ (nominal Ir(IV) ox. state). In Figure 3.10b are shown $\mu(T)_{\text{eff}}$ data for $\text{BaLaIn}_{1-y}\text{Ca}_y\text{IrO}_6$ for $0 \leq y \leq 1.0$ and we see similar values of $\mu(T)_{\text{eff}}$ for $T > 100$ K. In Figure 3.11 is shown the fit value of μ_{eff} vs. the nominal Ir oxidation state state for both compound series. We see that, even for nominal oxidation state near 4.0, both compound series exhibit μ_{eff} values significantly less than the value $1.73 \mu_B$ expected for an $s = 1/2$ free spin. With increasing oxidation state, the moment decreases even further.

As mentioned earlier, values of μ_{eff} much less than the nominal values are not uncommon in iridates and have been observed in SrIrO_3 ($0.117 \mu_B$) [49], 5M BaIrO_3 ($0.215 \mu_B$) [50], 6M BaIrO_3 ($0.276 \mu_B$) [27], 9M BaIrO_3 ($0.13 \mu_B$) [2], Sr_2IrO_4 ($0.33\text{--}0.50 \mu_B$) [25,51], Ba_2IrO_4 ($0.18 \mu_B$) [52], $\text{Ba}_3\text{ZnIr}_2\text{O}_9$ ($0.26 \mu_B$) [13], $\text{Ba}_3\text{TiIr}_2\text{O}_9$ ($0.28 \mu_B$) [13], $\text{Ba}_3\text{CeIr}_2\text{O}_9$ ($0.31 \mu_B$) [53], $\text{Y}_2\text{Ir}_2\text{O}_7$ ($0.54 \mu_B$) [54], $\text{Sr}_3\text{Ir}_2\text{O}_7$ ($0.69 \mu_B$) [26], and $\text{Sr}_2\text{TiIrO}_6$ ($0.699 \mu_B$) [23]. Among these compounds, resistivity has been measured for SrIrO_3 , all above mentioned polymorphs of BaIrO_3 , Sr_2IrO_4 , Ba_2IrO_4 , $\text{Y}_2\text{Ir}_2\text{O}_7$ and $\text{Sr}_3\text{Ir}_2\text{O}_7$ and each exhibits either metallic (SrIrO_3 , 5M

and 6M BaIrO₃), small gap semiconducting (9M BaIrO₃, Sr₂IrO₄, Ba₂IrO₄) or variable range hopping behavior (Y₂Ir₂O₇). Indeed, for the systems studied here, we observe small gap semiconducting behavior for temperatures above 300K, where the moments are well-developed. It is also worth noting that the Seebeck effect data in the same temperature region, do not resemble that expected for medium-size bandgap semiconductor (0.5–1.0 eV). These results indicate that in the present systems, like several of the small- μ_{eff} compounds listed above, the delocalization of Ir valence electrons is responsible for moment reduction.

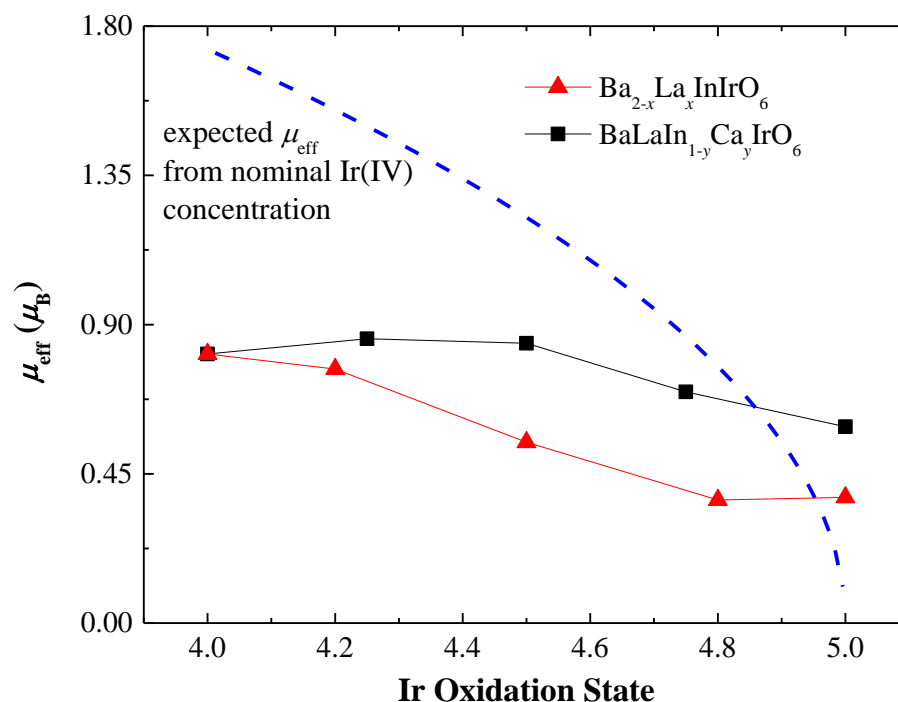


Figure 3.11. A plot of μ_{eff} as a function of Ir oxidation state for $\text{Ba}_{2-x}\text{La}_x\text{InIrO}_6$ (triangles) and $\text{BaLaIn}_{1-y}\text{Ca}_y\text{IrO}_6$ (squares). The dashed line is the trend the expected μ_{eff} values should follow when considering spin-orbit coupling effects.

It should be noted that sizeable effective moments of 0.38 and 0.59 μ_B are observed for BaInIrO_6 and BaLaCaIrO_6 , respectively, both of which should have a formal oxidation state

corresponding to Ir(V) which should be non-magnetic. Other examples of non-zero μ_{eff} values for Ir(V) have been reported in literature [1,23,55–57]. These were attributed to either the weakening of SOC interactions through structural distortion or the presence of a small amount of Ir(IV) due to oxygen vacancies, which are common in perovskites. It is also a possibility that BaInIrO_6 and BaLaCaIrO_6 possess a small amount of Ir(VI) due to the presence of electropositive ions (i.e. Ba^{2+} and Ca^{2+}) which are known to stabilize higher Ir oxidation states [23,29,58].

3.4 Conclusions

The $\text{Ba}_{2-x}\text{La}_x\text{InIrO}_6$ ($x = 0-1$) solid solution was found to transition from the 6M polytype structure to a disordered distorted perovskite structure with the $Pbnm$ space group. Based on our neutron diffraction refinements, BaLaInIrO_6 showed little tendency toward B -site ordering and the octahedra tilted along all three axes with the Glazer tilt scheme $a^-a^-c^+$. The $\text{BaLaIn}_{1-y}\text{Ca}_y\text{IrO}_6$ ($y = 0-1$) system retained a perovskite structure throughout the entire series, transitioning gradually from a disordered and orthorhombically-distorted form to an ordered cubic form. Both systems were found to be semiconducting with transitions in the dominant charge carrier. The resistivity of the $\text{Ba}_{2-x}\text{La}_x\text{InIrO}_6$ series was observed to increase with increasing La content and was largely affected by the structure transition, characterized by a large drop in the band gap at $x = 0.5$. There was not an abrupt change observed in the Seebeck behavior. The gradual n-type to p-type transition with temperature was suppressed with increased Ir(IV) concentration. For the $\text{BaLaIn}_{1-y}\text{Ca}_y\text{IrO}_6$ series, increasing the Ir(V) concentration via Ca substitution was found to both increase the resistivity as well as cause the

electrons to become the dominant charge carriers. The increasing resistivity is likely caused by the greater separation of the Ir ions due to ordering on the *B*-site. Curie-Weiss behavior was observed above 100 K in magnetic susceptibility data for both $\text{Ba}_{2-x}\text{La}_x\text{InIrO}_6$ and $\text{BaLaIn}_{1-y}\text{Ca}_y\text{IrO}_6$. For both systems, the trends in the μ_{eff} values going from Ir(IV) to Ir(V) did not correlate well with the predicted nominal values. In both series, the μ_{eff} values for compounds with Ir oxidation state closer to 4 tended to be too low, whereas those with oxidation state close to 5 tended to be too high. Other iridates similar to this work's compounds, where Ir(IV) is the only magnetic ion and μ_{eff} is much lower than predicted, were also found to be quite conductive suggesting the lower values are caused by electron delocalization.

3.5 Methods and Materials

Black polycrystalline samples were prepared by mixing and grinding stoichiometric amounts of BaCO_3 (Cerac, 99.9%), La_2O_3 (Stanford Materials, 99.999%), IrO_2 , CaCO_3 (Mallinckrodt, 99.8%) and In_2O_3 (Stanford Materials, 99.99%) using an agate mortar and pestle. The carbonates and La_2O_3 were dried overnight at 120 °C and 850 °C, respectively. IrO_2 was obtained by decomposing IrCl_3 (Alfa Aesar, 99.9%) at 750 °C under air flow for 12 h. The samples were then pelletized and sintered at 1200 °C for 36 h with intermittent grinding.

Initial XRD characterization of the samples was performed using a Rigaku Miniflex II diffractometer with Cu $K\alpha$ radiation and a graphite monochromator. Single-crystal Si sample holders were used to maximize peak intensity and aid detection of minor impurities in the XRD patterns. A fixed-time scan was employed with collection parameters of a 2θ range of 10-70° with a step size of 0.02° and a dwell time of 2.0 s. Lattice parameters for all samples were

extracted using the Le Bail method [59] on the GSAS software with EXPGUI user interface [60,61]. Room-temperature (298 K) time-of-flight neutron diffraction data for BaLaInIrO₆ were collected at Oak Ridge National Laboratory on the POWGEN (BL-11A) beam line using center wavelength of 1.33 Å. Approximately 1 g of the sample was loaded into a 6 mm vanadium sample can and data was collected over about 3 h. Structure refinement was performed using the Rietveld method [62] on the GSAS software with EXPGUI user interface [60,61]. Crystal structures were generated using the VESTA software [63]. Seebeck and resistivity measurements were performed at high temperatures (300–800 K) on an ULVAC-RIKO ZEM 3 under a static helium atmosphere. Low-temperature (5–300 K) magnetization measurements were obtained using a Quantum Design MPMS.

3.6 References

- [1] G. Cao, T.F. Qi, L. Li, J. Terzic, S.J. Yuan, L.E. DeLong, G. Murthy, R.K. Kaul, Novel Magnetism of Ir⁵⁺ (*5d*⁴) Ions in the Double Perovskite Sr₂YIrO₆, *Phys. Rev. Lett.* 112 (2014) 56402. doi:10.1103/PhysRevLett.112.056402.
- [2] G. Cao, J.E. Crow, R.P. Guertin, P.F. Henning, C.C. Homes, M. Strongin, D.N. Basov, E. Lochner, Charge density wave formation accompanying ferromagnetic ordering in quasi-one-dimensional BaIrO₃, *Solid State Commun.* 113 (2000) 657–662.
- [3] J. Chaloupka, G. Jackeli, G. Khaliullin, Zigzag Magnetic Order in the Iridium Oxide Na₂IrO₃, *Phys. Rev. Lett.* 110 (2013) 97204. doi:10.1103/PhysRevLett.110.097204.
- [4] D. Pesin, L. Balents, Mott physics and band topology in materials with strong spin-orbit interaction, *Nat. Phys.* 6 (2010) 376–381. doi:10.1038/nphys1606.
- [5] H.-M. Guo, M. Franz, Three-Dimensional Topological Insulators on the Pyrochlore Lattice, *Phys. Rev. Lett.* 103 (2009) 206805. doi:10.1103/PhysRevLett.103.206805.
- [6] J.-M. Carter, V.V. Shankar, M.A. Zeb, H.-Y. Kee, Semimetal and Topological Insulator in Perovskite Iridates, *Phys. Rev. B.* 85 (2012) 115105. doi:10.1103/PhysRevB.85.115105.
- [7] A.V. Powell, J.G. Gore, P.D. Battle, The magnetic properties of iridium in mixed-metal oxides, *J. Alloys Compd.* 201 (1993) 73–84. doi:10.1016/0925-8388(93)90864-J.

- [8] S. Vasala, M. Karppinen, $A_2B'B''O_6$ perovskites: A review, *Prog. Solid State Chem.* 43 (2015) 1–36. doi:10.1016/j.progsolidstchem.2014.08.001.
- [9] D. Harada, M. Wakeshima, Y. Hinatsu, The Structure and Magnetic Properties of New Iridium (IV) Perovskites Sr_2LnIrO_6 ($Ln=Ce, Tb$), *J. Solid State Chem.* 145 (1999) 356–360. doi:10.1006/jssc.1999.8223.
- [10] S.J. Mugavero, M.D. Smith, H.-C. zur Loye, The crystal growth and magnetic properties of Ln_2LiIrO_6 ($Ln=La, Pr, Nd, Sm, Eu$), *J. Solid State Chem.* 178 (2005) 200–206. doi:10.1016/j.jssc.2004.10.033.
- [11] L. Bufaiçal, L. Mendonça Ferreira, R. Lora-Serrano, O. Agüero, I. Torriani, E. Granado, P.G. Pagliuso, A. Caytuero, E. Baggio-Saitovich, Physical properties of disordered double-perovskite $Ca_{2-x}La_xFeIrO_6$, *J. Appl. Phys.* 103 (2008) 07F716. doi:10.1063/1.2830719.
- [12] I. Thumm, U. Treiber, S. Kemmler-Sack, Über Sauerstoffperowskite mit fünf- und vierwertigem Iridium Verbindungen vom Typ $Ba_2B^{3+}Ir^{5+}O_6$ und $Ba_3B^{3+}Ir^{4,5+}_2O_9$, *J. Solid State Chem.* 35 (1980) 156–166. doi:10.1016/0022-4596(80)90488-0.
- [13] T. Sakamoto, Y. Doi, Y. Hinatsu, Crystal structures and magnetic properties of 6H-perovskite-type oxides $Ba_3MIr_2O_9$ ($M=Mg, Ca, Sc, Ti, Zn, Sr, Zr, Cd$ and In), *J. Solid State Chem.* 179 (2006) 2595–2601. doi:10.1016/j.jssc.2006.04.055.
- [14] R.C. Byrne, C.W. Moeller, Magnetic interactions of ruthenium, rhodium, and iridium in the hexagonal barium titanate structure, *J. Solid State Chem.* 2 (1970) 228–235. doi:10.1016/0022-4596(70)90075-7.
- [15] M.A. Subramanian, G. Aravamudan, G. V. Subba Rao, Oxide pyrochlores - A review, *Prog. Solid State Chem.* 15 (1983) 55–143. doi:10.1016/0079-6786(83)90001-8.
- [16] S.M. Disseler, C. Dhital, A. Amato, S.R. Giblin, C. De La Cruz, S.D. Wilson, M.J. Graf, Magnetic order in the pyrochlore iridates $A_2Ir_2O_7$ ($A = Y, Yb$), *Phys. Rev. B - Condens. Matter Mater. Phys.* 86 (2012) 1–8. doi:10.1103/PhysRevB.86.014428.
- [17] J.M. Longo, P.M. Raccach, J.B. Goodenough, $Pb_2M_2O_{7-x}$ ($M = Ru, Ir, Re$) — Preparation and properties of oxygen deficient pyrochlores, *Mater. Res. Bull.* 4 (1969) 191–202. doi:10.1016/0025-5408(69)90056-7.
- [18] S.M. Disseler, S.R. Giblin, C. Dhital, K.C. Lukas, S.D. Wilson, M.J. Graf, Magnetization and Hall effect studies on the pyrochlore iridate $Nd_2Ir_2O_7$, *Phys. Rev. B - Condens. Matter Mater. Phys.* 87 (2013) 1–5. doi:10.1103/PhysRevB.87.060403.
- [19] B.F. Phelan, J. Krizan, W. Xie, Q. Gibson, R.J. Cava, New material for probing spin-orbit coupling in iridates, *Phys. Rev. B - Condens. Matter Mater. Phys.* 91 (2015) 1–6. doi:10.1103/PhysRevB.91.155117.
- [20] Y. Singh, S. Manni, J. Reuther, T. Berlijn, R. Thomale, W. Ku, S. Trebst, P. Gegenwart, Relevance of the Heisenberg-Kitaev model for the honeycomb lattice iridates A_2IrO_3 , *Phys. Rev. Lett.* 108 (2012) 1–5. doi:10.1103/PhysRevLett.108.127203.
- [21] C. Cosio-Castaneda, P. de la Mora, F. Morales, R. Escudero, G. Tavizon, Magnetic

- behavior of the $\text{Bi}_{2-y}\text{Sr}_y\text{Ir}_2\text{O}_7$ pyrochlore solid solution, *J. Solid State Chem.* 200 (2013) 49–53. doi:10.1016/j.jssc.2013.01.009.
- [22] N. Segal, J.F. Vente, T.S. Bush, P.D. Battle, Structural and magnetic properties of $\text{Sr}_{4-x}\text{M}_x\text{IrO}_6$ ($\text{M} = \text{Ca}, \text{Zn}, \text{Cd}, \text{Li}, \text{Na}$), *J. Mater. Chem.* 6 (1996) 395–401. doi:10.1039/JM9960600395.
- [23] M.A. Laguna-Marco, P. Kayser, J.A. Alonso, M.J. Martínez-Lope, M. van Veenendaal, Y. Choi, D. Haskel, Electronic structure, local magnetism, and spin-orbit effects of Ir(IV)-, Ir(V)-, and Ir(VI)-based compounds, *Phys. Rev. B.* 91 (2015) 214433. doi:10.1103/PhysRevB.91.214433.
- [24] I. Terasaki, S. Ito, T. Igarashi, S. Asai, H. Taniguchi, R. Okazaki, Y. Yasui, K. Kobayashi, R. Kumai, H. Nakao, Y. Murakami, Novel Charge Ordering in the Trimer Iridium Oxide BaIrO_3 , *Crystals.* 6 (2016) 27. doi:10.3390/cryst6030027.
- [25] G. Cao, J. Bolivar, S. McCall, J. Crow, R. Guertin, Weak ferromagnetism, metal-to-nonmetal transition, and negative differential resistivity in single-crystal Sr_2IrO_4 , *Phys. Rev. B.* 57 (1998) R11039–R11042. doi:10.1103/PhysRevB.57.R11039.
- [26] G. Cao, Y. Xin, C.S. Alexander, J.E. Crow, P. Schlottmann, M.K. Crawford, R.L. Harlow, W. Marshall, Anomalous magnetic and transport behavior in the magnetic insulator $\text{Sr}_3\text{Ir}_2\text{O}_7$, *Phys. Rev. B.* 66 (2002) 214412. doi:10.1103/PhysRevB.66.214412.
- [27] J. Zhao, L. Yang, Y. Yu, F. Li, R. Yu, C. Jin, Structural and physical properties of the 6M BaIrO_3 : a new metallic iridate synthesized under high pressure, *Inorg. Chem.* 48 (2009) 4290–4. doi:10.1021/ic801707m.
- [28] I.I. Mazin, S. Manni, K. Foyevtsova, H.O. Jeschke, P. Gegenwart, R. Valentí, Origin of the insulating state in honeycomb iridates and rhodates, *Phys. Rev. B - Condens. Matter Mater. Phys.* 88 (2013) 1–6. doi:10.1103/PhysRevB.88.035115.
- [29] J. Flynn, J. Li, A.W. Sleight, A.P. Ramirez, M.A. Subramanian, Structure and Properties of Ir-Containing Oxides with Large Spin–Orbit Coupling: $\text{Ba}_2\text{In}_{2-x}\text{Ir}_x\text{O}_{5+\delta}$, *Inorg. Chem.* 55 (2016) 2748–2754. doi:10.1021/acs.inorgchem.5b02501.
- [30] G. Demazeau, D.-Y. Jung, J.-P. Sanchez, E. Colineau, A. Blaise, L. Fournes, Iridium(VI) stabilized in a perovskite-type lattice: $\text{Ba}_2\text{CaIrO}_6$, *Solid State Commun.* 85 (1993) 479–484. doi:10.1016/0038-1098(93)90004-7.
- [31] D.-Y. Jung, P. Gravereau, G. Demazeau, Stabilization of six-coordinated iridium(VI) in a perovskite oxygen lattice $\text{Ba}_2\text{M}\text{IrO}_6$ ($\text{M} = \text{Ca}, \text{Sr}$), *Eur. J. Solid State Inorg. Chem.* 30 (1993) 1025–1037.
- [32] R. Hoppe, K. Claes, Über oxoiridate: zur kenntnis von KIrO_3 , *J. Less Common Met.* 43 (1975) 129–142. doi:10.1016/0022-5088(75)90132-0.
- [33] A.W. Sleight, New ternary oxides of Re, Os, Ir and Pt with cubic crystal structures, *Mater. Res. Bull.* 9 (1974) 1177–1184. doi:10.1016/0025-5408(74)90035-X.
- [34] A.V. Powell, P.D. Battle, The electronic properties of non-stoichiometric barium iridate, $\text{BaIrO}_{3-\delta}$, *J. Alloys Compd.* 191 (1993) 313–318. doi:10.1016/0925-8388(93)90085-2.

- [35] A. Talanov, W.A. Phelan, Z.A. Kelly, M.A. Siegler, T.M. McQueen, Control of the iridium oxidation state in the hollandite iridate solid solution $K_{1-x}Ir_4O_8$, *Inorg. Chem.* 53 (2014) 4500–4507. doi:10.1021/ic5001667.
- [36] C. Cosio-Castaneda, G. Tavizon, A. Baeza, P.D. La Mora, R. Escudero, Structure and magnetic properties of the weak ferromagnet $Sr_{2-x}La_xIrO_4$, *J. Phys. Condens. Matter.* 19 (2007) 446210. doi:10.1088/0953-8984/19/44/446210.
- [37] C.D. Ling, B.J. Kennedy, Q. Zhou, J.R. Spencer, M. Avdeev, Synthesis, structures, and phase transitions of barium bismuth iridium oxide perovskites Ba_2BiIrO_6 and $Ba_3BiIr_2O_9$, *J. Solid State Chem.* 183 (2010) 727–735. doi:10.1016/j.jssc.2010.01.017.
- [38] Y. Doi, Y. Hinatsu, Y. Shimojo, Y. Ishii, Crystal Structure and Magnetic Properties of 6H-Perovskite $Ba_3NdRu_2O_9$, *J. Solid State Chem.* 161 (2001) 113–120. doi:10.1006/jssc.2001.9296.
- [39] A.M. Glazer, The classification of tilted octahedra in perovskites, *Acta Crystallogr. Sect. B Struct. Crystallogr. Cryst. Chem.* 28 (1972) 3384–3392. doi:10.1107/S0567740872007976.
- [40] S. Sasaki, C.T. Prewitt, R.C. Liebermann, The crystal structure of $CaGeO_3$ perovskite and the crystal chemistry of the $GdFeO_3$ -type perovskites, *Am. Mineral.* 68 (1983) 1189–1198.
- [41] R.H. Buttner, E.N. Maslen, Electron difference density and structural parameters in $CaTiO_3$, *Acta Crystallogr. Sect. B Struct. Sci.* 48 (1992) 644–649. doi:10.1107/S0108768192004592.
- [42] M. Marezio, J.P. Remeika, P.D. Dernier, The crystal chemistry of the rare earth orthoferrites, *Acta Crystallogr. Sect. B Struct. Crystallogr. Cryst. Chem.* 26 (1970) 2008–2022. doi:10.1107/S0567740870005319.
- [43] G. Baud, M. Capestan, Sur de nouvelles perovskites ternaires contenant du rhenium pentavalent, *Comptes Rendus Hebd. Des Seances l'Academie Des Sci. Ser. C.* 267 (1968) 314–317.
- [44] K. Ouchetto, F. Archaimbault, A. Pineau, J. Choisnet, Chemical and structural characterization of a new barium ceroplatinate: Ba_2CePtO_6 a double perovskite mixed oxide, *J. Mater. Sci. Lett.* 10 (1991) 1277–1279. doi:10.1007/BF00720945.
- [45] U. Amador, C.J.D. Hetherington, E. Moran, M.A. Alario-Franco, Ba_2PrPtO_6 : A novel double perovskite, *J. Solid State Chem.* 96 (1992) 132–140. doi:10.1016/S0022-4596(05)80305-6.
- [46] R.D. Shannon, Revised effective ionic radii and systematic studies of interatomic distances in halides and chalcogenides, *Acta Crystallogr. Sect. A.* 32 (1976) 751–767. doi:10.1107/S0567739476001551.
- [47] A.W. Sleight, J.M. Longo, R. Ward, Compounds of Osmium and Rhenium with the Ordered Perovskite Structure, *Inorg. Chem.* 1 (1962) 245–250. doi:10.1021/ic50002a010.
- [48] W.T. Fu, D.J.W. IJdo, Re-examination of the structure of Ba_2MIrO_6 ($M=La, Y$): space

- group revised, *J. Alloys Compd.* 394 (2005) L5–L8.
doi:10.1016/j.jallcom.2004.10.049.
- [49] J.G. Zhao, L.X. Yang, Y. Yu, F.Y. Li, R.C. Yu, Z. Fang, L.C. Chen, C.Q. Jin, High-pressure synthesis of orthorhombic SrIrO₃ perovskite and its positive magnetoresistance, *J. Appl. Phys.* 103 (2008) 1–6. doi:10.1063/1.2908879.
- [50] J.G. Zhao, L.X. Yang, Y. Yu, F.Y. Li, R.C. Yu, C.Q. Jin, Physical properties of the 5M BaIrO₃: A new weak ferromagnetic iridate synthesized under high pressure, *Solid State Commun.* 150 (2010) 36–39. doi:10.1016/j.ssc.2009.10.012.
- [51] A.J. Gatimu, R. Berthelot, S. Muir, A.W. Sleight, M.A. Subramanian, Synthesis and characterization of Sr₂Ir_{1-x}M_xO₄ (M=Ti, Fe, Co) solid solutions, *J. Solid State Chem.* 190 (2012) 257–263. doi:10.1016/j.jssc.2012.02.058.
- [52] H. Okabe, M. Isobe, E. Takayama-Muromachi, A. Koda, S. Takeshita, M. Hiraishi, M. Miyazaki, R. Kadono, Y. Miyake, J. Akimitsu, Ba₂IrO₄: A spin-orbit Mott insulating quasi-two-dimensional antiferromagnet, *Phys. Rev. B.* 83 (2011) 155118. doi:10.1103/PhysRevB.83.155118.
- [53] Y. Doi, Y. Hinatsu, The structural and magnetic characterization of 6H-perovskite-type oxides Ba₃LnIr₂O₉ (Ln = Y, lanthanides), *J. Phys. Condens. Matter.* 16 (2004) 2849–2860. doi:10.1088/0953-8984/16/16/009.
- [54] H. Liu, W. Tong, L. Ling, S. Zhang, R. Zhang, L. Zhang, L. Pi, C. Zhang, Y. Zhang, Magnetic order, spin dynamics and transport properties of the pyrochlore iridate Y₂Ir₂O₇, *Solid State Commun.* 179 (2014) 1–5. doi:10.1016/j.ssc.2013.11.004.
- [55] T. Dey, A. Maljuk, D. V. Efremov, O. Kataeva, S. Gass, C.G.F. Blum, F. Steckel, D. Gruner, T. Ritschel, A.U.B. Wolter, J. Geck, C. Hess, K. Koepf, J. van den Brink, S. Wurmehl, B. Büchner, Ba₂YIrO₆: A cubic double perovskite material with Ir⁵⁺ ions, *Phys. Rev. B.* 93 (2016) 14434. doi:10.1103/PhysRevB.93.014434.
- [56] M. Bremholm, S.E. Dutton, P.W. Stephens, R.J. Cava, NaIrO₃ - A pentavalent post-perovskite, *J. Solid State Chem.* 184 (2011) 601–607. doi:10.1016/j.jssc.2011.01.028.
- [57] N. Segal, J.F. Vente, T.S. Bush, P.D. Battle, Structural and magnetic properties of Sr_{4-x}M_xIrO₆ (M = Ca, Zn, Cd, Li, Na), *J. Mater. Chem.* 6 (1996) 395–401. doi:10.1039/JM9960600395.
- [58] D.-Y. Jung, G. Demazeau, J. Etourneau, M.A. Subramanian, Preparation and characterization of new perovskites containing Ir(VI) and Ir(V) [BaM_{0.50}Ir_{0.50}O_{2.75} and BaM_{0.25}Ir_{0.75}O₃ (M = Li or Na)], *Mater. Res. Bull.* 30 (1995) 113–123. doi:10.1016/0025-5408(94)00115-4.
- [59] A. Le Bail, Whole powder pattern decomposition methods and applications: A retrospection, *Powder Diffr.* 20 (2005) 316–326. doi:10.1154/1.2135315.
- [60] A.C. Larson, R.B. Von Dreele, General Structure Analysis System (GSAS), Los Alamos Natl. Lab. Rep. LAUR 86-74 (1994).
- [61] B.H. Toby, EXPGUI, a graphical user interface for GSAS, *J. Appl. Crystallogr.* 34 (2001) 210–213. doi:10.1107/S0021889801002242.

- [62] H.M. Rietveld, A profile refinement method for nuclear and magnetic structures, *J. Appl. Crystallogr.* 2 (1969) 65–71. doi:10.1107/S0021889869006558.
- [63] K. Momma, F. Izumi, VESTA 3 for three-dimensional visualization of crystal, volumetric and morphology data, *J. Appl. Crystallogr.* 44 (2011) 1272–1276. doi:10.1107/S0021889811038970.

Chapter 4: Structure Determination and Magnetic Characterization of $A_{1+x}Rh_{2-x}O_4$ ($A^{2+} = \text{Co, Ni, Cu}$) Spinel

Abstract

Three members of the spinel family $A_{1+x}Rh_{2-x}O_4$ ($A^{2+} = \text{Co, Ni, Cu}$) were prepared and their structures characterized using X-ray and neutron diffraction and CoRh_2O_4 and CuRh_2O_4 was successfully prepared stoichiometrically while attempts to prepare NiRh_2O_4 resulted in a spinel phase with a large unreacted Rh_2O_3 impurity. Instead, a pure spinel phase was obtained by substituting a small amount of Ni for Rh resulting in the novel composition $\text{Ni}_{1.25}\text{Rh}_{1.75}\text{O}_4$. CoRh_2O_4 was found to have a normal cubic spinel structure ($Fd\bar{3}m$) whereas CuRh_2O_4 and $\text{Ni}_{1.25}\text{Rh}_{1.75}\text{O}_4$ crystallized in tetragonally distorted spinel structures ($I4_1/amd$) due to Jahn-Teller effects. The magnetic behavior of each spinel was also characterized using magnetic susceptibility measurements. Antiferromagnetic behavior was observed in $\chi(T)$ data for CoRh_2O_4 ($T_N = 24.9(1)$ K, $\mu_{\text{eff}} = 4.42(1)$ μ_B) and CuRh_2O_4 ($T_N = 24(1)$ K, $\mu_{\text{eff}} = 1.97(1)$ μ_B). Their magnetic structures were determined, for the first time, to be an antiferromagnetic *A*-type and an *ab*-plane helical structure, respectively. A divergence in ZFC and FC $\chi(T)$ data was observed for $\text{Ni}_{1.25}\text{Rh}_{1.75}\text{O}_4$ as well as a lack of long-range ordering in low temperature neutron data both of which suggest spin-glasslike behavior.

Publications based on this chapter:

- [1] L. Ge, J. Flynn, J.A.M. Paddison, M.B. Stone, S. Cadler, A.P. Ramirez, M.A. Subramanian, M. Mourigal, Spin order and dynamics in the perfect and distorted diamond-lattice Heisenberg antiferromagnets CoRh_2O_4 and CuRh_2O_4 . (In preparation)
- [2] J. Flynn, J. Li, M.A. Subramanian, The true composition of NiRh_2O_4 (In preparation)

4.1 Motivation for Study

The spinel family (AB_2X_4) is known for having many different properties and has been widely used as a host for interesting or unusual magnetic behavior. Due to the spatial arrangement of the A - and B -sites, spinels often display frustrated magnetic properties such as spin glasses or unusual magnetic structures [1–3]. For instance, CuIr_2S_4 has been reported to have spin glass magnetism [4] and behavior of FeSc_2S_4 has been described as somewhere between a spin-orbital liquid and an antiferromagnet [5–7]. The spinel structure is typically very rigid and is not as susceptible to distortion away from cubic symmetry or site vacancies compared to the perovskite structure. Nevertheless, there are a few reported examples of spinels that are tetragonally distorted due to Jahn-Teller effects such as $\text{MnCr}_{2-x}\text{Mn}_x\text{O}_4$ [8] and a couple $AB_2\text{O}_4$ families ($A^{2+} = \text{Ni}, \text{Cu}$; $B^{3+} = \text{Cr}, \text{Rh}$) [9–11]. Since Rh^{3+} is diamagnetic, the ARh_2O_4 spinel family are candidates for interesting magnetism as spinels with only A - A magnetic interactions are not very common.

This work aims to characterize and compare members ARh_2O_4 that have both Jahn-Teller active (Ni^{2+} , Cu^{2+}) and inactive (Co^{2+}) ions in the A site. Although all three of these compounds are known, little has been reported beyond basic structural and magnetic information. For instance, each member is reported to show antiferromagnetic character [11] but as NiRh_2O_4 and CuRh_2O_4 are tetragonally distorted, it is unknown what effect this distortion may have on the A - A interactions.

4.2 Structural Characterization

Rietveld refinements were performed for CoRh_2O_4 , CuRh_2O_4 , and $\text{Ni}_{1.25}\text{Rh}_{1.75}\text{O}_4$ using TOF neutron diffraction data. The refinement for CoRh_2O_4 (Figure 4.1) was done using the cubic spinel structure with space group $Fd\bar{3}m$ and structural parameters are summarized in Table 4.1. Asymmetric broadening on right side of every peak was observed likely caused by unrelieved thermal stress within the structure. This broadening was modeled by including a “strain phase” with the same symmetry as the main phase but with slightly smaller lattice parameters.

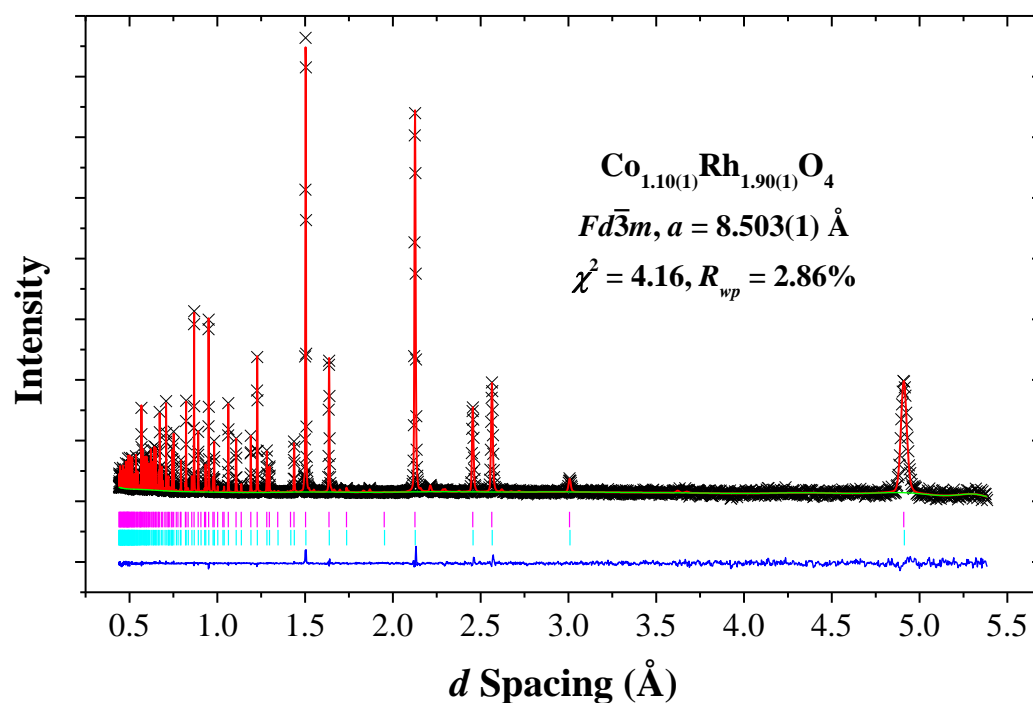


Figure 4.1. Time-of-flight neutron diffraction pattern for $\text{Co}(\text{Rh}_{1.90(1)}\text{Co}_{0.10(1)})\text{O}_4$ with calculated intensities (red) and difference (blue) and background (green) curves. The magenta tick marks indicate the allowed reflections for $Fd\bar{3}m$ and the teal tick marks indicate the “strain phase” used to model the asymmetric broadening.

The results of this work's CoRh_2O_4 refinement are consistent with previous reports [12,13] with two notable differences. First, the RhO_6 octahedra are less distorted in this work's structure compared to previous reports. This results in shortened Co–O bonds which leads to better bond-valence sums (BVS) [14] of 1.79 for Co and 3.05 for Rh than previously reported. Second, the refinement resulted in a small degree of site mixing with 5.0(6) % of Co on the B-site and formally, a refined chemical formula of $\text{Co}(\text{Rh}_{1.90(1)}\text{Co}_{0.10(1)})\text{O}_4$.

Table 4.1. Summarized crystallographic information $\text{CoRh}_{1.90(1)}\text{Co}_{0.10(1)}\text{O}_4$.

	Site	<i>x</i>	<i>y</i>	<i>z</i>	Occ.	U_{iso} (\AA^2)
Co	8 <i>a</i>	0	0	0	1.0	0.0021(2)
Rh/Co	16 <i>d</i>	5/8	5/8	5/8	0.95(1)/0.05(1)	0.0002(1)
O	32 <i>e</i>	0.2601(1)	0.2601(1)	0.2601(1)	1.0	0.0023(1)
Bond Distances (\AA)			Bond Angles ($^\circ$)			
Co–O	4×1.989(1)		O–Co–O	4×109.5(1)		
Rh–O	6×2.044(1)		O–Rh–O	3×85.10(1)		
			“	3×94.90(3)		

The Rh deficiency originates from the presence of a small Rh_2O_3 impurity phase. To maintain overall charge imbalance, either octahedral Co ions are 3+, i.e. $\text{Rh}(\text{III})_{1.9}\text{Co}(\text{III})_{0.1}$, or 5% of the Rh ions are 4+, i.e. $\text{Rh}(\text{III})_{1.8}\text{Rh}(\text{IV})_{0.1}\text{Co}(\text{II})_{0.1}$. One way to determine the oxidation states would be to compare the theoretical bond distances for each case to the values determined from the refinement; however, the average ionic radii on the B-site for the two extreme cases mentioned above are too similar (0.662 vs. 0.666 \AA) to favor one case over the other.

Although NiRh_2O_4 has been previously reported and characterized by XRD [15], our attempts to prepare it were unsuccessful as a significant amount of Rh_2O_3 remained unreacted.

Pure samples were obtained by instead substituting about 12.5% of the Rh for Ni resulting in a nominal formula of $\text{NiRh}_{1.75}\text{Ni}_{0.25}\text{O}_4$. The reason why preparing pure NiRh_2O_4 was so difficult is not immediately clear. The only other reported preparations of NiRh_2O_4 mention the use of carbonates in the solid state reactions [11,16]. Since carbonates tend to be more reactive than their counterparts, it's possible that the combination of NiO and Rh_2O_3 is not reactive enough to complete the reaction.

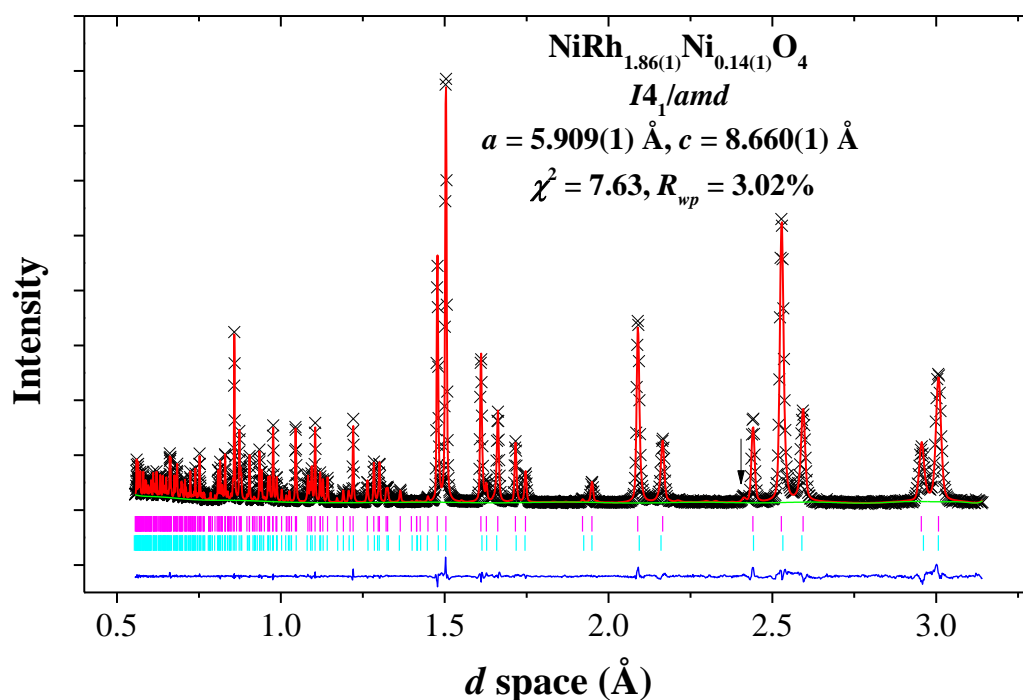


Figure 4.2. Time-of-flight neutron diffraction pattern for $\text{NiRh}_{1.86(1)}\text{Ni}_{0.14(1)}\text{O}_4$ with calculated intensities (red) and difference (blue) and background (green) curves. The magenta tick marks indicate the allowed reflections for $I4_1/amd$ and the teal tick marks indicate the “strain phase” used to model the asymmetric broadening.

NiRh_2O_4 crystallizes in a lower-symmetry structure compared to CoRh_2O_4 due to a Jahn-Teller distortion caused by the lifting of degeneracy in the Ni^{2+} t_2 orbitals [11,15,16]. Rietveld refinement of the diffraction data (Figure 4.2) gave refined formula of $\text{NiRh}_{1.86(1)}\text{Ni}_{0.14(1)}\text{O}_4$ and

a structure model comparable to NiRh₂O₄ [15] with $\bar{I}4_1/amd$ symmetry but slightly smaller lattice parameters. Other crystallographic data is summarized in Table 4.2. Asymmetric broadening was also observed in the neutron data but unlike CoRh₂O₄, the broadening appears sporadic, occurring on different sides of different peaks or, occasionally, not at all. Taking an approach similar to that used for CoRh₂O₄, this unusual broadening could be modeled using a less tetragonally distorted “strain phase”.

Table 4.2. Summarized crystallographic information for NiRh_{1.86(1)}Ni_{0.14(1)}O₄.

	Site	<i>x</i>	<i>y</i>	<i>z</i>	Occupancy	
Ni	4 <i>a</i>	0	3/4	1/8	1.0	
Rh/Ni	8 <i>d</i>	0	0	1/2	0.93(1)/0.07(1)	
O	16 <i>h</i>	0	0.0133(1)	0.2655(1)	1.0	
Anisotropic atomic displacement parameters (Å ²)						
	<i>U</i> ₁₁	<i>U</i> ₂₂	<i>U</i> ₃₃	<i>U</i> ₁₂	<i>U</i> ₁₃	<i>U</i> ₂₃
Ni	0.0061(2)	0.0061(2)	0.0041(3)	0.0	0.0	0.0
Rh/Ni	0.0027(4)	0.0016(4)	0.0011(3)	0.0	0.0	0.0008(2)
O	0.0054(3)	0.0041(3)	0.0042(3)	0.0	0.0	-0.0005(2)
Bond Distances (Å)			Bond Angles (°)			
Ni–O	4×1.975(1)		O–Ni–O	2×104.0(1)		
Equatorial B–O	4×2.039(1)		“	2×112.3(1)		
Axial B–O	2×2.033(1)		O–B–O	3×87.17(5)		
			“	3×92.83(5)		

Similar to CoRh_{1.90}Co_{0.10}O₄, the Ni substitution into the B-site causes a charge imbalance that must be compensated. Since there two oxidation states for Ni (2+/3+) and Rh (3+/4+) that are typically observed in oxides, this can be done in a few ways assuming only

Ni(II) is found in the tetrahedral sites. The Ni oxidation state can be all 2+, $\text{Ni}(\text{Ni}(\text{II})_{0.07}\text{Rh}(\text{IV})_{0.07}\text{Rh}(\text{III})_{0.84})_2\text{O}_4$, or all 3+, $\text{Ni}(\text{Ni}(\text{III})_{0.07}\text{Rh}(\text{III})_{0.93})_2\text{O}_4$. The average ionic radii on the *B*-site for the extreme cases are 0.664 Å and 0.662 Å, respectively. Since these values are smaller than the Rh^{3+} radius (0.665 Å), it is not possible to reliably establish which oxidation states are present using lattice parameters or bond distances.

The tetrahedral sites are elongated along the *c* axis with O-Ni-O bond angles of 104.0(1)° and 112.3(1)° due to Jahn-Teller distortion produced by the degeneracy in the Ni t_2 orbitals. The tetrahedral distortion displaces the oxygens that, in turn, leads to distortion of the octahedral sites. The BVS values for Ni, Rh, and O sites were calculated to be 1.68, 3.10, and 1.96, respectively. The composition was refined to be $\text{NiRh}_{1.86(1)}\text{Ni}_{0.14(1)}\text{O}_4$ which indicates that not all of the nominal Ni content was successfully substituted into the octahedral sites. Variable temperature neutron diffraction data for $\text{Ni}_{1.25}\text{Rh}_{1.75}\text{O}_4$ show that the tetragonally distorted spinel structure is present down to 4 K. Refinements of the lattice parameters shows the distortion increases as temperature decreases and the structure contracts, indicated by the increased separation of *a* and *c* (Figure 4.3).

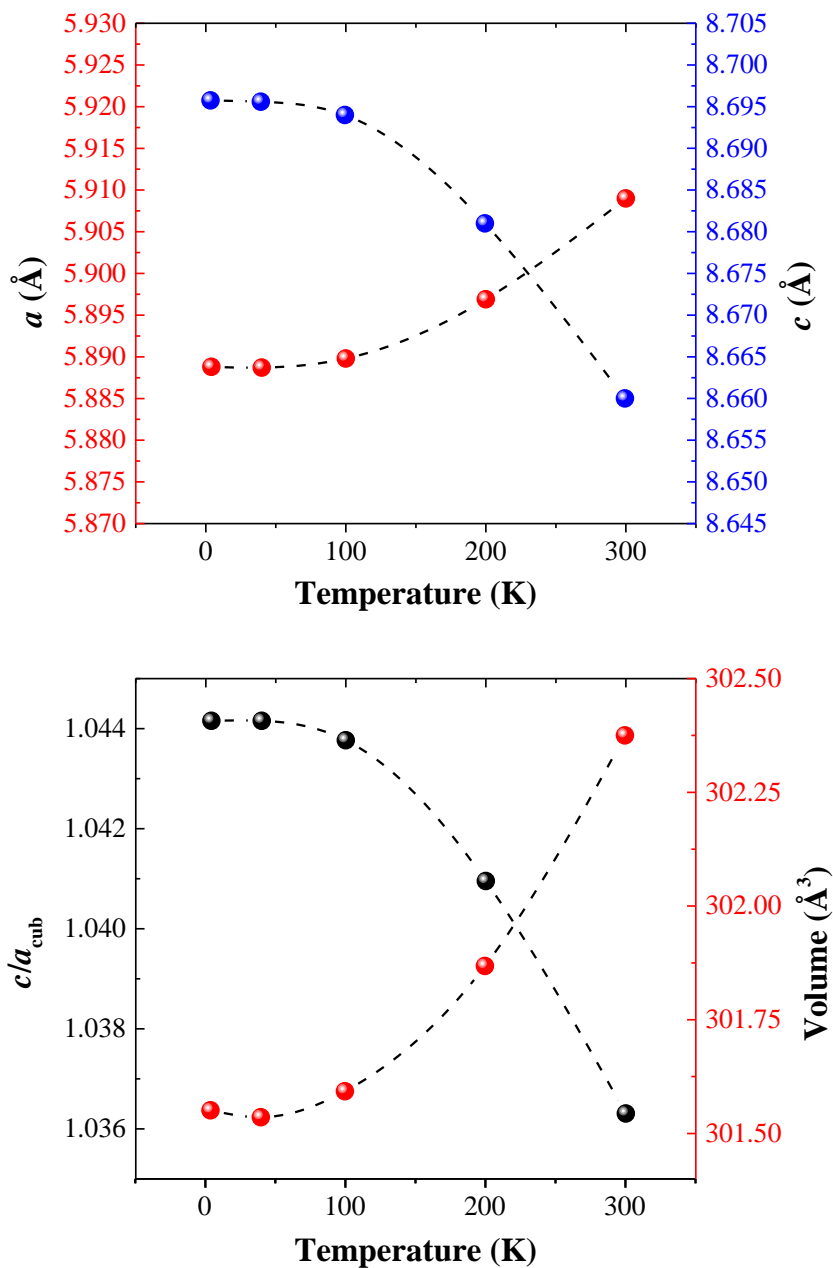


Figure 4.3. Temperature dependent plots of (top) the lattice parameters a and c and (bottom) the c/a_{cub} ratio and volume for $\text{Ni}_{1.25}\text{Rh}_{1.75}\text{O}_4$.

The structure of CuRh_2O_4 is similar to NiRh_2O_4 in that it is distorted by a Jahn-Teller effect but in the opposite direction. The Jahn-Teller effects in NiRh_2O_4 result in cooperative elongation of the unit cell along the c axis with respect to the cubic spinel unit cell whereas the

distortion seen in CuRh_2O_4 is compression. The CuRh_2O_4 structure has been described by both x-ray [12,17] and neutron diffraction [18] as a tetragonally distorted spinel at room temperature but transitions to the cubic form at 600 °C [18]. There has been some debate over whether the correct room temperature space group is $I4_1/amd$ or $I\bar{4}2d$. The room temperature neutron diffraction pattern for our sample of CuRh_2O_4 is shown in Figure 4.4.

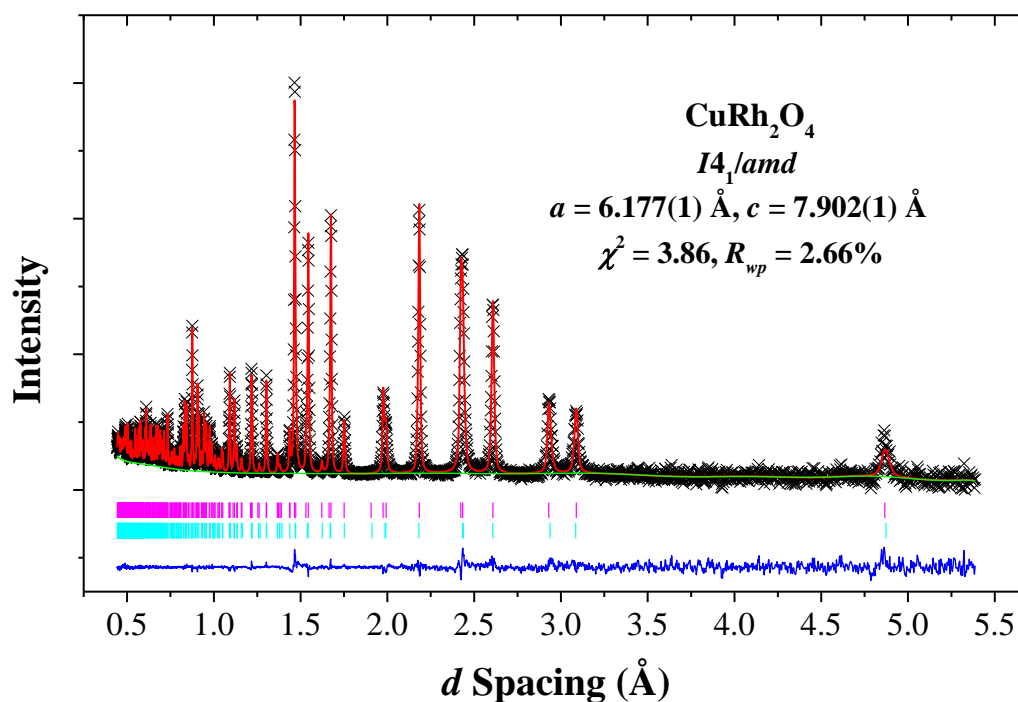


Figure 4.4. Time-of-flight neutron diffraction pattern for CuRh_2O_4 with calculated intensities (red) and difference (blue) and background (green) curves. The magenta tick marks indicate the allowed reflections for $I4_1/amd$ and the teal tick marks indicate the “strain phase” use to model the asymmetric broadening.

Based on the Rietveld refinement, it was concluded that the appropriate room-temperature space group is $I4_1/amd$, consistent with the most recent studies [10,18]. The refined atomic parameters are summarized in Table 4.3. Similar to CoRh_2O_4 and $\text{Ni}_{1.25}\text{Rh}_{1.75}\text{O}_4$,

asymmetric broadening was also observed in the neutron data for CuRh_2O_4 . The broadening was irregular similar to $\text{Ni}_{1.25}\text{Rh}_{1.75}\text{O}_4$ and could be modeled using a more tetragonally distorted “strain phase”.

Table 4.3. Summarized crystallographic information for CuRh_2O_4 .

	Site	x	y	z	Occupancy	$U_{\text{iso}} (\text{\AA}^2)$
Cu	$8e$	0	3/4	0.1368(3)	1.0	0.0017(2)
Rh	$8d$	0	0	1/2	1.0	0.0005(1)
O	$16h$	0	0.0334(1)	0.2430(1)	1.0	–
Anisotropic atomic displacement parameters (\AA^2)						
	U_{11}	U_{22}	U_{33}	U_{12}	U_{13}	U_{23}
O	0.0021(2)	0.0010(2)	0.0022(2)	0.0	0.0	-0.0002(1)
Bond Distances (\AA)			Bond Angles ($^\circ$)			
Cu–O	2×1.942(1)		O–Cu–O	2×128.8(2)		
“	2×2.029(1)		“	2×102.6(1)		
Equatorial Rh–O	4×2.044(1)		O–Rh–O	3×84.62(5)		
Axial Rh–O	2×2.042(1)		“	3×95.38(5)		

Unlike CoRh_2O_4 and $\text{Ni}_{1.25}\text{Rh}_{1.75}\text{O}_4$, no evidence for site mixing was observed indicating a stoichiometric formula. Bond valence sums of 3.05 for Rh, 1.97 for O and 1.79 for Cu, were found to be consistent with literature values [18]. The Rh octahedral are distorted with O-Rh-O bond angles of $95.38(4)^\circ$ and $84.62(5)^\circ$. In turn, the Cu tetrahedral are flattened with two distinct O-Cu-O bond angles of $128.8(2)^\circ$ and $102.6(1)^\circ$. The refined crystal structure also indicates Cu is displaced off of the ideal $4a$ site and instead randomly sits on the $8e$ site which is split along the c axis. This displacement is not observed in any reported structure for CuRh_2O_4 , however, fitting the above data with Cu on the ideal $4a$ site resulted in a largely

anisotropic thermal ellipsoid with a very high U_{33} value suggesting the Cu was not present on that site. Displacing the Cu to the $8e$ site, which is split along the c axis, resulted in a more spherical ellipsoid. The typical explanation for an ion to displace from the ideal site to compensate for being underbonded [19]. In this case, the displacement only improved the Cu BVS by 0.004 which is essentially negligible and makes the reason for the displacement unclear.

It is interesting to compare the three structures since CoRh_2O_4 is a cubic spinel while the other two are both tetragonally distorted but in opposite directions. Figure 4.5 illustrates the splitting caused on the t_2 and e orbitals by Jahn-Teller elongation and compression.

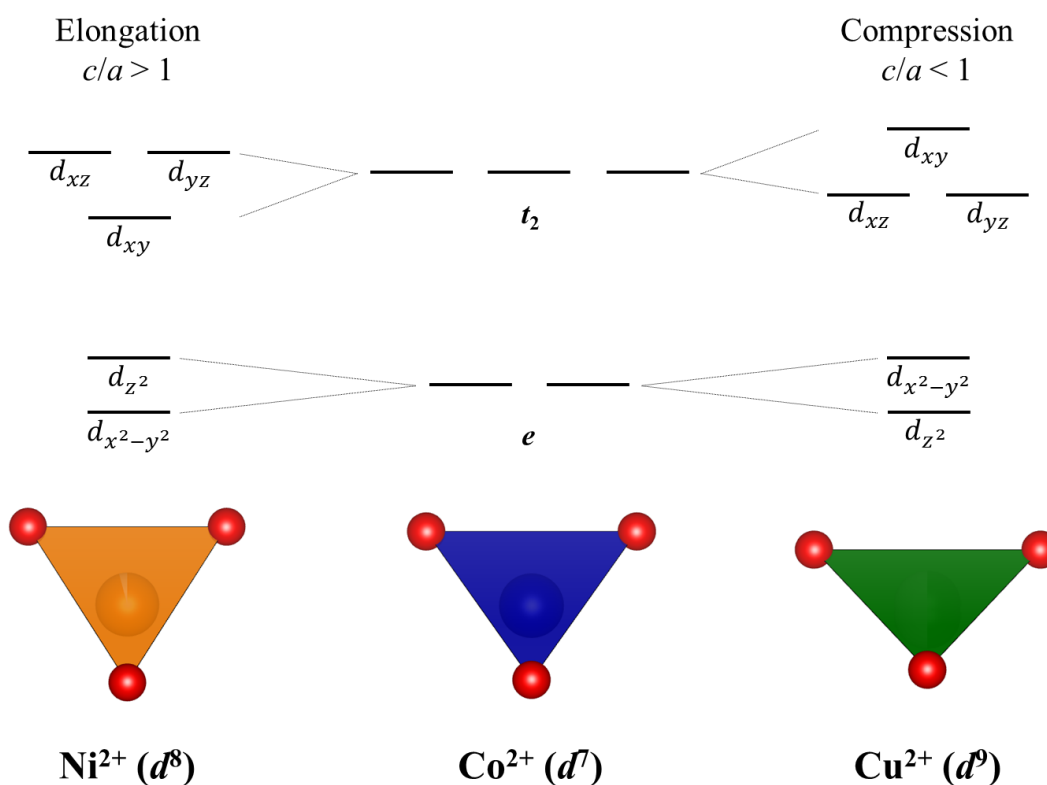


Figure 4.5. Orbital diagrams illustrating of the splitting of the t_2 and e orbitals (center) caused by Jahn-Teller elongation (left) and compression (right).

The compression brings the O ions closer to the xy plane causing the $d_{x^2-y^2}$ and d_{xy} orbitals to increase in energy while the rest of the orbitals decrease to compensate. Conversely, elongation moves the anions closer to the z axis which increases the energy of the d_{z^2} , d_{xz} and d_{yz} orbitals. The specific distortions in the Ni and Cu tetrahedra can be rationalized by examining the stabilization energy (SE) caused of the two distortions (shown in Figure 4.6). For Ni^{2+} , the elongation gives the best SE value of $-0.67\Delta_{\text{JT}}$, where Δ_{JT} is the Jahn-Teller splitting energy. Cu^{2+} , on the other hand, is best stabilized by compression which gives an SE value of $-0.67\Delta_{\text{JT}}$ as well.

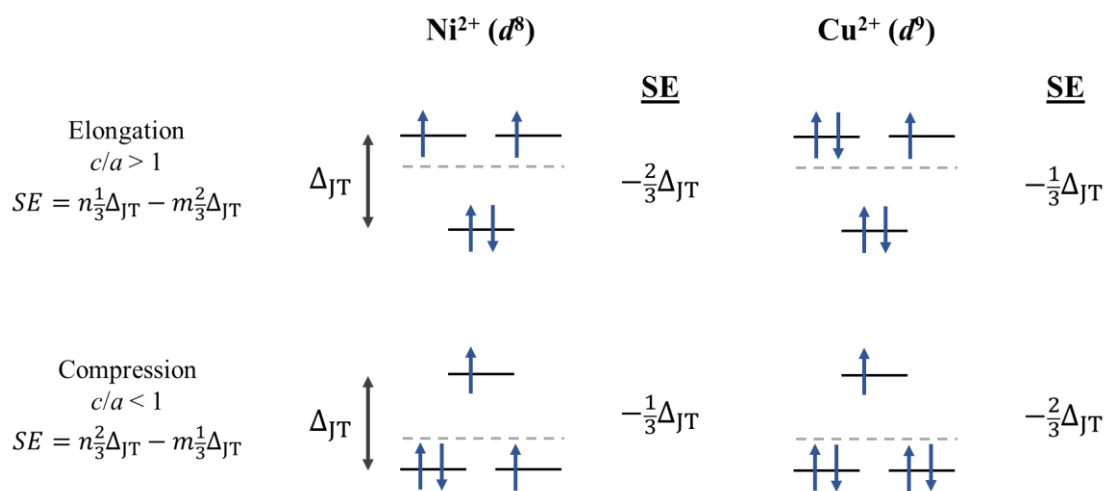


Figure 4.6. Schematic showing the different stabilization energies (SE) for Ni^{2+} and Cu^{2+} produced by Jahn-Teller compression and elongation. The values m and n are the number of electrons in the lower and upper orbitals, respectively. The grey dotted line represents the relative position of the unsplit t_2 orbitals.

4.3 Magnetic Characterization

4.3.1 *CoRh₂O₄*

The $1/\chi(T)$ data for CoRh_2O_4 (Figure 4.7) shows antiferromagnetic (AFM) behavior with a T_N of 25 K. Above 50 K, $1/\chi(T)$ is linear indicating Curie-Weiss behavior and fitting yields values of $4.43(1) \mu_B$ and $-34.4(1)$ K for the magnetic moment (μ_{eff}) and Weiss constant (θ), respectively. These results are consistent with previous studies on CoRh_2O_4 [11,20]. The magnetic moment is quite large compared to the theoretical spin-only value of $3.87 \mu_B$ for a tetrahedrally coordinated d^7 ion. This discrepancy is common in Co-containing oxides and is likely caused by an unquenched orbital contribution to the moment. The ratio $f = |\theta|/T_N$ can give an indication of how frustrated a magnetic system is. The further this ratio is from 1, the stronger the frustration is with $f > 10$ indicating a strongly frustrated system [21]. The f value calculated for CoRh_2O_4 is 1.4 suggesting a very low degree of frustration. Large peak intensity changes were observed in the neutron diffraction pattern for CoRh_2O_4 upon cooling from 40 K to 4 K and the development of new reflections forbidden by the nuclear space group symmetry (Figure 4.8). As indicated by the temperature-dependence of the integrated Bragg intensity (Figure 4.8 inset), these peaks were associated with the development of long-range magnetic order beginning at $T_N = 24.88(9)$ K, which correlates well with the behavior and value seen in the susceptibility data. The magnetic Bragg peaks were indexed to the magnetic space group $I4_1'/a'm'd$ which has a magnetic propagation vector $\mathbf{k} = (0, 0, 0)$ with respect to the conventional unit cell. Refinement of the diffraction data ($R_{\text{wp}} = 8.11\%$; $R_{\text{mag}} = 7.62\%$) yields an ordered magnetic moment of $3.11(5) \mu_B$, which is close to the expected value of $3.0 \mu_B$ for a spin-3/2 ion.

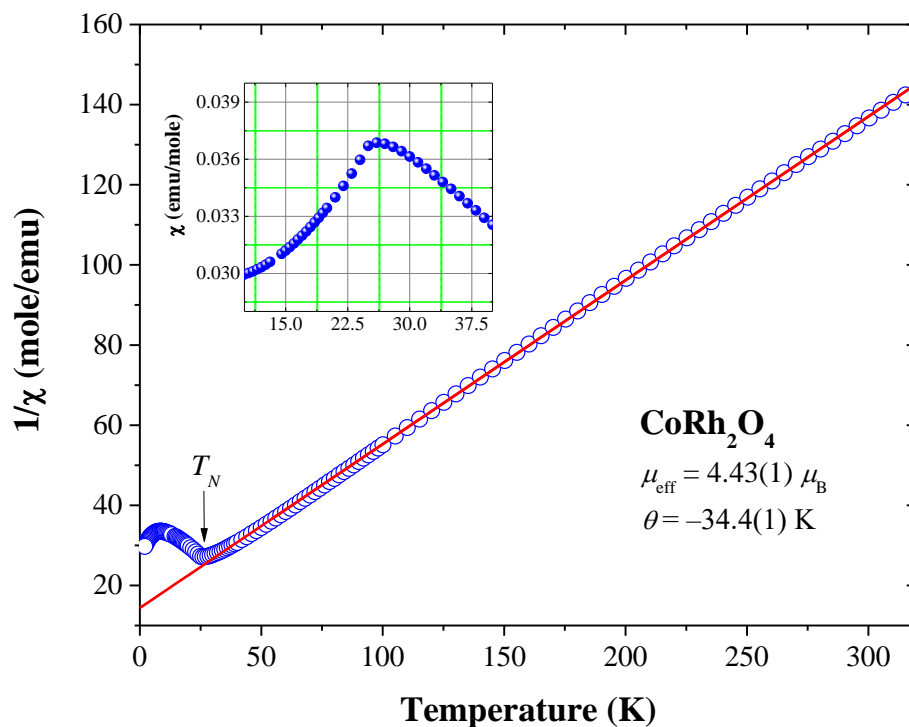


Figure 4.7. $1/\chi(T)$ plot for CoRh_2O_4 shows antiferromagnetic (AFM) behavior ($T_{\text{N}} = 25 \text{ K}$) with the red line showing the fit to the Curie-Weiss Law. Inset shows close-up view of the AFM transition.

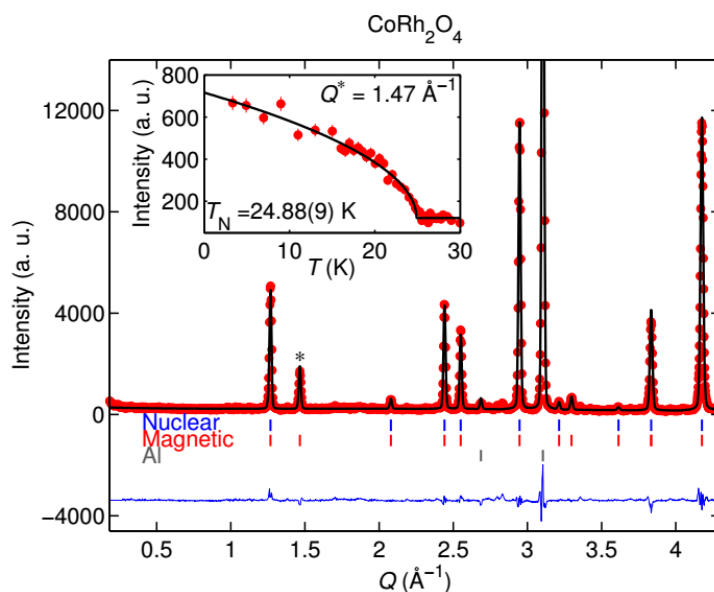


Figure 4.8. Rietveld refinement on CoRh_2O_4 powder neutron diffraction data collected at $T = 4 \text{ K}$. Contribution from nuclear peaks (blue ticks), magnetic peaks (red ticks) and Al can (gray ticks) are considered. The inset shows the temperature dependence of the second magnetic peak intensity (highlighted with asterisk).

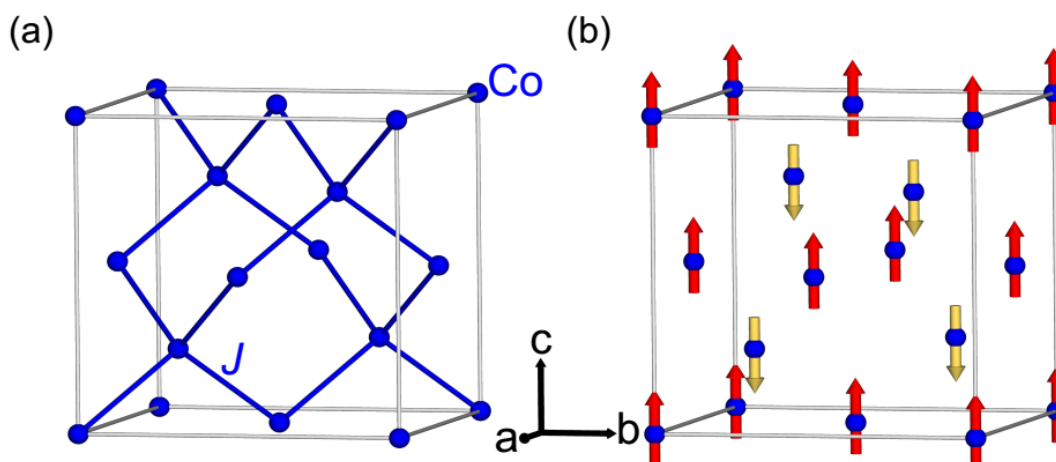


Figure 4.9. Unit cells displaying (a) the nearest neighbor interactions (J) and (b) the A-type antiferromagnetic magnetic structure (red and yellow arrows) of CoRh_2O_4 .

The magnetic structure (Figure 4.9b) is an A-type AFM structure where there are ferromagnetic intraplanar ordering with antiferromagnetic interplanar ordering. Other examples of oxides with this magnetic structure include many manganate perovskites [22–24] and Na_xCoO_2 layered structures [25,26]. The A-site exchange mechanism for a spinel was first introduced by Blasse [11] who proposed a *A-O-B-O-A* exchange interaction (Figure 4.10). He proposed that a direct *A-A* exchange or a traditional *A-O-A* superexchange were unlikely as the exchange distances required for those interactions in the spinel are too long. Blasse demonstrated that substituting Al for Rh in CoRh_2O_4 and decreasing the orbital overlap in the O-B-O interaction caused T_N to decrease indicating a weakening of the AFM interactions. This superexchange can explain the CoRh_2O_4 magnetic structure as shown in Figure 4.10. The empty $\text{Rh}^{3+} e_g$ orbitals allows for direct interaction between the O electrons which results in anti-aligned electron spins in Co.

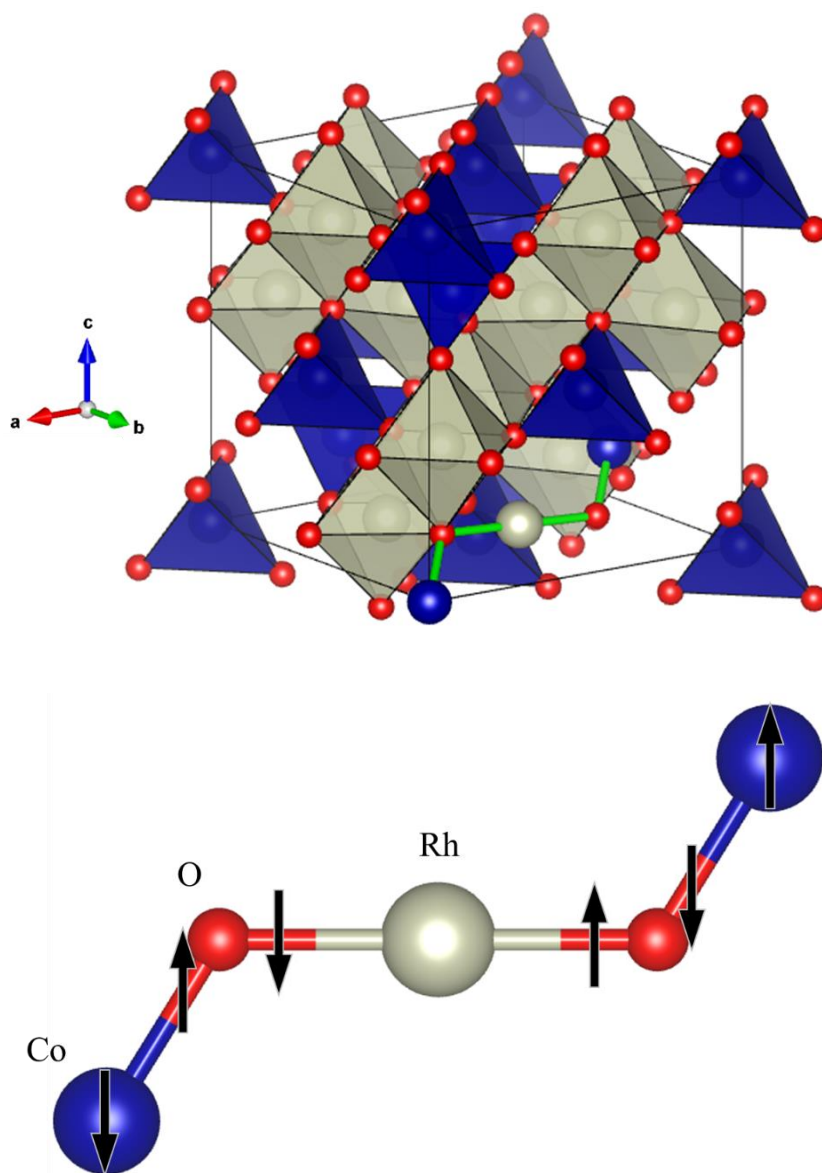


Figure 4.10. Schematics showing (top) the relative position of one Co-O-Rh-O-Co superexchange pathways (green lines) within CoRh₂O₄ and (bottom) illustrating how the superexchange results in AFM ordering.

4.3.2 Ni_{1.25}Rh_{1.75}O₄

The high temperature region of $1/\chi(T)$ for Ni_{1.25}Rh_{1.75}O₄ was slightly non-linear and was corrected for by subtracting a temperature-independent paramagnetism term (χ_0) from the

susceptibility. This method is common when dealing with magnetism for 4d and 5d transition metals (TMs) [27–32]. The χ_0 value used for $\text{Ni}_{1.25}\text{Rh}_{1.75}\text{O}_4$ was 1.5×10^{-3} emu/mol which is comparable to values reported for other rhodate compounds in literature. The $1/(\chi(T) - \chi_0)$ data (Figure 4.11) shows show paramagnetic behavior above 90 K and fitting gives μ_{eff} and θ values of $2.77(1) \mu_B/\text{f.u.}$ and $34.5(1)$ K, respectively.

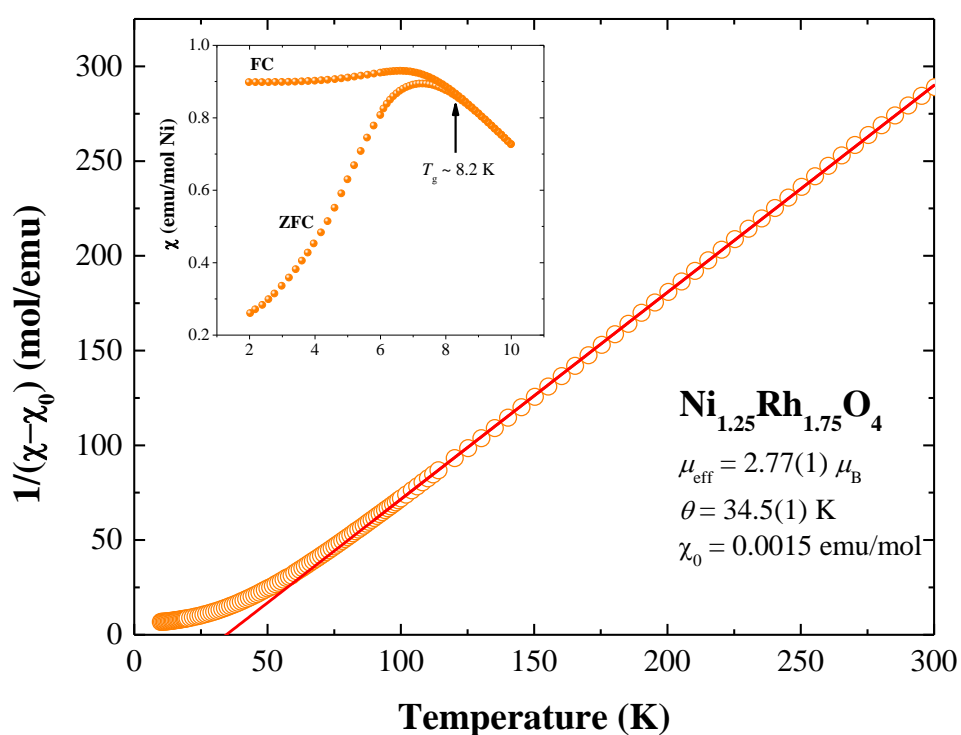


Figure 4.11. $1/(\chi(T) - \chi_0)$ plot for $\text{Ni}_{1.25}\text{Rh}_{1.75}\text{O}_4$ with the fit to Curie-Weiss behavior (red line) above 90 K. Upward deviation from CW below suggests AFM correlations. Inset shows close-up view reveals of large divergence between field-cooled (FC) and zero field-cooled (ZFC) data typical of spin-glass behavior. T_g is the spin-glass transition temperature.

As discussed above, the Ni substitution on B-site creates a charge imbalance that can be compensated via two possible mixtures of valence states: $\text{Ni(II)[Ni(III)}_{0.07}\text{Rh(III)}_{0.93}]_2\text{O}_4$ or $\text{Ni(II)[Ni(II)}_{0.07}\text{Rh(IV)}_{0.07}\text{Rh(III)}_{0.86}]_2\text{O}_4$. These creates a range of $2.97\text{--}3.19 \mu_B/\text{f.u.}$ for a

predicted theoretical spin-only moment which is slightly above the experimental μ_{eff} value of $2.77(1) \mu_B$. Below 90 K, $1/(\chi(T) - \chi_0)$ begins to deviate upward indicating the presence of AFM correlations which conflicts with the positive θ value that suggests ferromagnetic (FM) correlations. A possible explanation for the discrepancy is that the introduction of magnetic Ni ions on to *B*-site interrupts the Ni-O-Rh-O-Ni superexchange and creates a competition between AFM and FM interactions. Both Ni^{2+} and Ni^{3+} have occupied e_g orbitals. This adds an additional electron to the superexchange at the *B*-site and results in ferromagnetically aligned Ni ions on the *A*-site (Figure 4.12).

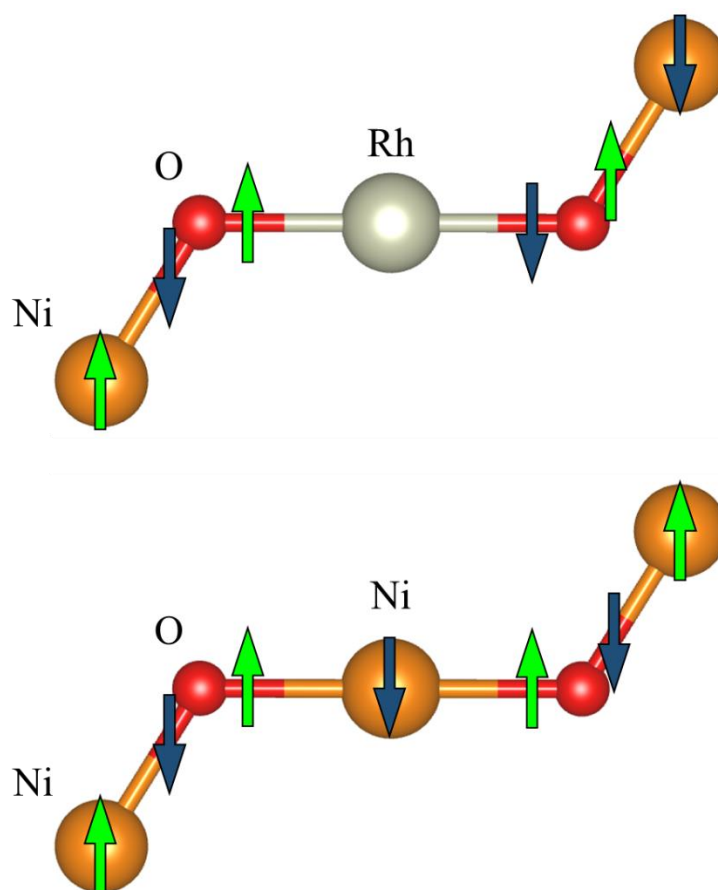


Figure 4.12. Superexchange mechanisms in $\text{Ni}_{1.25}\text{Rh}_{1.75}\text{O}_4$. Rh on the *B*-site allows for an antiferromagnetic *A-A* interaction between the Ni ions. Substituting Ni for Rh interrupts the exchange and results in ferromagnetic *A-A* and antiferromagnetic *A-B* interactions.

Examination of the region below 10 K shows what seems to be an AFM-like transition at ~ 7.5 K. Comparing the field-cooled (FC) and zero field-cooled (ZFC) data (Figure 4.11 inset) reveals a large divergence in $\chi(T)$ beginning at ~ 8.2 K. This feature is typically an indication of spin-glass behavior. Analysis of the low temperature neutron diffraction data (4–200 K) shows no observable changes in any of the peak intensities (Figure 4.13) signifying a lack of long-range magnetic ordering present down to 4 K. This observation, in conjunction with the divergence of the ZFC and FC $\chi(T)$ data, is strong evidence that $\text{Ni}_{1.25}\text{Rh}_{1.75}\text{O}_4$ is a spin-glass material. This behavior is likely caused by a combination of the Jahn-Teller distortion and the disruption of the superexchange by the presence of the magnetic Ni ions in the B site.

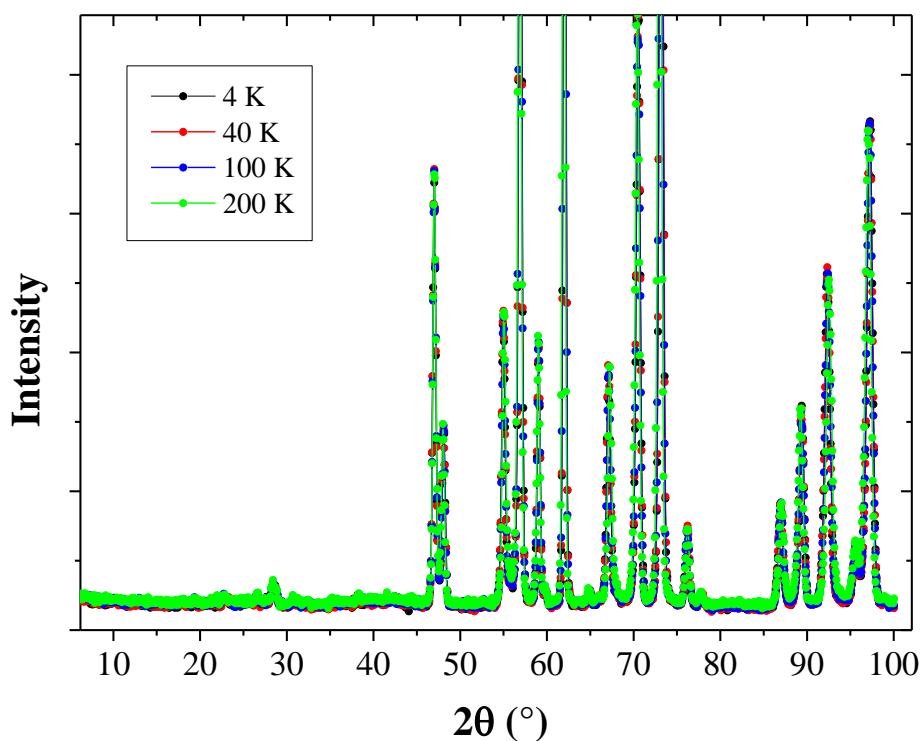


Figure 4.13. Variable temperature neutron diffraction data (4–200 K) for $\text{Ni}_{1.25}\text{Rh}_{1.75}\text{O}_4$. The lack of new peaks or intensity changes indicates there is no long-range magnetic ordering.

4.3.3 CuRh_2O_4

The examination of the $1/\chi(T)$ data for CuRh_2O_4 reveals AFM transition was observed at $T_N = 24.5$ K (Figure 4.14). Similar to $\text{Ni}_{1.25}\text{Rh}_{1.75}\text{O}_4$, a non-linear trend in the high temperature data was observed and corrected for using a χ_0 term of 3×10^{-4} emu/mol that is comparable to values reports in literature [32,33]. The CW modeling above ~ 140 K gave values of $1.94(1) \mu_B$ and $-108(1)$ K for μ_{eff} and θ , respectively. The μ_{eff} value is slightly above the theoretical spin-only moment of $1.73 \mu_B$ for $S = 1/2$ but compares well experimental values reported for CuRh_2O_4 in literature [11,32]. The moment is likely greater due to incompletely quenched orbital contribution similar to CoRh_2O_4 .

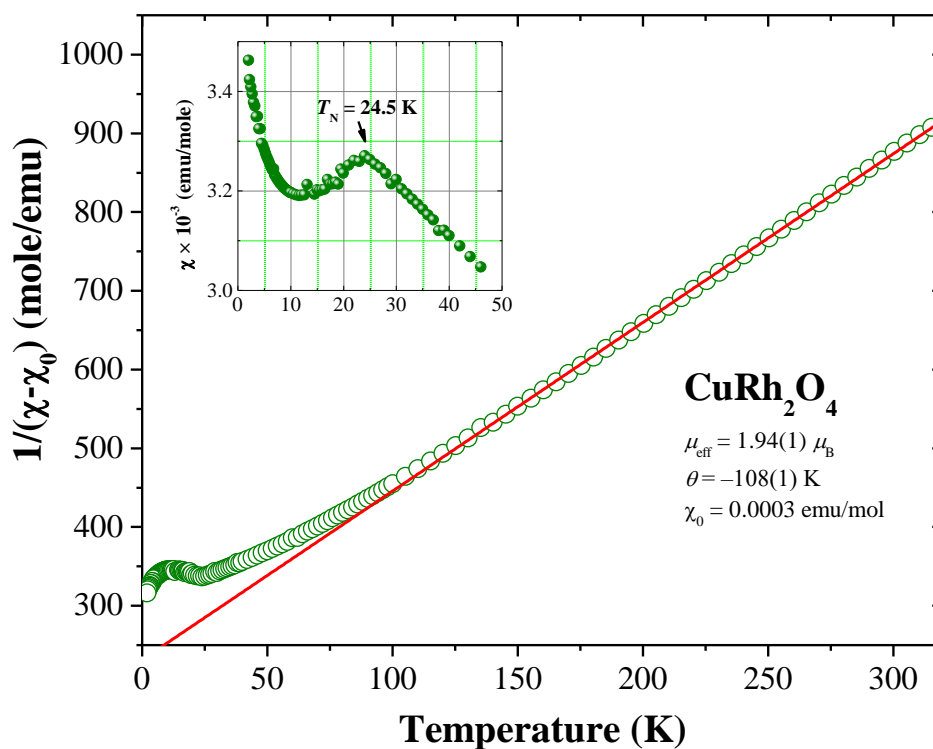


Figure 4.14. $1/(\chi(T) - \chi_0)$ plot for CuRh_2O_4 shows AFM behavior ($T_N = 24.5$ K) with the red line showing the fit to the Curie-Weiss Law. Inset shows close-up view of the AFM transition with an upward trend beginning at ~ 11 K.

The value obtained for θ is negative and correlates well with the observed AFM behavior; however, it is rather large compared to the value for T_N . Calculating f gives a value of 4.5 suggesting a moderate degree of frustration. Below 140 K, there is an upward deviation from the CW behavior similar to $\text{Ni}_{1.25}\text{Rh}_{1.75}\text{O}_4$ suggesting the beginning of AFM correlations. An upturn in the $\chi(T)$ data was observed below T_N beginning at ~ 12 K. Similar behavior is reported in literature but the cause is unclear. A possible explanation is the presence of impurity spins either within CuRh_2O_4 or as an impurity that was too dilute to be detected by X-ray or neutron diffraction.

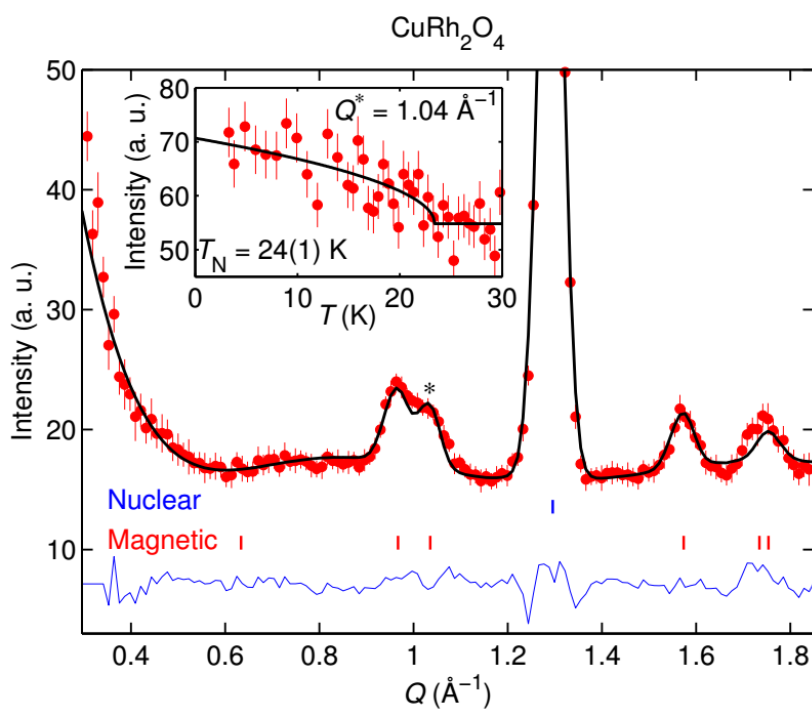


Figure 4.15. Rietveld refinement on CuRh_2O_4 powder neutron diffraction data at $T = 4$ K. Contribution from nuclear peaks (blue ticks) and magnetic peaks (red ticks) are considered. The inset shows the temperature dependence of the second magnetic peak intensity (highlighted with asterisk).

Low temperature neutron diffraction data reveal the emergence of new diffraction peaks upon cooling from 40 K to 4 K (Figure 4.15) that, like CoRh_2O_4 , are not allowed by the nuclear structure. The temperature dependence of the peak intensity (Figure 4.15 inset) suggests that these new peaks are associated with long-range AFM ordering with $T_N = 24(1)$ K which correlates well with the value seen in the $\chi(T)$ data. The magnetic peaks were indexed to the magnetic space group $I4_1221'$ and Rietveld refinements ($R_{\text{wp}} = 6.53\%$; $R_{\text{mag}} = 18.8\%$) revealed the magnetic structure to be an ab -helix type structure with $\mu_{\text{ord}} = 0.56(6) \mu_B$ (Figure 4.16b). The propagation vector was found to be $\mathbf{k} = (0, 0, 0.790(4))$ which signifies a 108° rotation of the magnetic moments within the ab plane as you move from layer to layer of Cu ions along the c axis.

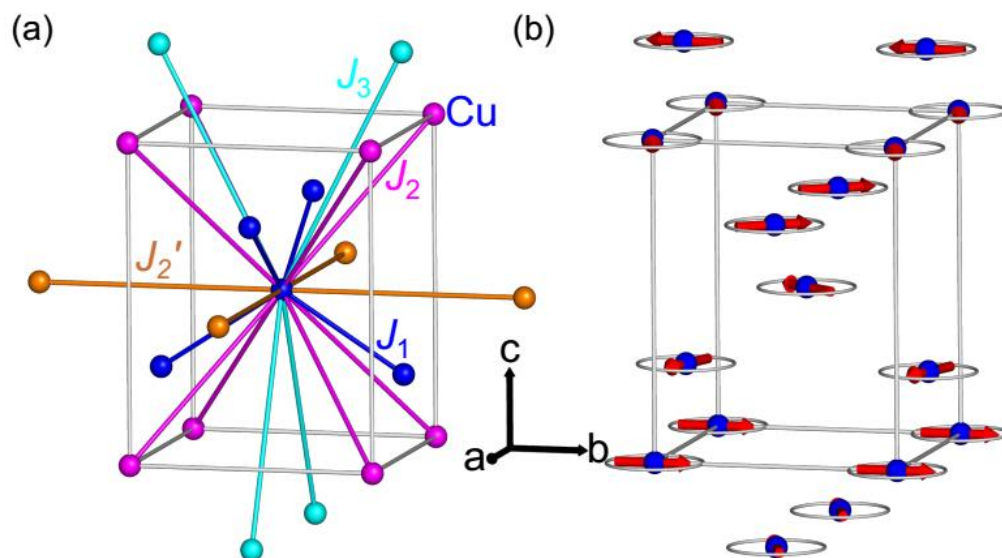


Figure 4.16. Unit cells displaying (a) the nearest neighbor interactions (J_n) with different colors to distinguish the different orders of neighbors and (b) the incommensurate helical magnetic structure (red arrows) of CuRh_2O_4 . The gray rings serve as a guide to the eye for the propagation and orientation of the magnetic moments.

Helical magnetic structures are somewhat uncommon but they are often seen in barium hexaferrites such as $\text{BaFe}_{12}\text{O}_{19}$ and $\text{Ba}_2\text{Mg}_2\text{Fe}_{12}\text{O}_{12}$ [34–36]. The divergence from the *A*-type magnetic structure seen in CoRh_2O_4 is undoubtedly linked to the compression of the tetrahedral site by the Jahn-Teller effect that changes the overlap between the Cu and O orbitals, disrupting the superexchange.

4.4 Conclusions

CoRh_2O_4 , CuRh_2O_4 and the novel composition $\text{Ni}_{1.25}\text{Rh}_{1.75}\text{O}_4$ were successfully prepared using standard solid state methods. X-ray and neutron diffraction refinements confirmed the reported cubic and tetragonal spinel structures for CoRh_2O_4 and CuRh_2O_4 while $\text{Ni}_{1.25}\text{Rh}_{1.75}\text{O}_4$ was observed to have a tetragonal spinel structure similar to NiRh_2O_4 . The distortions in both CuRh_2O_4 and $\text{Ni}_{1.25}\text{Rh}_{1.75}\text{O}_4$ are caused by Jahn-Teller effects though they are distorted in opposite directions due to differences in the filling of the t_2 orbitals. In CuRh_2O_4 , the Cu was found to sit on the $8e$ site rather than the ideal $4a$ site despite a negligible difference in the BVS. No site displacements were seen in CoRh_2O_4 and $\text{Ni}_{1.25}\text{Rh}_{1.75}\text{O}_4$.

Antiferromagnetic transitions were observed in both CoRh_2O_4 ($T_N = 24.9(1)$ K) and CuRh_2O_4 ($T_N = 24(1)$ K) and Curie-Weiss behavior in the high temperature region. The extracted μ_{eff} values for both compounds were larger ($4.43(1)$ and $1.94(1)$ μ_B , respectively) than their expected spin-only values (3.87 and 1.73 μ_B , respectively) due to an unquenched orbital contribution. The θ value for CuRh_2O_4 was found to be larger than T_N indicating there may be magnetic frustration present in the lattice. CoRh_2O_4 was determined, via low temperature neutron refinements, to have an *A*-type AFM structure, which agrees well with a

Co-O-Rh-O-Co superexchange mechanism. The low temperature data for CuRh_2O_4 gave an *ab*-plane helix magnetic structure. There is no reason Cu should not follow the same superexchange as in CoRh_2O_4 which suggests the differences in magnetic structure is linked to lattice compression from the Jahn-Teller effect. This distortion changes the bond angles of the CuO_4 tetrahedra, which will affect the overlap between Cu *d* and O *p* orbitals and disrupt the superexchange.

The magnetic behavior of $\text{Ni}_{1.25}\text{Rh}_{1.75}\text{O}_4$ is more complex compared to its Co and Cu analogs. Paramagnetic behavior was observed above 90 K and fitting the region gave μ_{eff} and θ values of $2.77(1) \mu_B/\text{f.u.}$ and $34.5(1) \text{ K}$, respectively. The magnetic moment is a bit lower than the range of spin-only values based on the possible mixture of Rh and Ni oxidation states. Below 90 K, antiferromagnetic correlations begin to dominate as indicated by deviation from Curie-Weiss behavior. Conversely, the positive value for θ suggests the presence of ferromagnetic interactions. A case for competing ferromagnetic and antiferromagnetic correlations can be made based on how the Ni substitution affects the Ni-O-Rh-O-Ni superexchange. A divergence in the ZFC and FC $\chi(T)$ data ($\sim 8.5 \text{ K}$) in addition to the lack of evidence for long-range ordering in our low temperature neutron diffraction studies indicates that $\text{Ni}_{1.25}\text{Rh}_{1.75}\text{O}_4$ is a spin-glass material.

4.5 Methods and Materials

Black, polycrystalline samples were prepared by intimately mixing and grinding stoichiometric amounts of CoCO_3 (Baker Adamson, 99.9%), CuO (Aldrich, 99.99%), NiO_2 (Baker Adamson, 99.9%) and Rh_2O_3 in an agate mortar. The Rh_2O_3 was obtained by

decomposing RhCl_3 (Johnson Matthey, 99.9%) at 850 °C for 12 h under air flow. For CoRh_2O_4 and CuRh_2O_4 , the samples were pelletized and sintered at 900-950 °C for 36 h (CuRh_2O_4) and 900-1000 °C for 36 h (CoRh_2O_4) with intermittent grinding. For $\text{Ni}_{1.25}\text{Rh}_{1.75}\text{O}_4$, samples were heated as loose powders at 1075 °C under O_2 flow for 48 h with intermittent grinding.

Initial (XRD) characterization of the samples was done on a Rigaku Miniflex II diffractometer using $\text{Cu K}\alpha$ radiation and a graphite monochromator. Single-crystal Si sample holder were used to maximize peak intensity and aid detection of minor impurities. A fixed time scan was used with collection parameters of a 2θ range of 10-70° with a step size of 0.02° and a dwell time of 2.0 s. Room-temperature (298 K) time-of-flight neutron diffraction data for all samples were collected at Oak Ridge National Laboratory on the POWGEN (BL-11A) beamline using center wavelength of 1.33 Å. Approximately 2 g of sample was loaded into 6 mm vanadium sample cans and data was collected over about 3 hours.

Structure refinement was performed using the Rietveld method [37] on the GSAS software with EXPGUI user interface [38,39]. Low temperature (4–200 K) neutron diffraction data was collected at Oak Ridge National Laboratory using the HB2A and SEQUOIA beamlines. Crystal structures were generated using VESTA and PyMol software [40,41]. The magnetic space groups for CoRh_2O_4 and CuRh_2O_4 were determined using Isodistort [42] and low temperature nuclear structures were refined using the Rietveld method [37] on the Fullprof suite [43]. Low-temperature (5–300 K) magnetization measurements were obtained using a Quantum Design MPMS.

4.6 References

- [1] L.A. Fenner, A.S. Wills, S.T. Bramwell, M. Dahlberg, P. Schiffer, Zero-point entropy of the spinel spin glasses CuGa_2O_4 and CuAl_2O_4 , *J. Phys. Conf. Ser.* 145 (2009) 12029. doi:10.1088/1742-6596/145/1/012029.
- [2] M.A. Hakim, M. Manjurul Haque, M. Huq, P. Nordblad, Spin-glass-like ordering in the spinel ZnFe_2O_4 ferrite, *Phys. B Condens. Matter.* 406 (2011) 48–51. doi:10.1016/j.physb.2010.10.010.
- [3] S.H. Lee, H. Takagi, D. Louca, M. Matsuda, S. Ji, H. Ueda, Y. Ueda, T. Katsufuji, J.H. Chung, S. Park, S.W. Cheong, C. Broholm, Frustrated magnetism and cooperative phase transitions in spinels, *J. Phys. Soc. Japan.* 79 (2010) 1–14. doi:10.1143/JPSJ.79.011004.
- [4] K.M. Kojima, R. Kadono, M. Miyazaki, M. Hiraishi, I. Yamauchi, A. Koda, Y. Tsuchiya, H.S. Suzuki, H. Kitazawa, Magnetic frustration in iridium spinel compound CuIr_2S_4 , *Phys. Rev. Lett.* 112 (2014) 1–5. doi:10.1103/PhysRevLett.112.087203.
- [5] G. Chen, L. Balents, A.P. Schnyder, Spin-orbital singlet and quantum critical point on the diamond lattice: FeSc_2S_4 , *Phys. Rev. Lett.* 102 (2009) 6–9. doi:10.1103/PhysRevLett.102.096406.
- [6] L. Mittelstädt, M. Schmidt, Z. Wang, F. Mayr, V. Tsurkan, P. Lunkenheimer, D. Ish, L. Balents, J. Deisenhofer, A. Loidl, Spin-orbital and quantum criticality in FeSc_2S_4 , *Phys. Rev. B.* 91 (2015) 125112. doi:10.1103/PhysRevB.91.125112.
- [7] K.W. Plumb, J. Morey, J.A. Rodriguez-Rivera, H. Wu, A.A. Podlesnyak, T.M. McQueen, C.L. Broholm, Antiferromagnetic and Orbital Ordering on a Diamond Lattice Near Quantum Criticality, arXiv. (2016) 1–16. <http://arxiv.org/abs/1603.08033>.
- [8] P. Holba, M. Nevřiva, E. Pollert, Tetragonal distortion of spinel solid solutions MnCr_2O_4 - Mn_3O_4 , *Mater. Res. Bull.* 10 (1975) 853–860. doi:10.1016/0025-5408(75)90202-0.
- [9] M. Tovar, R. Torabi, C. Welker, F. Fleischer, Structural and magnetic properties of Cu-Ni-Cr spinel oxides, *Phys. B Condens. Matter.* 385–386 I (2006) 196–198. doi:10.1016/j.physb.2006.05.181.
- [10] W.A. Dollase, H.S.C. O'Neill, The Spinel CuCr_2O_4 and CuRh_2O_4 , *Acta Crystallogr. Sect. C Cryst. Struct. Commun.* 53 (1997) 657–659. doi:10.1107/S0108270197000486.
- [11] G. Blasse, New Type of Superexchange in the Spinel Structure - Some Magnetic Properties of Oxides $\text{Me}^{2+}\text{Co}_2\text{O}_4$ and $\text{Me}^{2+}\text{Rh}_2\text{O}_4$ with Spinel Structure, *Philips Res. Reports.* 18 (1963) 383–392.
- [12] F. Bertaut, F. Forrat, J.F. Dulac, Rhodites spinelles, *Comptes Rendus Hebd. Des Seances l'Academie Des Sci.* 249 (1959) 726–728.
- [13] C. Cascales, I. Rasines, The spinels CoRh_2O_4 and Co_2RhO_4 , *Mater. Chem. Phys.* 10 (1984) 199–203. doi:10.1016/0254-0584(84)90048-8.

- [14] I.D. Brown, The bond-valence method: an empirical approach to chemical structure and bonding., in: M. O’Keeffe, A. Navrotsky (Eds.), *Struct. Bond. Cryst. II*, Academic Press, New York, 1981: pp. 1–30.
- [15] J. Dulac, Spinelles deformes dans le systeme rhodite de nickel et de cuivre, *Bull. La Société Française Minéralogie Cristallogr.* 92 (1969) 25–29.
- [16] J.E. Mitchell, *Synthesis and Magnetic Properties of Spinel-Based Transition Metal Oxides and Related Species*, McMaster University, 2009.
- [17] D.D. Khanolkar, Crystal structure data of some Rhodites and Ruthenites, *Curr. Sci.* 30 (1961) 52–53.
- [18] Ismunandar, B.J. Kennedy, B.A. Hunter, Phase transformation in CuRh_2O_4 : a powder neutron diffraction study, *Mater. Res. Bull.* 34 (1999) 135–143. doi:10.1016/S0025-5408(98)00201-3.
- [19] O. Chmaissem, Y. Eckstein, C.G. Kuper, Structure and a bond-valence-sum study of the 1-2-3 superconductors $(\text{Ca}_x\text{La}_{1-x})(\text{Ba}_{1.75-x}\text{La}_{0.25+x})\text{Cu}_3\text{O}_y$ and $\text{YBa}_2\text{Cu}_3\text{O}_y$, *Phys. Rev. B.* 63 (2001) 174510. doi:10.1103/PhysRevB.63.174510.
- [20] T. Suzuki, H. Nagai, M. Nohara, H. Takagi, Melting of antiferromagnetic ordering in spinel oxide CoAl_2O_4 , *J. Phys. Condens. Matter.* 19 (2007) 145265. doi:10.1088/0953-8984/19/14/145265.
- [21] A.P. Ramirez, Strongly Geometrically Frustrated Magnets, *Annu. Rev. Mater. Sci.* 24 (1994) 453–480. doi:10.1146/annurev.ms.24.080194.002321.
- [22] T. Hotta, S. Yunoki, M. Mayr, E. Dagotto, A-type antiferromagnetic and C-type orbital-ordered states in LaMnO_3 using cooperative Jahn-Teller phonons, *Phys. Rev. B.* 60 (1999) 15009–15012. doi:10.1103/PhysRevB.60.R15009.
- [23] J. Hemberger, A. Krimmel, T. Kurz, H.-A. Krug von Nidda, V.Y. Ivanov, A.A. Mukhin, A.M. Balbashov, A. Loidl, Structural, magnetic, and electrical properties of single-crystalline $\text{La}_{1-x}\text{Sr}_x\text{MnO}_3$, *Phys. Rev. B.* 66 (2002) 94410. doi:10.1103/PhysRevB.66.094410.
- [24] A.I. Kurbakov, A. V. Lazuta, V.A. Ryzhov, V.A. Trounov, I.I. Larionov, C. Martin, A. Maignan, M. Hervieu, Crystal structure and magnetic and transport properties of $^{154}\text{Sm}_{0.5}\text{Sr}_{0.5}\text{MnO}_3$: A-type antiferromagnetic phase and ferromagnetic polarons, *Phys. Rev. B - Condens. Matter Mater. Phys.* 72 (2005) 1–10. doi:10.1103/PhysRevB.72.184432.
- [25] S.P. Bayrakci, I. Mirabeau, P. Bourges, Y. Sidis, M. Enderle, J. Mesot, D.P. Chen, C.T. Lin, B. Keimer, Magnetic ordering and spin waves in $\text{Na}_{0.82}\text{CoO}_2$, *Phys. Rev. Lett.* 94 (2005) 20–23. doi:10.1103/PhysRevLett.94.157205.
- [26] L.M. Helme, A.T. Boothroyd, R. Coldea, D. Prabhakaran, D.A. Tennant, A. Hiess, J. Kulda, Three-dimensional spin fluctuations in $\text{Na}_{0.75}\text{CoO}_2$, *Phys. Rev. Lett.* 94 (2005) 20–23. doi:10.1103/PhysRevLett.94.157206.
- [27] R.C. Byrne, C.W. Moeller, Magnetic interactions of ruthenium, rhodium, and iridium in the hexagonal barium titanate structure, *J. Solid State Chem.* 2 (1970) 228–235.

doi:10.1016/0022-4596(70)90075-7.

- [28] N. Furuta, S. Asai, T. Igarashi, R. Okazaki, Y. Yasui, I. Terasaki, M. Ikeda, T. Fujita, M. Hagiwara, K. Kobayashi, R. Kumai, H. Nakao, Y. Murakami, Unconventional magnetism in the layered oxide LaSrRhO_4 , *Phys. Rev. B - Condens. Matter Mater. Phys.* 90 (2014) 1–7. doi:10.1103/PhysRevB.90.144402.
- [29] Y. Shimoda, Y. Doi, M. Wakeshima, Y. Hinatsu, Magnetic properties of quadruple perovskites $\text{Ba}_4\text{LnRu}_3\text{O}_{12}$ (Ln=La, Nd, Sm–Gd, Dy–Lu), *J. Solid State Chem.* 183 (2010) 33–40. doi:10.1016/j.jssc.2009.10.007.
- [30] M.J. Davis, M.D. Smith, K.E. Stitzer, H.-C. zur Loye, High temperature flux growth, structural characterization, and magnetic properties of $\text{Ca}_{3.15}\text{Li}_{0.85}\text{IrO}_6$, $\text{Sr}_3\text{LiIrO}_6$, $\text{Ca}_3\text{LiRuO}_6$ and $\text{Sr}_3\text{LiRuO}_6$, *J. Alloys Compd.* 351 (2003) 95–100. doi:10.1016/S0925-8388(02)01082-4.
- [31] S.-J. Kim, M.D. Smith, J. Darriet, H.-C. zur Loye, Crystal growth of new perovskite and perovskite related iridates: $\text{Ba}_3\text{LiIr}_2\text{O}_9$, $\text{Ba}_3\text{NaIr}_2\text{O}_9$, and $\text{Ba}_{3.44}\text{K}_{1.56}\text{Ir}_2\text{O}_{10}$, *J. Solid State Chem.* 177 (2004) 1493–1500. doi:10.1016/j.jssc.2003.11.037.
- [32] R. Endoh, O. Fujishima, T. Atake, N. Matsumoto, M. Hayashi, S. Nagata, Antiferromagnetic transition in CuRh_2O_4 , *J. Phys. Chem. Solids.* 60 (1999) 457–462. doi:10.1016/S0022-3697(98)00310-2.
- [33] S. Hara, H. Sato, Structure and Magnetism of Novel Copper Molybdenum Oxides $\eta\text{-CuMoO}_4$ and $\beta\text{-Cu}_3\text{Mo}_2\text{O}_9$, *J. Phys. Soc. Japan.* 82 (2013) 54802. doi:10.7566/JPSJ.82.054802.
- [34] Y. Tokunaga, Y. Kaneko, D. Okuyama, S. Ishiwata, T. Arima, S. Wakimoto, K. Kakurai, Y. Taguchi, Y. Tokura, Multiferroic M-type hexaferrites with a room-temperature conical state and magnetically controllable spin helicity, *Phys. Rev. Lett.* 105 (2010) 17–20. doi:10.1103/PhysRevLett.105.257201.
- [35] K. Taniguchi, N. Abe, S. Ohtani, H. Umetsu, T.H. Arima, Ferroelectric polarization reversal by a magnetic field in multiferroic Y-type hexaferrite $\text{Ba}_2\text{Mg}_2\text{Fe}_{12}\text{O}_{12}$, *Appl. Phys. Express.* 1 (2008) 0313011–0313013. doi:10.1143/APEX.1.031301.
- [36] R.C. Pullar, Hexagonal ferrites: A review of the synthesis, properties and applications of hexaferrite ceramics, *Prog. Mater. Sci.* 57 (2012) 1191–1334. doi:10.1016/j.pmatsci.2012.04.001.
- [37] H.M. Rietveld, A profile refinement method for nuclear and magnetic structures, *J. Appl. Crystallogr.* 2 (1969) 65–71. doi:10.1107/S0021889869006558.
- [38] A.C. Larson, R.B. Von Dreele, General Structure Analysis System (GSAS), Los Alamos Natl. Lab. Rep. LAUR 86-74 (1994).
- [39] B.H. Toby, EXPGUI, a graphical user interface for GSAS, *J. Appl. Crystallogr.* 34 (2001) 210–213. doi:10.1107/S0021889801002242.
- [40] K. Momma, F. Izumi, VESTA 3 for three-dimensional visualization of crystal, volumetric and morphology data, *J. Appl. Crystallogr.* 44 (2011) 1272–1276. doi:10.1107/S0021889811038970.

- [41] The PyMOL Molecular Graphics System, (n.d.).
- [42] B.J. Campbell, H.T. Stokes, D.E. Tanner, D.M. Hatch, ISODISPLACE: A web-based tool for exploring structural distortions, *J. Appl. Crystallogr.* 39 (2006) 607–614. doi:10.1107/S0021889806014075.
- [43] J. Rodríguez-Carvajal, Recent advances in magnetic structure determination by neutron powder diffraction, *Phys. B Condens. Matter.* 192 (1993) 55–69. doi:10.1016/0921-4526(93)90108-I.

General Conclusions and Future Work

This dissertation presented and discussed the preparation and characterization of both novel and previously known materials. We demonstrated that the series $\text{Ba}_2\text{In}_{2-x}\text{Ir}_x\text{O}_{5+\delta}$ ($x = 0-1.4, 2$) undergoes a series of structural transitions spanning several perovskite-related structures leading to several novel compositions included $\text{Ba}_2\text{In}_{1.62}\text{Ir}_{0.38}\text{O}_{5.49}$ which was shown to contain a relatively large amount of Ir(VI) (~50%). This was the first time Ir(VI) was stabilized without the aid of an oxygen-rich atmosphere or flux methods. In addition to novel compositions, $\text{Ba}_2\text{InIrO}_6$ was found to crystallize as a monoclinic distortion of the previously reported 6H structure with a different ordering on the In and Ir ions. This serves as a great example about how there is still more to learn even about compounds we already know about.

For the novel solid solutions series $\text{Ba}_{2-x}\text{La}_x\text{InIrO}_6$ ($x = 0-1.0$) and $\text{BaLaIn}_{1-y}\text{Ca}_y\text{IrO}_6$ ($y = 0-1.0$), several changes in structure, magnetic moment, and charge transport were observed. The $\text{Ba}_{2-x}\text{La}_x\text{InIrO}_6$ series exhibits a transition from a 6M polytype to an orthorhombic perovskite structure with increased La content. The $\text{BaLaIn}_{1-y}\text{Ca}_y\text{IrO}_6$ series transitioned from a disordered orthorhombic perovskite to an ordered cubic perovskite with increased Ca content. Seebeck measurements for both systems showed that Ir(IV)-rich compounds tended to have a n-type conduction mechanism while Ir(V)-rich compounds appeared to be p-type. Both systems were found to be semiconducting and the magnitude of the resistivity is dependent on the crystal structure and Ir environment. Characterization of the magnetic behavior showed that while both systems exhibit paramagnetic behavior, their μ_{eff} values do not correlate well with moments expected for Ir(IV) and Ir(V). While this deviation appears to be somewhat common in conductive iridates, it would be interesting to study analogous Os and Re oxides to see if they

exhibit similar electronic behavior. Additionally, the inclination of In to share sites with Ir in $\text{Ba}_2\text{In}_{2-x}\text{Ir}_x\text{O}_{5+\delta}$, $\text{Ba}_{2-x}\text{La}_x\text{InIrO}_6$, and $\text{BaLaIn}_{1-y}\text{Ca}_y\text{IrO}_6$ indicates there is something special about the pairing. Ir is known to form ordered perovskites with metals similar in size to In^{3+} such as Y^{3+} and Sc^{3+} . This suggests the behavior is linked to the fact that In possesses a full d shell. It would therefore be interesting to see if similar site sharing could be achieved by pairing Ir with other Group 13 elements such as Ga or Tl.

While CoRh_2O_4 and CuRh_2O_4 had been previously reported, we were the first to perform more detailed structural and magnetic characterization on them and the novel composition, $\text{Ni}_{1.25}\text{Rh}_{1.75}\text{O}_4$. Neutron and X-ray diffraction studies confirmed that CoRh_2O_4 crystallizes in a normal cubic spinel structure ($Fd\bar{3}m$). CuRh_2O_4 and $\text{Ni}_{1.25}\text{Rh}_{1.75}\text{O}_4$, were found to be tetragonally-distorted spinels ($I4_1/amd$) due to cooperative Jahn-Teller compression and elongation, respectively. In terms of their magnetic behavior, antiferromagnetic behavior was observed for both CoRh_2O_4 ($T_N = 24.9(1)$ K, $\mu_{\text{eff}} = 4.42(1)$ μ_B) and CuRh_2O_4 ($T_N = 24(1)$ K, $\mu_{\text{eff}} = 1.97(1)$ μ_B) confirming previous literature reports. Their magnetic moments were a bit higher than predicted spin-only values due to unquenched orbital contributions. Additionally, the magnetic structures of CoRh_2O_4 and CuRh_2O_4 were determined, for the first time, to be an antiferromagnetic A -type and an ab -plane helical structure, respectively. For $\text{Ni}_{1.25}\text{Rh}_{1.75}\text{O}_4$, a divergence in ZFC and FC $\chi(T)$ data was observed in addition to a lack of long-range ordering in low temperature neutron data both of which suggest this compound is a spin-glass. A possible competition between ferromagnetic and antiferromagnetic correlations was also observed for $\text{Ni}_{1.25}\text{Rh}_{1.75}\text{O}_4$. These magnetic behaviors are likely the result of superexchange disruption caused by the presence of a magnetic ion on the B-site. This hypothesis could be tested by

preparing other members of a general $\text{NiRh}_{2-x}\text{M}_x\text{O}_4$ spinel family to study how the behavior is affected by varying concentration of different magnetic ions.

The investigations presented in this dissertation demonstrate that there is always more to learn and study even when dealing with previously known compounds or structures types that have been heavily studied like the perovskite and spinel structures. As researchers and scientists, it is our duty not only to seek out new ideas and technologies but to also to occasionally look back and find something that we missed the first time around.

"The worst thing you can ever do is think that you know enough."

– Arnold Schwarzenegger

Bibliography

- Abragam, A., Bleaney, B., *Electron Paramagnetic Resonance of Transition Ions*, Oxford University Press, London, 1970.
- Amador, U., Hetherington, C.J.D., Moran, E., Alario-Franco, M.A., $\text{Ba}_2\text{PrPtO}_6$: A novel double perovskite, *J. Solid State Chem.* 96 (1992) 132–140. doi:10.1016/S0022-4596(05)80305-6.
- Battle, P.D., Kim, S.H., Powell, A.V., The crystal structure and electronic properties of $\text{Ba}_4\text{Ru}_3\text{MO}_{12}$ (M =Li, Na, Mg, Zn), *J. Solid State Chem.* 101 (1992) 161–172. doi:10.1016/0022-4596(92)90212-E.
- Baud, G., Capestan, M., Sur de nouvelles perovskites ternaires contenant du rhenium pentavalent, *Comptes Rendus Hebd. Des Seances l'Academie Des Sci. Ser. C.* 267 (1968) 314–317.
- Bayrakci, S.P., Mirabeau, I., Bourges, P., Sidis, Y., Enderle, M., Mesot, J., Chen, D.P., Lin, C.T., Keimer, B., Magnetic ordering and spin waves in $\text{Na}_{0.82}\text{CoO}_2$, *Phys. Rev. Lett.* 94 (2005) 20–23. doi:10.1103/PhysRevLett.94.157205.
- Bendersky, L.A., Gayle, F.W., Electron diffraction using transmission electron microscopy, *J. Res. Natl. Inst. Stand. Technol.* 106 (2001) 997–1012. doi:10.6028/jres.106.051.
- Bertaut, F., Forrat, F., Dulac, J.F., Rhodites spinelles, *Comptes Rendus Hebd. Des Seances l'Academie Des Sci.* 249 (1959) 726–728.
- Bielecki, J., Parker, S.F., Ekanayake, D., Rahman, S.M.H., Börjesson, L., Karlsson, M., Short-range structure of the brownmillerite-type oxide $\text{Ba}_2\text{In}_2\text{O}_5$ and its hydrated proton-conducting form BaInO_3H , *J. Mater. Chem. A.* 2 (2014) 16915–16924. doi:10.1039/C4TA03213F.
- Blasse, G., New Type of Superexchange in the Spinel Structure - Some Magnetic Properties of Oxides $\text{Me}^{2+}\text{Co}_2\text{O}_4$ and $\text{Me}^{2+}\text{Rh}_2\text{O}_4$ with Spinel Structure, *Philips Res. Reports.* 18 (1963) 383–392.
- Bragg, W.H., Bragg, W.L., The Reflection of X-rays by Crystals, *Proc. R. Soc. A Math. Phys. Eng. Sci.* 88 (1913) 428–438. doi:10.1098/rspa.1913.0040.
- Bremholm, M., Dutton, S.E., Stephens, P.W., Cava, R.J., NaIrO_3 - A pentavalent post-perovskite, *J. Solid State Chem.* 184 (2011) 601–607. doi:10.1016/j.jssc.2011.01.028.
- Brown, I.D., The bond-valence method: an empirical approach to chemical structure and bonding., in: M. O'Keeffe, A. Navrotsky (Eds.), *Struct. Bond. Cryst. II*, Academic Press, New York, 1981: pp. 1–30.
- Bufaical, L., Mendonça Ferreira, L., Lora-Serrano, R., Agüero, O., Torriani, I., Granado, E., Pagliuso, P.G., Caytuero, A., Baggio-Saitovich, E., Physical properties of disordered double-perovskite $\text{Ca}_{2-x}\text{La}_x\text{FeIrO}_6$, *J. Appl. Phys.* 103 (2008) 07F716. doi:10.1063/1.2830719.
- Buttner, R.H., Maslen, E.N., Electron difference density and structural parameters in CaTiO_3 , *Acta Crystallogr. Sect. B Struct. Sci.* 48 (1992) 644–649. doi:10.1107/S0108768192004592.

- Byrne, R.C., Moeller, C.W., Magnetic interactions of ruthenium, rhodium, and iridium in the hexagonal barium titanate structure, *J. Solid State Chem.* 2 (1970) 228–235.
doi:10.1016/0022-4596(70)90075-7.
- Bzdušek, T., Rüegg, A., Sigrist, M., Weyl semimetal from spontaneous inversion symmetry breaking in pyrochlore oxides, *Phys. Rev. B.* 91 (2015) 165105.
doi:10.1103/PhysRevB.91.165105.
- Campbell, B.J., Stokes, H.T., Tanner, D.E., Hatch, D.M., ISODISPLACE: A web-based tool for exploring structural distortions, *J. Appl. Crystallogr.* 39 (2006) 607–614.
doi:10.1107/S0021889806014075.
- Cao, G., Bolivar, J., McCall, S., Crow, J., Guertin, R., Weak ferromagnetism, metal-to-nonmetal transition, and negative differential resistivity in single-crystal Sr_2IrO_4 , *Phys. Rev. B.* 57 (1998) R11039–R11042. doi:10.1103/PhysRevB.57.R11039.
- Cao, G., Crow, J.E., Guertin, R.P., Henning, P.F., Homes, C.C., Strongin, M., Basov, D.N., Lochner, E., Charge density wave formation accompanying ferromagnetic ordering in quasi-one-dimensional BaIrO_3 , *Solid State Commun.* 113 (2000) 657–662.
- Cao, G., Qi, T.F., Li, L., Terzic, J., Yuan, S.J., DeLong, L.E., Murthy, G. Kaul, R.K., Novel Magnetism of Ir^{5+} ($5d^4$) Ions in the Double Perovskite Sr_2YIrO_6 , *Phys. Rev. Lett.* 112 (2014) 56402. doi:10.1103/PhysRevLett.112.056402.
- Cao, G., Subedi, A., Calder, S., Yan, J.-Q., Yi, J., Gai, Z., Poudel, L., Singh, D.J., Lumsden, M.D., Christianson, A.D., Sales, B.C., Mandrus, D., Magnetism and electronic structure of $\text{La}_2\text{ZnIrO}_6$ and $\text{La}_2\text{MgIrO}_6$: Candidate $J_{\text{eff}} = 1/2$ Mott insulators, *Phys. Rev. B.* 87 (2013) 155136. doi:10.1103/PhysRevB.87.155136.
- Cao, G., Xin, Y., Alexander, C.S., Crow, J.E., Schlottmann, P., Crawford, M.K., Harlow, R.L., Marshall, W., Anomalous magnetic and transport behavior in the magnetic insulator $\text{Sr}_3\text{Ir}_2\text{O}_7$, *Phys. Rev. B.* 66 (2002) 214412. doi:10.1103/PhysRevB.66.214412.
- Carter, J.-M., Shankar, V.V., Zeb, M.A., Kee, H.-Y., Semimetal and Topological Insulator in Perovskite Iridates, *Phys. Rev. B.* 85 (2012) 115105. doi:10.1103/PhysRevB.85.115105.
- Cascales, C., Rasines, I., The spinels CoRh_2O_4 and Co_2RhO_4 , *Mater. Chem. Phys.* 10 (1984) 199–203. doi:10.1016/0254-0584(84)90048-8.
- Chaikin, P.M., A Introduction to Thermopower for Those Who Might Want to Use It to Study Organic Conductors and Superconductors, in: V.Z. Kresin, W.A. Little (Eds.), *Org. Supercond.*, Plenum Press, New York, 1990: pp. 101–115.
- Chaloupka, J., Jackeli, G., Khaliullin, G., Zigzag Magnetic Order in the Iridium Oxide Na_2IrO_3 , *Phys. Rev. Lett.* 110 (2013) 97204. doi:10.1103/PhysRevLett.110.097204.
- Chen, G., Balents, L., Schnyder, A.P., Spin-orbital singlet and quantum critical point on the diamond lattice: FeSc_2S_4 , *Phys. Rev. Lett.* 102 (2009) 6–9.
doi:10.1103/PhysRevLett.102.096406.
- Choy, J.-H., Kim, D.-K., Hwang, S.-H., Demazeau, G., Jung, D.-Y., XANES and EXAFS Studies on the Ir-O Bond Covalency in Ionic Iridium Perovskites, *J. Am. Chem. Soc.* 117 (1995) 8557–8566. doi:10.1021/ja00138a010.

- Chmaissem, O., Eckstein, Y., Kuper, C.G., Structure and a bond-valence-sum study of the 1-2-3 superconductors $(\text{Ca}_x\text{La}_{1-x})(\text{Ba}_{1.75-x}\text{La}_{0.25+x})\text{Cu}_3\text{O}_y$ and $\text{YBa}_2\text{Cu}_3\text{O}_y$, *Phys. Rev. B.* 63 (2001) 174510. doi:10.1103/PhysRevB.63.174510.
- Corr, S.A., Seshadri, R., *Synthetic Methodologies*, in: *Compr. Inorg. Chem. II From Elem. to Appl.*, 2nd ed., Elsevier Ltd., 2013: pp. 1–15. doi:10.1016/B978-0-08-097774-4.00401-0.
- Cosio-Castaneda, C., de la Mora, P., Morales, F., Escudero, R., Tavizon, G., Magnetic behavior of the $\text{Bi}_{2-y}\text{Sr}_y\text{Ir}_2\text{O}_7$ pyrochlore solid solution, *J. Solid State Chem.* 200 (2013) 49–53. doi:10.1016/j.jssc.2013.01.009.
- Cosio-Castaneda, C., Tavizon, G., Baeza, A., La Mora, P.D., Escudero, R., Structure and magnetic properties of the weak ferromagnet $\text{Sr}_{2-x}\text{La}_x\text{IrO}_4$, *J. Phys. Condens. Matter.* 19 (2007) 446210. doi:10.1088/0953-8984/19/44/446210.
- Cullity, B.D., Stock, S.R., *Elements of X-Ray Diffraction*, 3rd ed., Prentice Hall, Upper Saddle River, 2001.
- Cussen, E.J., Sloan, J., Vente, J.F., Battle, P.D., Gibb, T.C., 15R $\text{SrMn}_{1-x}\text{Fe}_x\text{O}_{3-\delta}$ ($x = 0.1$); A New Perovskite Stacking Sequence, *Inorg. Chem.* 37 (1998) 6071–6077.
- da Silva, C.C., Sombra, A.S.B., Temperature Dependence of the Magnetic and Electric Properties of $\text{Ca}_2\text{Fe}_2\text{O}_5$, *Mater. Sci. Appl.* 2 (2011) 1349–1353. doi:10.4236/msa.2011.29183.
- Davis, M.J., Smith, M.D., Stitzer, K.E., zur Loye, H.-C., High temperature flux growth, structural characterization, and magnetic properties of $\text{Ca}_{3.15}\text{Li}_{0.85}\text{IrO}_6$, $\text{Sr}_3\text{LiIrO}_6$, $\text{Ca}_3\text{LiRuO}_6$ and $\text{Sr}_3\text{LiRuO}_6$, *J. Alloys Compd.* 351 (2003) 95–100. doi:10.1016/S0925-8388(02)01082-4.
- De Graef, M., McHenry, M.E., *Structure of materials: an introduction to crystallography, diffraction and symmetry*, Cambridge University Press, Cambridge, 2007.
- Demazeau, G., Jung, D.-Y., Sanchez, J.-P., Colineau, E., Blaise, A., Fournes, L., Iridium(VI) stabilized in a perovskite-type lattice: $\text{Ba}_2\text{CaIrO}_6$, *Solid State Commun.* 85 (1993) 479–484. doi:10.1016/0038-1098(93)90004-7.
- Dey, T., Maljuk, A., Efremov, D.V., Kataeva, O., Gass, S., Blum, C.G.F., Steckel, F., Gruner, D., Ritschel, T., Wolter, A.U.B., Geck, J., Hess, C., Koepf, K., van den Brink, J., Wurmehl, S., Büchner, B., Ba_2YIrO_6 : A cubic double perovskite material with Ir^{5+} ions, *Phys. Rev. B.* 93 (2016) 14434. doi:10.1103/PhysRevB.93.014434.
- Disseler, S.M., Dhital, C., Amato, A., Giblin, S.R., De La Cruz, C., Wilson, S.D., Graf, M.J., Magnetic order in the pyrochlore iridates $\text{A}_2\text{Ir}_2\text{O}_7$ ($A = \text{Y}, \text{Yb}$), *Phys. Rev. B - Condens. Matter Mater. Phys.* 86 (2012) 1–8. doi:10.1103/PhysRevB.86.014428.
- Disseler, S.M., Giblin, S.R., Dhital, C., Lukas, K.C., Wilson, S.D., Graf, M.J., Magnetization and Hall effect studies on the pyrochlore iridate $\text{Nd}_2\text{Ir}_2\text{O}_7$, *Phys. Rev. B - Condens. Matter Mater. Phys.* 87 (2013) 1–5. doi:10.1103/PhysRevB.87.060403.
- Doi, Y., Hinatsu, Y., The structural and magnetic characterization of 6H-perovskite-type oxides $\text{Ba}_3\text{LnIr}_2\text{O}_9$ ($\text{Ln} = \text{Y}, \text{lanthanides}$), *J. Phys. Condens. Matter.* 16 (2004) 2849–2860. doi:10.1088/0953-8984/16/16/009.

- Doi, Y., Hinatsu, Y., Shimojo, Y., Ishii, Y., Crystal Structure and Magnetic Properties of 6H-Perovskite $\text{Ba}_3\text{NdRu}_2\text{O}_9$, *J. Solid State Chem.* 161 (2001) 113–120.
doi:10.1006/jssc.2001.9296.
- Dollase, W.A., O'Neill, H.S.C., The Spinels CuCr_2O_4 and CuRh_2O_4 , *Acta Crystallogr. Sect. C Cryst. Struct. Commun.* 53 (1997) 657–659. doi:10.1107/S0108270197000486.
- Dulac, J., Spinelles deformes dans le systeme rhodite de nickel et de cuivre, *Bull. La Société Française Minéralogie Cristallogr.* 92 (1969) 25–29.
- Endoh, R., Fujishima, O., Atake, T., Matsumoto, N., Hayashi, M., Nagata, S., Antiferromagnetic transition in CuRh_2O_4 , *J. Phys. Chem. Solids.* 60 (1999) 457–462.
doi:10.1016/S0022-3697(98)00310-2.
- Fenner, L.A., Wills, A.S., Bramwell, S.T., Dahlberg, M., Schiffer, P., Zero-point entropy of the spinel spin glasses CuGa_2O_4 and CuAl_2O_4 , *J. Phys. Conf. Ser.* 145 (2009) 12029.
doi:10.1088/1742-6596/145/1/012029.
- Flynn, J., Li, J., Ramirez, A.P., Subramanian, M.A., The effect of iridium oxidation state on the electronic properties of perovskite-type solid solutions: $\text{Ba}_{2-x}\text{La}_x\text{InIrO}_6$ and $\text{BaLaIn}_{1-y}\text{Ca}_y\text{IrO}_6$, *J. Solid State Chem.* 247 (2017) 53–59. doi:10.1016/j.jssc.2016.12.017.
- Flynn, J., Li, J., Sleight, A.W., Ramirez, A.P., Subramanian, M.A., Structure and Properties of Ir-Containing Oxides with Large Spin–Orbit Coupling: $\text{Ba}_2\text{In}_{2-x}\text{Ir}_x\text{O}_{5+\delta}$, *Inorg. Chem.* 55 (2016) 2748–2754. doi:10.1021/acs.inorgchem.5b02501.
- Frenzen, S., Müller-Buschbaum, H., Zur Kristallchemie eines Natrium-Cadmium-Oxoimidats: $\text{Na}_3\text{Cd}_2\text{IrO}_6$, *Zeitschrift Für Naturforsch. B.* 51 (1996) 822–825. doi:10.1515/znb-1996-0611.
- Fu, W.T., IJdo, D.J.W., Re-examination of the structure of Ba_2MIR_6 (M=La, Y): space group revised, *J. Alloys Compd.* 394 (2005) L5–L8. doi:10.1016/j.jallcom.2004.10.049.
- Furuta, N., Asai, S., Igarashi, T., Okazaki, R., Yasui, Y., Terasaki, I., Ikeda, M., Fujita, T., Hagiwara, M., Kobayashi, K., Kumai, R., Nakao, H., Murakami, Y., Unconventional magnetism in the layered oxide LaSrRhO_4 , *Phys. Rev. B - Condens. Matter Mater. Phys.* 90 (2014) 1–7. doi:10.1103/PhysRevB.90.144402.
- Galasso, F.S., *Perovskites and High Tc Superconductors*, Routledge, London, 1990.
- Gatimu, A.J., Berthelot, R., Muir, S., Sleight, A.W., Subramanian, M.A., Synthesis and characterization of $\text{Sr}_2\text{Ir}_{1-x}\text{M}_x\text{O}_4$ (M=Ti, Fe, Co) solid solutions, *J. Solid State Chem.* 190 (2012) 257–263. doi:10.1016/j.jssc.2012.02.058.
- Glazer, A.M., The classification of tilted octahedra in perovskites, *Acta Crystallogr. Sect. B Struct. Crystallogr. Cryst. Chem.* 28 (1972) 3384–3392.
doi:10.1107/S0567740872007976.
- Goldschmidt, V.M., Die Gesetze der Krystallochemie, *Naturwissenschaften.* 14 (1926) 477–485. doi:10.1007/BF01507527.
- Goodenough, J.B., Ceramic solid electrolytes, *Solid State Ionics.* 94 (1997) 17–25.
doi:10.1016/S0167-2738(96)00501-2.
- Goodenough, J.B., Oxide-ion conduction in $\text{Ba}_2\text{In}_2\text{O}_5$ and $\text{Ba}_2\text{In}_2\text{MO}_8$ (M = Ce, Hf, or Zr), *Solid State Ionics.* 44 (1990) 21–31.

- Greedan, J.E., Frustrated rare earth magnetism: Spin glasses, spin liquids and spin ices in pyrochlore oxides, *J. Alloys Compd.* 408–412 (2006) 444–455.
doi:10.1016/j.jallcom.2004.12.084.
- Greedan, J.E., Geometrically frustrated magnetic materials, *J. Mater. Chem.* 11 (2001) 37–53.
doi:10.1039/b003682j.
- Greedan, J.E., Raju, N.P., Maignan, A., Simon, C., Pedersen, J.S., Niraimathi, A.M., Gmelin, E., Subramanian, M.A., Frustrated pyrochlore oxides, $\text{Y}_2\text{Mn}_2\text{O}_7$, $\text{Ho}_2\text{Mn}_2\text{O}_7$, and $\text{Yb}_2\text{Mn}_2\text{O}_7$: Bulk magnetism and magnetic microstructure, *Phys. Rev. B.* 54 (1996) 7189–7200. doi:10.1103/PhysRevB.54.7189.
- Gregory, D.H., Weller, M.T., Phases in the System $\text{Ba}_2\text{M}_{2-x}\text{Cu}_x\text{O}_{4+\delta}$, $\text{M} = \text{In, Sc}$: Structure and Oxygen Stoichiometry, 1993. doi:10.1006/jssc.1993.1331.
- Guo, H.-M., Franz, M., Three-Dimensional Topological Insulators on the Pyrochlore Lattice, *Phys. Rev. Lett.* 103 (2009) 206805. doi:10.1103/PhysRevLett.103.206805.
- Hahn, T., ed., *International Tables for Crystallography Volume A: Space-group symmetry*, 5th ed., International Union of Crystallography, Chester, England, 2006.
doi:10.1107/97809553602060000100.
- Hakim, M.A., Manjurul Haque, M., Huq, M., Nordblad, P., Spin-glass-like ordering in the spinel ZnFe_2O_4 ferrite, *Phys. B Condens. Matter.* 406 (2011) 48–51.
doi:10.1016/j.physb.2010.10.010.
- Hara, S., Sato, H. Structure and Magnetism of Novel Copper Molybdenum Oxides $\eta\text{-CuMoO}_4$ and $\beta\text{-Cu}_3\text{Mo}_2\text{O}_9$, *J. Phys. Soc. Japan.* 82 (2013) 54802. doi:10.7566/JPSJ.82.054802.
- Harada, D., Wakeshima, M., Hinatsu, Y., The Structure and Magnetic Properties of New Iridium (IV) Perovskites $\text{Sr}_2\text{LnIrO}_6$ ($\text{Ln} = \text{Ce, Tb}$), *J. Solid State Chem.* 145 (1999) 356–360. doi:10.1006/jssc.1999.8223.
- Hasan, M.Z., Kane, C.L., Colloquium: Topological insulators, *Rev. Mod. Phys.* 82 (2010) 3045–3067. doi:10.1103/RevModPhys.82.3045.
- Hayashi, K., Demazeau, G., Pouchard, M., Hagenmuller, P., Preparation and Magnetic Study of a New Iridium(V) Perovskite: $\text{LaLi}_{0.5}\text{Ir}_{0.5}\text{O}_3$, *Mater. Res. Bull.* 15 (1980) 461–467.
- Helme, L.M., Boothroyd, A.T., Coldea, R., Prabhakaran, D., Tennant, D.A., Hiess, A., Kulda, J., Three-dimensional spin fluctuations in $\text{Na}_{0.75}\text{CoO}_2$, *Phys. Rev. Lett.* 94 (2005) 20–23.
doi:10.1103/PhysRevLett.94.157206.
- Hemberger, J., Krimmel, A., Kurz, T., Krug von Nidda, H.-A., Ivanov, V.Y., Mukhin, A.A., Balbashov, A.M., Loidl, A., Structural, magnetic, and electrical properties of single-crystalline $\text{La}_{1-x}\text{Sr}_x\text{MnO}_3$, *Phys. Rev. B.* 66 (2002) 94410.
doi:10.1103/PhysRevB.66.094410.
- Holba, P., Nevřiva, M., Pollert, E., Tetragonal distortion of spinel solid solutions $\text{MnCr}_2\text{O}_4\text{-Mn}_3\text{O}_4$, *Mater. Res. Bull.* 10 (1975) 853–860. doi:10.1016/0025-5408(75)90202-0.
- Hoppe, R., Claes, K., Über oxoimidate: zur kenntnis von KIrO_3 , *J. Less Common Met.* 43 (1975) 129–142. doi:10.1016/0022-5088(75)90132-0.
- Hotta, T., Yunoki, S., Mayr, M., Dagotto, E., A-type antiferromagnetic and C-type orbital-ordered states in LaMnO_3 using cooperative Jahn-Teller phonons, *Phys. Rev. B.* 60 (1999) 15009–15012. doi:10.1103/PhysRevB.60.R15009.

- Hsieh, D., Qian, D., Wray, L., Xia, Y., Hor, Y.S., Cava, R.J., Hasan, M.Z., A topological Dirac insulator in a quantum spin Hall phase., *Nature*. 452 (2008) 970–974. doi:10.1038/nature06843.
- Huq, A., Hodges, J.P., Gourdon, O., Heroux, L., Powgen: A third-generation high-resolution high-throughput powder diffraction instrument at the Spallation Neutron Source, *Zeitschrift Für Krist. Proc.* 1 (2011) 127–135. doi:10.1524/zkpr.2011.0019.
- Ismunandar, Kennedy, B.J., Hunter, B.A., Phase transformation in CuRh_2O_4 : a powder neutron diffraction study, *Mater. Res. Bull.* 34 (1999) 135–143. doi:10.1016/S0025-5408(98)00201-3.
- Jiang, P., Li, J., Ozarowski, A., Sleight, A.W., Subramanian, M.A., Intense Turquoise and Green Colors in Brownmillerite-Type Oxides Based on Mn^{5+} in $\text{Ba}_2\text{In}_{2-x}\text{Mn}_x\text{O}_{5+x}$, *Inorg. Chem.* 52 (2013) 1349–57. doi:10.1021/ic3020332.
- Jung, D.-Y., Demazeau, G., Etourneau, J., Subramanian, M.A., Preparation and characterization of new perovskites containing Ir(VI) and Ir(V) [$\text{BaM}_{0.50}\text{Ir}_{0.50}\text{O}_{2.75}$ and $\text{BaM}_{0.25}\text{Ir}_{0.75}\text{O}_3$ ($\text{M} = \text{Li}$ or Na)], *Mater. Res. Bull.* 30 (1995) 113–123. doi:10.1016/0025-5408(94)00115-4.
- Jung, D.-Y., Gravereau, P., Demazeau, G., Stabilization of six-coordinated iridium(VI) in a perovskite oxygen lattice $\text{Ba}_2\text{M}\text{IrO}_6$ ($\text{M} = \text{Ca}$, Sr), *Eur. J. Solid State Inorg. Chem.* 30 (1993) 1025–1037.
- Kakinuma, K., Yamamura, H., Haneda, H., Atake, T., Oxide-ion conductivity of $(\text{Ba}_{1-x}\text{La}_x)_2\text{In}_2\text{O}_{5+x}$ system based on brownmillerite structure, *Solid State Ionics*. 140 (2001) 301–306. doi:10.1016/S0167-2738(01)00853-0.
- Keeble, D.J., Wicklein, S., Dittmann, R., Ravelli, L., MacKie, R.A., Egger, W., Identification of A- and B-site cation vacancy defects in perovskite oxide thin films, *Phys. Rev. Lett.* 105 (2010) 3–6. doi:10.1103/PhysRevLett.105.226102.
- Khanolkar, D.D., Crystal structure data of some Rhodites and Ruthenites, *Curr. Sci.* 30 (1961) 52–53.
- Kim, S.-J., Smith, M.D., Darriet, J., zur Loye, H.-C., Crystal growth of new perovskite and perovskite related iridates: $\text{Ba}_3\text{LiIr}_2\text{O}_9$, $\text{Ba}_3\text{NaIr}_2\text{O}_9$, and $\text{Ba}_{3.44}\text{K}_{1.56}\text{Ir}_2\text{O}_{10}$, *J. Solid State Chem.* 177 (2004) 1493–1500. doi:10.1016/j.jssc.2003.11.037.
- Kojima, K.M., Kadono, R., Miyazaki, M., Hiraishi, M., Yamauchi, I., Koda, A., Tsuchiya, Y., Suzuki, H.S., Kitazawa, H., Magnetic frustration in iridium spinel compound CuIr_2S_4 , *Phys. Rev. Lett.* 112 (2014) 1–5. doi:10.1103/PhysRevLett.112.087203.
- König, V.E., Landolt-Börnstein. Neue Serie. Vol II/2, Springer, Berlin, 1966.
- Kuang, X., Jing, X., Loong, C.K., Lachowski, E.E., Skakle, J.M.S., West, A.R., A new hexagonal 12-layer perovskite-related structure: $\text{Ba}_6\text{R}_2\text{Ti}_4\text{O}_{17}$ ($\text{R} = \text{Nd}$ and Y), *Chem. Mater.* 14 (2002) 4359–4363. doi:10.1021/cm020374m.
- Kurbakov, A.I., Lazuta, A.V., Ryzhov, V.A., Trounov, V.A., Larionov, I.I., Martin, C., Maignan, A., Hervieu, M., Crystal structure and magnetic and transport properties of $^{154}\text{Sm}_{0.5}\text{Sr}_{0.5}\text{MnO}_3$: A-type antiferromagnetic phase and ferromagnetic polarons, *Phys. Rev. B - Condens. Matter Mater. Phys.* 72 (2005) 1–10. doi:10.1103/PhysRevB.72.184432.

- Laguna-Marco, M.A., Kayser, P., Alonso, J.A., Martínez-Lope, M.J., van Veenendaal, M., Choi, Y., Haskel, D., Electronic structure, local magnetism, and spin-orbit effects of Ir(IV)-, Ir(V)-, and Ir(VI)-based compounds, *Phys. Rev. B.* 91 (2015) 214433. doi:10.1103/PhysRevB.91.214433.
- Larson, A.C., Von Dreele, R.B., General Structure Analysis System (GSAS), Los Alamos Natl. Lab. Rep. LAUR 86-74 (1994).
- Le Bail, A., Whole powder pattern decomposition methods and applications: A retrospection, *Powder Diffr.* 20 (2005) 316–326. doi:10.1154/1.2135315.
- Lee, S.H., Takagi, H., Louca, D., Matsuda, M., Ji, S., Ueda, H., Ueda, Y., Katsufuji, T., Chung, J.H., Park, S., Cheong, S.W., Broholm, C., Frustrated magnetism and cooperative phase transitions in spinels, *J. Phys. Soc. Japan.* 79 (2010) 1–14. doi:10.1143/JPSJ.79.011004.
- Li, Q., Sun, L., Huo, L., Zhao, H., Grenier, J.-C., Electrode properties of Co-doped $\text{Ca}_2\text{Fe}_2\text{O}_5$ as new cathode materials for intermediate-temperature SOFCs, *Int. J. Hydrogen Energy.* 35 (2010) 9151–9157. doi:10.1016/j.ijhydene.2010.06.048.
- Ling, C.D., Kennedy, B.J., Zhou, Q., Spencer, J.R., Avdeev, M., Synthesis, structures, and phase transitions of barium bismuth iridium oxide perovskites $\text{Ba}_2\text{BiIrO}_6$ and $\text{Ba}_3\text{BiIr}_2\text{O}_9$, *J. Solid State Chem.* 183 (2010) 727–735. doi:10.1016/j.jssc.2010.01.017.
- Liu, H., Tong, W., Ling, L., Zhang, S., Zhang, R., Zhang, L., Pi, L., Zhang, C., Zhang, Y., Magnetic order, spin dynamics and transport properties of the pyrochlore iridate $\text{Y}_2\text{Ir}_2\text{O}_7$, *Solid State Commun.* 179 (2014) 1–5. doi:10.1016/j.ssc.2013.11.004.
- Longo, J.M., Raccach, P.M., Goodenough, J.B., $\text{Pb}_2\text{M}_2\text{O}_{7-x}$ (M = Ru, Ir, Re) — Preparation and properties of oxygen deficient pyrochlores, *Mater. Res. Bull.* 4 (1969) 191–202. doi:10.1016/0025-5408(69)90056-7.
- Marezio, M., Remeika, J.P., Dernier, P.D., The crystal chemistry of the rare earth orthoferrites, *Acta Crystallogr. Sect. B Struct. Crystallogr. Cryst. Chem.* 26 (1970) 2008–2022. doi:10.1107/S0567740870005319.
- Matsuura, H., Miyake, K., Effect of Spin–Orbit Interaction on $(4d)^3$ - and $(5d)^3$ -Based Transition-Metal Oxides, *J. Phys. Soc. Japan.* 82 (2013) 73703. doi:10.7566/JPSJ.82.073703.
- Mazin, I.I., Manni, S., Foyevtsova, K., Jeschke, H.O., Gegenwart, P., Valentí, R. Origin of the insulating state in honeycomb iridates and rhodates, *Phys. Rev. B - Condens. Matter Mater. Phys.* 88 (2013) 1–6. doi:10.1103/PhysRevB.88.035115.
- Mitchell, J.E. *Synthesis and Magnetic Properties of Spinel-Based Transition Metal Oxides and Related Species*, McMaster University, 2009.
- Mitchell, R.H., *Perovskites: Modern and Ancient*, Almaz Press, Thunder Bay, 2002.
- Mitome, M., Okamoto, M., Bando, Y., Yamamura, H., Structure analysis of $\text{Ba}_2\text{In}_2\text{O}_5$ and related compounds by electron microscopy, *J. Vac. Sci. Technol. B Microelectron. Nanom. Struct.* 19 (2001) 2284. doi:10.1116/1.1421566.
- Mittelstädt, L., Schmidt, M., Wang, Z., Mayr, F., Tsurkan, V., Lunkenheimer, P., Ish, D., Balents, L., Deisenhofer, J., Loidl, A., Spin-orbiton and quantum criticality in FeSc_2S_4 , *Phys. Rev. B.* 91 (2015) 125112. doi:10.1103/PhysRevB.91.125112.

- Momma, K., Izumi, F., VESTA 3 for three-dimensional visualization of crystal, volumetric and morphology data, *J. Appl. Crystallogr.* 44 (2011) 1272–1276.
doi:10.1107/S0021889811038970.
- Mugavero, S.J., Gemmill, W.R., Roof, I.P., zur Loye, H.C., Materials discovery by crystal growth: Lanthanide metal containing oxides of the platinum group metals (Ru, Os, Ir, Rh, Pd, Pt) from molten alkali metal hydroxides, *J. Solid State Chem.* 182 (2009) 1950–1963. doi:10.1016/j.jssc.2009.05.006.
- Mugavero, S.J., Smith, M.D., zur Loye, H.-C., $\text{La}_9\text{RbIr}_4\text{O}_{24}$: A Rubidium-Containing Oxide with a New Structure Type, *Inorg. Chem.* 45 (2006) 946–948. doi:10.1021/ic051890s.
- Mugavero, S.J., Smith, M.D., zur Loye, H.-C., The crystal growth and magnetic properties of $\text{Ln}_2\text{LiIrO}_6$ (Ln=La, Pr, Nd, Sm, Eu), *J. Solid State Chem.* 178 (2005) 200–206.
doi:10.1016/j.jssc.2004.10.033.
- Mugavero, S.J., Smith, M.D., Yoon, W.-S., zur Loye, H.-C., $\text{Nd}_2\text{K}_2\text{IrO}_7$ and $\text{Sm}_2\text{K}_2\text{IrO}_7$: Iridium(VI) Oxides Prepared under Ambient Pressure, *Angew. Chemie Int. Ed.* 48 (2009) 215–218. doi:10.1002/anie.200804045.
- Muñoz, A., de la Calle, C., Alonso, J.A., Botta, P., Pardo, V., Baldomir, D., Rivas, J., Crystallographic and magnetic structure of $\text{SrCoO}_{2.5}$ brownmillerite: Neutron study coupled with band-structure calculations, *Phys. Rev. B.* 78 (2008) 54404.
doi:10.1103/PhysRevB.78.054404.
- Obradors, X., Labarta, A., Isalgué, A., Tejada, J., Rodriguez, J., Pernet, M., Magnetic frustration and lattice dimensionality in $\text{SrCr}_3\text{Ga}_4\text{O}_{19}$, *Solid State Commun.* 65 (1988) 189–192. doi:10.1016/0038-1098(88)90885-X.
- Okabe, H., Isobe, M., Takayama-Muromachi, E., Koda, A., Takeshita, S., Hiraishi, M., Miyazaki, M., Kadono, R., Miyake, Y., Akimitsu, J., Ba_2IrO_4 : A spin-orbit Mott insulating quasi-two-dimensional antiferromagnet, *Phys. Rev. B.* 83 (2011) 155118.
doi:10.1103/PhysRevB.83.155118.
- Okamoto, Y., Nohara, M., Aruga-Katori, H., Takagi, H., Spin-liquid state in the $S=1/2$ hyperkagome antiferromagnet $\text{Na}_4\text{Ir}_3\text{O}_8$, *Phys. Rev. Lett.* 99 (2007) 4–7.
doi:10.1103/PhysRevLett.99.137207.
- Orchard, A.F., *Magnetochemistry*, Oxford University Press, New York, 2003.
- Ou, X., Wu, H., Impact of spin-orbit coupling on the magnetism of Sr_3MIrO_6 (M = Ni, Co), *Sci. Rep.* 4 (2014) 4609. doi:10.1038/srep04609.
- Ouchetto, K., Archaimbault, F., Pineau, A., Choisnet, J., Chemical and structural characterization of a new barium ceroplatinate: $\text{Ba}_2\text{CePtO}_6$ a double perovskite mixed oxide, *J. Mater. Sci. Lett.* 10 (1991) 1277–1279. doi:10.1007/BF00720945.
- Patrakeev, M.V., Kharton, V.V., Kozhevnikov, V.L., Bakhteeva, Y.A., Naumovich, E.N., Shaula, A.L., Yaremchenko, A.A., Leonidov, I.A., Marques, F.M.B., Oxygen nonstoichiometry and mixed conductivity of $\text{SrFe}_{1-x}\text{M}_x\text{O}_{3-\delta}$ (M=Al, Ga): Effects of B-site doping, *Solid State Sci.* 8 (2006) 476–487.
- Petitgrand, D., V Maleyev, S., Bourges, P., Ivanov, A.S., Pseudodipolar interaction and antiferromagnetism in $R_2\text{CuO}_4$ compounds ($R = \text{Pr, Nd, Sm, and Eu}$), *Phys. Rev. B.* 59 (1999) 1079–1104. doi:10.1103/PhysRevB.59.1079.

- Pesin, D., Balents, L., Mott physics and band topology in materials with strong spin-orbit interaction, *Nat. Phys.* 6 (2010) 376–381. doi:10.1038/nphys1606.
- Phelan, B.F., Krizan, J., Xie, W., Gibson, Q., Cava, R.J., New material for probing spin-orbit coupling in iridates, *Phys. Rev. B - Condens. Matter Mater. Phys.* 91 (2015) 1–6. doi:10.1103/PhysRevB.91.155117.
- Plumb, K.W., Morey, J., Rodriguez-Rivera, J.A., Wu, H., Podlesnyak, A.A., McQueen, T.M., Broholm, C.L., Antiferromagnetic and Orbital Ordering on a Diamond Lattice Near Quantum Criticality, *arXiv.* (2016) 1–16. <http://arxiv.org/abs/1603.08033>.
- Powell, A.V., Battle, P.D., The electronic properties of non-stoichiometric barium iridate, *BaIrO_{3-δ}*, *J. Alloys Compd.* 191 (1993) 313–318. doi:10.1016/0925-8388(93)90085-2.
- Powell, A.V., Gore, J.G., Battle, P.D., The magnetic properties of iridium in mixed-metal oxides, *J. Alloys Compd.* 201 (1993) 73–84. doi:10.1016/0925-8388(93)90864-J.
- Pullar, R.C., Hexagonal ferrites: A review of the synthesis, properties and applications of hexaferrite ceramics, *Prog. Mater. Sci.* 57 (2012) 1191–1334. doi:10.1016/j.pmatsci.2012.04.001.
- Quantum Design, Physical Property Measurement System Hardware and Operations Manual, 2nd ed., Quantum Design, 1999.
- Ramezanipour, F., Greedan, J.E., Grosvenor, A.P., Britten, J.F., Cranswick, L.M.D., Garlea, V.O., Intralayer Cation Ordering in a Brownmillerite Superstructure: Synthesis, Crystal, and Magnetic Structures of Ca₂FeCoO₅, *Chem. Mater.* 22 (2010) 6008–6020. doi:10.1021/cm1023025.
- Ramirez, A.P., Strongly Geometrically Frustrated Magnets, *Annu. Rev. Mater. Sci.* 24 (1994) 453–480. doi:10.1146/annurev.ms.24.080194.002321.
- Rietveld, H.M., A profile refinement method for nuclear and magnetic structures, *J. Appl. Crystallogr.* 2 (1969) 65–71. doi:10.1107/S0021889869006558.
- Rigaku Corporation, X-Ray Diffractometer MiniFlex II Instruction Manual, 2nd ed., Rigaku Corporation, 2006.
- Rodríguez-Carvajal, J., Recent advances in magnetic structure determination by neutron powder diffraction, *Phys. B Condens. Matter.* 192 (1993) 55–69. doi:10.1016/0921-4526(93)90108-I.
- Rolle, A., Roussel, P., Giridharan, N., Suard, E., Vannier, R., A neutron diffraction study of the oxygen diffusion in molybdenum doped Ba₂In₂O₅, *Solid State Ionics.* 179 (2008) 1986–1995. doi:10.1016/j.ssi.2008.06.021.
- Rolle, A., Daviero-Minaud, S., Roussel, P., Rubbens, A., Vannier, R.N., Structure of Ba₂In_{2-x}V_xO_{5+x} phases: Complementarity of diffraction, Raman and absorption techniques, *Solid State Ionics.* 179 (2008) 771–775. doi:10.1016/j.ssi.2008.01.068.
- Sakamoto, T., Doi, Y., Hinatsu, Y., Crystal structures and magnetic properties of 6H-perovskite-type oxides Ba₃MIr₂O₉ (M=Mg, Ca, Sc, Ti, Zn, Sr, Zr, Cd and In), *J. Solid State Chem.* 179 (2006) 2595–2601. doi:10.1016/j.jssc.2006.04.055.
- Sasaki, S., Prewitt, C.T., Liebermann, R.C., The crystal structure of CaGeO₃ perovskite and the crystal chemistry of the GdFeO₃-type perovskites, *Am. Mineral.* 68 (1983) 1189–1198.

- Segal, N., Vente, J.F., Bush, T.S., Battle, P.D., Structural and magnetic properties of $\text{Sr}_{4-x}\text{M}_x\text{IrO}_6$ (M = Ca, Zn, Cd, Li, Na), *J. Mater. Chem.* 6 (1996) 395–401.
doi:10.1039/JM9960600395.
- Siegrist, T., Chamberland, B.L., The crystal structure of BaIrO_3 , *J. Less-Common Met.* 170 (1990) 93–99.
- Shannon, R.D., Revised effective ionic radii and systematic studies of interatomic distances in halides and chalcogenides, *Acta Crystallogr. Sect. A.* 32 (1976) 751–767.
doi:10.1107/S0567739476001551.
- Shimoda, Y., Doi, Y., Wakeshima, M., Hinatsu, Y., Magnetic properties of quadruple perovskites $\text{Ba}_4\text{LnRu}_3\text{O}_{12}$ (Ln=La, Nd, Sm–Gd, Dy–Lu), *J. Solid State Chem.* 183 (2010) 33–40. doi:10.1016/j.jssc.2009.10.007.
- Shin, S., Hatakeyama, Y., Ogawa, K., Shimomura, K., Catalytic Decomposition of NO over brownmillite-like compounds, $\text{Ca}_2\text{Fe}_2\text{O}_5$ and $\text{Sr}_2\text{Fe}_2\text{O}_5$, *Mater. Res. Bull.* 14 (1979) 133–136.
- Singh, Y., Manni, S., Reuther, J., Berlijn, T., Thomale, R., Ku, W., Trebst, S., Gegenwart, P., Relevance of the Heisenberg-Kitaev model for the honeycomb lattice iridates A_2IrO_3 , *Phys. Rev. Lett.* 108 (2012) 1–5. doi:10.1103/PhysRevLett.108.127203.
- Sleight, A.W., New ternary oxides of Re, Os, Ir and Pt with cubic crystal structures, *Mater. Res. Bull.* 9 (1974) 1177–1184. doi:10.1016/0025-5408(74)90035-X.
- Sleight, A.W., Longo, J.M., Ward, R., Compounds of Osmium and Rhenium with the Ordered Perovskite Structure, *Inorg. Chem.* 1 (1962) 245–250. doi:10.1021/ic50002a010.
- Speakman, S.A., Misture, S.T., In-Situ X-Ray and Neutron Diffraction Study of $\text{Ba}_2\text{In}_2\text{O}_5$, *Mater. Sci. Forum.* 378–381 (2001) 339–339.
- Subramanian, M.A., Aravamudan, G., Subba Rao, G.V., Oxide pyrochlores - A review, *Prog. Solid State Chem.* 15 (1983) 55–143. doi:10.1016/0079-6786(83)90001-8.
- Subramanian, M.A., Ramirez, A.P., Marshall, W.J., Structural Tuning of Ferromagnetism in a 3D Cuprate Perovskite, *Phys. Rev. Lett.* 82 (1999) 1558–1561.
doi:10.1103/PhysRevLett.82.1558.
- Sullivan, E., Greaves, C., Fluorine insertion reactions of the brownmillerite materials $\text{Sr}_2\text{Fe}_2\text{O}_5$, $\text{Sr}_2\text{CoFeO}_5$, and $\text{Sr}_2\text{Co}_2\text{O}_5$, *Mater. Res. Bull.* 47 (2012) 2541–2546.
doi:10.1016/j.materresbull.2012.05.002.
- Suzuki, T., Nagai, H., Nohara, M., Takagi, H. Melting of antiferromagnetic ordering in spinel oxide CoAl_2O_4 , *J. Phys. Condens. Matter.* 19 (2007) 145265. doi:10.1088/0953-8984/19/14/145265.
- Takagi, H., Niitaka, S., Highly Frustrated Magnetism in Spinel, in: C. Lacroix, P. Mendels, F. Mila (Eds.), *Introd. to Frustrated Magn.*, Springer Berlin Heidelberg, Berlin, 2010: pp. 155–175. doi:10.1007/978-3-642-10589-0.
- Takayama, T., Kato, A., Dinnebier, R., Nuss, J., Kono, H., Veiga, L.S.I., Fabbris, G., Haskel, D., Takagi, H., Hyperhoneycomb iridate $\beta\text{-Li}_2\text{IrO}_3$ as a platform for Kitaev Magnetism, *Phys. Rev. Lett.* 114 (2015) 2–6. doi:10.1103/PhysRevLett.114.077202.

- Talanov, A., Phelan, W.A., Kelly, Z.A., Siegler, M.A., McQueen, T.M., Control of the iridium oxidation state in the hollandite iridate solid solution $K_{1-x}Ir_4O_8$, *Inorg. Chem.* 53 (2014) 4500–4507. doi:10.1021/ic5001667.
- Taniguchi, K., Abe, N., Ohtani, S., Umetsu, H., Arima, T.H., Ferroelectric polarization reversal by a magnetic field in multiferroic Y-type hexaferrite $Ba_2Mg_2Fe_{12}O_{12}$, *Appl. Phys. Express.* 1 (2008) 0313011–0313013. doi:10.1143/APEX.1.031301.
- Terasaki, I., Ito, S., Igarashi, T., Asai, S., Taniguchi, H., Okazaki, R., Yasui, Y., Kobayashi, K., Kumai, R., Nakao, H., Murakami, Y., Novel Charge Ordering in the Trimer Iridium Oxide $BaIrO_3$, *Crystals.* 6 (2016) 27. doi:10.3390/cryst6030027.
- Thumm, I., Treiber, U., Kemmler-Sack, S., Über Sauerstoffperowskite mit fünf- und vierwertigem Iridium Verbindungen vom Typ $Ba_2B^{3+}Ir^{5+}O_6$ und $Ba_3B^{3+}Ir^{4,5+}_2O_9$, *J. Solid State Chem.* 35 (1980) 156–166. doi:10.1016/0022-4596(80)90488-0.
- Thumm, I., Treiber, U., Kemmler-Sack, S., Zur Struktur von $Ba_3SmRu_2O_9$, $Ba_3SmIrRuO_9$ und Ba_2InIrO_6 , *Zeitschrift Für Anorg. Und Allg. Chemie.* 477 (1981) 161–166. doi:10.1002/zaac.19814770622.
- Toby, B.H., EXPGUI, a graphical user interface for GSAS, *J. Appl. Crystallogr.* 34 (2001) 210–213. doi:10.1107/S0021889801002242.
- Tokunaga, Y., Kaneko, Y., Okuyama, D., Ishiwata, S., Arima, T., Wakimoto, S., Kakurai, K., Taguchi, Y., Tokura, Y. Multiferroic M-type hexaferrites with a room-temperature conical state and magnetically controllable spin helicity, *Phys. Rev. Lett.* 105 (2010) 17–20. doi:10.1103/PhysRevLett.105.257201.
- Tovar, M., Torabi, R., Welker, C., Fleischer, F., Structural and magnetic properties of Cu-Ni-Cr spinel oxides, *Phys. B Condens. Matter.* 385–386 I (2006) 196–198. doi:10.1016/j.physb.2006.05.181.
- Tilley, R.J.D., *Understand Solids: The Science of Materials*, 1st ed., John Wiley & Sons, Ltd, West Sussex, 2004.
- Ueno, G., Sato, S., Kino, Y., The low-temperature tetragonal phase of $NiCr_2O_4$, *Acta Crystallogr. Sect. C Cryst. Struct. Commun.* 55 (1999) 1963–1966. doi:10.1107/S0108270199011713.
- ULVAC-RIKO, Inc., Model ZEM-3 Thermoanalyzer: Power Conversion Efficiency Measuring Instrument Instruction Manual.
- Vasala, S., Karppinen, M., $A_2B'B''O_6$ perovskites: A review, *Prog. Solid State Chem.* 43 (2015) 1–36. doi:10.1016/j.progsolidstchem.2014.08.001.
- Wakeshima, M., Harada, D., Hinatsu, Y., Crystal structures and magnetic properties of ordered perovskites $A_2R^{3+}Ir^{5+}O_6$ (A=Sr, Ba; R=Sc, Y, La, Lu), *J. Alloys Compd.* 287 (1999) 130–136.
- West, A.R., *Basic Solid State Chemistry*, 2nd ed., John Wiley & Sons, Ltd, New York, 1999.
- Witczak-Krempa, W., Chen, G., Kim, Y.B., Balents, L., Correlated Quantum Phenomena in the Strong Spin-Orbit Regime, *Annu. Rev. Condens. Matter Phys.* 5 (2014) 57–82. doi:10.1146/annurev-conmatphys-020911-125138.

- Wollan, E.O., Koehler, W.C., Neutron Diffraction Study of the Magnetic Properties of the Series of Perovskite-Type Compounds $[(1-x)\text{La}, x\text{Ca}]\text{MnO}_3$, *Phys. Rev.* 100 (1955) 545–563. doi:10.1103/PhysRev.100.545.
- Woodward, P.M., Octahedral Tilting in Perovskites. I. Geometrical Considerations, *Acta Crystallogr. Sect. B Struct. Sci.* 53 (1997) 32–43. doi:10.1107/S0108768196010713.
- Woodward, P.M., Octahedral Tilting in Perovskites. II. Structure Stabilizing Forces, *Acta Crystallogr. Sect. B Struct. Sci.* 53 (1997) 44–66.
- Yang, L., Pisoni, A., Magrez, A., Katrych, S., Arakcheeva, A., Dalla Piazza, B., Prša, K., Jaćimović, J., Akrap, A., Teyssier, J., Forró, L., Rønnow, H.M., Crystal Structure, Transport, and Magnetic Properties of an Ir^{6+} Compound $\text{Ba}_8\text{Al}_2\text{IrO}_{14}$, *Inorg. Chem.* 54 (2015) 4371–4376. doi:10.1021/acs.inorgchem.5b00157.
- Yao, T., Uchimoto, Y., Kinuhata, M., Inagaki, T., Yoshida, H., Crystal structure of Ga-doped $\text{Ba}_2\text{In}_2\text{O}_5$ and its oxide ion conductivity, *Solid State Ionics.* 132 (2000) 189–198. doi:10.1016/S0167-2738(00)00658-5.
- Zhang, G.B.B., Smyth, D.M.M., Defects and transport of the brownmillerite oxides with high oxygen ion conductivity - $\text{Ba}_2\text{In}_2\text{O}_5$, *Solid State Ionics.* 82 (1995) 161–172. doi:10.1016/0167-2738(95)00196-2.
- Zhao, J.G., Yang, L.X., Yu, Y., Li, F.Y., Yu, R.C., Fang, Z., Chen, L.C., Jin, C.Q., High-pressure synthesis of orthorhombic SrIrO_3 perovskite and its positive magnetoresistance, *J. Appl. Phys.* 103 (2008) 1–6. doi:10.1063/1.2908879.
- Zhao, J.G., Yang, L.X., Yu, Y., Li, F.Y., Yu, R.C., Jin, C.Q., Physical properties of the 5M BaIrO_3 : A new weak ferromagnetic iridate synthesized under high pressure, *Solid State Commun.* 150 (2010) 36–39. doi:10.1016/j.ssc.2009.10.012.
- Zhao, J.G., Yang, L.X., Yu, Y., Li, F.Y., Yu, R.C., Jin, C.Q., Structural and physical properties of the 6M BaIrO_3 : a new metallic iridate synthesized under high pressure., *Inorg. Chem.* 48 (2009) 4290–4. doi:10.1021/ic801707m.

Appendix A: Linear Magnetoresistance in BaIrO₃

Abstract

BaIrO₃ was found to exhibit non-saturating positive linear magnetoresistance (LMR), despite ferromagnetic order, which usually results in a negative saturating magnetoresistance. Based on other reports of positive LMR in literature, we believe the phenomenon in BaIrO₃ caused by quantum interference effects. The anomalous Hall effect was also observed and the sign of the charge carriers was found primarily positive based on experimental Hall coefficients with some fluctuations in carrier sign around T_C . This behavior may be attributed to either a depletion of carrier concentration due to the opening of the band gap or an anisotropic scattering time which has been observed in quasi-one-dimensionality of the 9M crystal structure.

A.1 Introduction

A.1.1 BaIrO₃

BaIrO₃ crystallizes at ambient temperature and pressure as a monoclinically distorted, quasi-one-dimensional 9R polytype structure (often called a “9M” polytype) with $C2/m$ symmetry. It can be described as a zigzag network of corner-sharing Ir₃O₁₂ trimers of face-sharing IrO₆ octahedra aligned roughly along the c axis (Figure A.1a) [1]. In addition to the 9M polytype, two monoclinically distorted 5H and 6H polytypes (or “5M” and “6M”) have been stabilized [2,3]. The 5M polytype (Figure A.1b) forms at 3.0 GPa and is stable up to 5.0 GPa where the 6M polytype (Figure A.1c) forms and is stable up to 10.0 GPa [4]. Above 10 GPa, BaIrO₃ crystallizes as an ideal perovskite structure or 3C polytype. This transition series is

similar to that of BaRuO₃ which transitions according to a 9R-4H-6H-3C sequence with increasing pressure [5–7].

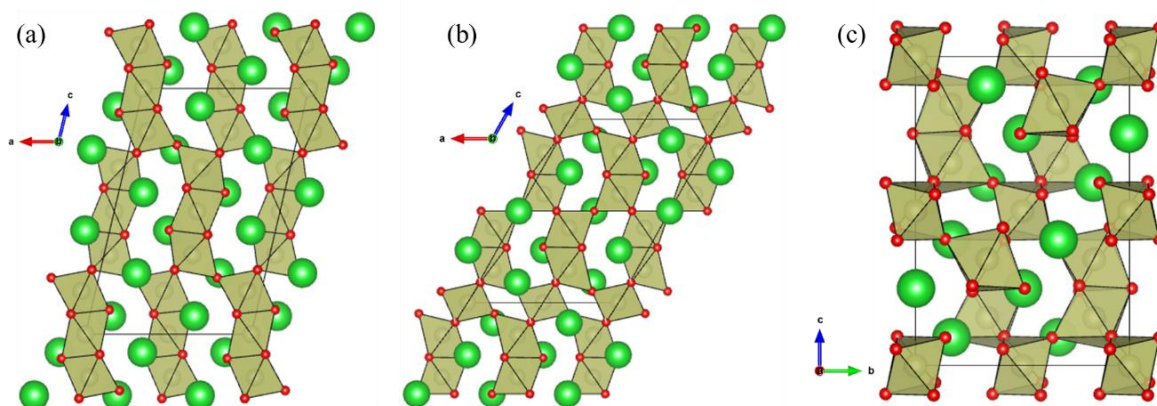


Figure A.1. Crystal structures of the (a) 9M, (b) 5M, and (c) 6M polymorphs of BaIrO₃ (Ba = green, Ir = brown, O = red).

The 9M phase of BaIrO₃ has been studied extensively in recent years and is theorized to be spin-orbit Mott insulator (SOMI) [8]. It is a weak ferromagnet with a saturated moment of only $\sim 0.04 \mu_B$ which was originally thought to be due to canted antiferromagnetic interactions [9]. However, more recent studies have argued the low moment is due to $d-p$ orbital hybridization and small exchange splitting [10]. Interestingly, the ferromagnetic transition is accompanied by a simultaneous anomaly in the electrical resistivity at the T_C that is consistent with the formation of a charge density wave. Its magnetic behavior, electrical resistivity and thermopower have all been reported to have anisotropic properties due to the distinctive crystal structure [10,11].

A.1.2 Magnetoresistance

Magnetoresistance, often called “ordinary” magnetoresistance (OMR), was first reported by William Thomson in 1856 [12] and is a phenomenon that involves the change in the electrical resistivity upon application of a magnetic field (H). In OMR, when a conductive material is placed in a magnetic field that is perpendicular to the current flow (I) in the material, the trajectory of the charge carriers becomes curved. This increases the number of scattering events and causes an increase in the resistivity of the material ranging from a few percent to as high as 200% [13].

Magnetic order adds a layer of complexity and gives rise to several unique types of magnetoresistance. For example “giant” magnetoresistance and “tunneling” magnetoresistance are the result of separating ferromagnetic thin films with either antiferromagnetic nor insulating materials [14,15]. These effects have led to many advancements in spintronic devices such as memory storage [16] but the magnetoresistance in bulk ferromagnetic materials is different. While most materials have a positive magnetoresistance for reasons discussed above, ferromagnets exhibit negative magnetoresistance (NMR) due to ordering of electronic spin domains. The magnitude of the effect is typically $< 30\%$ and is most intense near the Curie temperature (T_C).

Bulk ferromagnets also exhibit “anisotropic” magnetoresistance (AMR) meaning the effect is different depending on whether H is perpendicular (\perp) or parallel (\parallel) to I . AMR can be defined as $\Delta\rho_{\text{AMR}} = \rho_{\parallel} - \rho_{\perp}$ [17] and is a result of spin-orbit coupling (SOC). The magnitude of AMR will, therefore, vary from material to material depending on the strength of the SOC and orbital anisotropy [18].

The dependence of OMR on H is typically quadratic (i.e. H^2) [19]; however, some materials display linear magnetoresistance (LMR) such as elemental bismuth [20]. LMR is somewhat uncommon but can occur in specific circumstances. The most common route to LMR is through disorder which causes fluctuations in carrier mobility. Disorder can also lead to positive LMR in ferromagnetic materials due to quantum interference effects [21]. The combination of ferromagnetic ordering and disorder leads to electron-electron interactions that cause their wavefunctions to interfere coherently. This theory has been previously proposed to explain the behavior observed in disordered paramagnetic metals [22].

A.3 Characterization of BaIrO₃

A.3.1 Single Crystals

Single crystals of BaIrO₃ were prepared via a molten flux reaction of BaCl₂ and IrCl₃. The sizes of the crystals were varied and the crystal shapes tended to be anisotropic with dimensions of the larger ones being about 1 mm × 0.5 mm × 0.5 mm (Figure A.2). The anisotropic shape makes sense considering the length of the c axis of the unit relative to the a and b axes. The purity and crystal structure of single crystals was confirmed using powder XRD diffraction.

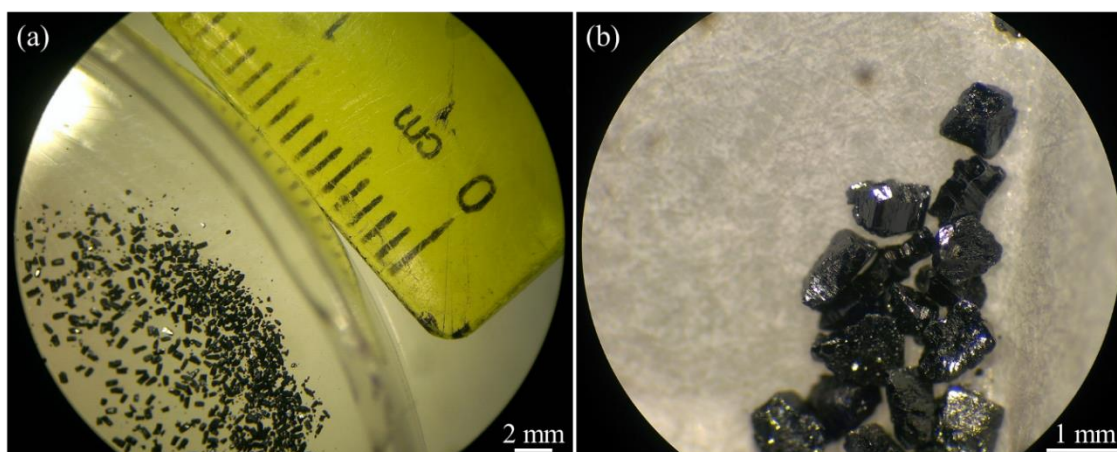


Figure A.2. Photos of example BaIrO_3 single crystals showing (a) relative size and (b) close-up view of crystal shapes.

A.3.2 Electronic Properties

Resistivity ($\rho(T)$) data (Figure A.3) for BaIrO_3 shows semiconductor with an unusual bump in the data at $T_C \approx 160$ K.

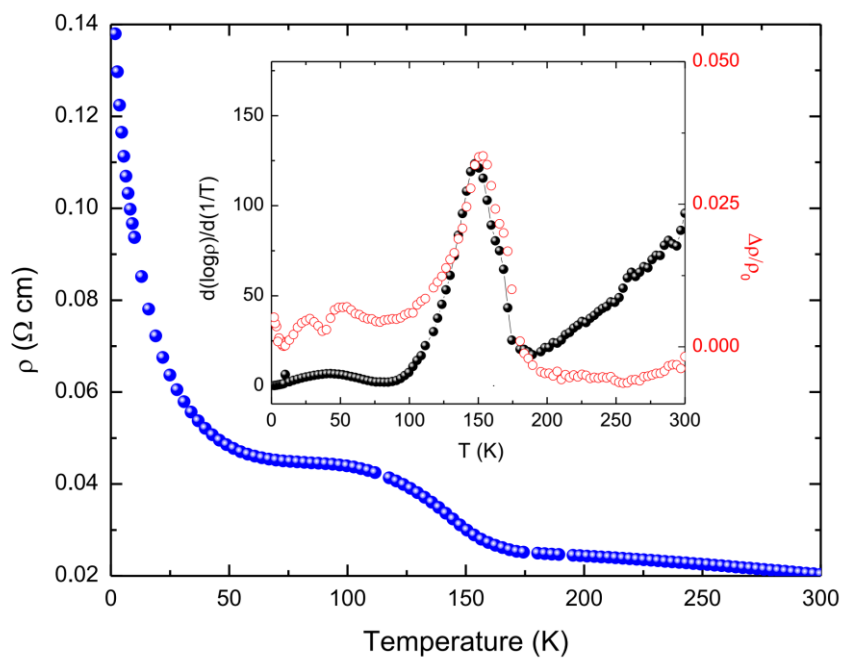


Figure A.3. $\rho(T)$ plot for BaIrO_3 exhibiting an anomaly at $T_C \approx 160$ K. Inset is an overlay plot of $-d \log \rho / d(T^{-1})$ and $\Delta\rho/\rho_0(T)$.

This feature has been reported in literature and attributed to the formation of a charge density wave and the opening of a small band gap [10,23]. The derivative of the resistivity, $-d \log \rho / d(T^{-1})$, exhibits a negative intensity peak at T_C likely due to the onset of ferromagnetic order. Similar peaks are commonly observed in ferromagnets but are usually positive as ferromagnets are typically metallic conductors [24].

As mentioned earlier, BaIrO₃ is known to exhibit weak ferromagnetism with a very small ordered moment of $\sim 0.04 \mu_B/\text{Ir}$ [10]. Thus, the magnetoresistance ($\Delta\rho/\rho_0$) for BaIrO₃ is expected to be negative. Contrary to this prediction, $\Delta\rho/\rho_0$ was found to be positive (Figure A.3 inset) exhibiting a peak at T_C . There are examples of ferromagnet metals with peaks in $\Delta\rho/\rho_0(T)$ near T_C in literature such as Pr_{0.5}Sr_{0.5}CoO₃ and La_{0.7}Sr_{0.3}MO₃ perovskites [25,26], however, the peaks for these compounds were all negative in sign.

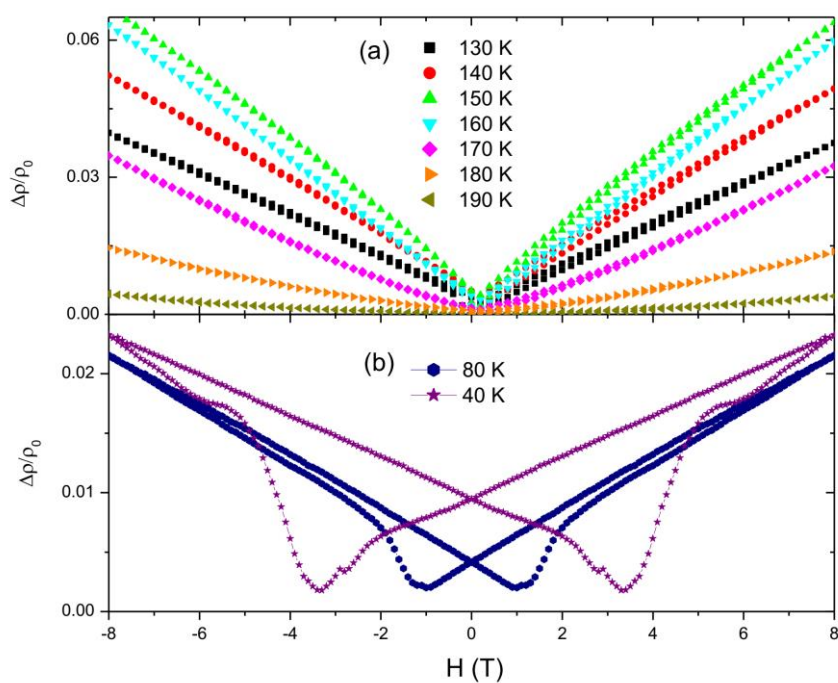


Figure A.4. Plots of $\Delta\rho/\rho_0(H)$ BaIrO₃ (a) near $T_C \approx 160$ K and (b) well below T_C .

This suggests the $\Delta\rho/\rho_0(T)$ behavior is more complex. The field dependence of $\Delta\rho/\rho_0$ supports a more complex mechanism as positive LMR is observed in $\Delta\rho/\rho_0(H)$ within ± 30 K of T_C (Figure A.4). Hysteresis is observed in $\Delta\rho/\rho_0(H)$ well below T_C due to ferromagnetic ordering.

In addition to the positive LMR, BaIrO₃ exhibits the anomalous Hall effect (AHE), where transverse resistivity (ρ_{xy}) has a dependence on the magnetization (M) in the sample, behavior common to ferromagnets. The relationship between AHE and the H -dependence of ρ_{xy} can be expressed as $\rho_{xy} = R_H H + R_{\text{AHE}} M$ where R_H and R_{AHE} are the “normal” and anomalous Hall coefficients, respectively [27]. The $\rho_{xy}(H)$ data for BaIrO₃ are plotted in Figure A.5.

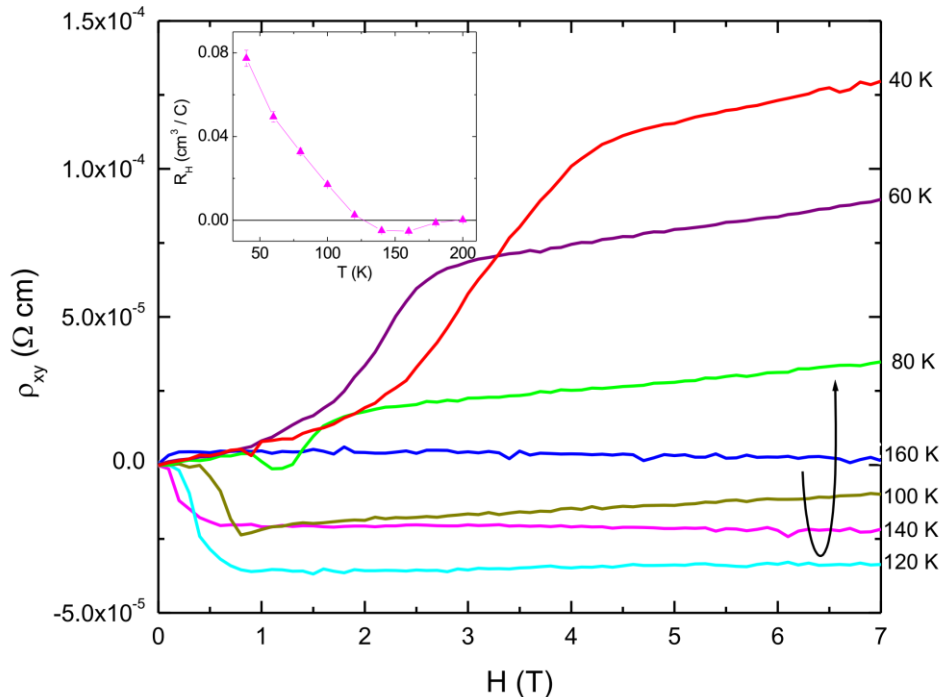


Figure A.5. $\rho_{xy}(T)$ plot for BaIrO₃ for $T = 40$ – 160 K. The black arrow is a guide for the trend for decreasing T . The inset is a plot of $R_H(T)$ exhibiting a positive-negative-positive sign change near T_C .

The AHE term dominates ρ_{xy} at low H , meaning R_H can be extracted increasing H until M is saturated effectively producing a constant AHE term. While the sign of R_H is primarily positive and correlates well with previous thermopower studies on BaIrO_3 [11,23], there is a slight transition with decreasing temperature from positive to negative then back to positive around T_C (Figure A.5 inset). This behavior may be attributed to either a depletion of carrier concentration due to the opening of the band gap, as observed in some transition metal dichalcogenides [28], or an anisotropic scattering time which has been observed in quasi-one-dimensional metals [29].

Positive LMR has also been observed in ferromagnets with strong disorder and low carrier densities [21] as well as in geometrically-constrained ferromagnetic thin films [30]. In both of these studies, the positive LMR is similar to BaIrO_3 and shows no indication of saturation even at high T , suggesting a similar mechanism for the LMR in all three systems. The models for both the thin film and low carrier density systems link the positive LMR to quantum interference effects. These models do not fit BaIrO_3 perfectly as our samples are single crystals, not thin films and our Hall measurements yield a relatively high carrier density on the order of 10^{22} cm^{-3} . We therefore speculate that the quasi-one-dimensional structure of BaIrO_3 makes it more susceptible to disorder and contributes to quantum interference effects.

A.4 Conclusions and Future Studies

Our studies show that BaIrO_3 exhibits an AHE and unexpected positive LMR, the latter of which we attribute to quantum interference effect. These properties arise in part due to the

large SOC, competing energy scales, and possibly the quasi-one-dimensionality of the 9M structure. Future studies on polycrystalline samples, which have a cleaner gap [31], may provide further insight into the effects of disorder, as well as into the significance of the quasi-one-dimensionality, which will no longer be in play.

One remaining mystery concerns $\Delta\rho/\rho_0(T)$, which appears near T_C , implying a relationship to the charge or magnetic order where the spin or charge fluctuations associated with the low- T ordering might augment the quantum effects. Future studies that clarify the nature of the charge order in this system, and its relation to the magnetic order, may help us further comprehend the positive LMR in BaIrO₃.

A.5 Methods and Materials

Single crystals of were prepared using IrCl₃ · xH₂O in a BaCl₂ flux, which were ground together via mortar and pestle. The mixture was heated at 1000–1025 °C for 3 h in an alumina crucible and then cooled at a rate of 2 °C/h to 900 °C, then allowed to cool to room temperature. The excess BaCl₂ was dissolved by submerging in an ultrasonic water bath and the BaIrO₃ crystals were then filtered, collected, and dried. Silver epoxy was used for current/voltage contacts and were applied directly to the single crystals. All transport measurements were performed in a commercial cryostat in a standard DC four-probe configuration with the current, I , parallel to the c axis.

A.6 References

- [1] T. Siegrist, B.L. Chamberland, The crystal structure of BaIrO₃, *J. Less-Common Met.* 170 (1990) 93–99.
- [2] J.G. Zhao, L.X. Yang, Y. Yu, F.Y. Li, R.C. Yu, C.Q. Jin, Physical properties of the 5M BaIrO₃: A new weak ferromagnetic iridate synthesized under high pressure, *Solid State Commun.* 150 (2010) 36–39. doi:10.1016/j.ssc.2009.10.012.
- [3] J. Zhao, L. Yang, Y. Yu, F. Li, R. Yu, C. Jin, Structural and physical properties of the 6M BaIrO₃: a new metallic iridate synthesized under high pressure, *Inorg. Chem.* 48 (2009) 4290–4. doi:10.1021/ic801707m.
- [4] J.-G. Cheng, J.A. Alonso, E. Suard, J.-S. Zhou, J.B. Goodenough, A new perovskite polytype in the high-pressure sequence of BaIrO₃, *J. Am. Chem. Soc.* 131 (2009) 7461–9. doi:10.1021/ja901829e.
- [5] C.Q. Jin, J.-S. Zhou, J.B. Goodenough, Q.Q. Liu, J.G. Zhao, L.X. Yang, Y. Yu, R.C. Yu, T. Katsura, A. Shatskiy, E. Ito, High-pressure synthesis of the cubic perovskite BaRuO₃ and evolution of ferromagnetism in ARuO₃ (A = Ca, Sr, Ba) ruthenates., *Proc. Natl. Acad. Sci. U. S. A.* 105 (2008) 7115–7119. doi:10.1073/pnas.0710928105.
- [6] S.-T. Hong, A.W. Sleight, Crystal Structure of 4H BaRuO₃: High Pressure Phase Prepared at Ambient Pressure, *J. Solid State Chem.* 128 (1997) 251–255. doi:http://dx.doi.org/10.1006/jssc.1996.7200.
- [7] P.C. Donohue, L. Katz, R. Ward, The Crystal Structure of Barium Ruthenium Oxide and Related Compounds, *Inorg. Chem.* 4 (1965) 306–310. doi:10.1021/ic50025a010.
- [8] W. Ju, G.Q. Liu, Z. Yang, Exotic spin-orbital Mott insulating states in BaIrO₃, *Phys. Rev. B - Condens. Matter Mater. Phys.* 87 (2013) 1–6. doi:10.1103/PhysRevB.87.075112.
- [9] R. Lindsay, W. Strange, B.L. Chamberland, R.O. Moyer, Weak ferromagnetism in BaIrO₃, *Solid State Commun.* 86 (1993) 759–763. doi:10.1016/0038-1098(93)90186-Q.
- [10] G. Cao, J.E. Crow, R.P. Guertin, P.F. Henning, C.C. Homes, M. Strongin, D.N. Basov, E. Lochner, Charge density wave formation accompanying ferromagnetic ordering in quasi-one-dimensional BaIrO₃, *Solid State Commun.* 113 (2000) 657–662.
- [11] T. Nakano, I. Terasaki, Giant nonlinear conduction and thyristor-like negative differential resistance in BaIrO₃ single crystals, *Phys. Rev. B.* 73 (2006) 3–4. doi:10.1103/PhysRevB.73.195106.
- [12] W. Thomson, On the Electro-Dynamic Qualities of Metals:--Effects of Magnetization on the Electric Conductivity of Nickel and of Iron, *Proc. R. Soc. London.* 8 (1856) 546–550. doi:10.1098/rspl.1856.0144.
- [13] D. Feng, G. Jin, *Introduction to condensed matter physics*, World Scientific, Hackensack, New Jersey, 2005.

- [14] M.N. Baibich, J.M. Broto, A. Fert, F.N. Van Dau, F. Petroff, P. Eitenne, G. Creuzet, A. Friederich, J. Chazelas, Giant magnetoresistance of (001)Fe/(001)Cr magnetic superlattices, *Phys. Rev. Lett.* 61 (1988) 2472–2475. doi:10.1103/PhysRevLett.61.2472.
- [15] S. Yuasa, T. Nagahama, A. Fukushima, Y. Suzuki, K. Ando, Giant room-temperature magnetoresistance in single-crystal Fe/MgO/Fe magnetic tunnel junctions, *Nat. Mater.* 3 (2004) 868–871. doi:10.1038/nmat1257.
- [16] S.A. Wolf, D.D. Awschalom, R.A. Buhrman, J.M. Daughton, S. von Molnár, M.L. Roukes, A.Y. Chtchelkanova, D.M. Treger, Spintronics: A Spin-Based Electronics Vision for the Future, *Science* (80-.). 294 (2001) 1488–1495. doi:10.1126/science.1065389.
- [17] T.R. Mcguire, R.I. Potter, Anisotropic Magnetoresistance in Ferromagnetic 3d Alloys, *IEEE Trans. Magn.* 11 (1975) 1018–1038. doi:10.1109/TMAG.1975.1058782.
- [18] M. Getzlaff, *Fundamentals of magnetism*, Springer, Berlin, 2008.
- [19] A.B. Pippard, *Magnetoresistance in metals*, Cambridge University Press, New York, 1989.
- [20] P. Kapitza, The Study of the Specific Resistance of Bismuth Crystals and Its Change in Strong Magnetic Fields and Some Allied Problems, *Proc. R. Soc. A Math. Phys. Eng. Sci.* 119 (1928) 358–443. doi:10.1098/rspa.1928.0103.
- [21] N. Manyala, Y. Sidis, J. DiTusa, G. Aeppli, D. Young, Z. Fisk, Magnetoresistance from quantum interference effects in ferromagnets, *Nature*. 404 (2000) 581–4. doi:10.1038/35007030.
- [22] P.A. Lee, T. V. Ramakrishnan, Disordered electronic systems, *Rev. Mod. Phys.* 57 (1985) 287–337. doi:10.1103/RevModPhys.57.287.
- [23] N.S. Kini, A. Bentien, S. Ramakrishnan, C. Geibel, Specific heat and transport study of the co-existence of charge-density-wave and weak ferromagnetism in BaIrO₃, *Phys. B Condens. Matter.* 359–361 (2005) 1264–1266. doi:10.1016/j.physb.2005.01.395.
- [24] M.E. Fisher, J.S. Langer, Resistive anomalies at magnetic critical points, *Phys. Rev. Lett.* 20 (1968) 665–668. doi:10.1103/PhysRevLett.20.665.
- [25] R. Mahendiran, P. Schiffer, Double magnetic transition in Pr_{0.5}Sr_{0.5}CoO₃, *Phys. Rev. B.* 68 (2003) 24427. doi:10.1103/PhysRevB.68.024427.
- [26] Y. Wenhao, Y. Zhang, D. Cao, J. Yang, W. Bai, Y. Chen, G. Wang, X. Dong, C. Duan, X. Tang, Highly orientated growth and characterization of La_{0.7}Sr_{0.3}MnO₃ thin films with different orientations on SrTiO₃ substrates by chemical solution deposition method, *J. Appl. Phys.* 117 (2015) 3–7. doi:10.1063/1.4906947.
- [27] N. Nagaosa, J. Sinova, S. Onoda, A.H. MacDonald, N.P. Ong, Anomalous Hall effect, *Rev. Mod. Phys.* 82 (2010) 1539–1592. doi:10.1103/RevModPhys.82.1539.
- [28] D. V. Evtushinsky, A.A. Kordyuk, V.B. Zabolotnyy, D.S. Inosov, B. Büchner, H. Berger, L. Patthey, R. Follath, S. V. Borisenko, Pseudogap-Driven Sign Reversal of the

- Hall Effect, *Phys. Rev. Lett.* 100 (2008) 236402.
doi:10.1103/PhysRevLett.100.236402.
- [29] N. Wakeham, N.E. Hussey, Hall effect in quasi-one-dimensional metals in the presence of anisotropic scattering, *Phys. Rev. B - Condens. Matter Mater. Phys.* 85 (2012) 1–5.
doi:10.1103/PhysRevB.85.235117.
- [30] A. Gerber, I. Kishon, I.Y. Korenblit, O. Riss, A. Segal, M. Karpovski, B. Raquet, Linear positive magnetoresistance and quantum interference in ferromagnetic metals, *Phys. Rev. Lett.* 99 (2007) 1–4. doi:10.1103/PhysRevLett.99.027201.
- [31] J.G. Zhao, L.X. Yang, K. Mydeen, F.Y. Li, R.C. Yu, C.Q. Jin, Effects of pressure on electrical property of BaIrO₃, *Solid State Commun.* 148 (2008) 361–364.
doi:10.1016/j.ssc.2008.09.043.